Regulation of adipose tissue biology by mitochondrial protease CLPP

Inaugural-Dissertation

Zur

Erlangung des Doktorgrades

der Mathematisch-Naturwissenschaftlichen Fakultät

der Universität zu Köln

vorgelegt von

Harshita Kaul

aus Indien

Köln 2023

Berichterstatter: Prof. Dr. Aleksandra Trifunovic

                       Prof. Dr. Thomas Langer

Tag der mündlichen Prüfung: 13. Dezember 2023

If you can keep your head when all about you

Are losing theirs and blaming it on you,

If you can trust yourself when all men doubt you,

But make allowance for their doubting too;

.

.

If you can make one heap of all your winnings

And risk it on one turn of pitch-and-toss,

And lose, and start again at your beginnings

And never breathe a word about your loss;

If you can force your heart and nerve and sinew

To serve your turn long after they are gone,

And so hold on when there is nothing in you

Except the Will which says to them: 'Hold on!'

.

.

Yours is the Earth and everything that's in it,
And—which is more—you'll be a Man, my son! ''

- ' If ' by Rudyard Kipling

To nani, mamma and me

TABLE OF CONTENTS

List of Figures

Introduction

Results - Chapter 1

Results - Chapter 2

Discussion

List of Tables

Abbreviations

^{18}F-FDG-PET – Flourine-18 fluorodeoxyglucose positron emission tomography
1C – One carbon
AAR – Amino acid response
ACC - Acetyl coA carboxylase
ACC – Acetyl coA carboxylase
ACLY - Acetyl coA lyase
ACLY – ATP citrate lyase
ACS - Acyl-coA synthases
ACS – acetyl-CoA synthetase
ACSL5 – Long-chain-fatty-acid—coA ligase 5
ACSS1 - Acyl-CoA synthetase short chain family member 1
ACSS1 – Acyl-coA synthetase short chain family member 1
ADP - Adenosine diphosphate
AMP - Adenosine monophosphate
ASNS – Asparagine synthetase (glutamine-hydrolyzing)
ATF3 – Activating transcription factor 3
ATF4 – Activating transcription factor 4
ATF5 – Activating transcription factor 5
ATGL – Adipose triglyceride lipase
ATP - Adenosine triphosphate
BAT – Brown adipose tissue
BCAA – Branch chain amino acids
BCFA – Branch chain fatty acids
BiP – Binding immunoglobin protein
BMP7 - Bone morphogenic protein 7
BMPs – Bone Morphogenic Proteins
C/EBPs – CCAAT-enhancer-binding proteins
CACT - Carnitine- acylcarnitine translocase
CACT – Carnitine-acylcarnitine translocase
CAMKII – Ca^{2+}/calmodulin-dependent protein kinase II
cAMP – cyclic AMP
CARE - CCAAT-enhancer binding protein-activating transcription factor response element
CBP - CCAAT/enhancer-binding protein
CGI-58 – Comparative gene identification-58
CHOP – CCAAT/enhancer binding protein (C/EBP) homology protein
ChREBP - Carbohydrate response element-binding protein
CI – Complex I
CIDEA – Cell death-inducing DNA fragmentation factor-like effector A
CII – Complex II
CIII – Complex III

CIV – Complex IV

CJs - Cristae Junctions

CK – Creatine kinase

CLPP - Caseinolytic peptidase P proteolytic subunit

CLPs- Common lymphoid progenitors

CLPX - Caseinolytic peptidase X

CM - Cytoplasmic mitochondria

CMP- Common myeloid progenitors

CoQ – Coenzyme Q

COX2 - Cyclooxygenase-2

CPT1 - Carnitine palmitoyltransferase 1

CPT1B – Carnitine palmitoyltransferase 1B

CPT2 – Carnitine palmitoyltransferase 2

CREB – CAMP responsive element binding protein

CTCF – CCCTC-binding factor

CTP – Citrate transporter protein

CV – Complex V

CYP2E1 – Cytochrome P450 family 2 subfamily E polypeptide 1

D-loop - Displacement Loop

DARS2 – Aspartyl-tRNA synthetase 2

DGAT1 – Diacylglycerol acyltransferase 1

DGAT2 – Diacylglycerol acyltransferase 2

DIO2 – Iodothyronine deiodinase 2

DNA - Deoxyribonucleic acid

DNL – *de novo* lipogenesis

DRP1 - Dynamin related protein-1

dsDNA - Double stranded DNA

ECM - Extra cellular matrix

EF-Tu - Elongation factor thermo unstable

EFG1 – Elongation factor G1

EFG2 – Elongation factor G2

ER - Endoplasmic reticulum

ERAL1 – Era like 12S mitochondrial rRNA chaperone 1

$FADH_2$ – Flavin adenine dinucleotide

FAO – Fatty acid oxidation

FAs - Fatty acids

FASN - Fatty acid synthase

FDR – False discovery rate

FFAs – Free fatty acids

FGF21 – Fibroblast growth factor-21

FMN – Flavin mono nucleotide

G6P – Glucose 6-phosphate

GCN2 – General control non-depressible 2

GFM1 - Elongation factor G1

GFM2 - Elongation factor G2

GLUT1 – Glucose transporter 1

GLUT4 – Glucose transporter 4

GMP- Granulocyte-monocyte progenitor

GPCRs – G-protein coupled receptors

GPT2 – Glutamic pyruvate transaminase

GRP78 - Glucose regulated protein 78

GSH – Glutathione

GTP – Guanosine-5'-triphosphate

H_2O_2 - Hydrogen peroxide

H_2S – Hydrogen sulphide

HIF-1α - Hypoxia inducible factor 1 subunit α

HK2 – Hexokinase 2

HRI – Heme regulated inhibitor

HSPA9 – Heat shock protein family A (Hsp70) member 9

HSPC- Hematopoietic stem cells progenitors

IBM – Inner boundary membrane

IMM - Inner mitochondrial membrane

IMS – Inter membrane space

ISR - Integrated stress response

iWAT - Inguinal white adipose tissue

KEGG - Kyoto Encyclopedia of Genes and Genomes

LCFAs - Long chain fatty acids

LCFAs – Long chain fatty acids

LDs – Lipid droplets

MARS2 - Methionyl-tRNA synthetase 2

MCU – Mitochondrial calcium uniporter

MELAS - Mitochondrial encephalomyopathy, lactic acidosis and stroke-like episodes

MEP- Megakaryocyte + erythrocyte progenitor

MFN1 - Mitofusin 1

MFN2 - Mitofusin 2

MICOS - Mitochondrial contact site and cristae organizing system

mmBCFAs - Monomethyl branched-chain fatty acids

MPC – Mitochondrial pyruvate carrier

MRPP1 – Mitochondrial RNase P subunit 1

mtDNA - Mitochondrial DNA

MTHFD2 - Methylenetetrahydrofolate dehydrogenase

mtLSU – Mitochondrial ribosome (mitoribosome) large subunit

mTORC1 – Mammalian target of rapamycin complex 1

MTRFR - Mitochondrial translation release factor in rescue

mtSSB - Mitochondrial single stranded binding protein

mtSSU – Mitochondrial ribosome (mitoribosome) small subunit

mtUPR - Mitochondrial unfolded protein response

NADH – Nicotinamide adenine dinucleotide (reduced form)

NCR – Non-coding region

NE – Norepinephrine

NFAT – Nuclear factor of activated T cells

NSRE-I – Nutrient sensing response element I

NSRE-II – Nutrient sensing response element II

OAA – Oxaloacetic acid

OAT – Ornithine aminotransferase

OMM - Outer mitochondrial membrane

OPA1 - Optic atrophy 1

OXPHOS - Oxidative phosphorylation

PDH – Pyruvate dehydrogenase

PDK2 – Pyruvate dehydrogenase kinase isoform 2

PDK4 - Pyruvate dehydrogenase kinase isoform 4

PDM - Peri lipid droplet mitochondria

PERK – PKR-like ER Kinase

PGC-1a – Peroxisome proliferator-activated receptor-gamma (PPAR-γ) coactivator-1 α

PHDs - Prolyl hydroxylases

PIC – Pre initiation complex

PKA – Protein kinase A

PKR – Protein kinase R

PLIN5 - Perilipin 5

POLDIP2 – Polymerase delta-interacting protein 2

POLRMT – RNA Polymerase Mitochondrial

PP1 – Protein phosphatase complex 1

PQC – Protein quality control

PRDM16 – PR/SET domain containing 16

PSAT1 – Phosphoserine aminotransferase 1

PYCR1 - Pyrroline-5-carboxylate reductase 1

RNA – Ribonucleic acid

ROS – Reactive oxygen species

rRNAs - Ribosomal RNAs

SDHA – Succinate dehydrogenase complex flavoprotein subunit A

SDM – Strand displacement model

SHMT1 – Serine hydroxymethyltransferase 1

SHMT2 - Serine hydroxymethyltransferase 2

SIRT1 – Sirtuin 1

SLC25A44 - Solute carrier family 25 member 44

SNS – Sympathetic nervous system

SREBP1c – Sterol regulatory element-binding protein-1c

TAG - Triacylglycerol

TCA – Tricarboxylic acid cycle

TEFM / TFAM – Mitochondrial transcription elongation factor

TNF-α – Tumour necrosis factor- α

tRNAs - Transfer RNAs

UCP1 – Uncoupling protein 1

UMAP - Uniform Manifold Approximation and Projection

uORF – Upstream open reading frames
UPR – Unfolded protein response
VDAC - Voltage-dependent anion channel
WAT – White adipose tissue
YME1L1 – Yeast mtDNA escape 1-like
β-ARs – β adrenergic receptors

ABSTRACT

Mitochondria are essential for maintaining cellular homeostasis and orchestrating signaling, metabolism, and energetic pathways. Especially in the context of adipose tissue, dysfunction of mitochondria leads to altered adipocyte differentiation, lipid metabolism, insulin sensitivity, redox capacity, and thermogenesis. In response to mitochondrial OXPHOS dysfunction or altered proteostasis, stress responses are initiated in the cell inducing global cellular changes. CLPP, an ATP-dependent mitochondrial matrix localized protease, maintains mitochondrial physiology. This doctoral study investigates the effects of loss of CLPP and consequent mitochondrial dysfunction in adipose tissue biology (both white and brown adipose tissues) and systemic metabolism. Adapting multi-omics approaches in global and tissue-specific knockout mice models we have investigated the impact of CLPP depletion. Adipose-specific (AKO) and brown adipose (BKO) specific depletion of CLPP did not confer any systemic metabolic benefits, unlike the global CLPP knockout mice model. High-fat diet-induced dietary stress showed mild improved glucose clearance in BKO mice but not in AKO mice. Additionally, CLPP depletion led to widespread changes of transcriptome, proteome, and metabolome in both iWAT and BAT.

Interestingly CLPP depletion led to the formation of larger lipid droplets that were coupled with the formation of hollow mitochondria and cristae disorganization. This was further reflected in the defective functioning of mitochondrial supercomplexes and oxidative capacities in all the three CLPP deficient mice models. Furthermore, there was increased inflammation and associated immune changes in these mice. Metabolomics study showed accumulation of 2-hydroxyglutarate across all three mice models that were produced by the moonlighting function of a serine synthesis pathway enzyme, PHGDH. Interestingly, we found increased incidences of mitochondria-nucleus contacts and nuclear softening in KO brown adipocytes. The nuclear softening was reversed upon PHGDH inhibition and was correlated with the reversal of whitening of KO brown adipocytes. Finally, the study established that 2-hydroxyglutarate was responsible for the softening of the nucleus and larger lipid droplets. The nuclear softening was associated with a decrease in levels of heterochromatin marks, H3K9me3 and H3K27me3, which in turn might be responsible for the gene expression changes observed in the remodeled BAT upon CLPP loss.

Taken together, this study identifies a novel pathway of how dysfunctional mitochondria communicate to the nucleus via a signaling metabolite, 2 hydroxyglutarate, and consequently lead to remodeling of BAT.

Zusammenfassung

Mitochondrien sind für die Aufrechterhaltung der zellulären Homöostase und die Orchestrierung von Signal-, Stoffwechsel- und Energieströmen von wesentlicher Bedeutung. Insbesondere im Zusammenhang mit Fettgewebe führt eine Fehlfunktion der Mitochondrien zu einer veränderten Differenzierung der Fettzellen, einem veränderten Fettstoffwechsel, einer veränderten Insulinempfindlichkeit, einer veränderten Redoxkapazität und einer veränderten Thermogenese. Als Reaktion auf eine mitochondriale OXPHOS-Dysfunktion oder eine veränderte Proteostase werden in der Zelle Stressreaktionen ausgelöst, die zu globalen zellulären Veränderungen führen. CLPP, eine ATP-abhängige, in der mitochondrialen Matrix lokalisierte Protease, hält die mitochondriale Physiologie aufrecht. In dieser Doktorandenstudie werden die Auswirkungen des CLPP-Verlusts und der daraus resultierenden mitochondrialen Dysfunktion auf die Biologie des Fettgewebes (sowohl des weißen als auch des braunen Fettgewebes) und den systemischen Stoffwechsel untersucht. Durch die Anwendung von Multi-omics-Ansätzen in globalen und gewebespezifischen Knockout-Mausmodellen haben wir die Auswirkungen des CLPP-Verlusts untersucht. Die fettspezifische (AKO) und die gewebespezifische (BKO) Deletion von CLPP führte im Gegensatz zu den globalen CLPP-Knockout-Mäusen nicht zu einer Verbesserung des systemischen Stoffwechsels. Bei BKO-Mäusen führte eine fettreiche Diät zu einer leichten Verbesserung der Glukose-Clearance, nicht aber bei AKO-Mäusen. Darüber hinaus führte die CLPP-Depletion zu weitreichenden Veränderungen im Transkriptom, Proteom und Metabolom sowohl im iWAT als auch in der BAT.

Interessanterweise führte der CLPP-Mangel zur Bildung größerer Lipidtröpfchen, die mit der Bildung hohler Mitochondrien und einer Desorganisation der Cristae einhergingen. Dies spiegelte sich in allen drei CLPP-defizienten Mäusemodellen auch in einer gestörten Funktion der mitochondrialen Superkomplexe und der oxidativen Kapazitäten wider. Darüber hinaus traten bei diesen Mäusen vermehrt Entzündungen und damit verbundene Immunveränderungen auf. Die Metabolomics-Studie zeigte eine Anhäufung von 2-Hydroxyglutarat in allen drei Mäusemodellen, das durch die "Moonlighting"-Funktion eines Enzyms des Serinsyntheseweges, PHGDH, produziert wurde. Interessanterweise fanden wir in den braunen KO-Adipozyten ein erhöhtes Auftreten von Mitochondrien-Kern-Kontakten und eine Erweichung des Kerns. Die Erweichung des Kerns wurde durch die Hemmung von PHGDH rückgängig gemacht und korrelierte mit der Umkehrung der Weißfärbung der braunen KO-Adipozyten. Schließlich wurde in der Studie festgestellt, dass 2-Hydroxyglutarat für die Erweichung des Zellkerns und größerer Lipidtröpfchen verantwortlich ist. Die Erweichung des Zellkerns war mit einer Abnahme der Heterochromatin-Markierungen H3K9me3 und H3K27me3 verbunden, die wiederum für die Veränderungen der Genexpression verantwortlich sein könnten, die in der umgebauten BAT nach dem Verlust von CLPP beobachtet wurden.

Insgesamt zeigt diese Studie einen neuen Weg auf, wie dysfunktionale Mitochondrien über einen Signalstoff, 2-Hydroxyglutarat, mit dem Zellkern kommunizieren und folglich zum Umbau der BAT führen.

INTRODUCTION

Mitochondria

Origin

Mitochondria function as vital energy and homeostatic centers in most of living cells. These essential organelles house oxidative pathways responsible for providing around 90% of the cell's ATP. The first observation of mitochondria was made by Richard Altmann in 1890, who initially perceived these structures as simple bacteria-like entities residing within cells. He termed them "bioblasts" [15], and later, evolution based studies revealed that mitochondria indeed possess a prokaryotic origin [16]. As per the endosymbiotic theory, a heterotrophic archaeal host engulfed a free-living proteobacterium, marking the emergence of eukaryotes [17]. This hypothesis gains support from mitochondria possessing their independent genome. Throughout evolution, mitochondria lost or transferred the majority of their genes to the cell nucleus. In mammals, the mitochondrial genome comprises merely 37 genes, and out of 1130+ cellular proteins, it encodes only 13 proteins, all involved in core oxidative phosphorylation. The remaining proteins are encoded in the nucleus, necessitating for them to be imported into mitochondria through a complex system of translocase enzymes at the mitochondrial membrane [18].

Structure and function
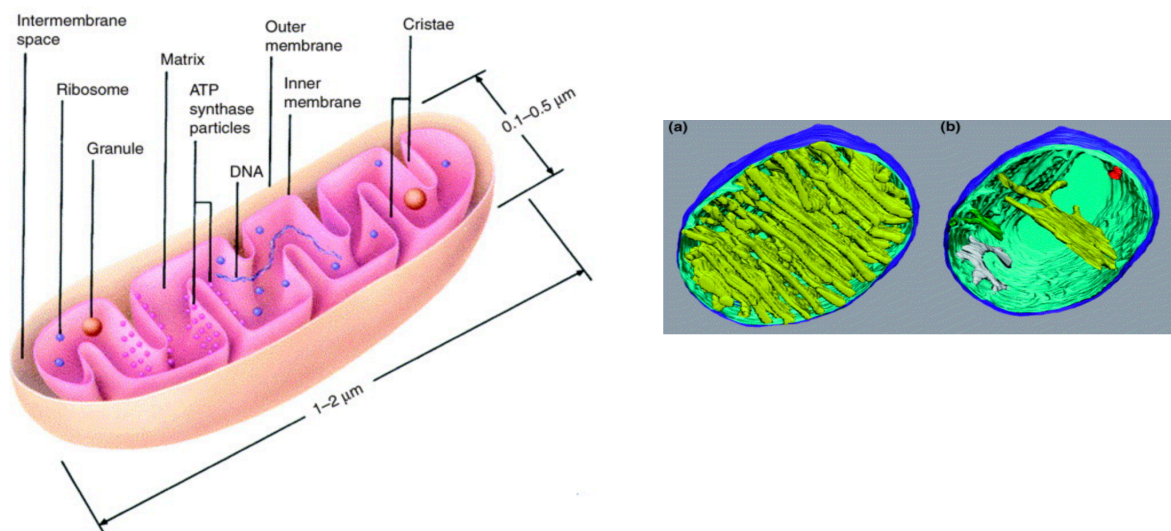
Figure A. Representation of the internal structures of mitochondria. *Adapted from [11]*

Mitochondria possess a dual-layered phospholipidic structure, consisting of an outer membrane (OMM) and an inner membrane (IMM). These membranes create two distinct compartments within the organelle – the intermembrane space (IMS) and the matrix (Fig. 1, [11, 19]). The two membranes differ in their composition and permeability. The lipid-rich OMM is very porous by nature and allows solutes smaller than approximately 5,000 Da to move freely through voltage-dependent anion channel

(VDACs) [20, 21]. Conversely, the protein-rich IMM possesses selective transporters that only facilitate specific molecule passage. Substances such as water, oxygen, and carbon dioxide can permeate freely, while most other molecules are restricted [22, 23]. This selective permeability enables the IMM to uphold an electrochemical membrane potential of approximately 120–180 mV in conjunction with oxidative phosphorylation (OXPHOS) enzymes [23]. The surface area of IMM is increased by diverse tubular formations of the membrane, or lamellar extensions known as cristae. Cristae can also create functionally distinct sub compartments called cristae junctions (CJ) [19]. Each of the components of mitochondrial structure impart unique functions and make mitochondria a hub of interactions and reactions, as described below.

The OMM is highly involved in establishing physical contacts between mitochondria and other organelles. One of the most well - described interaction is among mitochondria and endoplasmic reticulum (ER) at the mitochondrial – ER contact sites, that mediate sustained Ca2+ tunneling into mitochondria via VDAC on the OMM and mitochondrial calcium uniporter (MCU) at the IMM. Additionally, mitochondria have also shown to be closely associated with lipid droplets (LDs). Acute starvation stress leads to trafficking of fatty acids (FAs) to mitochondria from LDs closely associated to them. Autophagy – derived LDs to undergo lipolysis via the activity of cytoplasmic lipases, and liberate fatty acids that are further processed for the purpose of energy production [24]. A very interesting sub-population of mitochondria have been discovered in brown adipose tissue (BAT) cells, called the peri lipid droplet mitochondria (PDMs), which stay in close proximity to LDs and are proteomically distinct from cytoplasmic mitochondria (CMs). Their association with LDs is regulated by perilipin 5 (PLIN5), and instead of burning fatty acids, they contribute to the growth of LDs by supplying them with ATP or citrate for triacylglycerol (TAG) synthesis or de novo lipogenesis, respectively [25].

The IMM constitutes a highly impermeable membrane and controls the import of metabolites, ions, adenosine triphosphate (ATP) and adenosine diphosphate (ADP) from the cytoplasm, whereas cristae considered as inward folds of the IMM intensely shaped to maximize the surface for cellular energy demands. An Inner Boundary Membrane (IBM) runs parallel to OMM, and the interface between IBM and cristae is bounded by cristae junctions, which are stabilized by a multi-subunit complex named as mitochondrial contact site and cristae organizing system (MICOS). MICOS also additionally connects the OMM with the IMM [26]. The cristae house the electron transport chain (ETC) complexes and the ATP synthase, thus are crucial in the generation of the main cellular energy source, ATP through oxidative phosphorylation (OXPHOS). In fact, cristae disorganization is a major hallmark of mitochondrial dysfunction [27]. The innermost part of the mitochondria- called the matrix, encompasses numerous copies of the mitochondrial DNA (mtDNA) and the entire machinery for mtDNA replication, transcription and translation of encoded proteins. Moreover, many enzymes involved in the Tricarboxylic Acid Cycle (TCA), formation of iron – sulfur (Fe-S) clusters and FAO reside in the matrix [10, 28]. Mitochondria are extremely dynamic organelles and do not exist independently of each other.

Mitochondria have the unique capability to form connected structures and giant networks to promote co-ordinated outcomes. This happens through coordinated cycles

of mitochondrial fission and fusion and remodeling of mito-membranes at ultrastructural level, termed in the field as "Mitochondrial dynamics'. Mitochondrial fusion needs three large GTP-hydrolyzing enzymes of the dynamin superfamily. The mitofusins, MFN1 and MFN2, are located on the mitochondrial outer membrane and mediate outer membrane fusion. Studies reveal that mitofusins must be present on opposing mitochondria for fusion to occur and that mitofusins exist in both homo-oligomeric and heterooligomeric complexes, it is commonly thought that *trans* interactions between mitofusins mediate tethering of mitochondria during the fusion process [29]. IMM fusion is brought about by Optic atrophy 1 (OPA1). Cells lacking OPA1 show mitochondrial outer membrane fusion, but such events never progress to inner membrane fusion. The fusion is controlled by the stoichiometric balance between the long, unprocessed form of OPA1 (L-OPA1) and the soluble, short OPA1 (S-OPA1), that derives from L-OPA1 after being proteolytically cleaved [30]. Unlike mitofusins, Opa1 is needed on only one of two opposing mitochondria for inner membrane fusion to occur. Mitochondrial fission is the division of a mitochondrion into two smaller mitochondria. The central mediator of mitochondrial fission is dynamin-related protein 1 (DRP1), a GTP-hydrolyzing enzyme, which upon recruitment from a cytosolic pool onto the mitochondrial membrane, self organizes into a spiral structure to initiate fission [31]. Studies have shown that dysfunctional OXPHOS, nutrient availability and stress responses alter morphology of mitochondria, rendering them fragmented or hyperfused [32].
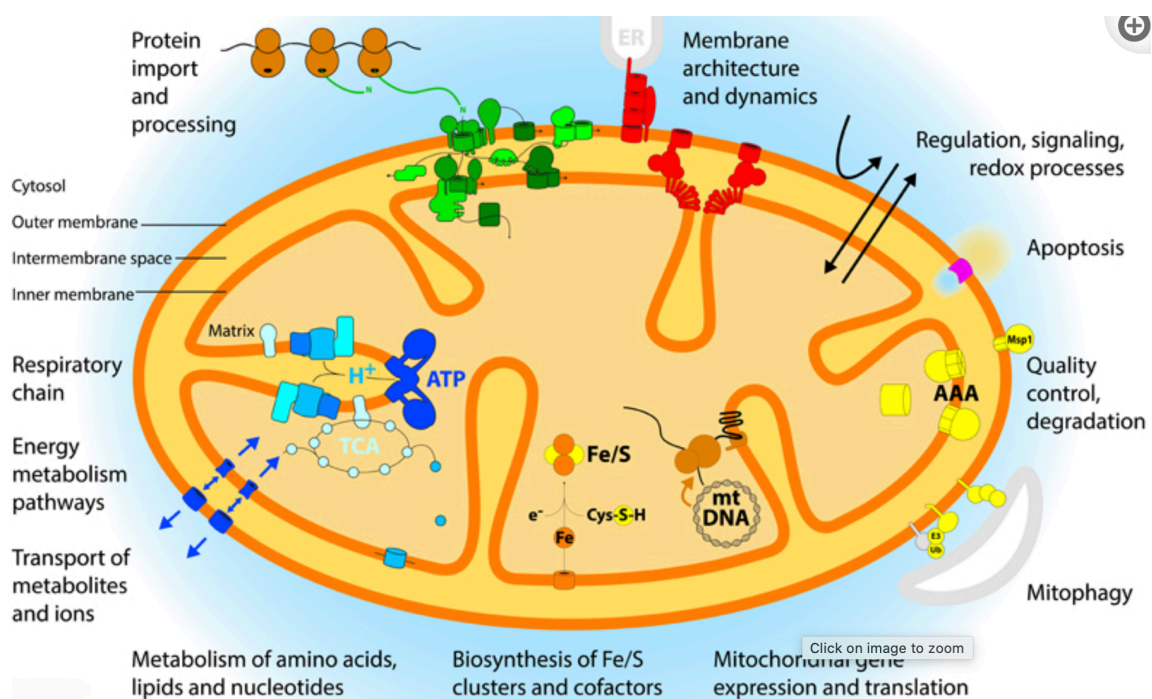
Figure B. Multifaceted roles of mitochondria in cellular homeostasis. Adapted from [8]

Basic overview of function

Mitochondria primarily contribute to cellular ATP through OXPHOS. Electrons in the electron transport chain (ETC) are contributed by electron carriers NADH and

FADH2. These carriers are regenerated via the tricarboxylic acid cycle (TCA) and catabolic β-oxidation of fatty acids [33].

Mitochondria play pivotal roles in regulating multiple metabolic pathways at different levels, such as metabolism of amino acids, lipids, nucleotides, and TCA metabolites [34]. They are also central to the biosynthesis of iron-sulfur (Fe-S) clusters [35], maintaining calcium homeostasis by engaging in signaling pathways involving Ca^{2+} [36], executing quality control and degradation processes such as mitophagy and apoptosis [37], influencing inflammation [38], and both generating and maintaining reactive oxygen species (ROS) [39, 40]. Mitochondrial quantity and size can differ across organisms, tissues, and even cell types. While absent in erythrocytes, a single oocyte may contain as many as 100,000 mitochondria due to the distinct energy and metabolic demands of various cell types or tissues [41, 42].

Mitochondria coordinate multiple metabolic pathways critical for bioenergetics and macromolecule biosynthesis comprising nucleotides, amino acids, fatty acids and heme and hence it is interesting to understand metabolic wiring in the cells from a mitochondrial lens. Mitochondria are indeed essential metabolic hubs for the generation of energy using diverse fuel sources such as carbohydrates, fats and proteins, as they are the site for TCA or Krebs cycle [33]. Under aerobic conditions. pyruvate, generated from glucose via cytoplasmic glycolysis, enters IMM though the Mitochondrial Pyruvate Carrier (MPC). Upon entry, pyruvate is converted either to acetyl-CoA via PDH, producing NADH or alternatively, OAA, with the activity of PC. Alternative sources of acetyl-CoA are the FAO, branch chain amino acids (BCAAs) including valine, leucine, isoleucine catabolism, and oxidation of ketone bodies. Acetyl-coA enters the TCA cycle to be ultimately oxidized to CO_2 with the simultaneous release of electron donors, that eventually supply the respiratory chain complexes in the mitochondria [43]. TCA cycle not only harbours catabolic pathways, but also orchestrates anabolic functions. TCA cycle intermediates are utilized as building blocks of cytosolic biosynthetic purposes such as purine, pyrimidine and porphyrin synthesis or act as *signaling molecules* regulating chromatin modifications, hypoxic responses or DNA methylation. As discussed above, acetyl CoA not just operates the fatty acid synthesis pathway but also the mevalonate pathway for cholesterol production. Acetyl-CoA has also been shown to alter the epigenetic landscape by promoting acetylation of histones or by directly affecting enzyme activities through supplying acetyl group for PTMs. Strikingly, succinate is involved in a process named as pseudohypoxia due to the suppression of prolyl hydroxylases (PHDs) and the consequent induction of HIF-1α (hypoxia induced factor 1α) [44]. Mitochondria are the primary site of FAO. Acyl-CoA synthases (ACS) convert dietary long chain fatty acids (LCFAs) to fatty acyl-CoAs. LCFAs are not capable of crossing the IMM. Therefore, they undergo esterification via CPT1 (Carnitine palmitoyltransferase 1) to generate acylcarnitines that move through the IMM by the carnitine- acylcarnitine translocase (CACT). Lastly, acylcarnitines are reconverted to acyl-CoAs in a process mediated by CPT2 (Carnitine palmitoyltransferase 2) in the mitochondria matrix. Acyl-CoAs undergo a series of enzymatic reactions catalyzed by chain length specific acyl-CoA dehydrogenases to ultimate yield 2 carbon shortened acyl-CoAs, one acetyl-CoA that powers TCA cycle, as well as supplies the ETC [45]. Aside from the abovementioned myriad functions

entailing ATP generation, Ca$^+$ buffering, heme, amino acid and phospholipid biosynthesis, synthesis of Fe-S clusters coupled to heme homeostasis [46], mitochondria are also implicated in cell survival, programmed cell death and inflammation and emission of cell intrinsic danger signals [47]. Moreover and beyond, mitochondria are also intimately linked to the management of metabolic by-products, such as clearance of ammonia (NH$_3$) which are by products of catabolism of amino acids and nucleotides- via the urea cycle to evade toxicity, hydrogen sulfide (H$_2$S) and sequestration of reactive oxygen species (ROS). Beyond the deleterious effects of ROS, hydrogen peroxide (H$_2$O$_2$) is shown to be instrumental in the propagation of signalling cascades promoting proliferation and differentiation [48].

Mitochondrial gene expression

A distinct feature that sets mitochondria apart from other organelles is that they are "semi-autonomous". They possess their own genome, mitochondrial DNA (mtDNA), which is a 16kb long circular molecule. It contains 37 genes, encoding 13 polypeptides for the core proteins of OXPHOS as well as 22 transfer RNAs (tRNAs) and 2 ribosomal RNAs (rRNAs) involved in mitochondrial translation. MtDNA is unique because the two strands of mtDNA differ in their base composition, with one being rich in guanines, the heavy strand (H), and the other, light (L) strand, being rich in cytosines, making it possible to separate the two by density centrifugation in alkaline CsCl$_2$ gradients [49]. Also present, is a 1kb non-coding region (NCR)- that contains the H-strand origin of replication (OH), the heavy and light strand promoter (HSP, LSP), the displacement loop (D-loop) region and the termination-associated sequence (TAS). The H-strand encodes the majority of transcripts such as 12 mRNAs, two rRNAs and 14 tRNAs, whereas L-strand accounts for encoding 8 tRNAs and 1 mRNA.
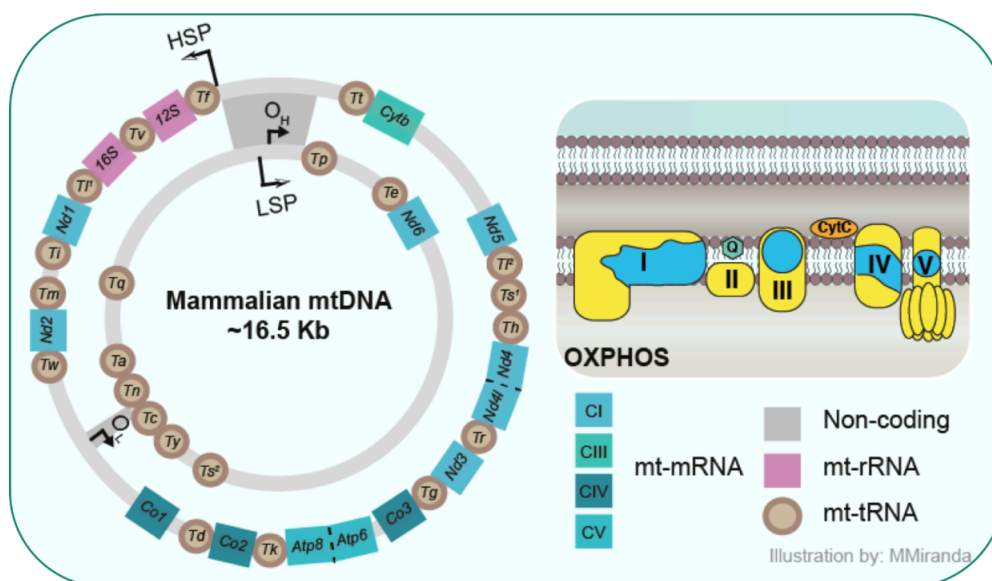
Figure C. Organization and coding capacity of mammalian mtDNA. *Adapted from* [6]

The mitochondrial genome is organized as tightly packed nucleoprotein complexes called nucleoids, generally tethered to the IMM [50]. Mitochondrial

transcription factor A (TFAM) has been shown to package the mtDNA via loop formations and cross-strand binding [51]. Further it also has been established that TFAM serves as a mtDNA copy number regulator [52] as well as controls the compaction of mtDNA [51]. Each nucleoid contains one or several copies of mtDNA [51, 53] and the number of mtDNA molecules per mitochondrion may vary greatly between tissues- from 100 to 10,000 copies per cell, depending on cellular requirements. Additionally, there can be variation in the sequence of mtDNA present in an individual, termed as mitochondrial heteroplasmy [54]. The mtDNA exhibits a non-Mendelian uniparental inheritance pattern. Due to the increased presence of mtDNA copy number within oocytes, it is exclusively transmitted through the female germ line, and the paternal mtDNA is degraded after fertiliization [54].

The mtDNA replication machinery is simpler than the nuclear replication machinery, and involves four main enzymes- the replicase DNA-polymerase gamma (POLG) [55], mitochondrial single strand binding protein (SSBP1) [56], the DNA helicase Twinkle (TWNK) [57] and the mitochondrial RNA polymerase (POLRMT) [58-60]. The mtDNA transcription occurs from HSP and LSP, present within the D loop. Transcription machinery is composed of POLRMT, TFAM and mitochondrial transcription factor B2 (TFB2M) – that form the initiation complex, and the mitochondrial transcription elongation factor (TEFM). mtDNA transcription is a well co-ordinated process. Mitochondrial transcription is initiated following the recruitment of POLRMT at the transcription start site, process supported by TFAM which inserts a sharp 180° bend of the DNA upstream of LSP and HSP [61]. Next, TFB2M is brought in close vicinity to the pre - initiation complex and causes DNA duplex melting, thus leading to formation and stabilization of the open initiation complex [34]. TFB2M and TFAM subsequently dissociate from the complex, paving way for TEFM to enter and activate the elongation process. In the elongation phase, POLRMT synthesizes primary polycistronic transcripts, that are further processed in order to produce tRNAs, mRNAs and rRNAs [62, 63]. Mitochondrial translation is also a tightly regulated process, considerably different from the cytoplasmic translation and shows high dependence on proteins encoded by the nuclear DNA. Mitochondria derived ribosomes from their bacterial progenitor. Mitochondrial ribosomes or mitoribosomes are assembled into a large 39S subunit (mtLSU), containing proteins encoded by the nucleus and the 16S rRNA, and into a small 28S (mtSSU) subunit, that has the 12S rRNA and around 30 nuclear – encoded proteins [64]. Mitoribosomes are specialized for the synthesis of the membrane-bound respiratory chain subunits and therefore predominantly associate with the inner membrane [65]. Initiation of translation consists of two steps, preinitiation step (involves pre-initiation complexes, PIC) followed by formation of the complete initiation complex [66]. Afterwards, mitochondrial - specific aminoacyl-tRNA synthetase, called MARS2, loads methionine to a corresponding tRNA (tRNAMet). The elongation phase is mediated by four major elongation factors; TUFM (EFTu), GFM1 (EFG1) and GUF1 [67]. The elongation proceeds through the aminoacyl (A) site of the mtSSU, P center of mtLSU P center, hence adding new amino acid to the being synthesized. Hydrolysis of the GTP powers the translocation of the ribosome through A, P and ultimately exit (E) tRNA binding site, which is the weakest one, thus allowing the release of the tRNA and the induction of a new elongation cycle.

Translation termination happens when a stop codon is encountered at the A site. It is mediated by ribosome release factors MTRFL1, MTRFR and GFM2 (also called EFG2) [67].

Oxidative phosphorylation (OXPHOS)-

Mitochondria serve a crucial role in generating metabolic energy in the form of ATP through mitochondrial the steps of oxidative phosphorylation. This OXPHOS system is intricately embedded within the IMM and comprises five protein complexes along with two electron carriers [68, 69]. The initial four complexes, collectively referred to as the electron transport chain (ETC), facilitate the movement of electrons across the chain, concurrently coupling this process with the transfer of protons across the IMM. This action establishes a proton gradient across the IMM, leading to the creation of a proton motive force that eventually results in ATP generation.
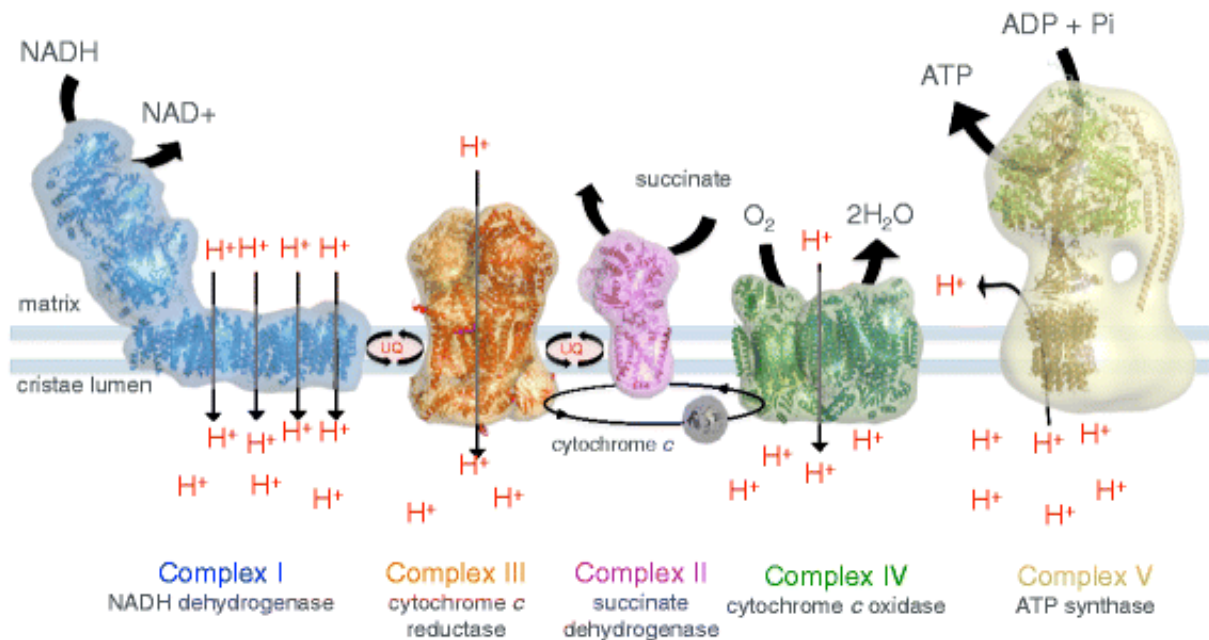
Figure D. Structure and organization of the components on the OXPHOS machinery. *Adapted from [10]*

The ETC is composed of four complexes with enzymatic activities – Complex I (NADH: ubiquinone oxidoreductase or CI), Complex II (succinate dehydrogenase, SDH or CII), Complex III (ubiquinol-cytochrome bc1 oxidoreductase or CIII) and Complex IV (cytochrome c oxidase or CIV), along with two mobile carriers of electrons, namely, ubiquinol and cytochrome c. Accompanied by activities of CI, CIII and CIV occurs the pumping of protons across the mitochondrial matrix to IMM, albeit by different mechanisms [70-72], leading to creation of electrochemical gradient. This proton electrochemical gradient is then utilized by F_1F_0-ATP synthase (Complex V or CV) to produce ATP by phosphorylating ATP. This combined operation of the ETC and CV forms what is known as the mitochondrial respiratory chain (MRC) [73].

CI is a "L-shaped" NADH dehydrogenase and serves as a pivotal entry point for electrons into the ETC [74]. It is the largest complex of OXPHOS, weighing around 1

MDa and composed of 45 subunits (14 core and 31 supernumerary) along with cofactors such as flavin mononucleotide (FMN) and Fe–S clusters. Of these subunits, 7 are encoded by mitochondrial DNA, while the remainder are nuclear-encoded [18]. CI has two arms, the hydrophobic arm that embeds in the IMM, and the soluble peripheral arm that extends into the matrix. The hydrophobic arm facilitates proton transport across the IMM. The soluble, matrix arm of CI, is responsible for NADH oxidation, and is formed by the seven mitochondrially encoded subunits [75]. The enzymatic core is supplemented by supernumerary subunits, that are responsible for CI assembly and stability [76]. The genes encoding these subunits are commonly targeted by mutations causing mitochondrial diseases [77], and dysfunction of CI has been associated with conditions like Parkinson's disease [78] and dementia [79].

CII consists of four protein subunits encoded by the nuclear genome [80]. The matrix-localized SDHA and SDHB form the succinate dehydrogenase domain [81], while SDHC and SDHD, situated as hydrophobic anchors in the IMM, are essential for electron transfer [82]. Four assembly factors, SDHAF1-F4, facilitate their assembly [83]. CII plays a dual role in respiration by catalyzing the oxidation of succinate to fumarate in the TCA cycle [80, 84] and facilitating electron transfer to ubiquinol in the ETC [84, 85].

CIII exists as a functional homodimer with three catalytic subunits – MT-CYB, encoded by mitochondrial DNA, UQCRFS1, Rieske subunits (containing two Fe-S clusters) and CYC, encoded by nuclear DNA. Functioning as a cytochrome c reductase, CIII engages in electron transfer by receiving electrons from both CI and II and transferring them to CIV through cytochrome c [86], and in the process, contributing to the transport of protons across the IMM. CIII's function is closely linked to the Q cycle mechanism, where electrons are transferred in a two-step process to cytochrome c [87, 88]. This intricate process involves both the oxidation and reduction of specific electron carriers within the complex. Furthermore, CIII is implicated in the assembly and maintenance of other ETC complexes, particularly CI - by affecting its stability [89], underscoring its role in maintaining mitochondrial function [90].

CIV comprises of 14 subunits, including three mitochondrially encoded catalytic (core) subunits, MT-CO1, MT-CO2, and MT-CO3, and 11 supernumerary subunits encoded by nuclear DNA. It serves as the rate-limiting complex of OXPHOS [91, 92] and facilitates the transfer of electrons from cytochrome c to molecular oxygen, concurrently transporting protons across the IMM. The assembly of CIV relies on 50 assembly factors and involves the modular assembly where it is constructed from three subcomplexes (modules), each centered around a core subunit [93]. These modules then come together to form the complete CIV structure [93].

CV comprises 17 distinct protein subunits, encoded both by mitochondria (MT-ATP6 and MT-ATP8) and the nucleus [94]. CV consists of two main functional domains: the F_0 domain embedded in the IMM and the F_1 domain located in the mitochondrial matrix. The F_0 domain is responsible for proton translocation across the IMM, facilitated by the

c-ring subunit. This movement of protons generates the energy required for ATP synthesis. The F_1 domain, on the other hand, houses the catalytic site responsible for the conversion of ADP and Pi into ATP. The operation of CV involves a coordinated rotation mechanism between these two domains [95]. As protons flow through the F_0 domain, it induces rotation in the c-ring, transmitting this mechanical energy to the F_1 domain. This rotation triggers conformational changes within the F_1 domain, enabling ATP synthesis [94]. This intricate coupling of proton movement and mechanical energy conversion underscores the efficiency of ATP production in cells. CV also plays a role in mitochondrial cristae formation. Its dimeric form has been found to shape the cristae by inducing bends in the IMM [96]. The angular association between the two monomers leads to the bending in IMM and this clustering of CV dimers at apex of cristae creates a proton trap within the strong positive curvature in the membrane [97]. Furthermore, CV dimers have been implicated in cell death pathways by potentially participating in the opening of the permeability transition pore, although this remains a topic of ongoing research and discussion [98].

Beyond individual enzyme complexes, these complexes form larger supramolecular assemblies, referred to as supercomplexes [99]. Supercomplexes encompass various stoichiometries of CI, CIII, and CIV, with the most recognized structure being the respirasome, composed of $CI/CIII_2/CIV$. Although the precise role of supercomplexes remains under debate, recent advancements have led to the elucidation of their crystal structure, thereby confirming respirasomes stable and functional units within OXPHOS [100, 101]. Additional supercomplexes, such as $CI/CIII_2$ [100], $CIII_2/CIV$ [102], and $CI_2/CIII_2/CIV_2$ [103] have also been identified. Specifically, from multiple native gel analysis across tissues and conditions, it is reported that almost 85% of CI, 55 - 65% of CIII and 15-25% of CIV is present into SCs, whereas CII is not detected in the SCs [104].

Traditionally, it was proposed that the OXPHOS complexes freely diffused within the IMM, a concept referred to as the fluid-state model [105, 106]. However, understanding shifted towards the solid-state model, which suggests the organization of OXPHOS into supercomplexes [106]. The assembly of these supramolecular structures is advantageous for the cell as they not only ensure effective, faster and error free channeling of the substrates of Q pool and cytochrome c, but also diminish production of ROS by preventing e- leakage. However, the existence of supercomplexes still remains controversial [107]. To address this controversy, very recently, "plasticity" model has been proposed, that partly reconciles both solid-state and fluid-state models. According to the model, respiratory SCs can co-exist with the individual ETC complexes [108].

Mitochondrial diseases

It is possible to group mitochondrial diseases into 1) OXPHOS disorders and their assembly factors, 2) defects in the upstream reactions that generate substrates for OXPHOS, 3) defects in relevant cofactors, 4) defects in mitochondrial DNA, RNA and protein synthesis and 5) defects in mitochondrial homeostasis. It is common to find more than one respiratory chain enzyme deficient. 49 percent of the known mitochondrial energy metabolism genes have combined defects, and 57 percent of

patients with OXPHOS defects have combined defects. Defects in complexes I, III, IV, and V are typically caused by deficiencies in mitochondrial DNA replication, RNA metabolism, or translation. A wide spectrum of mitochondrial disorders have been identified that manifest with a diverse set of symptoms [109].

Figure E. Gene defects (n = 251) of mitochondrial energy metabolism associated with human disease. *Gene defects that usually present as combined OXPHOS defects are highlighted in yellow (n = 123).* Adapted from [13]

The diseases can occur due to mutations in mtDNA itself, or due to aberrant nuclear encoded mitochondrial proteins [109]. Single-cell studies have brought to limelight that the proportion of mtDNA pathogenic variants must exceed a critical minimum level before a cell expresses a biochemical abnormality of the mitochondrial respiratory chain (the threshold effect) [110]. Some mitochondrial disorders affect a single organ (e.g., the eye in Leber hereditary optic neuropathy and the ear in nonsyndromic hearing loss. Most diseases present variety of symptoms. Defects in components of mtDNA replication, transcription, or translation machinery leads to disease conditions and phenotypes such as Leigh syndrome, Neurogenic weakness with ataxia and retinitis pigmentosa, Mitochondrial encephalomyopathy with lactic acidosis and stroke-like episodes, Kearns-Sayre syndrome, and Myoclonic epilepsy with ragged-red fibers- largely characterized by early death, cardiomyopathy, skeletal muscle atrophy, dystonia and deafness [111].A lot of mitochondrial diseases are associated with muscle weakness and myopathy [112]. Genes that are commonly defective in mitochondrial diseases are listed below, out of the 251 mapped defects, 37 are mtDNA encoded, and 210 are nuclear encoded, and 4 genes have been seen to be affected only in human neoplasm – beautifully summarized in [13]

Mitochondrial quality control

Mitochondria are dynamically responsive to the cellular environment and nutrient availability of organisms. As the primary energy producers, they adapt their function to changing conditions [113]. To guarantee mitochondrial health and accurate and sustained functionality, mitochondria employ various protein quality control (PQC) mechanisms. Chaperones and proteases play a crucial role in maintaining proper protein folding and eliminating damaged proteins, preventing the formation of toxic protein aggregates. Mitochondria harbor over 40 proteases—known as mitoproteases— that exist in different compartments, acting as safeguards of mitochondrial proteostasis and pivotal regulators of mitochondrial flexibility [114]. These versatile enzymes prevent the buildup of transient regulatory proteins in mitochondria, influence mitochondrial protein function through processing, and remove damaged proteins. Beyond quality control, mitochondrial proteases also govern critical processes like protein trafficking, activation, mitochondrial dynamics, mitophagy, and apoptosis [115, 116].

The ensemble of mitochondrial proteases is often referred to as the *mitochondrial degradome* [117]. Mitochondrial proteases, or mitoproteases, can be categorized into three subgroups based on their function and location: (a) intrinsic mitoproteases, predominantly operational within the mitochondrion; (b) pseudomitoproteases, functionally intact mitochondrial proteins that have lost their catalytic protease activity (such as subunits UQCRC1 and UQCRC2 of CIII); and (c) transient or roaming mitoproteases, intermittently translocated to mitochondria to engage in supplementary proteolytic tasks [14]. Dividing them by their catalytic cores, mitoproteases can be classified into Cys proteases, metalloproteases, and Ser proteases. Depending on their biochemical nature, these proteases can interact with diverse substrates and/or regulatory proteins to function as critical nodes in signaling pathways [14, 117].

Although a variety of proteases and peptidases are found within mitochondria, a major share of protein surveillance and quality control duties is carried out by four intrinsic AAA+ (ATPases Associated with various cellular Activities) proteases. These AAA+ proteases have a conserved ATP domain comprising roughly 230 amino acids, similar to many molecular motor proteins. Typically, these motors partake in processes involving the reorganization and recycling of proteins, membranes, or DNA within the cell [118]. Within mitochondria, membrane-integrated AAA+ metalloproteases are categorized into two types, determined by their orientation towards specific compartments: i-AAA protease- oriented towards intermembrane space and m-AAA proteases- oriented towards matrix [119]. Comprised of homologous and highly conserved subunits, they form cylinder-shaped complexes that allow proteolysis to occur within a sequestered space. A study found that these proteases harbor an AAA-type ATPase domain fused to a M48-type metallopeptidase domain [120], and an amino terminal transmembrane region anchors AAA protease subunits to the membrane [121].

The i-AAA protease is composed of 6 YME1L (yeast mtDNA escape 1-like) subunits [122]. It was also shown by a study on yeast i-AAA protease structure that the

ATPase domains form a spiral staircase at the top of the planar protease ring [120]. The paralogous m-AAA can form homooligomer of AFG3-like subunit 2 (AFG3L2), or heterooligomers of AFG3L2 and paraplegin (SPG7). In addition, a third m-AAA subunit called AFG3L2 is found in mice that can also form homo or hetero- oligomeric complexes [123]. A processing peptidase in the IMM, OMA1, has overlapping activity with m-AAA protease. Recent studies have shown that OMA1 triggers the integrated stress response upon mitochondrial dysfunction by cleaving the IMS protein DELE1 and translocating it to the cytosol, and eventually activating the canonical integrated stress response (ISR) kinase HRI [103]. An IM protease called PARL (Presenilins-associated rhomboid-like protein) is also known and has been shown to interact with i-AAA and the stomatin-like protein 2 (SLP2) [124].

Functionally, m-AAA protease exerts control over ribosome assembly and the synthesis of mitochondrially encoded subunits of the respiratory chain [125]. Respiratory deficiencies in yeast cells that lack the m-AAA protease are caused by impaired processing of the ribosomal subunit MRPL32, resulting in defective mitochondrial translation, which is also causal in hereditary spastic paraplegia [126] . Loss of the mammalian m-AAA subunit AFG3L2 also causes a decrease in mitochondrial calcium uptake that is due to induced mitochondrial fragmentation triggered by processing of OPA1 [127]. Furthermore, following the stress response, the YME1L1 subunit degrades inner membrane translocase subunit TIM17A, part of mitochondrial import, thereby decreasing protein import into the mitochondrion [128]. YME1L1 also plays a role in the control of mitochondrial membrane composition, modulation of cardiolipin levels and apoptotic resistance by degrading PRELI domain-containing protein 1 (PRELID1; Ups1 in yeast). PRELID1 forms a complex with the TP53-regulated inhibitor of apoptosis 1 in the intermembrane space, which prevents apoptosis by mediating intramitochondrial transport of phosphatidic acid that is necessary for the synthesis of cardiolipin [129]. As can be inferred, these mitoproteases are involved in the control of mitochondrial proteostasis, and hence have been proposed to contribute to the mitochondrial dysfunction observed during ageing [117].

The IMS harbours two serine proteases, HTRA2 (high temperature requirement mitochondrial serine protease A2)/Omi [130], and LACTB (β-lactamase-like protein) [131]. Additionally, the soluble mitochondrial serine AAA+ proteases, LONP and **CLPXP**, reside within the mitochondrial matrix.. Functionally, the two matrix proteases have been shown to have exclusive and indispensable roles in the mitochondria, with few instances of co-operativity between LONP1 and CLPP, as well as reported shared substrates between them [132, 133]. The Lon proteases are highly conserved nuclear encoded serine peptidases, conserved across all living species, including archaea and eubacteria. Mammals have two isoforms of Lon – LONP1, which is mitochondrially localized, and LONP2, which is peroxisomal. Both these proteins have been shown to be involved in degradation of oxidatively damaged proteins. The role of LONP2 is relatively lesser explored [134], whereas the role of LONP1 has been more characterized. Several target proteins have been shown to be to degraded by LONP1 under both normal conditions, and when they are damaged or mutated. These include aconitase, cytochrome *c* oxidase subunit 4 isoform 1, steroidogenic acute regulatory

protein (StAR), succinate dehydrogenase subunit 5, TFAM and glutaminase , as well as some haem-related enzymes such as cystathionine β-synthase, haem oxygenase 1 and 5-aminolevulinate synthase [135-142]. LONP1, and not the other AAA proteases, has the ability to prevent protein aggregation [143]. It has been shown to be ubiquitously expressed in most human tissues, with highest levels in brain, heart, skeletal muscle and liver, and lesser amounts in pancreas, lung, kidney and immune cells [144].The deficiency in mouse LONP1 leads to altered mitochondrial respiration and in the OXPHOS system [145]. LONP1 knockdown inhibits cellular proliferation and tumor and metastasis formation, whereas its overexpression increases tumorigenesis [117]. Furthermore, deletion of LONP1 in mice leads to early embryonic lethality, whereas heterozygous mice show decreased tumour susceptibility, which demonstrates the essential role of this proteolytic enzyme in life and disease [117]. A recent study showed that ablation of LONP1 in skeletal muscles in mice resulted in impaired mitochondrial protein turnover, resulting in mitochondrial dysfunction. This resulted in smaller muscle fibers and reduced strength. The retention of aberrant mitochondrial proteins in the muscle lead to loss of muscle by activation of autophagy-lysosome degradation [146]. A subsequent related study showed that skeletal muscle specific loss of LONP1 resulted in unfolded protein response activation or proteostatic stress in the muscle that had beneficial effects on the organismal systemic metabolism [147]. It is interesting to explore the tissue intrinsic role of LONP1 in various muscles and explore its potential as a therapeutic target in cases of myopathy.

Caseinolytic Mitochondrial Matrix Peptidase Proteolytic Subunit (CLPP)

The CLPXP protease complex in mammalian mitochondria has two major components: CLPP (caseinolytic peptidase P) and CLPX (caseinolytic peptidase X). CLPP contains proteolytic sites within its barrel, the access to which is limited due to a narrow axial pore that limits the passage of folded proteins [148]. A stable heptameric ring of human CLPP forms in the presence of CLPX and ATP [149]. Two CLPP heptameric rings form the catalytic tetradecamer chamber resembling a proteasome [149]. CLPX hexameric rings stack on either side of the CLPP chamber so that proteins unfold and move into the catalytic core under ATP-dependent conditions. CLPP is capable of cleaving small peptides without ATP, but CLPX is needed to recognize specific substrates [150].

The AAA+ ATPase, CLPX, is formed by six identical subunits that together make a homo-hexameric ring with an axial processing pore. CLPP, the barrel-shaped CLPP peptidase, which contains serine/histidine/aspartate triads (proteolytic active sites) sequestered in an internal chamber [9]. This arrangement creates a proteolytic chamber where protein substrates can be engaged and degraded. The proteolytic sites are accessible only through a narrow axial pore that limits the passage of folded proteins. CLPP subunits themselves have two functional domains: an ATPase domain at the N-terminus and a peptidase domain at the C-terminus. The ATPase domains are involved in binding and hydrolyzing ATP, providing the energy necessary for substrate translocation and unfolding. The peptidase domains are responsible for cleaving the unfolded or partially unfolded protein substrates into smaller fragments [151]. The CLPX component, an AAA+ ATPase, collaborates with CLPP to drive

substrate degradation. CLPX uses energy from ATP hydrolysis to unfold protein substrates and translocate them into the proteolytic chamber of CLPP [152]. The coordinated action of CLPX and CLPP ensures efficient and controlled degradation of damaged or misfolded proteins, preventing their accumulation within the mitochondrial matrix.

Among the array of mitochondrial proteases mentioned above, CLPXP stands out as one of the least explored in the context of mammalian systems. Our understanding of its functions and substrates in this context is just starting to unfold, shedding light on its intricate roles in regulating mitochondrial, cellular, and organismal physiology [14]. Bacterial ClpXP protease systems have provided crucial insights into the mechanistic and functional aspects of proteolytic machinery.
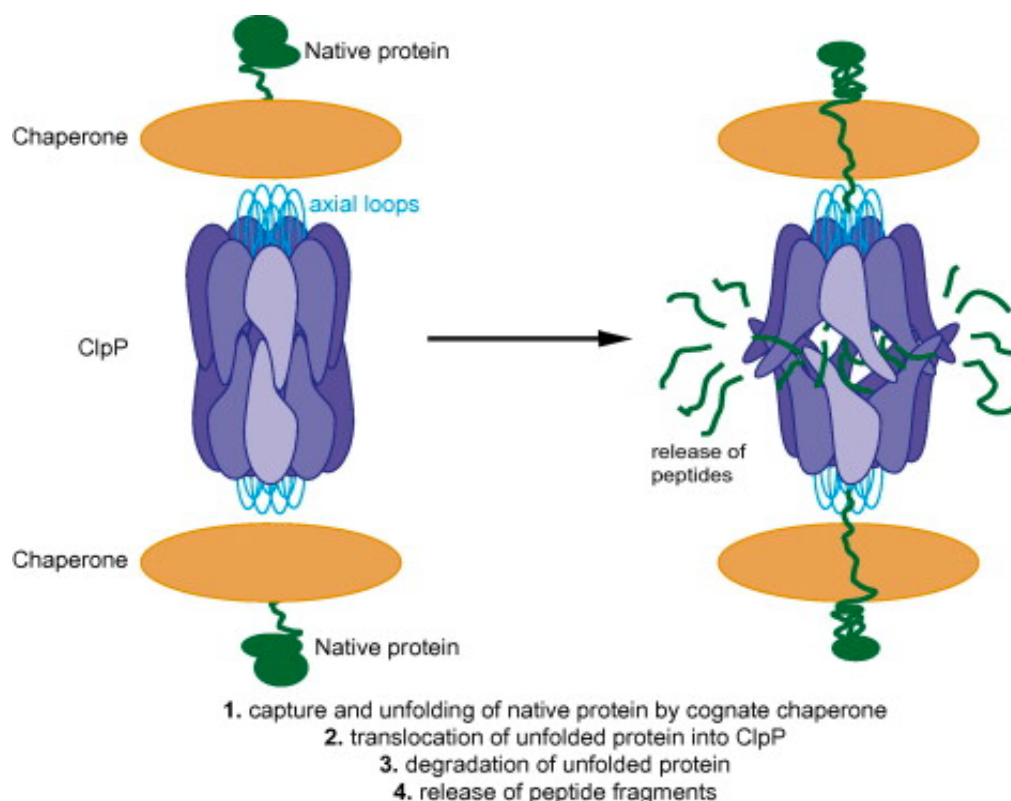
Figure F. CLPP mechanism of function. *Adapted from [9]*

It is involved in numerous cellular processes, including protein quality control, regulatory proteolysis, stress responses, and modulation of bacterial virulence [153]. It has been shown to target specific transcription factors such *srf* as to control gene expression [154, 155]. Additionally, ClpXP helps in degrading misfolded, damaged, or surplus proteins that could compromise cellular function. It participates in the regulation of specific stress responses in *E.coli*. For instance, the DNA repair protein RecN encodes a CLPXP recognition motif (Leu-Ala-Ala) that targets it for constant degradation. Upon DNA damage, RecN is induced and accumulates regardless of CLPXP's degradation, and once the stress is resolved, RecN degradation is efficiently orchestrated by ClpXP [156]. A similar regulatory role is observed in the degradation of the general stress response regulatory protein σS, in tandem with the adapter protein RssB [157, 158]. In certain bacteria like *S. aureus*, *P. aerugenosa* and *E. coli*,

CLPXP systems are implicated in antibiotic resistance and virulence by affecting the turnover of secretory proteins, degradation of antibiotics or expression of virulence factors like CodY, FtsZ and Spx [159].

Research on the protease in the nematode *C. elegans* (Called CLPP-1) has provided valuable insights into its role in proteostasis, development, and stress responses. CLPP forms the central proteolytic chamber of the complex. CLPP-1 regulates proteostasis and development *C. elegans*. For instance, down-regulation of *clpp-1* has been shown to have effects on embryonic viability, growth, and locomotion [160]. CLPP-1, seems to have a central role in mediating the UPR[mt] signals in worms by generating peptides through proteolysis of unfolded matrix proteins, which are exported by the HAF-1 transporter into the cytosol [161]. Through a yet unknown mechanism, these peptides seem to propagate the UPR[mt] signal by activating the transcription factor ATFS-1, which together with co-factors UBL-5 and DVE-1 stimulates expression of genes encoding mitochondrial chaperones and proteases [161, 162]. Additionally, a genome wide RNAi screen showed that UPR[mt] are attenuated in animals with reduced expression of *clpp-1*, thereby establishing its role in activation of UPR[mt] in worms [163].

Role of CLPP in mammals

Eukaryotic cells contain CLPP and CLPX orthologs in the mitochondrial matrix. Despite the extensive understanding of CLPP's structure and biochemical functions in prokaryotes, there is a noticeable gap in the understanding of the biological significance of CLPP in eukaryotic systems. Consistent with the proposed function of CLPP in cellular stress and protein quality control, its expression is upregulated in eukaryotic organisms in response to stressors, just as in prokaryotes [164-166]. A study in mammalian cells reported that the accumulation of unfolded proteins in the mitochondrial matrix led increased expression of *Clpp* in parallel to mitochondrial chaperones such as HSPD1 (heat shock protein family D (Hsp60) member 1), HSPA1 (Heat shock 70 kDa protein 1) and DNAJA3 (DnaJ Heat Shock Protein Family (Hsp40) Member A3) and this increased expression was dependent on transcription factors CHOP (CCAAT/enhancer binding protein (C/EBP) homology protein(and C/EBPß [164, 167]. Likewise, a progressive increase of CLPP protein levels was reported due to the faulty assembly of mitochondrial iron–sulfur clusters results from frataxin deficiency in Friedreich's ataxia [168]. Hepatic CLPP levels were reported to be reduced in response to a high-fat and high-fructose diet (a model for non-alcoholic steatotic hepatitis (NASH)), contributing to mitochondrial dysfunction and stress response activation. Conversely, CLPP overexpression or activation was shown to reverse the detrimental effects, highlighting its potential therapeutic role [169]. In humans, CLPP protein was shown to be down-regulated along with reduction in its mRNA levels in response to a dominant negative mutation of mtHSP60 that resulted in spastic paraplegia in a patient [170]. Another defining study reported human recessive mutations in CLPP (by employing a combination of linkage analysis, homozygosity mapping, and exome sequencing) to be causal of Perrault syndrome, characterized by symptoms like premature ovarian failure, sensorineural hearing loss, and growth retardation [171]. It was also shown in the first study on CLPP in mice, that

mouse model of CLPP loss also closely phenocopied faithfully these physiological aspects of the human disease [172].

Many studies to understand deeply, the role of CLPP in mammals followed these initial observations, spearheaded by our lab. We reported that the CLPP$^{-/-}$ mice were born in non-Mendelian ratio, with some of them likely dying *in utero*, since no postnatal lethality prior to weaning was observed [173]. Additionally, another independent study on mice lacking CLPP (in a different background) revealed significant infertility in both female and male, along with hearing loss [172]. There were clear disruptions in spermatogenesis, noticeable even at the spermatid stage, and failure in ovarian follicular differentiation [172]. The mice had moderate respiratory deficiency and were in fact protected against ulcerative dermatitis [172]. A subsequent study reported that CLPP was essential for oogenesis, with 4-fold increase in atretic follicles at 3 months, and reduced number of primordial follicles at 6-12 months in the ovaries of CLPP$^{-/-}$ mice [174]. Our lab also showed that CLPP-deficient mice also have improved glucose metabolism and are almost completely resistant to diet-induced obesity while having a normal lifespan despite recapitulating several Perrault syndrome phenotypes (shortened posture, sterility, sensory-neuronal hearing loss) [175].

Our lab provided further insights on tissue specific roles of CLPP. We showed that loss of CLPP surprisingly ameliorated a severe mitochondrial cardiomyopathy and impaired respiration in the heart resulting from DARS2 (mitochondrial aspartyl tRNA synthase) deficiency. This loss of CLPP led to an enhanced *de novo* synthesis of individual subunits of OXPHOS, thereby alleviating the observed mitochondrial deficiencies [176]. As a result of the absence of CLPP, mitochondrial protein synthesis slowed down (deregulated translation), resulting in more efficient production of OXPHOS subunits, which alleviated respiratory deficiency [176]. CLPP depletion was beneficial in other mitochondrial dysfunction models as well, with mutations in respiratory chain subunits or assembly factors [175]. Additionally, in the absence of CLPP, neurodegeneration of DARS2-deficient neurons is delayed due to milder OXPHOS dysfunction and possibly improved NAD+/NADH ratio within the mitochondria [177]. This in turn leads to a decreased neuroinflammation and improved motor functions in two double-deficient models (Purkinje cell-specific or forebrain neuron-specific DARS2/CLPP double knockout mice) [177].

Specifically, we reported evidence showing that mammalian CLPP regulates mitochondrial translation through degradation of ERAL1, a rRNA chaperone indispensable for the assembly of the small 28S subunit of the mitochondrial ribosome [173]. We also proved that many of the beneficial effects seen upon CLPP loss were majorly attributed to the fact that it stabilized MRC complexes, primarily CI [175]. Additionally, we also reported that the NADH-oxidizing N-module within CI undergoes an independent and higher rate of turnover than the rest of the complex [175]. This turnover is mediated by CLPP, which selectively eliminates and degrades the damaged parts of N-module, thereby allowing faster adaptation to changes in redox status [175]. This 'salvage pathway' prevents accumulation of dysfunctional CI and ensures energy efficiency by bypassing the need to synthesize and assemble the entire complex *de novo* [175]. In fact, one of our initial studies from the lab revealed

that the beneficial effects seen upon CLPP loss were independent of mammalian UPR^{mt} , which is in contrast to the studies on CLPP in lower organisms [14].
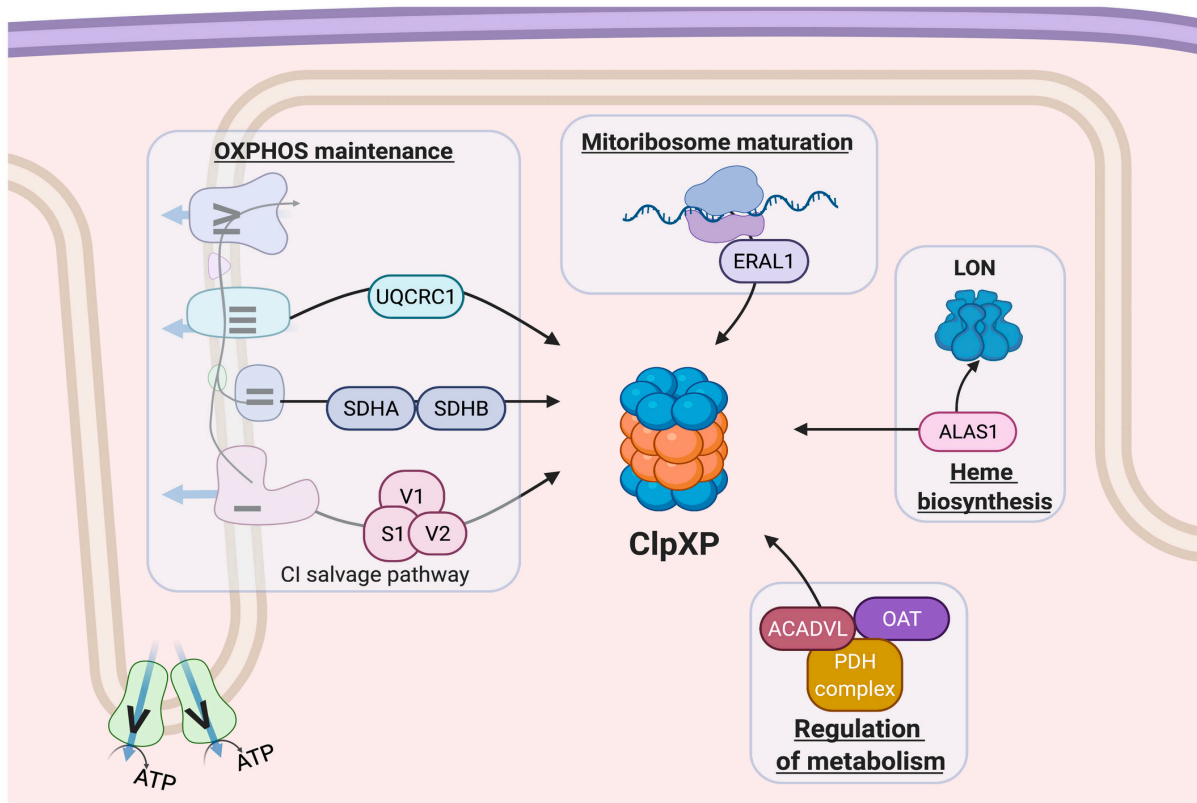
Figure G. Schematic overview of unique and overlapping functions of mammalian CLPP. Adapted from [14]

Deeper insights into the likely targets of CLPP were gained from a study from our lab that identified OAT, HSPA9 and POLDIP38/POLDIP2 (polymerase delta interacting-protein 38) and as novel bona fide CLPP substrates, using a combination of altered processing patterns, protein accumulation and stabilization in CLPP-deficient mice and interaction with CLPP [178]. The study also proposed that CLPP participates in the cooperative degradation of UQCRC1 (CIII subunit) [178]. Furthermore, a CLPP-substrate screen using inactivated CLPP revealed proteins involved in mitochondrial translation (EFG1 and P32/C1QBP) and post-transcriptional processing of mtRNAs (MRPP1 and PNPT1) to be CLPP substrates, in addition to ERAL1 [173]. In the context of cancer cells, it is also shown that SDHA and SDHB are degraded by CLPXP in cancer cells and MEFs. CLPXP prevents the accumulation of dysfunctional SDHA subunits in acute myeloid leukemia cells [179].

Additionally, a fascinating example of how these two matrix proteases cooperate to shape mitochondrial function is the biosynthesis of heme. The most important housekeeping and rate-limiting enzymes in heme biosynthesis is 5-aminolevulinic acid synthase (ALAS1). The end product of the pathway, heme, is a known-negative feedback regulator of ALAS1 levels [180], and this regulation is controlled by LON-dependent proteolytic degradation [141]. ALAS1 is partially unfolded by the CLPX chaperone, according to another study, but without CLPP in its proteome [181, 182], However, a parallel study showed that ALAS1 forms a heme-

dependent complex with the entire ClpXP protease, which in turn mediates ALAS1 degradation and executes the known-negative feedback regulation [183]. Through this haemin-mediated oxidative modification of ALAS1, LON is still recruited to the ClpXP-ALAS1 complex [183]. As demonstrated by the global analysis of the mitochondrial proteome, loss of CLPP in the heart results in elevated levels of ALAS1 despite elevated levels of both CLPX and LONP1, thereby shedding further light on this interplay. Additionally, based on recent substrate screens [173, 184, 185], CLPP and LON seem to share a few substrates that are highly complementary. Recent studies have shown that PDIP38/POLDIP2 can be used to execute and maintain this close relationship with defined adaptor proteins [186].

Mitochondrial stress signalling

Mitochondria have the ability to adjust to both internal and external stresses in order to maintain cellular equilibrium. This dynamic adaptation, which is neceaasry to maintain cellular homeostasis and energy production, is achieved through the activation of versatile signaling pathways, which constitute the mitochondrial stress response. Additionally, since the mitochondrial proteome stems from both nuclear encoded and mitochondrially encoded genes, a precise coordination between these compartments is needed for proper expression and assembly. This interplay poses significant challenges to maintaining mitochondrial protein homeostasis. As a consequence, cells have evolved robust quality control mechanisms and a continuous communication network between the mitochondria and the nucleus, facilitating proteome adaptation through retrograde signaling in response to diverse stresses [187, 188].Extensive investigations across various model organisms including yeast, *C. elegans*, cultured cells, and mouse models have unraveled intricate mitochondrial stress response pathways in response to ETC dysfunction [189].

In lower organisms like yeast and *C. elegans*, ETC dysfunction triggers a mitochondrial unfolded protein response (UPR[mt]) (in *C. elegans*), while in yeast, it engages a retrograde response to uphold the membrane potential. Initially, UPR[mt] was thought to be a stress response that is upregulated upon ETC dysfunction. It constitutes a transcriptional response that involves activation of mitochondrial chaperones and proteases that act to restore organelle proteostasis [161, 190, 191]. Notably, the UPR[mt] demonstrates a protective effect in ETC-deficient worms, [189]. Initial investigations involving the overexpression of a misfolded matrix protein, ΔOTC, in COS7 cells elicited a temporary transcriptional increase in the mitochondrial chaperones and proteases [164]. In mammalian cells, it was established that mitochondrial proteotoxic stress led to CHOP activation, resulting in increased expression of UPR[mt] responsive genes [164, 167]. The CHOP binding sites of promoters of UPR[mt] responsive genes are generally flanked by two conserved regions, mitochondrial UPR elements 1 and 2 (*MURE1* and *MURE2*) [167]. However, there is still lack of clarity in the validity of this notion since not many transcription factors are identified that bind to *MURE1* and *MURE2* [167]. However, increase of *Chop* mRNA in cells derived from multiple mitochondrial patients as well as mitochondrial disease models, testify the importance of CHOP in mediating mammalian stress response [192, 193]. Multiple defects in the mitochondria trigger the stress responses. Notably, in vivo

studies utilizing heart-specific knockout of DARS2 (mitochondrial aspartyl-tRNA synthetase) displayed an upregulation of mitochondrial chaperones and proteases [194]. Similarly, heart-specific knockout of five distinct mitochondrial proteins that regulate mtDNA gene expression from mtDNA replication to transcription to mRNA maturation and stability, upto mitochondrial translation (TWINKLE, TFAM, POLRMT, LRPPC, and MLTERF4 (mitochondrial transcription termination factor 4)) consistently led to the augmentation of mitochondrial biogenesis, chaperones, proteases, OXPHOS assembly factors, and mitochondrial apoptosis-related proteins, which is the classic signature of UPR^mt [192]. Recent scrutiny of the mitochondrial stress response in Deletor mice, which express a mutant mtDNA helicase TWINKLE, divulged a mild mitochondrial unfolded protein response (UPR^mt) during the advanced stages of the disease, particularly in skeletal muscle [193]. Following these studies, it has now been widely observed and reported that ETC dysfunction in mammals predominantly activates a wider **Integrated Stress Response** that orchestrates metabolic reprogramming, coupled with a mitophagy pathway that facilitates the degradation of damaged mitochondria. Notably, distinct from UPR^mt markers, a noticeable increase in the levels of activating transcription factors (ATF4, ATF5, and CHOP) precedes the activation of the genuine UPR^mt indicators in mammalian contexts [176, 194].

Integrated Stress Response (ISR)

The ISR represents a universal cellular response that orchestrates global protein synthesis modulation in reaction to various physiological and pathological stressors [1] These stressors encompass external factors such as viral infections, hypoxia, nutrient deficiencies, as well as internal triggers like protein accumulation, endoplasmic reticulum stress, or mitochondrial dysfunction [195, 196]. As our understanding of these intricate stress response mechanisms deepens, we unravel the complex interplay between cellular compartments in maintaining proteostasis and adapting to diverse stress challenges [1]. Depending on the nature of the stress stimuli, the ISR is typically activated by one or more members of a family of kinases that phosphorylate downstream players in the pathway [1]. The four kinases have conserved kinase domains but divergent regulatory domains that allows their activation in response to different forms of stress [197]. *The heme-regulated inhibitor (HRI, EIF2AK1)* is mainly activated by heme shortage. HRI possesses heme-binding domains that sense heme deficiency. Its activation inhibits globin synthesis to balance cellular levels of heme/globin [198]. Additionally, HRI was shown to be involved in the protection of erythroid precursors during iron deficiency, erythropoietic protoporphyria and β-thalassemia [198]. *The double-stranded RNA-dependent protein kinase (PKR, EIF2AK2)* has a double stranded RNA (dsRNA) binding domain which makes it responsive to viral dsRNAs . Indeed, PKR stands out as the player in ISR that can sense viruses [199]. PKR is autophosphorylated and activated upon its dimerization, where phosphorylation on Thr 446 in the activation loop of the kinase domain is required for its full activity [200]. It is also stimulated in response to pro-inflammatory stimuli, cytokines, growth factors, and oxidative stress. *The PKR-like ER kinase (PERK, EIFAK3)* is activated by endoplasmic reticulum stress as part of the unfolded protein response (UPR), which is an important process in maintaining proteostasis in

the ER. Accumulation of misfolded proteins in the ER leads to ER stress which activates the UPR [201]. In its inactive state, PERK has its N-terminal domain inserted in the ER lumen where it is associated with the 78 kDa Hsp70 chaperone binding immunoglobulin protein (BiP), or glucose-regulated protein (GRP78).
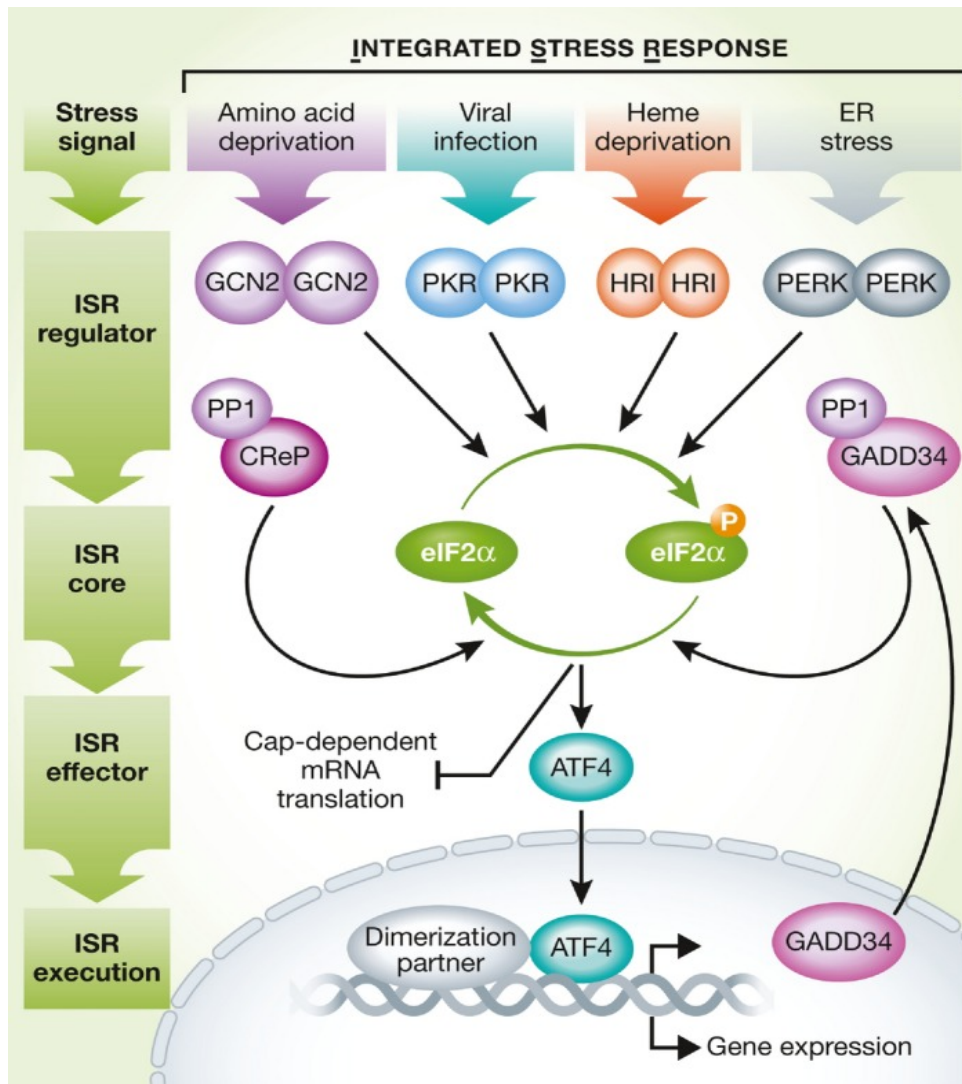
Figure H. Basic overview of the steps of ISR. *Adapted from [1]*

Accumulation of unfolded proteins slated for the secretory pathway leads to UPR activation and dissociates BiP/GRP78 from PERK, leading to its dimerization and activation [202, 203]. *The general control non-derepressible 2 (GCN2, EIF2AK4)* is mainly activated by deacetylated His-tRNA due to low amino acid content [204].

The ISR, triggered by diverse stress signals and metabolic cues, prompts the phosphorylation of eIF2α, effectively stalling global translation [205]. Concurrently, a select subset of transcripts, including activating transcription factor 4 (ATF4), undergoes preferential translation, ensuring effective responses to cellular stress [205]. The most crucial step of the integrated stress response (ISR) lies the pivotal event of eukaryotic translation initiation factor 2 (eIF2α) phosphorylation at serine 51. eIF2 is formed of 3 subunits (α, β and γ), and activating any one of the mentioned kinases leads to the phosphorylation of the α subunit of eIF2 at Serine 52 (p-eIF2α)

[206]. This event shifts eIF2 to a non-competitive inhibitor of the GEF eIF2B, which is formed of two copies of 5 subunits (α, β, γ, δ and ε). The ε subunit of eIF2B carries its catalytic nucleotide exchange activity [206]. The γ subunit of eIF2 interacts with the ε subunits of eIF2B which leads to an open conformation of eIF2γ, facilitating the exchange of GDP and GTP [206]. However, phosphorylation of eIF2α due to an active ISR sterically hinders eIF2γ-eIF2Bε interactions and impedes the formation of an active TC [205]. This globally impedes 5′Cap-dependent protein synthesis[1]. However, the translation of specific master proteins of ISR is activated by a very interesting mechanism. For instance, the mRNAs encoding ATF4 and ATF5 have upstream open reading frames (uORFs) in their 5'-UTR that prevent their translation under normal conditions [207]. Specifically, the most well-characterized ISR effector ATF4 has multiple uORFs in its 5'-UTR which requires the TC to re-initiate for proper translation [3]. Under unstressed conditions, ribosomes scan the mRNA and encounter the first uORF. However, TC incorporates to the ribosome in time to translate the second inhibitory uORF instead, leading to decomposition of the complex and failed translation of ATF4 [3]. In stressed conditions, due to limited available amounts of TC, the ribosome to scan further until it reaches the main ORF and forms a proper translation machinery with TC, leading to elevated translation of the mRNA (Fig) [208].
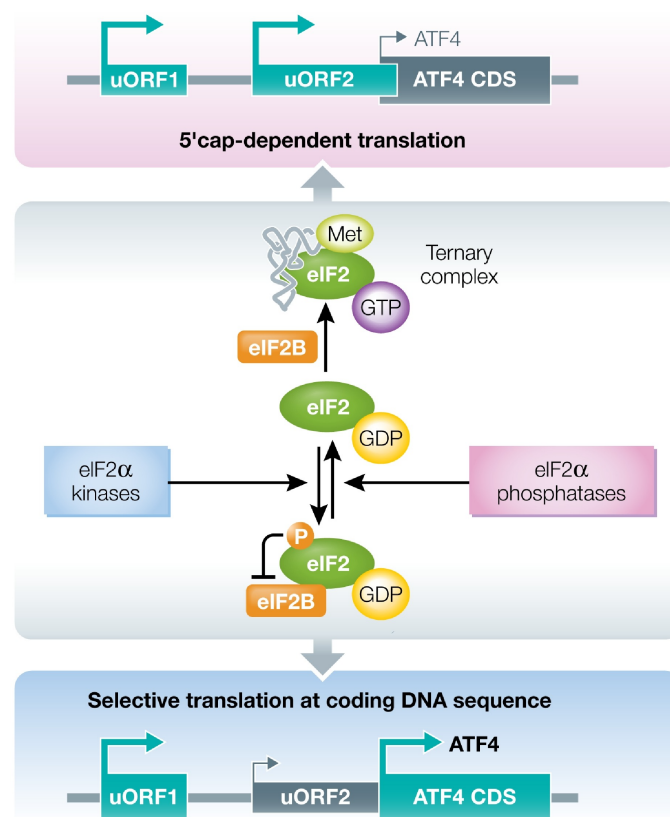
Figure I. eIF2 dependent two-pronged control of translation - canonical ISR response. *Adapted from [1]*

Termination of ISR is also as important, to ultimately determine cell fate and also restore homeostasis [209]. The termination is mediated by protein phosphatase 1 complex (PP1), which is formed of a catalytic subunit (PP1c) and one of two regulatory subunits [1]. The PP1 regulatory subunit 15A (PP1R15A) also known as growth and

DNA-damage-inducible protein (GADD34) and PP1R15B or the constitutive repressor of eIF2α phosphorylation (CReP) are both activated by ATF4 [210]. While CreP helps maintain normal levels of eIF2αP even under normal conditions, GADD34 actively dephosphorylates p-eIF2α under stressed conditions since it also contains uORFs in its 5'-UTR and is directly upregulated by p-eIF2α – in the form of a feedback mechanism [210]. It has also been recently shown that CHOP acts as a rheostat to attune ISR duration depending on the extent of mitochondrial dysfunction. CHOP, in association with C/EBPβ prevents overactivation of ATF4 [211].

Emerging research has unveiled a direct connection between mitochondrial stress and ISR; involving the inner mitochondrial membrane (IMM) protease OMA1. This protease is proposed to become activated during mitochondrial stress, cleaving the IMM protein DELE1 [103]. Intriguingly, the cleaved DELE1 accumulates in the cytosol, where it interacts with and triggers the activation of HRI. This event, in turn, gives rise to the activation of the mitoISR [103, 212]. By means of ATF4 activation, the mitoISR initiates the transcription of downstream target genes, which encompass enzymes pivotal for 1C metabolism, serine biosynthesis, transsulfuration, the glutamate-to-proline conversion pathway, as well as GDF15 and FGF21 [196, 213]. Notably, these two cytokines are shown to be released from tissues when OXPHOS becomes deficient [214-216]. The upregulation of these genes, in addition to release of signaling molecules that can orchestrate systemic metabolism makes ISR an interesting node between OXPHOS deficiency, stress responses and associated metabolic rewiring.

ISR associated metabolic rewiring-
An interesting hallmark of ISR mediated gene expression changes is the metabolic rewiring that occurs due to upregulation of genes downstream of ATF4. Metabolic rewiring is in fact one of the major adaptive responses downstream of ATF4 activation that elicit pro survival cues. In models of mitochondrial dysfunction in mammals, the genes targeted by ATF4 are notably associated with folate-driven one-carbon metabolism (1C), branch chain amino acid metabolism, synthesis of glutathione and transsulfuration pathway and serine biosynthesis [196]. The intricate network of 1C metabolism encompasses a series of interconnected pathways, prominently featuring the methionine and folate cycles, which hold a pivotal position in cellular operations. These pathways furnish essential 1C units, also known as methyl groups, indispensable for the synthesis of crucial cellular components such as DNA, polyamines, amino acids, creatine, and phospholipids [217]. An influential participant in these cycles is S-adenosylmethionine, which acts as a potent donor of aminopropyl and methyl groups. This compound plays a central role in catalyzing DNA, associated protein, and RNA methylation, and has been implicated in cardiovascular diseases, nutritional disorders like obesity and type 2 diabetes etc [218]. Given its pivotal role in nucleic acid synthesis, inhibition of folate metabolism effectively halts cellular proliferation, a property capitalized upon in the use of mammalian folate transformation inhibitors like methotrexate and pemetrexed, which find wide application as antibiotics and chemotherapeutics [219]. Another activated pathway is the   transsulfuration pathway which is a vital metabolic route facilitating the transfer of sulfur from

homocysteine to cysteine. This pathway holds significance as it culminates in the production of essential sulfur metabolites, including cysteine, glutathione (GSH), and the gaseous signaling molecule hydrogen sulfide (H_2S).
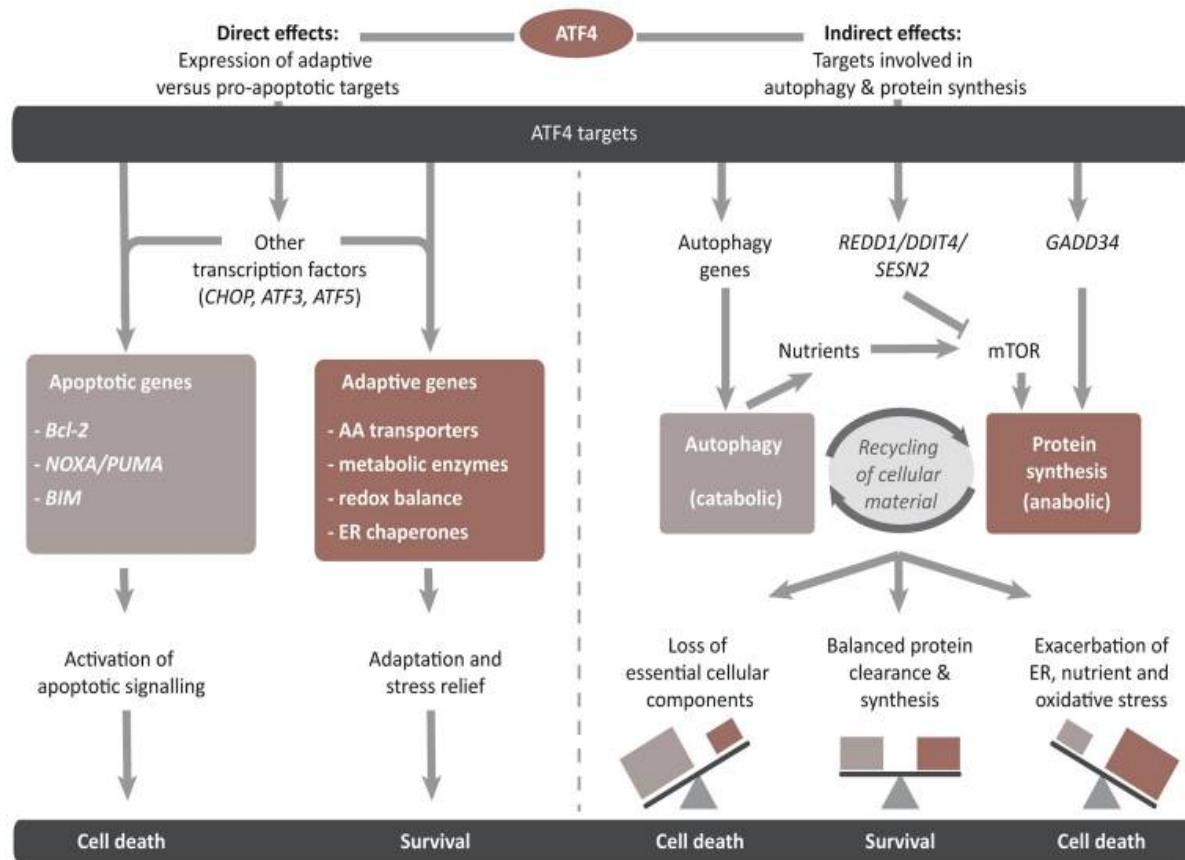
Figure J. ATF4 dependent regulation of diverse cellular processes. *Adapted from [3]*

Precise regulation of this pathway is important for cellular homeostasis since the intermediates involved in this reaction are crucial for oxido-reductive balance as well as responsive to cellular cues. This regulation involves intricate control mechanisms acting upon the key enzymes of the pathway, cystathionine β-synthase and cystathionine γ-lyase, at multiple levels [220]. Moreover, these enzymes specifically wield significant influence over cellular redox equilibrium by modulating levels of GSH. Interestingly, the intricate interplay between these enzymes and cellular nutrient sensing coupled to stress signaling becomes apparent, as mTORC1 signaling actively contributes to the synthesis of glutathione, and this connection is mediated through ATF4. ATF4 also controls the expression of cystine transporter SLC7A11, ultimately impacting glutathione synthesis [221]. Furthermore, ATF4's regulatory impact extends beyond redox status, as demonstrated in a separate study in neurons showcasing its substantial role as a major upstream controller of gene expression changes prompted by oxidative stress [222]. Disturbances within the transsulfuration pathway significantly contribute to the pathogenesis of several conditions, such as vascular dysfunction, Huntington's disease, and aging, underscoring its critical role in health and disease, with most of these conditions also having upregulation of integrated stress response [1]. Serine synthesis has also been linked to ISR. A study

showed that a decrease in Ser was observed upon depletion of the glycolytic substrate 3-phosphoglycerate, which cancer cells redirect towards *de novo* serine biosynthesis [223]. ATF4 has been shown to induce the expression of genes associated with both the transport and synthesis of serine, as well as those involved in the production of Asp, asparagine, and alanine (GPT2, ASNS, SHMT1, and PSAT1) [224]. Of the various pathways associated within the umbrella of ISR mediated and/or ATF4 regulated metabolic pathways, the *serine biosynthesis pathway* serves as the node for folate cycle and methionine cycle, thereby positing a string regulatory role in determining cellular homeostasis.
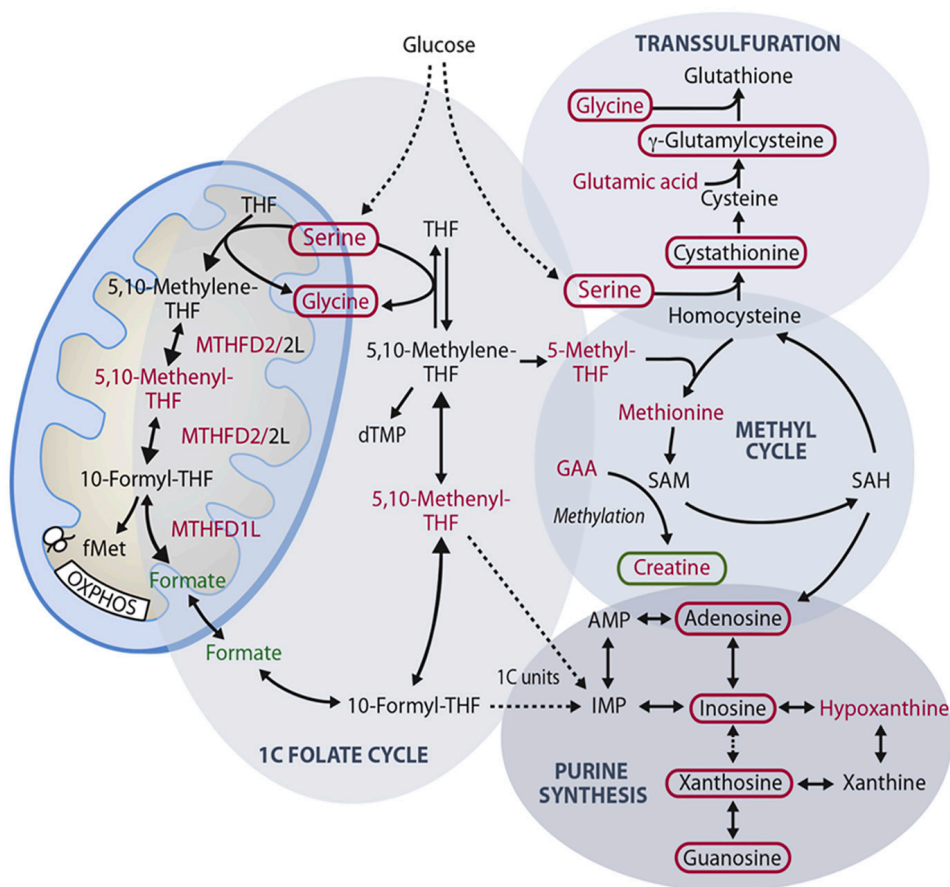
Figure K. Overview of ISR associated metabolic remodelling. *Adapted from [2]*

The interconversion of serine and glycine is mediated by hydroxymethyltransferases (SHMT1 and SHMT2), and serine is a major donor of the one carbon unit during its conversion to glycine [225].

Additionally, BCAA metabolism, which is intricately linked to OXPHOS dysfunction, plays a crucial role in the context of adipose tissue biology [226]. The metabolism of BCAAs– namely leucine, isoleucine, and valine – within adipocytes is a vital process that influences cellular function. These amino acids are transported into adipocytes and subsequently processed in the mitochondria, resulting in the formation of important intermediates, namely acetyl-CoA and succinyl-CoA [227]. These intermediates, in turn, facilitate robust pyruvate metabolism, leading to the generation of citrate and subsequent lipogenesis [228]. In this context, the research conducted by

Herman *et al*. [229] is notable, revealing the active involvement of adipocytes in converting BCAAs into precursors essential for lipogenesis, and underscoring the significance of maintaining a replenished TCA cycle to support maximal lipogenic rates. Recent metabolomic investigations into human obesity and metabolic dysfunction have further illuminated the connection between circulating BCAAs and the development of insulin resistance. Numerous analyses have consistently highlighted the accumulation of serum BCAAs as a molecular indicator of the insulin-resistant state, shedding light on the intricate interplay between amino acid metabolism and metabolic health [227].

Adipose Tissue

There are two main types of adipose tissues in mammals: white and brown. White adipose tissue (WAT) functions as the traditional storage site for fat. WAT is classified majorly according to its location- mainly segregated into *subcutaneous* (beneath the skin) and *visceral/omental* (within the abdomen, adjacent to internal organs) compartments. *Inguinal WAT (iWAT)* is the largest and most studied subcutaneous WAT depot, whereas the perigonadal WAT or (pgWAT or eWAT) is the most abundant form of visceral WAT [230]. Apart from its main role in storage of excess energy as fat, WAT also carries out essential immune and endocrine functions, while also providing thermal insulation and mechanical protection to internal organs. *Brown adipose tissue (BAT)* on the other hand majorly functions in burning fuel reserves to produce heat and modulate body temperature through non-shivering thermogenesis [231]. This is facilitated by uncoupling protein 1 (UCP1) that uncouples ATP production from the mitochondrial electrochemical gradient and in the process, generates heat. The presence of UCP1 is a characteristic feature of BAT. Both WAT and BAT play a vital role in maintaining systemic energy homeostasis and regulating insulin sensitivity and are important for health. For instance, disruption of WAT function is associated with insulin resistance [232] and on the other hand, activation of BAT improves insulin sensitivity and prevents weight gain [233].

Morphologically, brown adipocytes are different from white adipocytes as they have smaller multilocular lipid droplets (in contrast to a large unilocular lipid droplet in white adipocytes) and an overall more number and larger mitochondria [234]. Brown fat cells typically range from 15 to 50 μm, whereas white fat cells, capable of extensive lipid storage, can expand up to approximately 100 μm in diameter. The abundance of mitochondria lead to the darker brown color of these adipocytes. Adipocyte differentiation, termed as 'adipogenesis' for both white and brown adipocytes encompasses the first step of commitment to a distinct preadipocyte lineage and then, subsequent differentiation. The white and brown adipocytes arise from two different mesenchymal precursor cells- Myf5-negative, for white adipocytes and Myf5-positive (myogenic precursor) for brown adipocytes [235]. Even though they have different developmental origins, both white and brown adipocytes rely on some common core adipogenic factors for differentiation, such as the transcription factor peroxisome proliferator-activated receptor gamma (PPARγ), CCAAT/enhancer-binding proteins (C/EBPs) like C/EBPα, C/EBPβ and C/EBPδ and bone morphogenic proteins (BMPs) [236]. Some adipogenic factors are specific to brown adipocytes. These include

transcription factors like PR domain–containing protein-16 (PRDM16) that induces BAT-selective genes [237] and peroxisome proliferator–activated receptor γcoactivator-1α (PGC-1α) [238] that primarily regulates mitochondrial biogenesis, oxidative metabolism, and thermogenesis (As reviewed in [239]).

In addition to white and brown adipocytes, studies in the last few decades have revealed a third type of adipocytes called 'beige' or 'brite' adipocytes [240]. These cells are brown-like adipocytes present within the WAT depots, share similar developmental origins and resemble white adipocytes in their basic characteristics; but have the capacity of upregulating the expression of UCP1 upon cAMP stimulation [241].
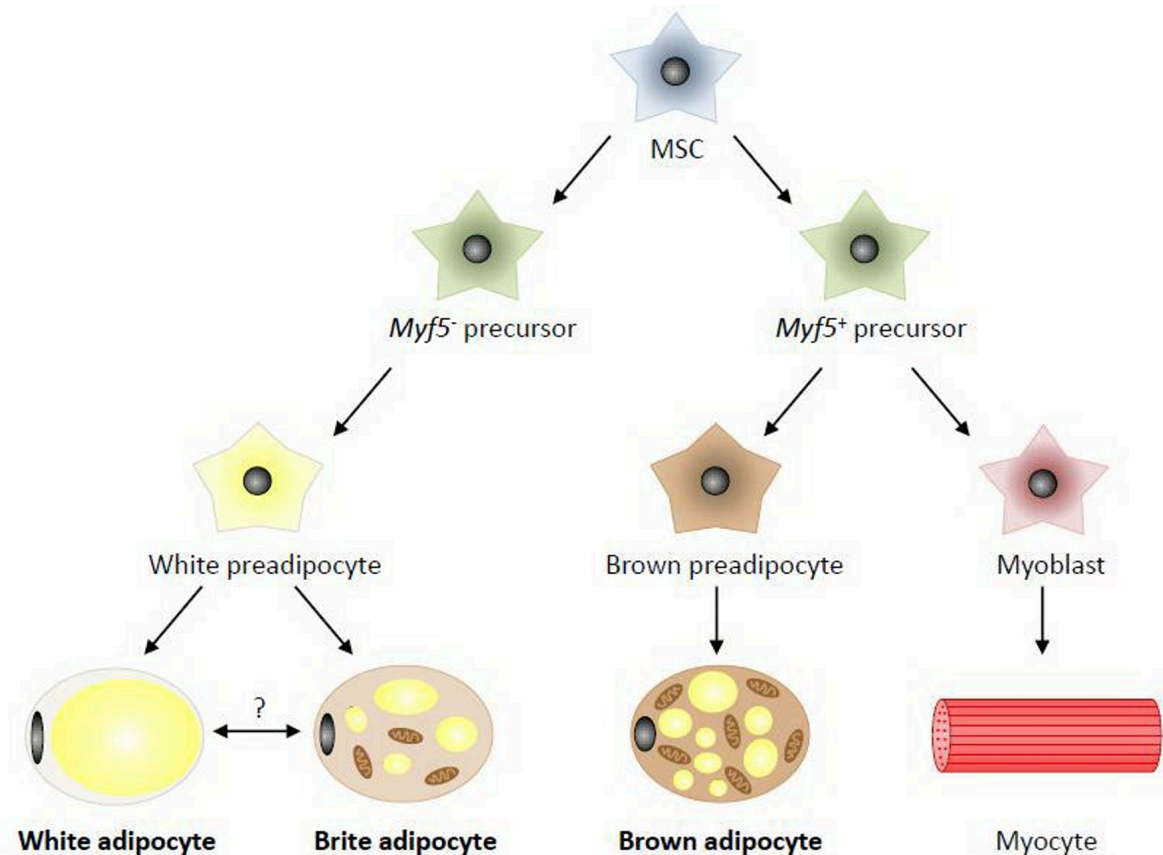
Figure L. The distinct and non-overlapping developmental lineages of WAT and BAT. *Adapted from [5]*

This phenomenon is termed 'browning' of white adipocytes. Several mediators of browning have been identified, such as COX2 (Cyclooxygenase-2), SIRT1 (Sirtuin 1), BMP7 (Bone morphogenic protein 7), Irisin etc. and all of them lead to browning via three core transcriptional regulators: PPARγ, PRDM16 and PGC-1α (As reviewed in [242]). All stimuli or agents that lead to browning so far- bind, interact, activate or inhibit one, or more of these three core factors. Browning of WAT has been shown to be induced by stimuli such as cold exposure, physical activity, hormones such as irisin and FGF21, and compound treatments such as rosiglitazone [243]. Additionally, dietary compounds like polyphenols and omega-3 fatty acids have also been implicated in promoting the browning of white adipose tissue. Induced browning of WAT is important in combating obesity as mice with a higher predisposition to browning show a lower weight gain and vice versa [244]. In addition, it is also shown that

browning increases the plasticity of the WAT depots by allowing a functional switch from energy storage to energy consumption, i.e. attaining a BAT-like state [245]. Although brite adipocytes are functionally similar to classical brown adipocytes, there are a few key differences that set them apart. Brown adipocytes are formed from Myf5-negative precursor cells [246] and each have their own distinct gene signature profiles, now also examined at single cell resolution [241]. Moreover, the expression of UCP1 and other thermogenic genes is basally low in brite adipocytes and needs to be 'induced'; whereas the brown adipocytes express high levels of these genes even at the basal conditions.

Adipose tissue in health and disease-

Adipose tissues play a crucial role in orchestrating metabolic health of an organism. WAT is responsive to nutrient intake by the organism and is important for the maintenance of normal glucose and serum triglyceride levels and insulin sensitivity. Mice mutants lacking WAT were reported to have severe metabolic abnormalities like insulin resistance, hyperglycemia, hyperlipidemia and fatty liver [247].
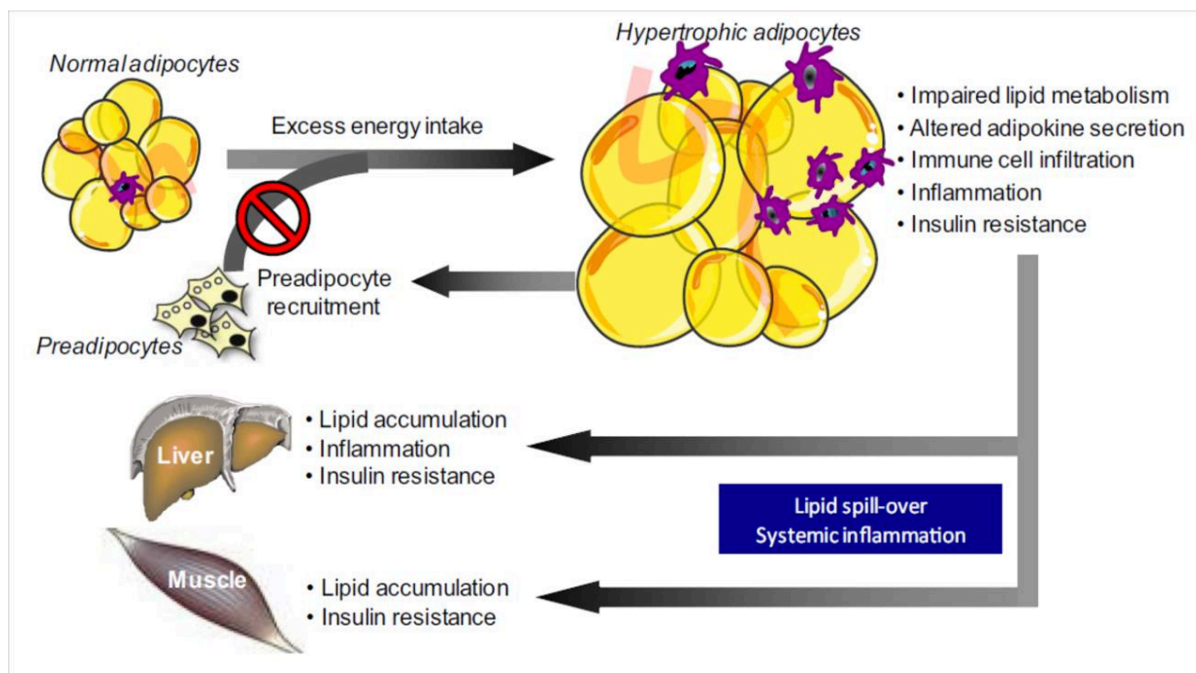
Figure M. Major hallmarks of white hypertrophic adipocytes commonly associated with metabolic disorders. *Adapted from [7]*

BAT, owing to its ability to burn fat and channelize it into thermogenesis, is a proven candidate for counter-acting nutrient overload, obesity and diabetes. Studies in humans have shown that the activity of BAT is inversely correlated with adiposity and its activation improves glucose clearance at a systemic level, thereby increasing insulin sensitivity [248]. In addition, it has been shown that BAT in mice can act as a sink and clear triglyceride rich proteins from circulation, thereby reducing hyperlipidemia [249]. It is estimated that BAT in humans has the capacity to contribute as much as 20% of the daily energy expenditure [250]. A recent review highlighted the importance of human BAT in diabetes and obesity as well as the possibility of BAT being a potential

drug target to treat these maladies [251]. Dysfunction in adipose tissues (both BAT and WAT) is now deemed as one of the major contributors to obesity and obesity-related metabolic disorders like the metabolic syndrome, type 2 diabetes and cardiovascular diseases [252]. On the other hand, a state of nutrient excess or positive energy balance, wherein the amount of calories ingested is higher than required, has been shown to lead to obesity and increase in adipocyte size (hypertrophy) in both WAT and BAT [253]. This causes white and brown adipocyte dysfunction as the hypertrophic adipocytes are limited in their capacity to expand due to related factors like local hypoxia and mechanics of extracellular matrix (ECM). White adipocyte dysfunction alters the lipid metabolism and results in release of signaling molecules called adipokines and pro-inflammatory factors, which not only impair adipocyte differentiation but also lead to increased infiltration of immune cells [254]. In addition, adipose tissue dysfunction leads to release of excess lipids in to the circulation and consequent accumulation on other non-adipose organs like liver and muscle [255]. This ectopic fat storage has been shown to lead to lipotoxicity and low grade systemic inflammation, thereby accentuating the development of obesity and related metabolic disorders [252]. In summary, both WAT and BAT play indispensable roles in orchestrating organismal metabolic health through their ability to respond to environmental and nutrient cues, as well as the capacity to communicate to other organs via molecules and metabolites – a theme that is also relevant for our study.

Role of mitochondria in adipose tissue

Initial observations from obese patients and mouse models of obesity shed light on the relevance of mitochondrial numbers and function in regulating lipid metabolism via adipose tissue. Inverse correlations have been reported between mitochondrial respiratory capacity and body mass index in adipose tissues from humans [256]. Furthermore, ADP-stimulated mitochondrial respiration, mtDNA copy number, and OXPHOS complex protein expression are dramatically decreased in the adipose tissues of obese subjects [256] . Another study showed that specifically, the steady state levels of OXPHOS complexes III, IV, and V are decreased in the adipose tissues of obese subjects [257]. A study in mice reported a 50% reduction in the abundance of mitochondrial populations in adipocytes isolated from eWAT from *ob/ob* mice (have a mutation in the leptin gene resulting in leptin deficiency), which are obese and diabetic [258]. Likewise, *db/db* mice (harbor a mutation in leptin receptor gene, leading to hyperinsulinemia and obesity) and the dietary HFD-fed mice showed a decreased level of mitochondrial biogenesis regulators, including PGC1α and estrogen-related receptor-α, and a resultant loss of mitochondrial mass and cristae structure [259]. Furthermore, treatment of adipocytes with tumor necrosis factor-α (TNF-α), which is an inflammatory cytokine that increases in obesity, led to mitochondrial dysfunction, smaller and condensed mitochondria with less cristae and lower intracellular ATP synthesis [260]. TNF-α treatment was also shown to reduce expression of OXPHOS genes and FAO genes in primary adipocytes [261]. Ectopic lipid accumulation is increased due to reduced fatty acid oxidation and energy expenditure due to mitochondrial dysfunction in the BAT of people with obesity and metabolic diseases [255]. In summary, nutrient excess leads to mitochondrial dysfunction, which in turn

accelerates obesity-related pathologies. This is potentiated by an overall proinflammatory tone, or in part due to the harmful effects of ROS [255].
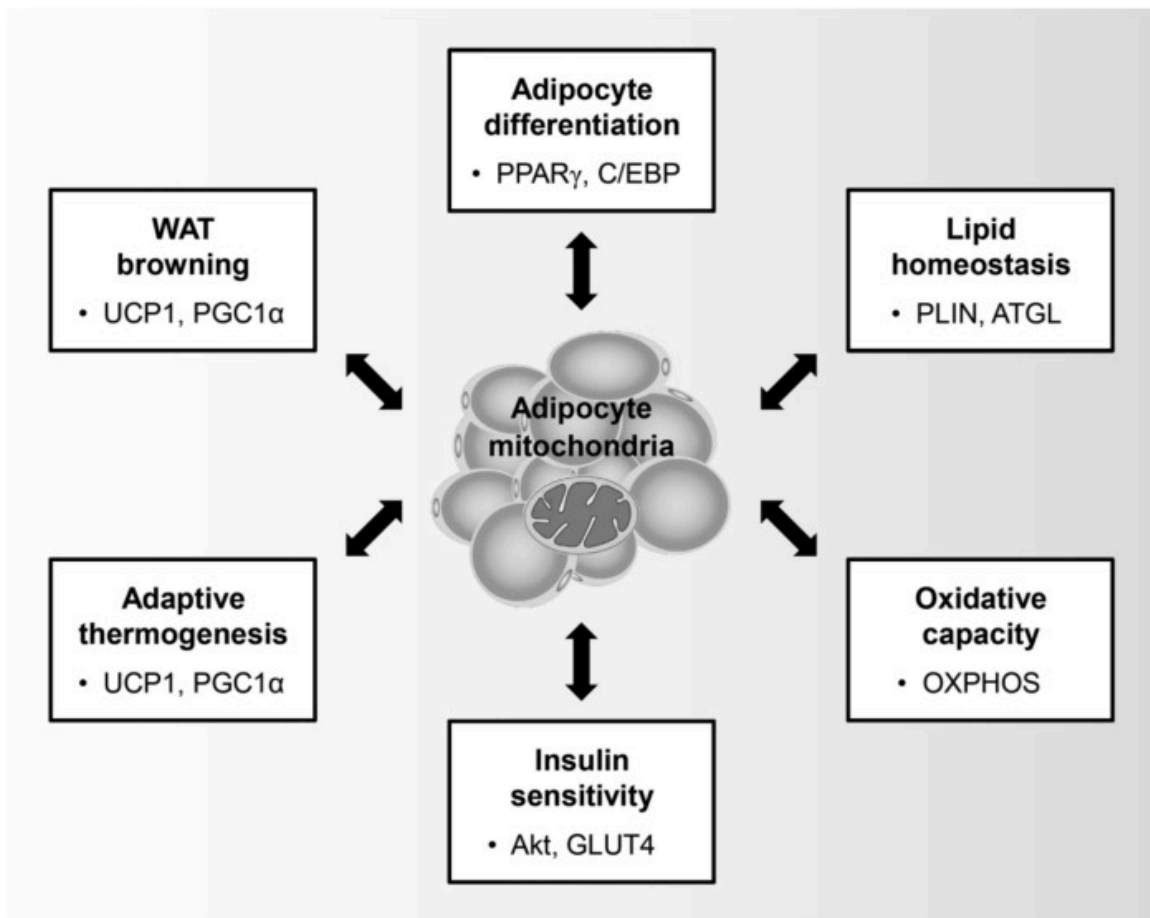
Figure N. Diverse role of mitochondria in adipose tissue (WAT and BAT). *Adapted from [4]*

Conversely, multiple studies on induced mitochondrial dysfunction by either drug treatments or genetic ablations, revealed altered lipid metabolism in adipocytes, with consequences on cellular and organismal homeostasis. It has been reported that the mitochondrial dysfunction with an OXPHOS CIII inhibitor causes triglyceride accumulation by inducing excessive lipogenesis in 3T3-L1 preadipocytes [262]. OPA1 (mitochondrial fusion protein) knockdown in 3T3L1 cells and loss of function model of adipose tissue led to reduced lipolysis and glycerol release by regulating PKA mediated phosphorylation of PLIN1, a protein localized on lipid droplet surface [263]. Activation of mitochondria in brown adipocytes accelerates heat generation by increasing the inner mitochondrial membrane UCP1 [264]. There are a myriad of studies with both systemic and tissue specific alterations of mitochondria and their effect on organismal physiology, which is beyond the scope of this thesis, but beautifully summarized in [4].

Brown Adipose Tissue - Thermogenesis in BAT

BAT is a special organ since it is the primary organ that has the capability of performing cold induced thermogenesis by producing heat. Thermogenesis is a critical process in that involves the conversion of chemical energy from stored triglycerides

into heat. This process is primarily mediated by the activation of thermogenesis signaling pathways that enhance mitochondrial respiration and energy expenditure. SNS activation is a fundamental trigger for thermogenesis in BAT. Upon cold exposure or other stimuli, sympathetic nerve fibers release norepinephrine (NE) onto BAT adipocytes. NE binds to β-adrenergic receptors (β-ARs) located on the cell surface. This binding activates the G-protein coupled receptor (GPCR) signaling pathway, leading to the activation of adenylate cyclase and an increase in intracellular cyclic AMP (cAMP) levels. Elevated cAMP levels activate protein kinase A (PKA). PKA phosphorylates multiple substrates, including hormone-sensitive lipase (HSL) and perilipin, leading to the initiation of lipolysis and the release of free fatty acids (FFAs) from lipid droplets. One of the key players in thermogenesis is Uncoupling Protein 1 (UCP1). As the proton gradient builds up due to increased mitochondrial respiration, UCP1 is activated. UCP1 forms a proton channel in the inner mitochondrial membrane that allows protons to re-enter the mitochondrial matrix without passing through ATP synthase. This uncoupling of the proton gradient from ATP synthesis leads to heat generation instead of ATP production. UCP1-KO mice raised at thermoneutrality fail to maintain the body temperature upon acute cold exposure, as would be expected from UCP1 deficiency.
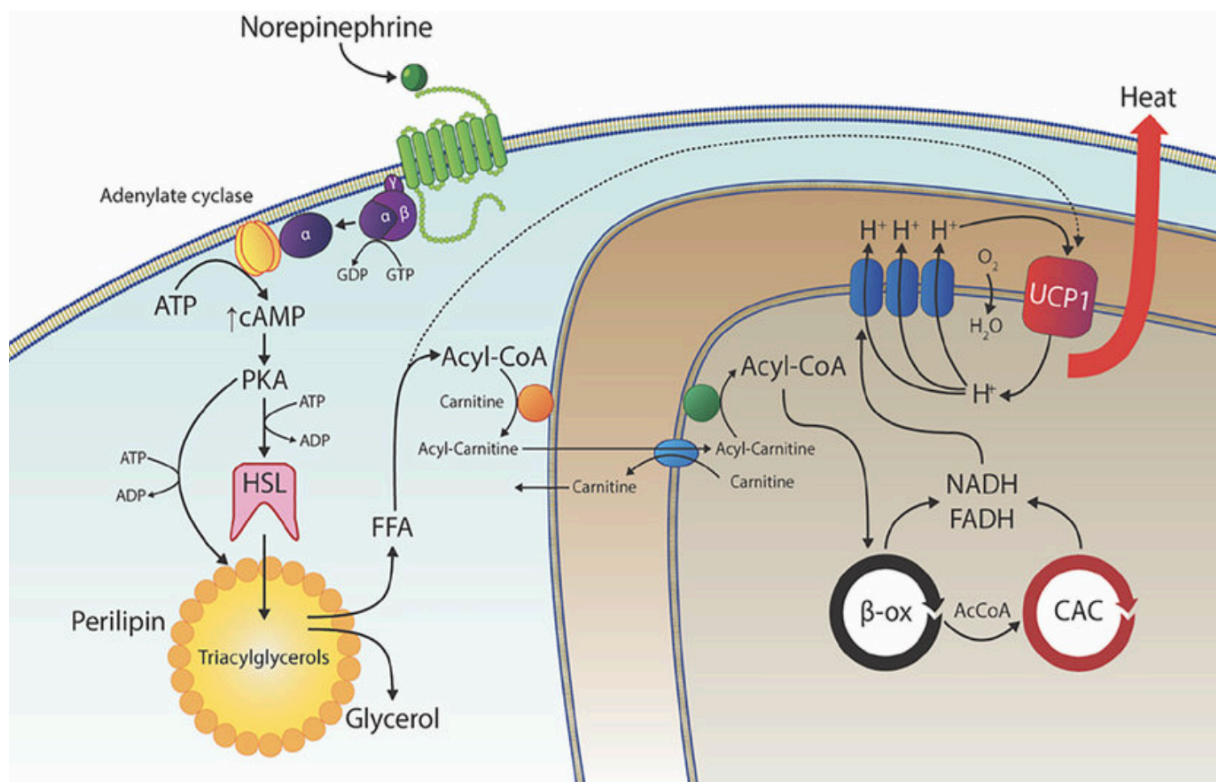
Figure O. Schematic representation of thermogenesis mechanism in a brown adipocyte.
Stimulation of β3-adrenergic receptors by norepinephrine from the nerves of the sympathetic nervous system triggers an intracellular signaling pathway that breaks the lipid drople in the adipocyte (lipolysis) by phosphorylation of the hormone-sensitive lipase (HSL), and mobilizes the fatty acids (FFA) released into the mitochondria These triglycerides are β-oxidized (β-ox), releasing acetyl-CoA that enters the citric acid cycle (CAC). The mitochondria of the brown adipocytes are unique by expressing the uncoupling protein 1 (UCP1) in the inner membrane, which allows the respiratory chain to be uncoupled, pumping back the protons of the intermembrane space. This nonsense process generates heat (thermogenesis). Adapted from [12]

A stepwise reduction of ambient temperature (cold adaptation) improves their thermogenic capacity and they develop a presentable cold tolerance [265]. Activation of thermogenesis is associated with thermogenic gene induction in BAT, such as DIO2 (Type 2 Iodothyronine Deiodinase), that converts the inactive thyroid hormone T4 into the active T3. T3 promotes UCP1 expression and enhances thermogenesis in BAT. CIDEA (Cell Death-Inducing DNA Fragmentation Factor Alpha-Like Effector A) is involved in lipid droplet formation and fusion. It is upregulated in BAT during cold exposure and contributes to lipid mobilization and thermogenesis. CPT1B (Carnitine Palmitoyltransferase 1b) facilitates fatty acid uptake and oxidation in mitochondria. Its upregulation enhances the availability of substrates for thermogenesis. FGF21 is induced in BAT upon cold exposure and contributes to the regulation of energy homeostasis, including thermogenesis. Peroxisome proliferator-activated receptor gamma coactivator-1 alpha (PGC-1α) is a master regulator of mitochondrial biogenesis and thermogenesis. It stimulates the expression of UCP1 and other thermogenic genes, promoting mitochondrial function and heat production.

Calcium signaling also plays a role in the regulation of thermogenesis. Calcium ions (Ca2+) increase upon sympathetic nerve activation and stimulate several processes. Calcium signaling is involved in the upregulation of UCP1 production. Elevated intracellular calcium levels trigger the activation of transcription factors, such as CREB (cAMP response element-binding protein), which bind to the UCP1 promoter region and enhance UCP1 gene expression. Another major pathway is the activation of the Ca²⁺/calmodulin-dependent protein kinase II (CaMKII). CaMKII activation stimulates PGC-1α (PPARγ coactivator 1α) expression, which, in turn, upregulates UCP1 and other thermogenic genes. increased cytosolic calcium levels activate the transcription factor NFAT (nuclear factor of activated T-cells), which translocates to the nucleus and regulates the expression of thermogenic genes. Lastly, The uptake of calcium into the mitochondria, a process called mitochondrial calcium uptake (MICU), influences oxidative phosphorylation and ATP synthesis. This influx of calcium into the mitochondria might contribute to mitochondrial uncoupling and thermogenesis [266]. Very interestingly, UCP1 independent thermogenesis has been shown to be mediated by a process called calcium cycling involving the endoplasmic reticulum. [267]

Overview of BAT metabolism and involvement of mitochondria

Deemed an 'energy sink', BAT utilizes a broad source of nutrients. The three main nutrients, carbohydrates, lipids (fats), and proteins, are taken up by BAT and are involved in a complex web of metabolic reactions.

Glucose uptake and cytosolic glycolysis

Glucose is the most common carbohydrate, and ¹⁸F-FDG-PET shows active glucose metabolism in human BAT [268]. Glucose transporters (GLUTs) mediate cellular glucose uptake. Four GLUTs have been reported in mammals, and BAT specifically expresses GLUT1 and GLUT4. Upon uptake, glucose is phosphorylated by hexokinase 2 (HK2) into glucose 6-phosphate (G6P), which channelizes glucose within the brown adipocytes into various reactions post uptake. G6P is then further metabolized by glycolytic enzymes like pyruvate kinase M (PKM) at the final step [269].

Cold exposure leads to significant increase in *Glut1* and *Glut4* expression in BAT of mice [270, 271], and β3-adrenergic receptor (β3-AR) agonist triggers glycolysis in BAT [272]. Knockdown of *Glut1* and *Glut4* In brown adipocytes impairs isoproterenol (ISO) (cAMP activator)-stimulated glycolytic flux and oxygen consumption [273].

Mitochondrial pyruvate oxidation

The final product of glycolysis, pyruvate, enters mitochondria for further oxidation, which starts with mitochondrial pyruvate uptake mediated by Mitochondrial pyruvate carrier (MPC). A heterodimer encoded by two genes (*Mpc*1 and *Mpc*2), it connects the cytosolic glycolysis and mitochondrial oxidation [274, 275]. Pyruvate is then metabolized in the mitochondria by two enzymes-pyruvate dehydrogenase (PDH) and pyruvate carboxylase (PC). PDH reaction converts pyruvate to acetyl coA, which subsequently enters the TCA and is completely oxidized into CO_2 [276]. PC performs an anaplerotic reaction ot convert pyruvate into oxaloacetate, which is then incorporated with acetyl coA to form citrate [277].

In mice, cold exposure induces the expression of *Mpc1/2* in BAT [278], and conditional BAT specific deletion of *Mpc*1 leads to impaired cold adaptation [279]. In addition to MPC, BAT has higher PDH compared to WAT, muscle, and heart [280]. Furthermore, insulin leads to activation of PDH in BAT, which is repressed by fasting and high-fat diet feeding [281, 282]. PDH is deactivated by its kinase, PDH kinase (PDK), and interestingly, PDK2 and PDK4 are induced by cold exposure and β3-AR agonist in BAT, which may be involved in controlling the fate of glucose between oxidation and glycerol production [283, 284]. Consistently, even in humans, In comparison with WAT, BAT expresses a high level of mitochondrial proteins, especially those involved in the TCA cycle and OXPHOS [285]. Beyond alterations in mere expression of metabolic enzymes, functional studies also showed that glucose oxidation is stimulated in cultured brown adipocytes [286]. In tissue sections of rat interscapular BAT, insulin induces glucose uptake and glucose oxidation, as the conversion of [^{14}C]glucose into $^{14}CO_2$ is 10-fold higher upon insulin stimulation [286]. In isolated brown adipocytes, both insulin and β3-AR agonist stimulate the conversion of [^{14}C]glucose into $^{14}CO_2$ [287].

Most tissues, including BAT , use glucose to synthesize de novo fatty acids [288]. By converting glucose/pyruvate-derived acetyl coA into citrate, citrate is channeled to two major metabolic pathways within mitochondria. Citrate exits mitochondria via citrate transporter protein (CTP), as well as the TCA cycle [270]. Glucose is also an important source of acetyl coA, which provides building blocks for *de novo* fatty acid synthesis in most tissues, including BAT. Within mitochondria, glucose/pyruvate-derived ACC is converted by citrate synthase into citrate, which is channelized to two major metabolic pathways. First is the TCA cycle, and in the other pathway, citrate exits mitochondria into the cytosol through citrate transporter protein (CTP), which is encoded by gene *Slc25a1* [289]. It is then converted by ATP-citrate lyase (ACLY) back into ACC, the major carbon source for de novo fatty acid synthesis [290]. All lipogenic tissues, including liver and adipose tissues, use CTP and ACLY to connect glucose and fatty acid metabolism. ACLY levels increase in BAT but not in

WAT when mice are exposed to cold[271, 291]. It has also been shown that ACLY expression is regulated by mTORC1, a cold-activated metabolic sensor in BAT [292].

Lipolysis, Fatty acid uptake and β-oxidation

In humans [272], cold exposure has been shown to increase whole-body lipolysis [291], while microdialysis assays revealed glycerol release by human BAT. A relative decrease in lipid content has been observed in activated BAT in rodent models [293, 294].

There are three steps to TG lipolysis, catalyzed by ATGL, HSL, and monoacylglycerol lipase in sequential order. ATGL catalyzes the hydrolysis of TG to diacylglycerol (DAG) [295]. HSL and ATGL are both essential for induction of oxidative genes in brown adipocytes [296]. In ATGL-deficient mice, both whole-body and tissue-specific thermogenesis has been extensively studied. While whole-body ATGL-deficient mice lack cold adaptation [281], BAT-specific ATGL-deficient mice maintain body temperature after acute cold exposure despite hypertrophy and whitening, while consuming the same amount of oxygen [297]. It is interesting that adipose-specific ATGL-deficient mice phenocopy the whole body knockouts in defective thermogenesis [298].

Also observed is lipolysis-independent thermogenesis. Acute cold exposure with food access does not affect mice lacking BAT Comparative Gene Identification-58 (CGI-58), a lipolysis activator essential to stimulated LD lipolysis[299] . A mouse lacking CGI-58 in both BAT and WAT is cold-sensitive, suggesting that BAT lipolysis is not necessary for cold-induced thermogenesis [299]. Another study found that mice lacking lipid droplets in brown adipocytes can still maintain thermogenic activity during cold exposure, as were brown adipocytes of mice lacking both DGAT1 and DGAT2 [300].

Initial studies using [18]FTHA-PET/CT imaging reported enhanced fatty acid update in activated brown adipocytes [301]. Within these thermogenic adipocytes, both extracellular (from fatty acid uptake) and intracellular (from TG lipolysis) fatty acids are used up for mitochondrial β-oxidation. Metabolomics studies showed that cold exposure actives fatty acid β-oxidation in rat BAT [302]. β-oxidation involves successive carnitine acyltransferases (CPTs) moving acyl-coenzyme A (acyl-CoAs) into mitochondria. A specific transporter makes acylcarnitines cross mitochondrial membranes by CPT1. As soon as CPT2 enters the mitochondrial matrix, acyl-CoAs are generated from acylcarnitines [303]. In mice, cold exposure increases CPT1/2 mRNA expression[270, 271]. Acute cold exposure results in hypothermia in mice with adipose-specific CPT2 deletions, suggesting fatty acid oxidation is crucial to cold-induced BAT thermogenesis [304]. As a source of energy for thermogenesis, liver-derived acylcarnitines can also be uptaken by BAT, and carnitine supplementation protects mice from cold sensitivity with age [305].

De novo fatty acid synthesis and lipogenesis

BAT also actively produces fatty acids through *de novo* fatty acid synthesis and *de novo* lipogenesis (DNL), respectively. Considering BAT is specialized for heat production, it is not surprising that both de novo fatty acid synthesis and fat oxidation

are often activated simultaneously in BAT, which might results in a futile cycle [306, 307].

Three enzymes catalyze de novo fatty acid synthesis: ACLY (acetyl coA lyase), ACC (acetyl coA carboxylase), and FASN (fatty acid synthase).The enzyme ACLY produces cytosolic acetyl coA, the main building block of de novo fatty acid synthesis. ACC converts cytosolic acetyl coA into malonyl-CoA, which is the direct substrate of FASN to produce fatty acids [308] . Cold exposure increases ACLY expression in BAT, but not in WAT [291], while sustained cold exposure increases *Acly* and *Acc1/2* expression in BAT in a time-dependent manner in mice [271]. In BAT, chronic adrenergic activation increases DNL and TG/glycerol dynamics [309, 310].

The last step of TG synthesis is catalyzed by DGAT1/2. In primary brown adipocytes, DGAT2 is highly expressed, and 3-AR agonists increase DGAT2-mediated TG synthesis [311]. Studies showing incorporation of [^{3}H]-H_2O into BAT lipids testify enhanced DNL in BAT upon cold exposure in mice [271]. Cold exposure also induces several transcriptional factors in lipid metabolism such as CBP (CCAAT/enhancer-binding protein) [271] and ChREBP (carbohydrate response element-binding protein) [312]. Interestingly, cold temperature also exerts control over circadian rhythms of SREBP1c (sterol regulatory element-binding protein 1c) to activate DNL in BAT [313].

Other metabolites in BAT

According to metabolic profiling, **succinate** is a selectively accumulated metabolite in BAT when exposed to cold [314]. According to studies using stable isotope tracing, cultured brown adipocytes uptake and oxidize extracellular succinate [314]. SDH-mediated ROS production stimulates thermogenesis in cultured adipocytes and BATs of mice [314]. BAT selectively accumulates succinate following acute and chronic cold exposure, according to metabolic profiling. Research employing stable isotope tracing found that cultured brown adipocytes absorb and oxidize extracellular succinate [296]. Other studies also found that physiological ROS stimulate thermogenesis in BAT [315, 316]. Furthermore, succinate is a substrate for mitochondrial protein succinylation, which plays a key role in BAT energy metabolism [317].

BCAAs (valine, leucine, and isoleucine), have increasingly proven to play indispensable role in metabolic homeostasis in BAT [303]. It has been reported that cold exposure promotes BCAA clearance in mice and humans by actively utilizing BCAAs in mitochondria for thermogenesis [318]. In cold-activated BAT, 18F-Fluciclovine PET-CT imaging showed increased BCAA uptake, and [U-13C]leucine tracing revealed its oxidation and utilization [318]. A transporter for BCAAs, the SLC25A44 (Solute Carrier Family 25 Member 44) has also been identified as the mitochondrial transporter responsible for BCAA catabolism [318]. Additionally, BCAAs provide building blocks for de novo fatty acid synthesis in BAT, as adipocytes generate monomethyl branched-chain fatty acids (mmBCFAs, odd-chain FAs C15:0 and C17:0) by using BCAA-derived propionyl-CoA, in addition to glucose-derived acetyl coA [319]. In obese mice, mmBCFAs are significantly decreased because of BAT catabolic and synthesis fluxes [319].

Besides BCAAs, *glutamate* is another amino acid utilized by BAT. Cold exposure increases glutamate uptake specifically by BAT, but not by WAT [320]. The amino acid *alanine* (and not BCAAs or glutamate) has been shown to inhibit glucose utilization in rat BAT, preventing glucose wastage postprandial [321]. BAT thermogenesis depends heavily on *creatine*, another special metabolite [322]. CK (Creatine kinase), an enzyme specially enriched in BAT, converts creatine and ATP into phosphocreatine, an energy reservoir [323]. CK levels are also strongly induced upon cold exposure in both mouse and human brown adipocytes [324]. Very recently, specifically in BAT, the concept of a futile creatine cycle has been proposed, which seemingly assists BAT in acting as a sink [324]. Knocking out the creatine transporter or creatine synthesis enzyme, glycine amidinotransferase in BAT impairs thermogenesis and induces obesity [324, 325].

Mitochondria in BAT

Multiple studies shed light on the relevance of mitochondria in adipose tissue, autonomously and also non-autonomously in regulating systemic metabolism. A comprehensive study characterized the proteomic differences between isolated mitochondria from BAT and WAT in mice [326]. Their findings showed that the proteins involved in pathways related to fatty acid metabolism, OXPHOS, and the TCA cycle were highly expressed in BAT mitochondria compared to that in WAT [326]. In addition, some enzymes like ACSS1 (Acyl-CoA Synthetase Short Chain Family Member 1) and PDK4 (Pyruvate dehydrogenase lipoamide kinase isozyme 4) were detected only in BAT. It has also been shown that BAT preferentially activates LCFA and has much lower MCFA activation as compared to WAT. Treatment of adipocytes with the uncoupling agent, FCCP leads to a noteworthy reduction in insulin-triggered glucose uptake within adipocytes.

A very intriguing concept as emerged from studies on adipose specific (WAT and BAT or only BAT) mutants of mitochondrial proteins. Any perturbation that induces mild dysfunction in the mitochondria leads to systemic metabolic benefits due to a proposed concept called **"mito hormesis"**. For instance, adipose specific (BAT and WAT) TFAM knockout mice (called F-TFKO) exhibit decreased mtDNA copy number, altered levels of ETC proteins, and perturbed mitochondrial function with decreased CI activity and result in greater oxygen consumption and uncoupling in BAT [327].. Despite consuming more food, these mice are protected from obesity, insulin resistance and hepatosteatosis caused by age and diet [327]. This increase in mitochondria mediated burning of calories leads to protective effects in the mice [327]. Another study, however, presented a more nuanced outlook in adipose specific TFAM deletion in mice [328]. The adiponectin TFAM-KO mice used in the study were indeed resistant to weight gain and were protected from diet induced obesity [328]. However, thet displayed insulin resistance on both normal chow and high-fat diets, thereby hinting on context specific differences in TFAM removal from mice [328]. Additionally, suppression of TFAM via RNAi, shows a corresponding decrease in insulin-induced glucose uptake [329]. Similarly, adipose tissue specific MFN2 deletion remodels mitochondria, reduces OXPHOS capacity but in turn leads to increased insulin

sensitivity and resistance to obesity [330]. BAT specific removal of OPA1 results in improved whole body metabolic rates and energy expenditure in mice with a concomitant browning of WAT, resulting in protection from obesity [331]. Another study reported that OPA1 overexpression led to mitochondrial fragmentation in adipose tissues, leading to subsequent browning and improved systemic metabolism, increased insulin sensitivity and glucose tolerance [332]. It was also shown that whole body deletion of the mitochondrial protein VLCAD (very long-chain acyl-CoA dehydrogenase) led to improved insulin sensitivity and protection from weight gain, sue to concomitant activation of AMPK and downstream signalling [333]. Interestingly, adipose specific CPT2 knockout mice showed partial protection from inflammation in WAT but the effects were detrimental in BAT, leading to impaired thermogenesis and impaired FAO, reminiscent of the context specific effects of removal of mitochondrial proteins [304].

Mitochondrial ROS produced by OXPHOS CIII is crucial for the initiation of adipocyte differentiation of human mesenchymal stem cells, and conversely, adipogenesis is inhibited by mitochondria-targeted antioxidants [334]. Additionally, another study demonstrates mitochondrial ROS's significance in thermogenesis within brown and beige adipocytes. The observation on elevation of mitochondrial ROS during BAT thermogenesis indicates that thermogenic ROS impacts cysteine thiols' redox status, enhances respiration, with UCP1's Cys-253 identified as a key target [335].

Taken together, these studies highlight the context dependent effects of mitochondrial perturbations on adipose tissue biology. Mitochondria are intimately integrated with adipose tissue biology and its effect on systemic metabolism, thereby being potential therapeutic targets in obesity and metabolism related disorders.

OBJECTIVES

CLPP has been appreciated for its physiological role only recently. Even though its role in maintaining mitochondrial homeostasis is widely explored, physiological studies on CLPP are relatively scarce. Human patients with Perrault syndrome (which is the closest occurring disease to loss of CLPP mice models) report multiple organs being affected. Since the levels of CLPP vary amongst different tissues in mice, it is very intriguing to explore the tissue-autonomous role of CLPP in mice.

This doctoral study aimed to understand the adipose specific consequences of loss of CLPP on both systemic metabolism, and on tissue-autonomous functioning. Consolidating results from previous studies on loss of function models of CLPP, it could be anticipated that loss of CLPP would induce multifactorial changes at molecular, cellular, tissue as well as organismal levels. The pursuance of this research allowed us a model to uncover the interconnectedness between diverse concepts such as organismal physiology, systemic metabolism, mitochondrial dysfunction induced stress responses, ISR mediated metabolic rewiring, inter organellar cross talk, nuclear-mitochondrial synchrony and finally, metabolites as signalling entities.

In summary, the doctoral study encompassed the following broad goals –
1. Exploring adipose tissue non-autonomous role of CLPP in controlling systemic metabolism
2. Describing iWAT and BAT-autonomous effects of loss of CLPP
3. Investigating the mechanism behind CLPP loss mediated remodeling of BAT

MATERIALS AND METHODS

1. Animal handling and experiments
1.1 Experimental Mouse models

The conditional targeting for the mitochondrial ATP-dependent Clp protease proteolytic subunit (*Clpp*) gene was conducted by Taconic Artemis, Germany in Art B6/3.5 stem cell line on a C56BL/6 TacN background. *LoxP* sites were introduced flanking exons 3 and 5 and in addition, an *Frt* flanked puromycin selection marker was inserted into intron 5. Upon successful germline transmission, the *Clpp+/PuroR-fl* mice were mated with *Flp* deletor mice to remove the *PuroR* selection cassette. Finally, floxed mice (*Clpp^{fl/fl}*) were intercrossed with transgenic mice expressing Cre recombinase. To generate full body CLPP knockout mice, *Clpp^{fl/fl}* were mated with transgenic mice ubiquitously expressing CRE recombinase under control of the β-actin promoter, resulting in *Clpp^{+/-}* mice. Heterozygous *Clpp^{+/-}* mice were further intercrossed to obtain homozygous *Clpp^{-/-}* mice. Adipose tissue-specific knockout animals were generated by mating *Clpp^{fl/fl}* animals with transgenic mice expressing Cre recombinase under control of the control of mouse adiponectin (*Adipoq*) promoter (Adipoq-Cre mice), and mice expressing Cre recombinase under the control of mouse *Ucp1* promoter (Ucp1-Cre mice) respectively.

1.2 Animal care and breeding

All mice analyzed during this study were bred and raised in the CECAD animal facility. Experiments were approved and conducted in compliance with NIH guidelines and approval of the local government authorities (Landesamt für Natur, Umwelt und Verbraucherschutz Nordrhein-Westfalen; LANUV) All animals were kept in singleventilated cages at 22-24 °C under a 12h light/dark cycle, the light starting at 6 am. Mice were fed with *ad libitum* access to water and normal chow diet. For breeding one male was housed with 1-2 females of a similar age with 8 weeks being the earliest time point to start mating.

1.3 Phenotyping

Body weight

Body weight was assessed weekly of individual mice in the age from 4-16 weeks fed either NCD or HFD.

Body composition

The body fat content and lean mass was measured using the nuclear magnetic resonance (NMR) analyzer minispec mq7.5 (Bruker Optik).

Blood glucose measurement

Blood glucose levels were determined from whole venous tail blood using an automatic glucose monitor (Accu Check, Aviva) from either random fed or 6 h fasted animals.

Glucose tolerance test

Glucose tolerance tests were carried out in 18-20-week-old animals following a 6 h fast. After measuring fasted blood glucose levels, mice were injected intraperitoneally (i.p.) with 2 mg g-1

body weight glucose (20% glucose solution, Braun). Blood glucose levels were determined 15 min, 30 min, 60 min and 90 min post glucose injection.

Acute cold exposure and measurement of rectal body temperature

For acute cold exposure KO, AKO and BKO and control animals were individually housed in homecages with bedding material, however, without nesting material and exposed to 4°C. Rectal body temperature was measured using a rectal thermometer (Bioseb) prior to the experiment at ambient temperature. Afterwards body temperature was measured every hour for 7 h or until core body temperature dropped below 26°C.

1.4 Genotyping of mice
Isolation of DNA from tissues

Ear biopsies or tails from mice were lysed in 500 µL of DNA lysis buffer (100 mM Tris-HCl, 5 mMEDTA, 200 mM NaCl, 0.2% SDS (w/v), 0.2 mg/mL Proteinase K, pH 7.4) at 55°C with continuous shaking for 45 min. DNA of fully digested samples was precipitated using 500 µL of isopropanol (20 min centrifugation at max speed) and washed for one time with 500 µL 70% ethanol (15 min centrifugation at max speed). The DNA pellet was dried over tissue paper and subsequently dissolved in 150 µL ddH2O and stored at 4°C.

Genotyping PCR

To determine the genotype of different mice models, PCR reactions with specific primers of the respective genes were performed. *AdipoCre* genotyping was performed with the GOTaq polymerase/ buffer (Promega), while *Ucp1Cre* and *Clpp fl* genotyping was performed with DreamTaq polymerase (Thermo Fisher Scientific). The following PCR mix was prepared:

1 µL DNA
1 µL per Primer (10 µM), 2 primer per reaction
1 µL dNTP mix (1.25 mM each)
2 µL Dream Taq buffer (10X) for *Ucp1Cre* and *Clpp fl*
4 µL GoTaqPolymerase Buffer (5X) for *AdipoCre*
1.2 µL MgCl2 (25 mM) for Cox10
0.1 µL DreamTaq or GoTaq Polymerase
Up to 20 µL ddH2O

PCRs for confirming the genotype were run at the following program:

PCR conditions *AdipoCre*
94°C   2 min
94°C   20 sec ⎤
65°C   15 sec ⎬   -0.5°C per cycle   10x
68°C   10 sec ⎦
94°C   15 sec ⎤
60°C   15 sec ⎬   28x
72°C   10 sec ⎦

72°C   2 min
4°C   hold

Table 1 Primers for AdipoCre genotyping.

Primer	Sequence 5' --> 3'
Adipoq-Cre fw	GGA TGT GCC ATG TGA GTC TG
Adipoq-Cre rev	ACG GAC AGA AGC ATT TTC CA
Poscontrol fw	CTA GGC CAC AGA ATT GAA AGA TCT
Poscontrol rev	GTA GGT GGA AAT TCT AGC ATC ATC C

PCR conditions *Clpp fl*

95°C   5 min
95°C   30 sec ⎤
60°C   30 sec ⎬   30x
72°C   1 min   ⎦
72°C   10 min
4°C   hold

Table 2 Primers for Clpp fl genotyping.

Primer	Sequence 5' --> 3'
Clpp fw	GTGGATGATGGTCAGTAGAATCC
Clpp rev	CCCAGACATGATTCCTAGCAC
Clpp ko	TGTGCATTCTTACCATAGTCTGC

PCR conditions *Ucp1Cre*

95°C   5 min
95°C   30 sec ⎤
50°C   45 sec ⎬   41x
72°C   1 min   ⎦
72°C   10 min
4°C   hold

Table 3 Primers for Ucp1Cre genotyping.

Primer	Sequence 5' --> 3'
Ucp1-Cre fw	CAAGGGGCTATATAGATCTCCC
Ucp1-Cre rev1	ATCAGAGGTGGCATCCACAGGG
Ucp1-Cre rev2	GTTCTTCAGCCAATCCAAGGG

2. Molecular biology
2.1 Isolation of RNA from tissues

For isolation of total RNA from mouse tissue, the entire adipose tissue was homogenized in 1 mL Trizol (Life Technologies) and ceramic beads (Mobio, Dianova GmbH) with a FastPrep

homogenizer (MP Biomedicals) at 5500 rpm for 2Å~ 20 sec. After 5 min incubation at RT, 200 µL chloroform were added and mixed for 15 sec, before centrifugation at 12000 g for 15 min at 4 °C was performed. The aqueous upper phase containing the RNA was collected and precipitated with 500 µL isopropanol (10 min incubation at RT, following centrifugation at 12000 g for 10 min, 4°C). RNA pellet was washed with 75% ethanol (5 min centrifugation at 7500 g, 4 °C) and briefly dried. Finally, the RNA pellet was resuspended in 50 µL ultra-pure H2O and incubated at 60°C for 10 min. The RNA concentration and purity was determined with a NanoDrop ND-1000 UV-Vis spectrophotometer (Peqlab). Before cDNA synthesis, 10 µg RNA was digested with DNase I (New England Biolabs). The digestion mix (10 µg RNA, diluted 10X digestion buffer and 1 µL DNase I in a total volume of 20 µL) was incubated 10 min at 37°C. Afterwards, heat inactivation of DNase I was performed at 75°C for 10 min. RNA concentration was redetermined and the samples were stored at −80°C.

2.2 cDNA synthesis

Isolate RNA further treated with DNase I (New England Biolabs, USA) to digest the residual DNA following this reaction mix:

RNA -   10 µg
10x DNase I Reaction Buffer - 3 µL
DNase I -   1 µL
UltraPure water Up to -   30 µL

This reaction mix was incubated for 10 min at 37°C and then another 10 min at 75°C for heat-inactivation of DNase I. Afterwards, the concentration of the samples was adjusted to 200 ng/µL.Next, copy DNA (cDNA) was synthesized from the digested samples using the High-Capacity Reverse Transcription kit (Applied Biosystems, USA). The reaction mix (total volume 20 µL) was prepared as follows:

RNA (200 ng/µL) -   10 µL
10x RT buffer -   2 µL
10x Random Primers -   2 µL
25x dNTP mix -   0.8 µL
MultiScribe Reverse Transcriptase - 1 µL
UltraPure water -   4.2 µL

The reaction mix was subjected to the following PCR program:
Annealing 25 -   10 min
Elongation 37°C - 120 min
Denaturation 85°C -   5 s
Hold - 4°C
The cDNA samples were stored at –20°C.

2.3 Quantitative real-time PCR (qPCR)

qPCR reactions were performed in 384-well plates using the Brilliant III Ultra-Fast SYBR Green qPCR Master Mix (Agilent Technologies) according to manufacturer's instruction. Per reaction 50 ng of cDNA were applied. The following program was run at the Applied Biosystems QuantStudio 7 Flex Real-Time PCR System (Fisher Scientific):

Initial denaturation 95 °C for 3 min
Denaturation 95 °C for 5 sec
Annealing & Elongation 60 °C for 15 sec
Elongation 72°C for 30 sec

Dissociation curve
Denaturation 95 °C for 15 sec
Annealing 60 °C for 1 min
Temperature increase until 95 °C for 15s

Relative target gene expression was calculated by normalization to endogenous control gene (*Hprt*) and was quantified using $2^{-\Delta\Delta Ct}$

Table 4 SYBR-green Primers used for qPCR.

Gene	Forward primer	Reverse primer
Hprt	GCCCCAAAATGGTTAAGGTT	TTGCGCTCATCTTAGGCTTT
Atf4	GCAAGGAGGATGCCTTTTC	GTTTCCAGGTCATCCATTCG
Phghd	GACCCCATCATCTCTCCTGA	GCACACCTTTCTTGCACTGA
Psat1	AGTGGAGCGCCAGAATAGAA	CTTCGGTTGTGACAGCGTTA
Mthfd2	CTGAAGTGGGAATCAACAGTGAG	GTCAGGAGAAACGGCATTGC

3. Biochemistry

3.1 Protein isolation from tissues

The entire adipose tissue pad was homogenized in 700-800 µL cold organ lysis buffer (50 mM HEPES pH 7.4, 50 mM NaCl, 1 % Triton-X-100 (v/v), 100 mM NaF, 10 mM EDTA, 0.1 % SDS (w/v), 10 mM Na-orthovanadate, 2 mM PMSF, 1x protease inhibitor cocktail (Sigma-Aldrich), 1x PhosphoSTOP phosphatase inhibitor cocktail (Roche)) with 1.4 mm ceramic beads (omni International, USA) in a Precellys tissue homogenizer (bertin technologies) - at 5500 rpm, 2 X 20", pause 30". The lysates were cleared by 45 min centrifugation (20000 g, 4°C) and transferred into fresh tubes. Determination of protein concentration was performed with Bradford reagent (Sigma Aldrich) according to the manufacturer's instruction. Protein lysates were stored at −80°C.

3.2 Protein isolation from cells

Cells were washed with PBS and on-plate lysis of cells was carried out. The cells were lysed with radioimmunoprecipitation assay (RIPA) buffer (50 mM Tris-HCl, pH 7.4; 1% v/v Triton-X; 0,5% w/v sodium deoxycholate; 0,1% w/v SDS; 150 mM NaCl; 2 mM EDTA; 50 mM NaF; 1x protease inhibitor cocktail) and incubated on ice for 30 min with occasional vortexing. Afterwards, the lysate was subjected to 10 cycles of sonication at 30 s intervals at 4°C with Bioruptor Pico (Diagenode, Belgium). Cell debris was pelleted at 14 000 g/ 4°C /15 min. Supernatant was collected and stored at –80 °C.

3.3 Isolation of mitochondria (cytoplasmic mitochondria and peri lipid droplet mitochondria separately) from BAT / iWAT-

BAT / iWAT was harvested and rinsed twice in PBS. The tissues were weighed and minced with fine scissors. The minced tissue was suspended SHE-BSA buffer (50 mM sucrose, 5 mM HEPES, 2 mM EGTA, pH 7.2, 2% FFA BSA) (1 mL/100 mg tissue). Homogenization was performed with a glass-teflon electric laboratory tissue homogenizer (7 strokes), followed by further finer homogenization with a glass-glass 15 mL dounce homogenizer (13 strokes).

The homogenate was transferred to a new 50 mL Falcon tube, wash the tube with SHE-BSA to collect tissue remnants stuck to the walls of the homogenizing tube. This was followed by centrifugation in a swinging bucket rotor at 900 × g for 10 min at 4 °C. The tube was carefully removed from the centrifuge and the supernatant was collected with a long syringe, by plunging through the floating fat layer, along the sides of the Falcon tube, without disrupting the fat layer. This is the fraction that contains CMs. The tube was immediately stored on ice. Care was taken not to disrupt the debris pellet at the bottom of the tube. The original falcon tube was immediately positioned horizontally on ice.

The fat layer was carefully scraped the into a new ice-cold 50 mL tube and resuspended with the same amount of SHE-BSA as the amount of the supernatant. This fraction contains the lipid-associated PDMs. The falcon tube was vigorously shaken to emulsify the fat layer and disrupt the PDMs from the fat droplets as much as possible. The two tubes, one containing CMs and the other, containing PDMs was centrifuged at 9000 × g, in a fixed angle centrifuge for 10 min at 4 °C. The supernatant was discarded. The pellet was washed with 1 mL SHE-BSA and the dissolved pellet was transferred to 1.5 mL Eppendorf tubes. The tubes were centrifuged at 9000 × g for 10 min at 4 °C. The supernatant was discarded. Pellets were resuspended with SHE buffer w/o BSA. Wither further downstream analyses was continued directly, or the mitochondria were snap-freeze in liquid N_2 for long-term storage.

3.4 SDS polyacrylamide gel electrophoresis (SDS-page) and western blot

Proteins were separated conducting polyacrylamide gel electrophoresis (PAGE) under denaturing conditions using the Mini-PROTEAN Tetra Cell (BioRad). 50 µg of protein lysate was incubated with Laemmli buffer (50 mM Tris-HCl, 2 %S DS, 10 % Glycerol, 1% 2 mercaptoethanol, 12.5 mM EDTA, 0.02% Bromophenol Blue, pH 6.8) at 95 ÅãC for 5 min. Samples were loaded onto a 8-12 % acrylamide gel (stacking gel: 5 % Acrylamide/ Bis acrylamide 40 (29:1), 12.5 mM Tris-HCl, 0.1 % SDS (w/v), 0.25 % APS, TEMED, pH 6.8, separation gel: 8-12% Acrylamide/Bis-acrylamide 40 (29:1), 37.5 mM Tris-HCl, 0.1 % SDS

43

(w/v), 0.1 % APS and TEMED pH 8.8) next to a protein ladder (PageRuler Prestained Protein Ladder, Thermo Fisher Scientific).

Electrophoresis was conducted at 90 V in running buffer (25 mM Tris-HCl, 250 mM Glycine, 0.1 % SDS pH 8.3) until the loading dye reached the separating gel and continued at 150 V until the end of the gel. Wet protein transfer was then performed in Criterion Blotter (BioRad) according to the manufacturer's instructions. Proteins were next transferred on a nitrocellulose membrane by wet transfer - in transfer buffer (30 mM Tris-Hcl, 240 mM Glycine, 0.037 % SDS, 20 % Methanol) in a blotting chamber at 400 mA for 2 h at 4°C. To assess the efficiency of the transfer, the membrane was stained with Ponceau-S solution (Sigma-Aldrich). Depending on the antibody's requirement membrane was blocked for 1 h either in 5 % milk-PBST, 3 % BSATBST or 2 % fish skin gelatin in TBST under gently rotation. Subsequently, primary antibodies were incubated under antibody specific conditions at 4°C. overnight. The following day, membranes were washed three times 5 min in PBST or TBST and incubated with secondary antibody for 1.5 h at RT. The membranes were washed again. Visualization of detected proteins was performed applying ECL solution (GE Healthcare) at the membrane. Finally, membranes were exposed to Super RX films (Fujifilm) and developed in an automatic film processor (Kodak). Films were scanned with V800 Transparency Scanner (Epson) at 600 dpi 16-bit greyscale.

Table 5 Primary antibodies used for western blot.

Antigen	Manufacturer	Cat. No.	Dilution
CLPP	Sigma Aldrich	WH0008192-M1	1:1000
EIF2A	Cell Signaling Tech. (CST)	5324	1:1000
GAPDH	Abcam	ab9484	1:1000
HSC70	Santa Cruz	sc- 7298	1:1000
LAMIN A/C	Cell Signaling Tech. (CST)	4777	1:1000
pEIF2A	abcam	ab32157	1:1000
PHGDH	Proteintech	14719-1-AP	1:1000

Table 6 Secondary antibodies used for western blot.

Antigen	Manufacturer	Cat. No.	Dilution
ECL anti-mouse IgG-peroxidase	Sigma-Aldrich	A4416	
ECL anti-rabbit IgG-peroxidase	Sigma-Aldrich	A6154	

3.5 Blue native polyacrylamide electrophoresis (BN-PAGE)

BN-PAGE was performed based on the NativePage Novex Bis-Tris Gel System (Life Technologies) following instruction manual. 10 µg mitochondria were lysed in 4 % digitonin. After incubation for 15 min on ice, samples were centrifuged at 20,000 g for 30 min at 4°C.

Supernatants were mixed with 10ul of loading dye (50 % glycerol, 5 % Coomassie) and loaded onto 4-16 % native acrylamide gels (Life Technologies). Electrophoresis was performed at 4°C at 150 mV overnight. Subsequently, the proteins were transferred from the gel onto a polyvinylidene difluoride (PVDF) membrane (BioRad) by western blot transfer (with no methanol and SDS) at 4°C for 16 h at constant current of 120 mA. After the transfer, the membrane was washed briefly, blocked in 5 % milk PBS-T for 1 h and incubated with antibodies against specific mitochondrial protein complexes for 1- 2 h at room temperature. Further steps were performed as described for SDS-PAGE.

Table 7 Primary antibodies used for BN PAGE analysis.

Antigen	Manufacturer	Cat. No.	Dilution
ATP5A1	Abcam	ab14748	1:1000
COX I	Molecular Probes	459600	1:1000
NDUFA9	Molecular Probes	459100	1:1000
NDUFV1	Proteintech	11238-1-AP	1:1000
SDHA	Molecular Probes	459200	1:10000
UQCRC1	Molecular Probe	459140	1:1000

3.6 In gel activity assays

In gel activity was performed for complex I and V. After completed BN-PAGE, the gel was shortly washed and incubated in NADH-nitrotetrazolium blue solution (for CI) (0.1 mg/mL NADH, 2.5 mg/mL nitrotetrazolium blue, 5 mM Tris/HCl pH 7.4) for 1 h at 37°C. Destaining of the gels was performed for 2 h at RT in destaining solution made of - 50 % (v/v) methanol, 10 % (v/v) acetic acid. Subsequent rehydration was performed in ddH2O.

For complex V activity, the gel was incubated overnight were incubated in an assay buffer comprising 35 mM Tris-HCl, 270 mM glycine, 14 mM magnesium sulfate, 0.075 % lead nitrate, and 0.8 mM ATP (pH 7.8) with 20 % methanol End point ATP hydrolysis activity was measured and was visualized as the white band comprising precipitated lead phosphate.. For imaging, the reaction was stopped with 50 % methanol. The gel was incubated for 30 min and then rinsed with deionized water.

The gel was documented using a V800 Transparency Scanner (Epson).

The experiments were performed in collaboration with Milica Popovic.

4. Histological analysis
4.1 Embedding of tissues in paraffin

After dissection, the entire adipose tissues were placed in tissue cassettes (Roth) and immersed in 5% (w/v) paraformaldehyde overnight at 4°C for fixation. The tissues were then placed in 15% sucrose in PBS until the tissue sank to the bottom (6-12 hrs) and then in 30% sucrose in PBS for overnight or until tissue sank. Next day tissues were dehydrated by passing them through increasing concentrations of ethanol for 2 h each (30% (v/v), 50% (v/v), 70% (v/v),

96% (v/v) and two times in 100% (v/v) ethanol). Afterwards they were incubated in xylol for two times 2 h and then transferred to paraffin, for the embedding in paraffin blocks. The fixed tissues (BAT and iWAT) were sectioned with a microtome (Leica) at 5 µm thickness and transferred onto poly-Llysine glass slides (VWR).

4.2 Haematoxylin & Eosin staining of paraffin-fixed tissues

Paraffin-embedded 3 um-thick intestinal tissue sections were deparaffinised with Xylol for 20min. Rehydration was performed by parring the tissue through decreasing amounts of ethanol solutions for 2min each (100% (v/v) ethanol, 96% (v/v) ethanol, and 75% (v/v) ethanol). Afterwards, sections were washed for 5min in tap water. Subsequently, sections were stained in Meyer's Haematoxylin for 2min, quickly washed in tepid tap water for 10sec and kept in tap water for 15min. After 15min, sections were additionally washed with ddH20 for 1min, followed by incubation for 1min in Eosin staining solution for counterstaining. The stained sections were dehydrated using increasing amount of ethanol solutions for 1min each and fixed in Xylol for 1min. Finally, slides were mounted with Entellan.

5. Omics analysis

5.1 Proteomics

Label free quantification of tissue proteome

The entire piece of frozen adipose tissue was ground to powder in liquid nitrogen and after the liquid nitrogen evaporated, the powder was resuspended in 100 µL of the urea lysis buffer (8 M Urea; 50 mM triethylammonium bicarbonate (TEAB); 1x protease inhibitor). The sample solution was subjected to sonication with the Bioruptor Pico sonication machine (Diagenode, Belgium) – cycle 30/30 s for 10 min. Afterwards, the sample was centrifuged at 20,000 g/15 min/4°C to pellet and the debris were discarded post centrifugation. The protein concentration of the samples was determined using the Bradford reagent (Sigma-Aldrich, USA) according to the manual and 55 µg of each sample was transferred to a new tube. The sample was treated with dithiothreitol (DTT, final conc. 5 mM) and incubated at 25 °C for 1 h. Then chloroacetamide was added (CAA, final conc. 40 mM) and incubated for 30 min in the dark. This was followed by treatment with lysyl endopeptidase (Lys-C), at the protease:sample protein ratio 1:75 and the incubated for 4 h at 25 °C. The sample was next diluted with 50 mM TEAB buffer to reach the final concentration of <=2 M Urea. Then trypsin was added in the 1:75 ratio and the trypsinisation was performed overnight at 25°C with mild agitation. The following day, the sample was acidified with formic acid (final conc. 1%) to stop the digestion. This was followed by loading the lysates on SDB RP StageTips supplied by the CECAD proteomics core facility and submitted to the facility for the mass spectrometry analysis according to the standard procedures of the facility. The raw data were analysed with the MaxQuant proteomics software. The samples were analyzed by CECAD proteomics facility.

5.2 Metabolomics

Metabolite Extraction for tissues

Metabolite extraction solution (50% methanol, 30% acetonitrile, 20% water, 5uM valined8 as internal standard) was added to (10-20mg) frozen BAT or iWAT tissue samples at an extraction ratio of 25ul/mg on dry ice. Samples were then homogenized using a Precellys 24 tissue homogenizer (Bertin technologies). The resulting sample suspension was vortexed, mixed at 4oC in a Thermomixer for 15 min at 1,500 rpm and then centrifuged at 16,000 x g for 20 min at 4oC. The supernatant was collected for LC-MS analysis.

5.3 Metabolite Extraction for cells

The cells were counted at seeding to estimate the amount of extraction solution to use. Using 500 µl extraction buffer per 10^6 cells is recommended as a starting point, although ratio may need to be optimized for certain cell types in a separate pilot experiment. The medium was removed from wells and cells were washed quickly with PBS 2X (less than 10 sec) at room temperature. Extra PBS was carefully removed by inverting the plate over a piece of tissue paper. After the last wash, each well was aspirated quickly to remove all residual PBS. The plate was placed on dry ice and 500 µl of extraction buffer was added per million cells. The plate was gently swirled so that cells are covered by the extraction buffer. The plate was incubated for 20 min on a dry ice-methanol bath to break cell membranes. The cells were scraped off the plate and the entire suspension was transferred into pre-chilled Eppendorf tubes. The cell extract suspension was shaken for 15 minutes at 4 °C in a Thermomixer at maximum speed (Thermomixer set at 4 °C and placed in a cold room for this step). The tubes were the centrifuged for 20 minutes at 4°C at maximum speed (13000 rpm or higher). Only the top 80% of the supernatant was collected and put into pre-labelled autosampler vials, taking care not to disturb the solid debris. A pooled sample was prepared by taking 10 µl of each sample from the same matrix. Samples were stored at -80 °C until further analysis.

5.4 Metabolite Extraction for cell culture media

80 µL of cell culture media was taken and centrifuged for 5 minutes (4°C) at maximum speed to eliminate dead cells. 50 µL of the supernatant was taken and added to pre-labelled Eppendorf tube containing 350 µL of extraction solution on dry ice. The samples were mixed for 15 minutes in a Thermomixer at 4 at maximum speed followed by centrifugation for 20 minutes at 4°C at maximum speed (13000 rpm or higher). Top 80% of the supernatant was carefully transferred the into an autosampler vial, taking care not to disturb the insoluble debris. A pooled sample was prepared by mixing equal volumes of each sample extract in a single vial. Samples were stored at -80 °C until further analysis.

5.5 Liquid chromatography coupled to mass spectrometry (LC-MS)

Hydrophilic interaction chromatographic (HILIC) separation of targeted metabolite (2-HG) was achieved using a Millipore Sequant ZIC-pHILIC analytical column (5 µm, 2.1 × 150 mm) equipped with a 2.1 × 20 mm guard column (both 5 mm particle size) with a binary solvent system. Solvent A was 20 mM ammonium carbonate, 0.05% ammonium hydroxide; Solvent B was acetonitrile. The column oven and autosampler tray were held at 40 °C and 4 °C, respectively. The chromatographic gradient was run at a flow rate of 0.200 mL/min as follows:

0–2 min: 80% B; 2-17 min: linear gradient from 80% B to 20% B; 17-17.1 min: linear gradient from 20% B to 80% B; 17.1-23 min: hold at 80% B. Samples were randomized and the injection volume was 5 µl. A pooled quality control (QC) sample was generated from an equal mixture of all individual samples and analysed interspersed at regular intervals.

Metabolites were measured with Vanquish Horizon UHPLC coupled to an Orbitrap Exploris 240 mass spectrometer (both Thermo Fisher Scientific) via a heated electrospray ionization source. The spray voltages were set to -2.8 kV, RF lens value at 70, the heated capillary held at 320 °C, and the auxiliary gas heater held at 280 °C. The flow rate for sheath gas, aux gas and sweep gas were set to 40, 15 and 0, respectively. For MS1 scans, mass range was set to m/z=100-600, AGC target set to standard and maximum injection time (IT) set to auto. Data acquisition for experimental samples used full scan and SIM (Selected Ion Monitoring) modes (targeting 2-HG m/z: 147.0299) at an Orbitrap resolution of 120000 in negative mode.

5.6 Targeted metabolomics for 2-HG quantification

The identity of metabolite. 2-HG was verified based on two criteria: (1) the precursor ion m/z corresponded to within 3 ppm of the expected mass derived from its chemical structure, and (2) the retention duration was within a 5% range compared to that of a purified reference sample analyzed using the identical chromatography technique.

The examination of chromatograms and integration of peak areas was carried out using the Tracefinder software (v5.1, Thermo Fisher Scientific). The peak area of each identified metabolite was adjusted based on the total ion count (TIC) of the respective sample to compensate for any discrepancies arising from sample preparation or instrument assessment. These measurements were done in collaboration with Frezza lab, CECAD Research Center.

6. Electron microscopy

6.1 Embedding procedure for adipose tissue

Samples were emersion fixed in 2% formaldehyde, 2% glutaraldehyde in 0.1M sodium cacodylate buffer (Applichem) for 48h. Samples were washed four times with 0.1 M sodium cacodylate buffer. Post-fixation was applied using 2% OsO_4 (Science Services) in 0,1M cacodylate buffer for 2 hours at 4°C. Samples were washed four times with 0.1M Cacodylate buffer and dehydrated using an ascending ethanol series (50%, 70%, 90%, 3x100%) for 20 min each. After incubation with a mix of 1:1 (v/v) ethanol/propylenoxide and two times with pure propylenoxide for 20 min each step, samples were infiltrated with a mixture of 1:1 (v/v) epon/propylenoxide for 5 h and 3:1 (v/v) epon/propylenoxide overnight each at 4°C. The next day samples were transferred into fresh pure epon and let them incubate 8 hours at 4°C before adding another pure epon step overnight at 4°C. The next day, epon was exchanged and samples were incubated for 2h at RT, placed into PELCO 21-cavity embedding mold (Plano, 10505) and cured for 72 h at 60°C.

6.2 Classical EM image acquisition

Ultrathin sections of 70 nm were cut using an ultramicrotome (Leica Microsystems, UC6) and a 45° diamond knife (Diatome, Biel, Switzerland) and stained with 1.5 % uranyl acetate for 15 min at 37°C and 3% lead citrate solution for 4 min at room temperature.
Images were acquired using a JEM-2100 Plus Transmission Electron Microscope (JEOL) operating at 80kV equipped with a OneView 4K camera (Gatan).

6.3 Serial sections and 3D reconstruction:

Ribbons of 5 ultrathin sections each were collected on Pioloform coated Slot-grids (Science Services, #G2010-Cu). The same cell was imaged in 60 consecutive sections and images were aligned to stack using FIJI with the TrakEM2 Plugin. Nucleus, Mitochondria and Lipid droplets were manually segmented using MIB (Microscope Imaging Browser, version 2.82). The model was transferred to IMARIS (version 9.9.1) for 3D reconstruction.

EM analysis was done in collaboration with Katrin Seidel and Dr. Felix Gaedke, Imaging facility, CECAD Research Center.

7. Immunofluorescence (IF)

For IF staining, cells were seeded and differentiated on coverslips. On the day of staining, cells were directly fixed for 15 min with 4% PFA/PBS (pH7.4) at RT. Three washed were given with PBS. Afterwards, cells were blocked with 5% BSA, 0.3% triton-X for 30 minutes at RT. Then coverslips were stained with primary antibodies diluted in 1% BSA, 0.3 % triton-X in PBS for 16 hr at 4°C. The next day, coverslips were washed three times with 0.3 % triton-X in PBS for 5 min and incubated with secondary antibodies. The secondary antibody solution was made in 0.3% triton-X in PBS fpr 30 mins at RT,in the dark. Final washes were given thrice with triton-X in PBS. The coverslips were dipped in water prior to mounting and then mounted on elvanol. Images were obtained on SP8 confocal microscope (Inverse, DMi 8 CS, Leica Microsystems).

Table 8 Primary antibodies used for immunofluorescence.

Antigen	Manufacturer	Cat. No.	Dilution
H3K9me3	Abcam	ab8898	1:100
H3K27me3	Abcam	ab195477	1:100
LAMINA/C	Cell Signaling Tech. (CST)	4777	1:100

Table 9 Secondary antibodies used for immunofluorescence.

Antigen	Manufacturer	Cat. No.	Dilution
Alexa Fluor 488 Dye	Thermo Fischer Scientific	A-11008	1:500
Alexa Fluor 647 dye	Thermo Fischer Scientific	A-21240	1:500

8. Image analysis
8.1 Analysis of CM and PDM from TEM images

TEM images were imported into QuPath[1], where three annotation classes, including Lipid Droplets (LD), Peridroplet Mitochondria (PDM), and Cytoplasmic Mitochondria (CM), were defined. These entities were manually labeled using QuPath's annotation tools and associated with their respective classes. To facilitate further analysis, the "Send Region to ImageJ" functionality was employed to export images from QuPath to ImageJ, conserving full resolution and transferring annotations as Overlays. These images were subsequently saved as TIFF files in ImageJ[2]. An ImageJ macro (FijiExport.ijm), was then executed in Fiji[3] to process these exported TIFF files. For each image, the macro created a dedicated folder containing both the image itself and the QuPath annotations saved as ROIs in a zip file. The overlays were converted into ROIs, with names corresponding to their class, such as LD, PDM, and CM.

Another ImageJ macro was used to analyze these generated folders, to quantify the dimensions of distinct classes of ROIs (LDs, PDMs, and CMs), especially the interface regions between PDMs and LDs. In pursuit of this, slightly dilated masks of LDs were generated and employed to mask the PDM masks, preserving solely the interface regions. These regions were subsequently skeletonized, and the resultant lines were saved as overlays atop the original images. The size of the skeletonized regions was measured and interpreted as indicative of the size of the interface region. Moreover, the perimeters of PDMs were quantified, and the ratio between the interface region and the perimeter was deemed the Contact Perimeter Fraction. All the measurements were compiled and saved in a CSV file.
This analysis was done in collaboration with Peter Zentis, Imaging facility, CECAD Research Center.

8.2 Nuclear segmentation and quantification

Fluorescence microscopy image analysis was conducted through an automated approach utilizing an ImageJ macro[1] executed in FIJI[2]. The analysis encompassed a series of sequential steps applied to all czi-images within a designated directory. The processing pipeline included initial local contrast enhancement to optimize images for subsequent machine learning-based segmentation. This segmentation was executed using the Stardist ImageJ-plugin[3], employing the pretrained 'Versatile (fluorescent nuclei)' model. Following segmentation, a size-based filtration process was implemented to eliminate regions of interest (ROIs) with an area less than 30 μm². Subsequently, measurements were performed on the original images using the retained ROIs, encompassing the quantification of signal intensity from the DAPI channel and the two distinct histone channels (H3K9Me3 and H3K27Me3) within each individual ROI. The measured values were normalized with respect to the dapi intensity of the corresponding ROI. These measurements were saved in tab-separated value (TSV) format, facilitating their subsequent utilization in comprehensive statistical analyses.
This analysis was done in collaboration with Peter Zentis, Imaging facility, CECAD Research Center.

9. FACS analysis

9.1 Single cell immunophenotyping from tissue

Obtaining single cells suspensions:

Bone marrow was flashed with 10 ml of FACS buffer from the femur of adult mice using a 27 G needle and syringe tough a 40 um strainer. BAT was dissected and immediately transferred in ice-cold digesting solution. Tissues were cut in little pieces with scissors and incubated in digesting solution containing Collagenase IV (1 mg/ml), and DNase I (0.01 mg/ml) in RPMI for 40 min at 37°C in the shaker. Digestion was stopped by adding 10% FBS on ice. Tissue homogenates where smashed and washed with FACS buffer against a 70 um strainer using the back of a syringe.

Staining of the cells:

Pellets were resuspended in 1 ml red blood cell lysis buffer (Roche) and incubated for 10 min at RT for lysis of erythrocytes. Subsequently, 10 ml FACS buffer (5% FCS in PBS) was added and cells were centrifuged at 300 g for 5 min at 4°C.

The cells were pre-incubated with fix viability dye in PBS (1:1000) for 10 min at RT, for BAT a mix of anti-mouse FcγIII/II receptor (CD16/CD32)-blocking antibodies (1:500) was added. After wash with FACS buffer, cells were stained with the fluorochrome-conjugated antibodies (0.25–1 µg; listed below). Only BAT cells were fixed and permeabilized with FoxP3 kit according to manufacturer instructions, and then incubated with iNOS and Arg-1 antibodies 20 min at RT for intracellular staining. After washing and filter, well were resuspended in 500 ul (BM) or 250 ul (BAT) of FACS buffer, 25 ul of counting beads were added to the samples to obtain absolute numbers. Cells were acquired on a FACS Symphony ™ A3 flow cytometer (BD) using Diva software (BD) and further analysed using FlowJo analytical software (FlowJo version 10.0.8, LLC). Compensation beads were use to generate compensation panel and calculated by diva software before sample acquisition. Background fluorescence levels of iNOS, Arg-1, CD80 and CD80 were determined by Fluorescence Minus One (FMO).

Buffers:

FACS buffer: 5 mg BSA + 5 ml EDTA 0,4 M + 500 ml of PBS

Digestion buffer: Merk DNAse I 250 ul if 200000 U/ml (final volume 50 ml)   or 0,2 mg/ml Liberase (Roche), 1 mg/ml collagenase IV in RPMI medium.

The experiment was done in collaboration with Ximena Hildebrandt, Peltzer lab, CECAD Research Center.

Table 10 List of antibodies used for FACS immunophenotyping.

Antibody	Conjugates	Clone	Catalog	Company
CD45	FITC	30-F11	103107	BioLegend
CD86	Brilliant Violet 510	GL-1	105039	BioLegend
Ter119	APC/Cyanine7	TER119	116223	BioLegend
CD19	APC/Cyanine7	6D5	115529	BioLegend
CD49b	APC/Cyanine7	DX5	108919	BioLegend
NK1.1	APC/Cyanine7	PK136	108723	BioLegend
CD3E	APC/Cyanine7	145-2C11	100329	BioLegend
B220	APC/Cyanine7	RA3-6B2	103223	BioLegend
MHCII	PerCP/Cyanine5.5	M5-114.15.2	107625	BioLegend
ARG1	PE/Cyanine7	A1exF5	25-3697-80	invitrogen
CD45	Alexa 700	30-F11	103127	BioLegend
INOS	PE	CXNFT	12-5920-80	Thermofisher
CD80	BV711	16-10A1	104743	BioLegend
CD16/32	Brilliant Violet 421	93	101331	BioLegend
CD127 (IL-7Rα)	PerCP/Cyanine5.5	A7R34	135021	BioLegend
CD172a (SIRPα)	PE/Dazzle™ 594	P84	144015	BioLegend
CD34	PE/Cyanine7	MEC14.7	119325	BioLegend
Ly-6A/E (Sca-1)	PE/Dazzle™ 594	D7	108137	BioLegend
CD135	PE	A2F10	135305	BioLegend
CD115	Brilliant Violet 605	AFS98	135517	BioLegend
CD117	Brilliant Violet 510	ack2	135119	BioLegend
CD11c	BUV395	HL3	564080	BD
CD11b	BUV661	M1/70	612977	BD
CD3	APC	17A2	100235	BioLegend
IFN-γ	Brilliant Violet 785	XMG1.2	505837	BioLegend
TruStain FcX™ (anti-mouse CD16/32)		93	101319	BioLegend

9.2 Lipid content analysis using BODIPY staining coupled to FACS

Cells were washed twice with PBS and 1X BODIPY solution in PBS was added to the cells. Staining was performed for 45 minutes in dark. Then cells were trypsinized at RT. Trypsinization was terminated by addition of FACS buffer (1X PBS with 2% BSA). The cells were then filtered using 60 uM cell strained and transferred into fresh Eppendorf tubes.

10. Cell culture

10.1 Isolation of BAT-MSCs

A 6-well plate was provided with 3 ml BAT collagenase digestion buffer (123 mM NaCl, 5 mM KCl, 1.3 mM $CaCl_2$, 5 mM glucose and 100 mM N-(2-hydroxyethyl)-piperazine-N'-2-ethansulfonic acid (HEPES) in water. Adjust pH with NaOH to 7.4) per well on ice, and 15 ml falcon tubes, 1.5 ml reaction tubes, 5 ml syringes, cannulas and a dish were sterilized with with 70% ethanol. A newborn mouse was decapitated and quickly transferred to the dish with 70% ethanol to achieve sterile conditions. The 2 brown fat pads were removed and transferred to one well of the 6-well plate with BAT collagenase digestion buffer. The fat pads were chopped with scissors, and the solution was transferred to a 15 ml falcon tube and store it on ice. The tail tip was cut off, and transferred to a 1.5 ml reaction tube and store it on ice for genotyping. The falcon tubes were transferred into the pre-warmed water bath for collagenase digestion. They were shaken thoroughly by hand every 5 min and incubated for about 30 min until all bigger tissue remnants have disappeared. The suspensions were sucked into 5 ml syringes using cannulas (0.9 x 70 mm; 20G x 2 .). The cannulas were removed, and one 100 µm nylon mesh was fixed at each syringe using a cut-off pipette tip and the suspension was filtered through the nylon mesh into a new 15 ml falcon tube. The falcon tubes were incubated on ice for 30 min. The middle phase of the suspensions was sucked into 5 ml syringes using cannulas. Care was taken not to use the upper phase (about 0.5 ml), which contains mature adipocytes, and the bottom phase (about 0.5 ml), which contains tissue remnants. The suspensions were filtered through 30 µm nylon meshes into new 15 ml falcon tubes as described above. The tubes were then centrifuged at 700 g for 10 min. The pellets were resuspended in 3 ml pre-warmed BAT-MSC culture medium and each suspension (derived from the BAT of one newborn mouse) was transferred into one well of a 6- well plate. The primary BAT-MSCs were incubated at 37°C and 5% CO_2 for 24 hours.

The cell isolation was done in collaboration with Dr. Thorsten Gnad, Pfiefer lab, University of Bonn.

10.2 Immortalization of BAT-MSCs

Primary BAT-MSCs (passage 0) were immortalized 24 hours after isolation by transduction with a lentivirus expressing the Simian Virus 40 (SV40) large T-Antigen (L-TAg) under control of the phosphoglycerate kinase (PGK) promoter (7). Expand immortalized brown preadipocytes (BATi) in BATi growth medium at 37°C and 5% CO_2. The virus solution was thawed and centrifuged at 16000 g for 1 min. 200 ng viral reverse transcriptase (for 1 well of a 6-well plate) was taken and mixed with 800 µl BATi growth medium. Medium from the cells was removed and incubated with 800 µl viral medium over night at 37°C and 5% CO_2. The viral medium was removed from the cells, and cells were washed 3 times with PBS and incubated with BATi growth medium at 37°C and 5% CO_2.

10.3 Cultivation and storage of BATi cells

Cells were maintained in growth medium at 37°C and 5% CO_2. Cultures were not allowed to become completely confluent for expansionCells were detached using trypsinization and then BATi growth medium was added to them. Suspensions were centrifuged for 5 min at 200 g. Pellets were resuspend in BATi growth medium and mixed with freezing medium at a ratio of 1:1 to achieve a final DMSO concentration of 10%. The optimal cell density is 1 million cells per ml. The cell suspensions were transferred into cryogenic vials (1 ml per vial) and incubated on ice for 15 min. Cryogenic vials were stored at -80°C for 24 hours. Afterwards transfer cryogenic cultures to liquid nitrogen (-196°C) for long-term storage.

10.4 Differentiation of BATi cells-

$1.8 \times 10_5$ cells per well of a 6-well plate were seeded in BATi growth medium (day -4). After 48 hours (day -2) the medium was removed and BATi differentiation medium was added. Adipogenic differentiation was induced after additional 48 hours (day 0) by exchanging BATi differentiation medium with BATi induction medium. Care was taken to prepare the medium freshly before use. Cultures need to be confluent when inducing adipogenesis.

After a 48 hours induction phase (day 2) the cells were maintained in BATi differentiation medium. Medium was replenished every second day until day 8, when the cells are differentiated into mature brown adipocytes.

10.5 Cell culture treatments-

Most treatments were started along with media change from day 3 to differentiation media. Cells were treated with 150uM Actinonin (in DMSO) for 96 hours, fresh actinonin added every second day, without media change. NCT-503 treatment (in DMSO) was done for 96 hours, was added to media at concentration of 20uM, with fresh addition every 24 hours. Cells were treated with Rotenone (in DMSO) at indicated concentrations for 12 hours.

11.   Cell biology

11.1 *Ex vivo* tissue adipocyte lipolysis activity

To determine lipolytic activity in BAT from CLPP KO mice and control, animals were fasted for 6 hours and BAT pads were surgically excised in sterile conditions and digested using collagenase type 2 (Worthington Biomedical Corp., LS004177) in 1X Krebs-Ringer Solution (KRH) (120 mM NaCl, 5 mM KCl, 1.25 mM $CaCl_2$, 0.5 mM $MgCl_2$, 1.5 mM NaH_2PO_4, 0.7 mM Na_2HPO_4, 25 mM HEPES, 5.5 mM glucose) containing 1% BSA (Roche, #03117057001). Each treatment condition was replicated in 2-4 separate experiments; for each experiment, fat pads from 4-5 mice were pooled and adipocytes incubated as described below. Approximately 150,000-200,000 isolated adipocytes from pooled BAT were incubated in KRH buffer + 4% BSA, 15 nM isoproterenol (ISO) (Sigma-Aldrich, I6379) or 10 µM forskolin (Fsk) (Sigma-Aldrich, F6886) for 180 min at 37°C with constant shaking at 140 rpm. Following the incubation period, lipolysis was assessed by measuring the release of free glycerol in the supernatant using Free Glycerol Reagent (Sigma-Aldrich, F6428) following the manufacturer's instructions using a Synergy H1 plate reader (BioTEK). Glycerol content was normalized to total cellular protein

content determined by Pierce™ Detergent Compatible Bradford Assay Kit (Thermo Scientific, #23246).

The measurements were done in collaboration with Dr. Thorsten Gnad, Pfiefer lab, University of Bonn.

11.2 *Ex vivo* OCR measurement on BAT tissue lysates using OROBOROS Oxygraph-2K

O_2 consumption in BAT tissue lysates was measured using an OROBOROS Oxygraph-2K electrode at 37°C, with magnetic stirring. Samples were transferred to the oxygraph chamber containing 2 ml incubation medium (0.5 mM EGTA, 3 mM MgCl2 6H2O, 60 mM K-lactobionate, 20 mM taurine, 10 mM KH2PO4, 20 mM HEPES, 110 mM sucrose and 1 g/l BSA, pH 7.1). *In vitro* respiration levels were recorded when reaching a steady state followed by addition of substrates (State 1: endogenous; state 2: ADP; state 3: succinate; state 4: oligomycin; uncoupled: FCCP). Respiration rates were normalised to total protein content.

The measurements were done in collaboration with Dr. Thorsten Gnad, Pfiefer lab, University of Bonn.

11.3 Respiration analysis using Seahorse Bioscience XFe-96 analyzer

The mitochondrial oxygen consumption rate (OCR) and the extracellular acidification rate (ECAR), which approximates glycolytic activity, were analyzed simultaneously using a standard mitochondrial stress test paradigm on the Seahorse Bioscience XFe-96 analyzer (Agilent Technologies, CA, USA). Differentiated BATi cells were assayed at day8 of differentiated state for OCR and ECAR measurements following the manufacturer's instructions (Agilent Technologies, CA, USA). The standard Seahorse XF Cell Mito Stress Test was used to determine basal and maximal respiration.

Hydration of the sensory cartridge-

This step was performed 24 hours prior to the assay. The utility plate and sensory cartridge were separated and the sensory cartridge was placed upside down on the bench side to the utility plate. Each well of the utility plate was filled with 200 µL Seahorse XF Calibrant, then sensory cartridge was lowered back onto the utility plate gently and avoid creating air bubbles. The cartridge was incubated in a non-CO_2, 37°C incubator for 12–18 h minimum. Care was taken to make sure the environment of the incubator was humidified.

Pre-assay preparation-

Before analysis, cells were washed three times with unbuffered assay media [DMEM (Sigma, Switzerland) diluted in water without phenol red supplemented with glucose (1mM), sodium pyruvate (1 mM) and glutamine (2 mM), and incubated 1 h in a CO_2- free incubator at 37 °C.

xFp cartridge sensors were hydrated and injection ports loaded by the following; Oligomycin (final concentration, 1uM) was added to the first well in the cartridge, FCCP (final concentration,1.5uM) to the second well and a mixture of rotenone-antimycin A (final concentration,1uM each) in the third well. Optimal concentrations of oligomycin, FCCP, antimycin A and rotenone were determined before, as they vary for different cell types. Once the cartridge ports were loaded, it was loaded onto the machine to begin calibration. After

calibration, the utility plate in the cartridge was replaced with the washed cells and the assay was started.

Post-assay normalization-

Post measurement, normalization of Seahorse data was done by In-situ Cell Counting Using a BioTek Cytation 5 (Agilent Technologies, CA, USA). The cells were stained with 1X membrane-permeable Hoechst 33342 and kept CO_2- free incubator at 37 °C for 45 minutes) the incubation time varies for different cells, but minimum time for optimal staining is 30 minutes. Hoechst-stained fluorescent nuclear images were captured using the autofocus capability in Gen5 software as single center images or stitched whole-well images. The nuclear number was counted using the Cell Analysis function in the Gen5 software program, and data were exported to normalize XF data. The whole-well cell number was extrapolated by multiplying the central partial counts by a factor of ~3.71, based on the ratio of well dimension to the image size.

Seahorse XFe Wave Software (Agilent) was applied to analyze the data. Basal respiration or acidification was calculated using the mean of the four OCR or ECAR measurements before the first injection. Leak respiration and maximal respiration were calculated as the mean of three OCR measurement cycles after oligomycin or FCCP injection, respectively. Maximal acidification was calculated as the mean of three ECAR measurement cycles after oligomycin injection. OCR data were corrected for non-mitochondrial oxygen consumption under rotenone and antimycin.

11.4 Isolated Mitochondria Respirometry using Seahorse Bioscience XFe-96 analyzer

Freshly isolated mitochondria (with pre-determined protein concentration) were re-suspended in respiration buffer (100 mM KCl, 10 mM KH2PO4, 2 mM MgCl2, 5 mM HEPES, 1 mM EGTA, 0.1% BSA, 1 mM GDP, pH 7.2) and kept on ice as described previously. One microgram per well were loaded into Seahorse XF96 microplate in 20 mL volume containing substrates. The loaded plate was centrifuged at 2,000 x g for 90 seconds at RT and an additional 115 mL of buffer+substrate was added to each well. Substrate concentrations were as follow: 5 mM Pyruvate + 5 mM Malate, 40 mM octanoyl-Carnitine + 1 mM Malate. ADP was injected at port A (3.5 mM final concentration), oligomycin at port B (3.5 mM), FCCP at port C (4 mM) and Antimycin A at port D (4 mM). Mix and measure times were 0.5 min and 4 min, respectively. A 2 min wait time was included for oligomycin-resistant respiration measurements. All steps were performed with pre-chilled buffers, equipment, and consumables, the hydration of cartridge was performed as mentioned above.

11.5 PHGDH activity assay

The PHGDH activity assay was performed according to manufacturer protocol, using a kit (ab273328) Cells in a 6 well plate were washed with PBS and rapidly homogenized on plate with 400 µl ice cold PHGDH Assay Buffer, and placed on ice for 10 mins. The homogenate was transferred to Eppendorf tubes and centrifuged at 10,000 x g for 5 mins at 4°C and supernatant was collected. The total protein concentration of cell lysate samples was measured using a

BCA assay. Volume corresponding to 30ug of total protein was added to a 96 well clear plate. Final volume was adjusted to 50 µl with PHGDH Assay Buffer. The plate was kept on ice.

Next, dilutions of NADH standard were made for the standard curve. 0, 2, 4, 6, 8 and 10 µl of 1.25 mM NADH standard (supplied in the kit) were added to a series of wells in a 96 well plate to generate 0, 2.5, 5, 7.5, 10 and 12.5 nmol/well of NADH Standard. Volume was adjusted to 50 µl/well with PHGDH assay buffer. 10ul of PHGDH positive control was pipetted to the well and final volume was adjusted to 50 µl with PHGDH assay buffer. The reaction mix was prepared by mixing 48ul of the assay buffer and 2ul of the developer for each well of the standards, positive control and the test samples. 50ul of this reaction mix was then added to each well and the plate was measured immediately at 450 nm in kinetic mode for 10-60 mins at 37°C using the EnSpire plate reader.

11.6 Atomic Force Microscopy measurements on cultured cell nuclei

AFM measurements were performed on cell monolayers plated on silicon elastomers using JPK NanoWizard 4 XP (Bruker Nano) atomic force microscope mounted on Zeiss AxioObserver inverted fluorescent microscope and operated via JPK SPM Control Software v.5. Triangular non-conductive Silicon Nitride cantilevers (MLCT, Bruker Daltonics) with a nominal spring constant of 0.01 Nm−1 were used for the nanoindentation experiments of the apical surface of cells and the nucleus. For all indentation experiments, forces of up to 3 nN were applied, and the velocities of cantilever approach and retraction were kept constant at 2 µm s−1 ensuring an indentation depth of 500nm. All analyses were performed with JPK Data Processing Software (Bruker Nano). Prior to fitting the Hertz model corrected by the tip geometry to obtain Young's Modulus (Poisson's ratio of 0.5), the offset was removed from the baseline, contact point was identified, and cantilever bending was subtracted from all force curves.

The AFM measurements were done in collaboration with Prof. Sara Wickstrom, MPI, Muenster.

12. Bioinformatics analysis

12.1 RNA-seq Analysis Pipeline

RNA-seq reads were preprocessed and aligned to the mouse genome (ftp://ftp.ensembl.org/pub/release-103/fasta/mus_musculus/dna/Mus_musculus.GRCm39.dna.toplevel.fa.gz) using the **nf-core/rnaseq pipeline** version 3.0 [336]. The resulting sample-specific read counts per gene were subsequently input to a **targets** [337] pipeline for Differential Gene Expression (DGE) by **DESeq2** version 1.32.0 [338] and Functional Enrichment (FE) analysis by **clusterProfiler** [339] 4.0.5. The underlying **Bioconductor** version was 3.13.1 [340], using the databases of **AnnotationDbi** version 1.54.1 [341]. The **R** version used was 4.1.2. These initial read counts and DGE results were the basis for all subsequent downstream analyses. FE analyses were at some points in the overall analysis pipeline computed anew.

12.2 Bulk Deconvolution

In order to rule out an influence of sample or genotype specific cell type composition on the observed bulk gene expression, the **BisqueRNA** R package [342] was used to predict the most likely cell type composition per sample based on the bulk RNA-seq read counts.

12.2.1 Dataset Used

The dataset by **Shamsi *et. al.*** [343] was chosen as a single cell reference to provide cell type specific expression information, because its tissue of origin was similar to ours. Unfortunately, the authors could not provide cell type assignments to individual cells, but only marker genes for their **UMAP** clusters [344], which in turn were assigned to cell types. Following the procedure described in their Methods, it was possible to reproduce a UMAP projection which was overall highly similar to theirs [Figure?]. To decompose it into clusters, the **Seurat** [345] FindClusters function was used with a resolution of 1.4 throughout most downstream analyses. However there are reasons to finally conclude that a resolution of 0.4 may have been a better choice (see below). To stay as close as possible to the original procedure, Seurat version 3.0 with R version 3.6.2 was used for these reconstructions.

12.2.2 Assigning Detailed and Coarse Cell Types to Cells

The **UCell** package version 2.0.1 [346] was used to assign cell type scores to the cells in the Shamsi *et al*. dataset, using the provided maker genes for their original clusters. Specifically the 10 marker genes with largest positive difference were used as positive markers, and the 10 markers with largest negative difference as negative markers. The UCell score alone however rarely suggests a unique assignment, because the cell types are related. To resolve this, two different approaches were tried:

A) Clustering the UCell score matrix:

A brute force approach was to use the matrix clustering capabilities of R package **ComplexHeatmap** version 2.12.1 [347] to cluster the entire UCell matrix (where rows=cells, columns=genotypes, matrix entries = UCell score for cell i on cell type j) simultaneously on rows and columns. This yields very clear visual clusters of related cells on related cell types. It is possible to extract the row and column dendrograms from the plot object, which then can be used to infer the matrix indices corresponding to the visual clusters. However, the approach has drawbacks: On the one hand, the full UCell matrix could not be clustered as a whole due to memory constraints. As a workaround 200 random sub-matrices were clustered, containing 1/3 of all cells at a time. On the other hand, turning dendrograms into clusters requires thresholds, which are as arbitrary as the thresholds required to reconcile the clusters resulting from the 200 random runs.

B) Identifying cell types with unusually high score in each UMAP cluster:

A more rigorous approach examines one UMAP cluster at a time, extracting, for each cell type at a time, the distribution of the type's UCell score and comparing it to the dataset-wide distribution using a t-test. For most clusters the distribution of the p-values of a one-sided t-test is strongly bimodal: there is a limited number of related cell types with p-values at or very close to zero, with the remaining ones at or close to one. If there is only one significant type, then the

cluster is clearly assigned. If there are more, it was assigned to a "coarse" cell type consisting of the union of the high-scoring types.

The scoring and cell type assignment analysis were run in R-4.2.1. Note that these analyses extended over one year, during which our R versions changed several times.

12.2.3 Running BisqueRNA

For the actual cell type decomposition of our bulk data, only cells from the RT (room temperature) condition of the Shamsi *et al.* dataset were used, and only genes which were also represented in our bulk data. This leaves 18953 genes and 22219 cells. Cell type assignment was based on the resolution 0.4 clustering of the [Shamsi et al.] cells. Attempting to avoid ambiguous cell type assignments, the t-test approach described above was used with a very stringent inclusion criterion: a cell type was retained as a defining type of a cluster if its p-value was maximally equal to 2.225074e-308 (the smallest number distinguishable from zero on the computer used), that is, essentially zero. This leaves 15 types, of which only two (B_cells and VSM_1_cells) are not composite. Assigning a given composite type to all cells in the clusters it is composed of, 738 cells remain without an assigned cell type. These unassigned cells were removed, leaving 21481 cells.

As bulk data, we used the salmon.merged.gene_counts_length_scaled.tsv output file of the nf-core pipeline, restricted to BAT samples.

BisqueRNA was then run with the bulk data of one genotype at a time (restricted to genes which were also represented in the single cell dataset) and the reduced single cell dataset with the composite cell types described above.

12.2.4 Identifying Genotype-Specific Predicted Cell-type Proportions

The ultimate goal of the deconvolution analysis was to understand whether the BAT genotypes differ with respect to cell type composition. This proved to be difficult, because the predicted coarse cell type proportions are highly variable even between the replicates of the same genotype (which may point to an issue with the analysis setup, most likely with the definition of the coarse cell types), and because the cell type composition is inevitable dominated by the frequent types, notably the B cells.

Even if the results were more well-behaved statistically, there is a fundamental issue which cannot be avoided: proportion data are "compositional" in the technical sense of being non-independent, because they must add up to a fixed number in each sample (here: to 1). It is therefore not possible to naively analyze variations in the frequency of one cell type independent of the variation of the others.

As the data did not allow to conclude statistically on the existence or not of genotype-specific differences in the cell type proportions, a visual representation was developed instead: The coordinates of the Seurat UMAP object were extracted and used as the basis of a ggplot2 object , in which cells used in the deconvolution were colored by their assigned coarse celltype, and the predicted proportion of each cell type in the bulk dataset was coded by transparency.

In this representation, coarse cell types derived from the resolution 0.4 clustering corresponded more clearly to the high-level features of the map than those from resolution 1.4 , which may suggest that this resolution is to be preferred.

12.3 Integration of RNA-seq, Proteomics, and Metabolomics Data

Mass spectroscopy proteomic and metabolomic data were available in addition to the RNA-seq data. Because these functional layers were not matched by individual (that is, samples were derived from different mice in each data layer), a horizontal integration of the data matrices by pasting them together by individual was not possible, and in consequence also no truly integrative data analysis could be performed. Instead, data from different layers were mostly compared visually, e.g. by scatterplots. In order to relate RNA-seq and metabolomics data, the PerformIntegPathwayAnalysis function of the **MetaboAnalystR** package **version** 4.0.0 [348] was used, with its output part re-coded such that labels could be displayed.

Reproducible Pipeline

The adapted PerformIntegPathwayAnalysis function is part of a targets pipeline which contains all steps of the analysis, including notably different visualization functions like scatterplots, volcano plots, Venn diagrams, and paired transcriptome/proteome heatmaps. The pipeline is available upon request.

The bioinformatics analysis was done in collaboration with Dr. Ulrike Göbel, Bioinformatics facility, CECAD Research Center.

2.5. CHEMICALS AND BIOLOGICAL MATERIALS

Table 11 List of chemicals and biological materials.

Chemical	Manufacturer	Country
2-mercaptoethanol	Sigma-Aldrich, USA	USA
20% glucose solution	Braun	Germany
30% LC-MS grade Acetonitrile	Fisher Scientific	USA
50% LC-MS grade Methanol	Fisher Scientific	Scientific
Acetic Acid	AppliChem	USA
Acetone	AppliChem	USA
Adenosine 5'-diphosphate sodium salt	Sigma-Aldrich	USA
Adenosine 5'-triphosphate disodium salt	Sigma-Aldrich	USA
Agar bacteriology grade	AppliChem	USA
Agarose NEEO ultra quality	Roth	Germany
Agarose-LE	Ambion	USA
Ammoniumpersulfat APS	Sigma-Aldrich	USA

Antimycin A	Sigma-Aldrich	USA
Bradford reagent	Sigma-Aldrich	USA
Bromophenol Blue	Merck	USA
BSA (Albumin from bovine serum) fatty acid free	Sigma-Aldrich	USA
Chloroform	AppliChem	USA
Coomassie Brilliant Blue G250	AppliChem	USA
DEPC	AppliChem	USA
Digitonin	Merck	USA
DMSO Dimethylsulfoxide	Sigma-Aldrich	USA
DTT Dithiothreitol	Sigma-Aldrich	USA
EDTA Ethylenediaminetetraacetic acid	Sigma-Aldrich	USA
EGTA Ethylene glycol-bis(2-aminoethylether)-N,N,N′,N′-tetraacetic acid	Sigma-Aldrich	USA
Ethanol abs.	AppliChem	USA
Ethidium Bromide (EtBr)	Sigma-Aldrich	USA
FCCP (Carbonyl cyanide-ptrifluoromethoxyphenylhydrazone)	Sigma-Aldrich	USA
Formaldehyde 38%	Roth	Germany
Glucose	AppliChem	USA
Glutamic Acid (L-)	Sigma-Aldrich	USA
Glutamine (L-)	Sigma-Aldrich	USA
Glutaraldehyde solution Grade I 50%	Sigma-Aldrich	USA
Glycerol	Sigma-Aldrich	USA
HCl 37%	VWR	Germany
HEPES-Molecular biology grade	AppliChem	USA
Histidine mono hydrochloride monohydrate (L-)	Sigma-Aldrich	USA
Isopropanol	AppliChem	USA
Magnesium chloride hexahydrate	Sigma-Aldrich	USA
Methanol	AppliChem	USA
Methionine (L-)	Sigma-Aldrich	USA
Milk powder	AppliChem	USA
PBS Buffer (10X Dulbecco's) Powder	AppliChem	USA
PBS Tablets	Calbiochem	USA
Phenol	AppliChem	USA
Phenol/Chloroform/Isoamylalcohol	Roth	Germany
Potassium chloride	AppliChem	USA
Potassium dihydrogen phosphate	AppliChem	USA
Potassium hydrogen phosphate	Merck	USA
Protease Inhibitor Cocktail	Sigma-Aldrich	USA
Protein Standard	Sigma-Aldrich	USA
Proteinase K	AppliChem	USA
Red cell lysis buffer	Fisher-Scientific	USA
Retinoic Acid	Sigma-Aldrich	USA

Rnase A	AppliChem	USA
RNAse ZAP	Sigma-Aldrich	USA
Rotenone	Calbiochem	USA
Rotiphorese Gel 40 (37.5:1)	Roth	Germany
SDS granules	AppliChem	USA
Serine (L-)	Sigma-Aldrich	USA
Sodium acetate solution (3M, pH 5,2)	AppliChem	USA
Sodium azide	AppliChem	USA
Sodium chloride for molecular biology	Sigma-Aldrich	USA
Sodium deoxycholate	AppliChem	USA
Sodium hydroxide	Sigma-Aldrich	USA
Sodium Orthovanadate	AppliChem	USA
Sodium Phosphate dibasic	Sigma-Aldrich	USA
Sodium Phosphate monobasic	Sigma-Aldrich	USA
Sodium pyruvate	Sigma-Aldrich	USA
Sodium succinate dibasic hexahydrate	Sigma-Aldrich	USA
Sucrose	Sigma-Aldrich	USA
TEMED	Sigma-Aldrich	USA
TMPD Tetramethyl-p-phenylenediamin	Sigma-Aldrich	USA
Tri-sodium citrate dihydrate	AppliChem	USA
Triton X-100, molecular biology grade	AppliChem	USA
Trizma Base	Sigma-Aldrich	USA
TRIzol reagent	Invitrogen	USA
TrypanBlue	Sigma-Aldrich	USA
Trypsin from bovine pancreas	VWR	Germany
Tween 20	AppliChem	USA
UltraPure distilled water	Gibco	USA
Valine-d8	CK isotopes	UK

RESULTS

1. CHAPTER 1 | Phenotypic and metabolic characterization of adipose-specific CLPP knockout mice

In order to understand the physiological relevance of the mitochondrial protein CLPP, previous studies in the lab had generated a whole-body knockout mouse model of CLPP [349]. CLPP was ubiquitously deleted using a β-actin promoter driven Cre recombinase, leading to a deletion of the protease domain of CLPP and a premature translational stop signal in *Clpp* mRNA, resulting in its nonsense-mediated decay (hereafter referred to as KO) [349].

Phenotypic characterization had revealed that these mice exhibited several beneficial metabolic effects like reduced body weight, increased leanness, lower overall fat content, improved resistance to diet-induced obesity and insulin sensitivity, under both baseline conditions and when challenged with HFD [349]. These systemic benefits in CLPP KO mice could either be due to tissue-specific benefits in the mice or due to an additive effect of multiple tissues. To comprehend the underlying mechanisms responsible for these observations, and to identify the tissue of their origin, liver-specific (LKO) and muscle-specific (MKO) CLPP knockout mice were also generated [349].
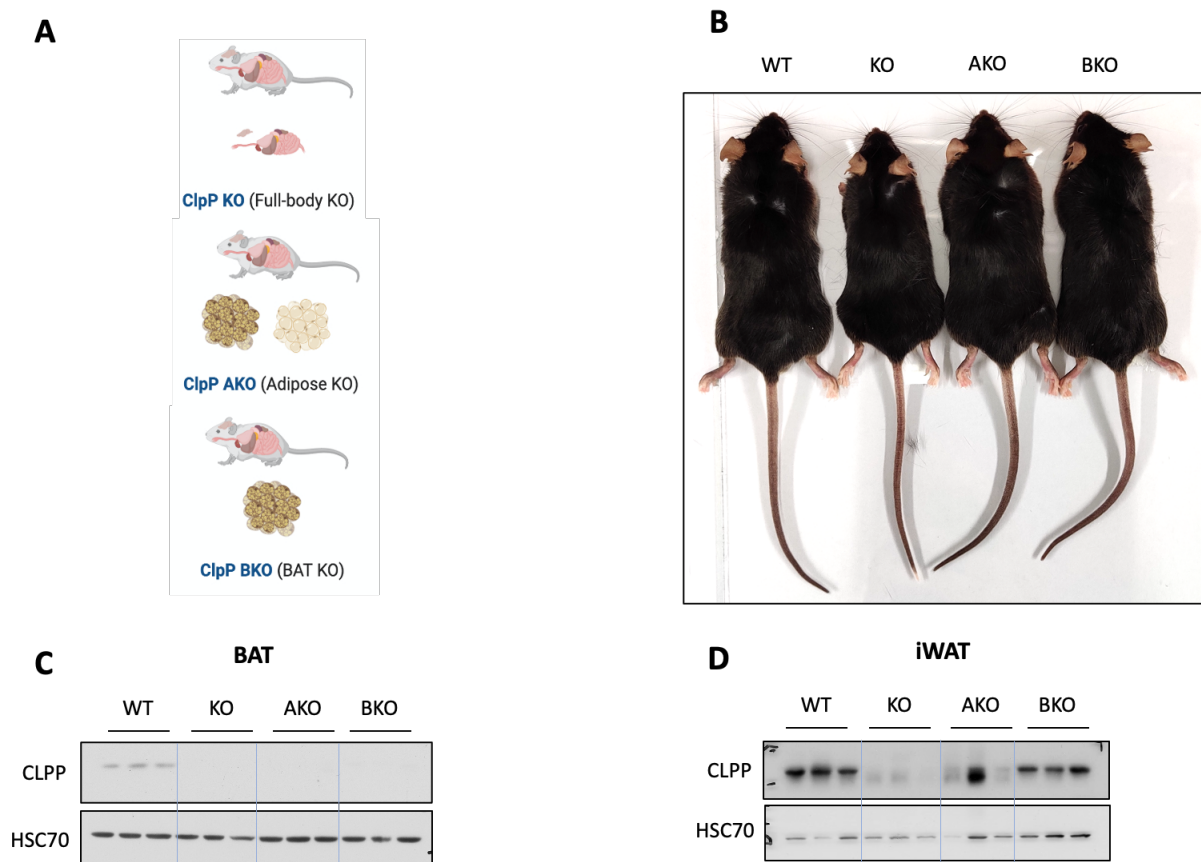

Figure 1.1 AKO and BKO mice differ from CLPP KO mice in body size. *A: Model explaining mode of generating adipose tissue-specific KO mice and representative images showing difference in body sizes of KO, AKO, and BKO mice. B-C: Immunoblot showing depletion of CLPP in BAT and iWAT of WT, KO, AKO and BKO mice. N=3.*

These tissue-specific knockout models did not show any protection from diet-induced obesity or insulin resistance, nor did they display differences in fat mass [349]. This indicated that the metabolic benefits were not arising from the liver or muscle.

Given the lack of metabolic improvements in the LKO and MKO mice, we shifted our focus to the metabolically relevant **adipose tissue depots** to explore the impact of loss of CLPP from adipose tissue on whole body metabolism. Specifically, we generated two tissue-specific knockout mice: pan adipose-specific knockout **(AKO)** and brown adipose-specific knockout **(BKO)** (Fig. 1.1A), by mating $Clpp^{fl/fl}$ mice with a) mice expressing CRE recombinase under the control of mouse adiponectin ($Adipoq$) promoter (Adipoq-Cre mice), and b) mice expressing CRE recombinase under the control of mouse $Ucp1$ promoter (Ucp1-Cre mice) respectively. AKO and BKO mice did not have a lean phenotype like KO mice and were similar in size as WT (Fig. 1.1A). Western blot analysis confirmed the successful removal of CLPP from both BAT and WAT in AKO and only from BAT in BKO mice (Fig. 1.1 B-C). A faint band of residual CLPP protein was seen in WAT immunoblot from AKO (Fig. 1.1C), and that could be attributed to non-adipocyte resident cells in the tissue such as tissue macrophages, that still possess functional CLPP.

To next determine the effect of adipose-specific loss of CLPP on body weight, mice fed normal chow diet (NCD) were monitored for a period of approximately 18 weeks.
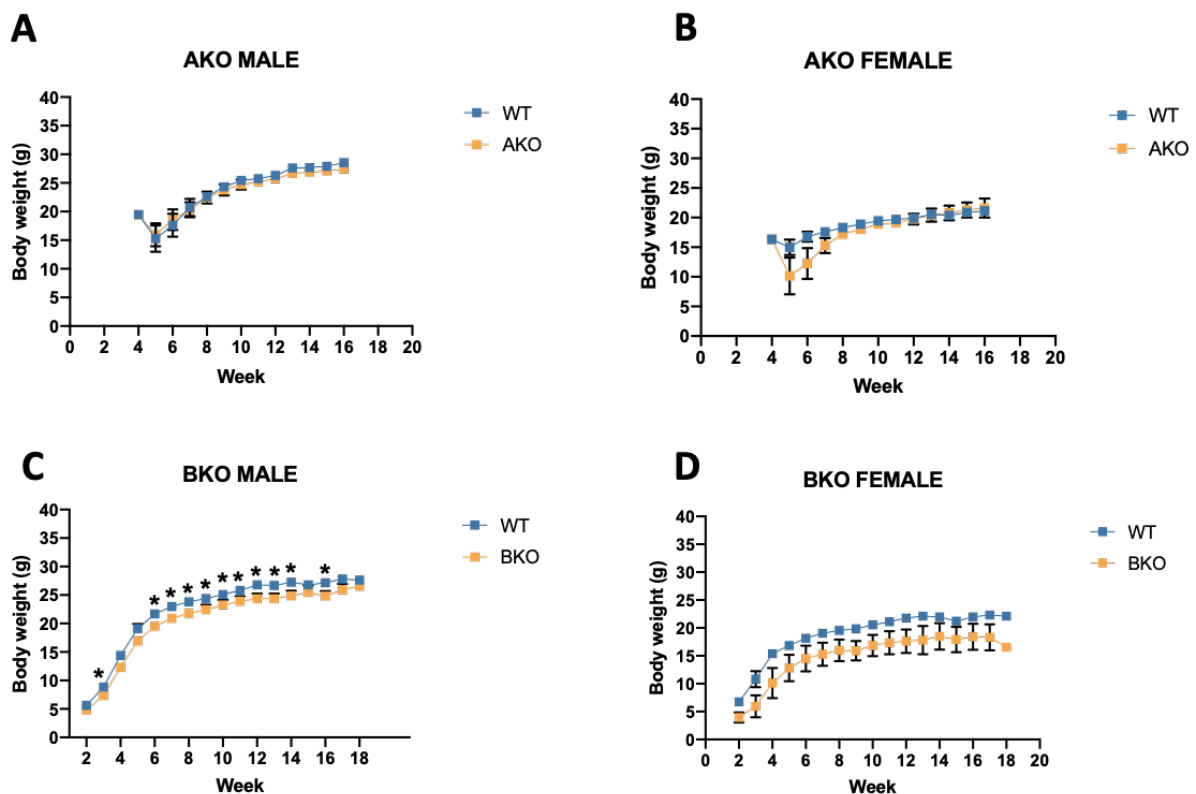
Figure 1.2 Body weight of AKO and BKO mice on NCD. *A-B: Graph representing gain in body weight with age in AKO male and female mice, Student's t test, data are presented as means ± SEM, N = 11 and 12 male of WT and AKO genotype respectively, 10 and 3 female of WT and AKO genotype respectively. C-D: Graph showing gain in body wzight of male and female BKO mice, Student's t test, data are presented as means ± SEM, N = 5 and 4 male of WT and BKO genotype respectively, 3 and 3 female of WT and BKO genotype respectively. Body weight was monitored till 18 weeks of age. * p < 0.05.*

In contrast to findings on KO mice, AKO mice (both male and female) did not have lower body weights than WT controls (Fig. 1.2A-B). BKO male mice had mild (10-15%) but significant reduction in body weight compared to the control mice, starting from six weeks of age, until 14 weeks (Fig. 1.2C), but the significance was not observed in female BKO mice (Fig. 1.2D). In general, there was an observed tendency of lower weight gain in BKO animals (Fig. 1.2 C-D), but it was not as pronounced as the 20-25% reduction that was reported in both genders for CLPP KO mice [349].
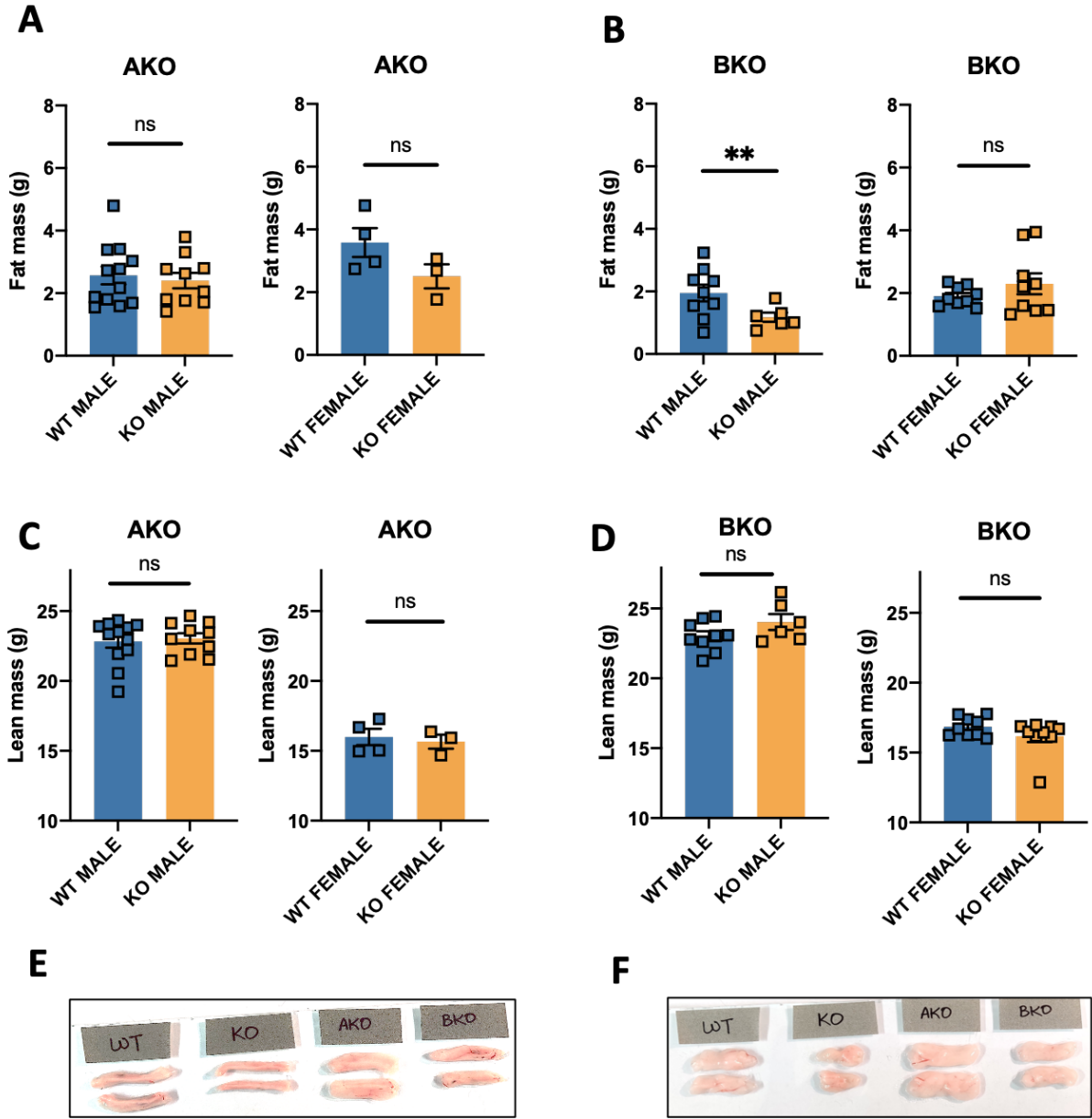
Figure 1.3 Body composition analysis of AKO and BKO mice on NCD. *A-B: Graph showing total fat mass in male and female mice of mentioned genotypes, as measured by NMR at 20 weeks of age. Student's t test, data are presented as means ± SEM. N = 12 and 10 male of WT and AKO genotype respectively, 4 and 3 female of WT and BKO genotype respectively $*p < 0.05$. C-D: Graph showing lean body mass in male and female mice of mentioned genotypes, as measured by NMR at 20 weeks of age. Student's t test, data are presented as means ± SEM. N = 9 and 6 male of WT and BKO genotype respectively, 9 and 9 female of WT and BKO genotype respectively. Body composition analysis was done at 20 weeks of age. E: Representative images showing excised fat from male and female mice of mentioned genotypes.*

Next, body composition of these mice was analyzed using magnetic resonance imaging. The fat mass of AKO mice (both male and female) was not different from WT controls (Fig. 1.3A). BKO male mice had 38% lower fat content compared to control mice (Fig. 1.3B), but no significant difference was observed in female BKO mice (Fig 1.3B). There were no significant differences in lean mass between AKO mice and their WT control mice (Fig. 1.3C) and BKO mice and their WT control mice (Fig. 1.3D), which further corroborated with no apparent decrease in the size of the mice (Fig. 1.1A).

For further analysis, we focused our attention on the two most abundant WAT depots in the mice, the inguinal WAT (iWAT) or perigonadal or epididymal WAT (eWAT). Images of the isolated iWAT and eWAT tissues from AKO mice showed similar tissue sizes as WT control mice (Fig. 1.3E-F). The WAT depots however, appeared to be smaller in 8 (out of the 20) analyzed BKO mice, irrespective of the gender, as represented in Fig. 1.3 E-F.
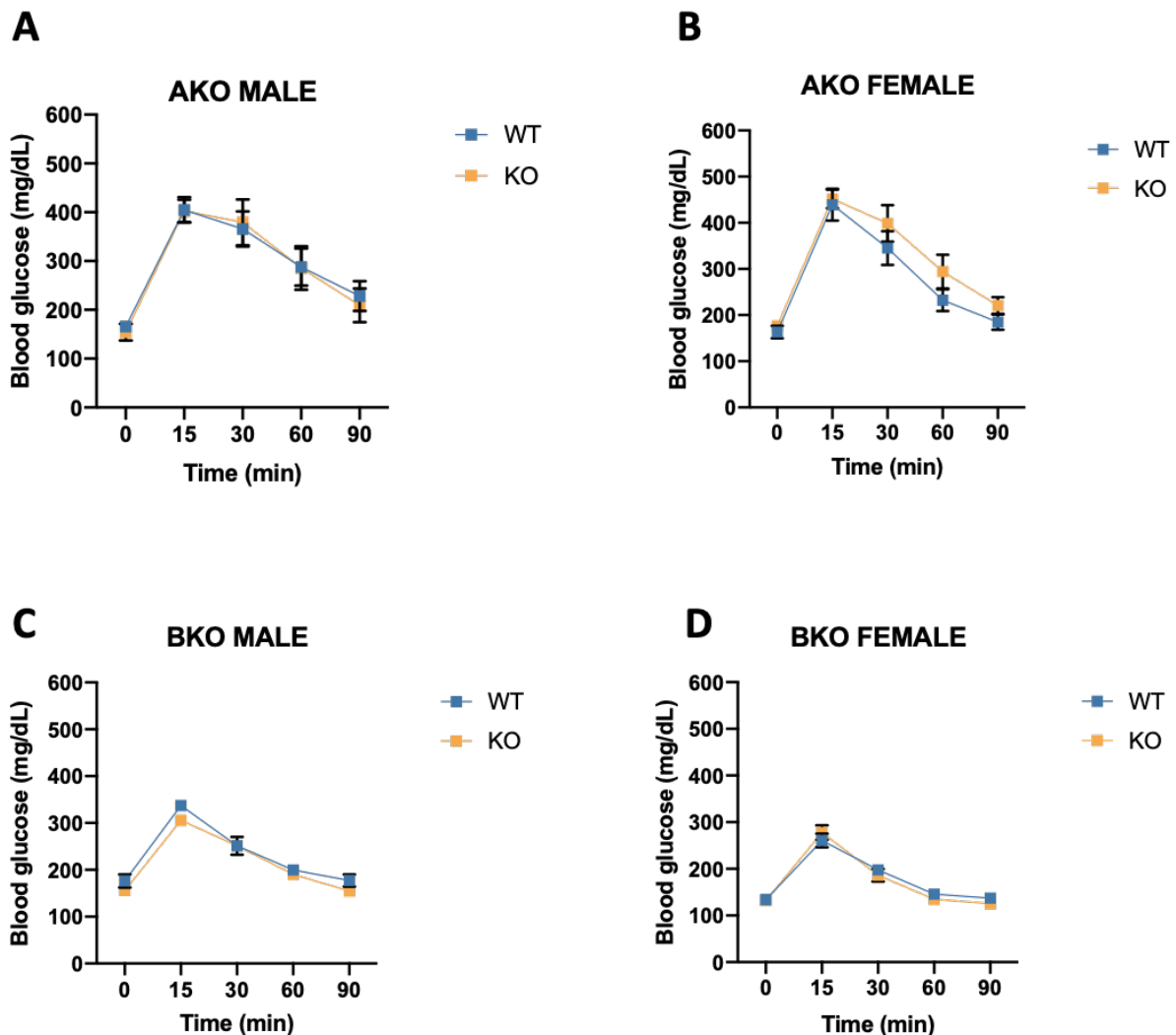
Figure 1.4 GTT analysis of AKO and BKO mice on NCD: *A-B Graph showing analysis of GTT in male and female AKO mice, Student's t test, data are presented as means ± SEM. N = 9 and 5 male of WT and AKO genotype respectively, 7 and 8 female of WT and BKO genotype respectively C-D: Graph representing traces of glucose clearance with time in male and female BKO mice. GTT was performed in the mice after 6h fast. Student's t test, data are presented as means ± SEM. N = 8 and 4 male of WT and BKO genotype respectively, 8 and 7 female of WT and BKO genotype respectively.*

Due to physiological variation between mice, this was not reflected at the level of average fat mass in female mice (Fig. 1.3B). These results hinted at potential lack of metabolic benefits in the AKO mice and very subtle benefits in BKO mice, in stark contrast to CLPP KO mice [349]. It is also important to note that sex specific differences were seen in the body weight and fat content of the BKO mice, which was not the case with AKO mice or KO mice.

We next investigated if this phenotype was reflected in the metabolic physiology of the mice. We checked for glucose clearance in the mice by glucose tolerance test (GTT). AKO mice (both male and female) did not show improved glucose clearance compared to the WT controls. (Fig 1.4A-B). The BKO male mice exhibited a subtle tendency towards improved glucose tolerance in the first phase of glucose uptake before the 30 minutes, although the results were not significant (Fig. 1.4C), whereas the female mice did not show any difference compared to the WT mice (Fig. 1.4D). Taken together, these results suggested that BKO mice possessed some modest metabolic benefits. These observations again contrasted with the findings from the whole body CLPP KO animals, where the KO mice had exhibited significantly improved glucose clearance irrespective of the gender [349].
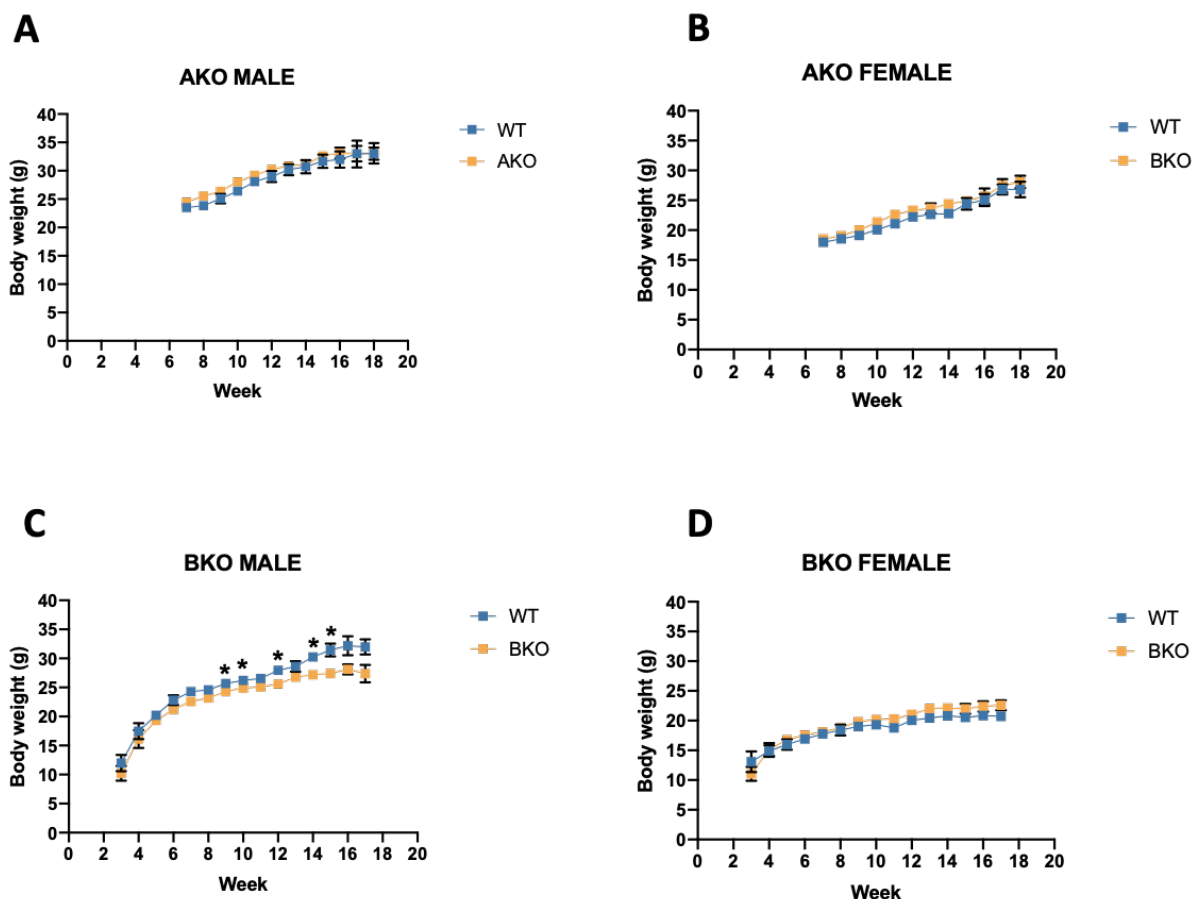
Figure 1.5 Body weight gain of AKO and BKO mice on HFD. *A-B: Graph representing gain in body weight with age in AKO male and female mice, Student's t test, data are presented as means ± SEM, N = 4 and 3 male of WT and AKO genotype respectively, 6 and 6 female of WT and AKO genotype respectively. C-D: Graph showing gain in body weight in male and female BKO mice, Student's t test, data are presented as means ± SEM, N = 4 and 4 male of WT and BKO genotype respectively, 3 and 4 female of WT and BKO genotype respectively. Body weight was monitored till 18 weeks of age, and HFD was started at 6 weeks of age. * p < 0.05.*

The partial metabolic benefits conferred to the mice upon loss of CLPP in BAT were not very pronounced under baseline diet conditions. To assess if AKO and BKO mice were able to cope better under metabolic stress, the mice were fed HFD, providing 60% calories from fat (lard) from 6 weeks of age for a period of 15 weeks. Therefore, all subsequent end point analyses were performed at 21-22 weeks of age, after 15 weeks of HFD feeding.
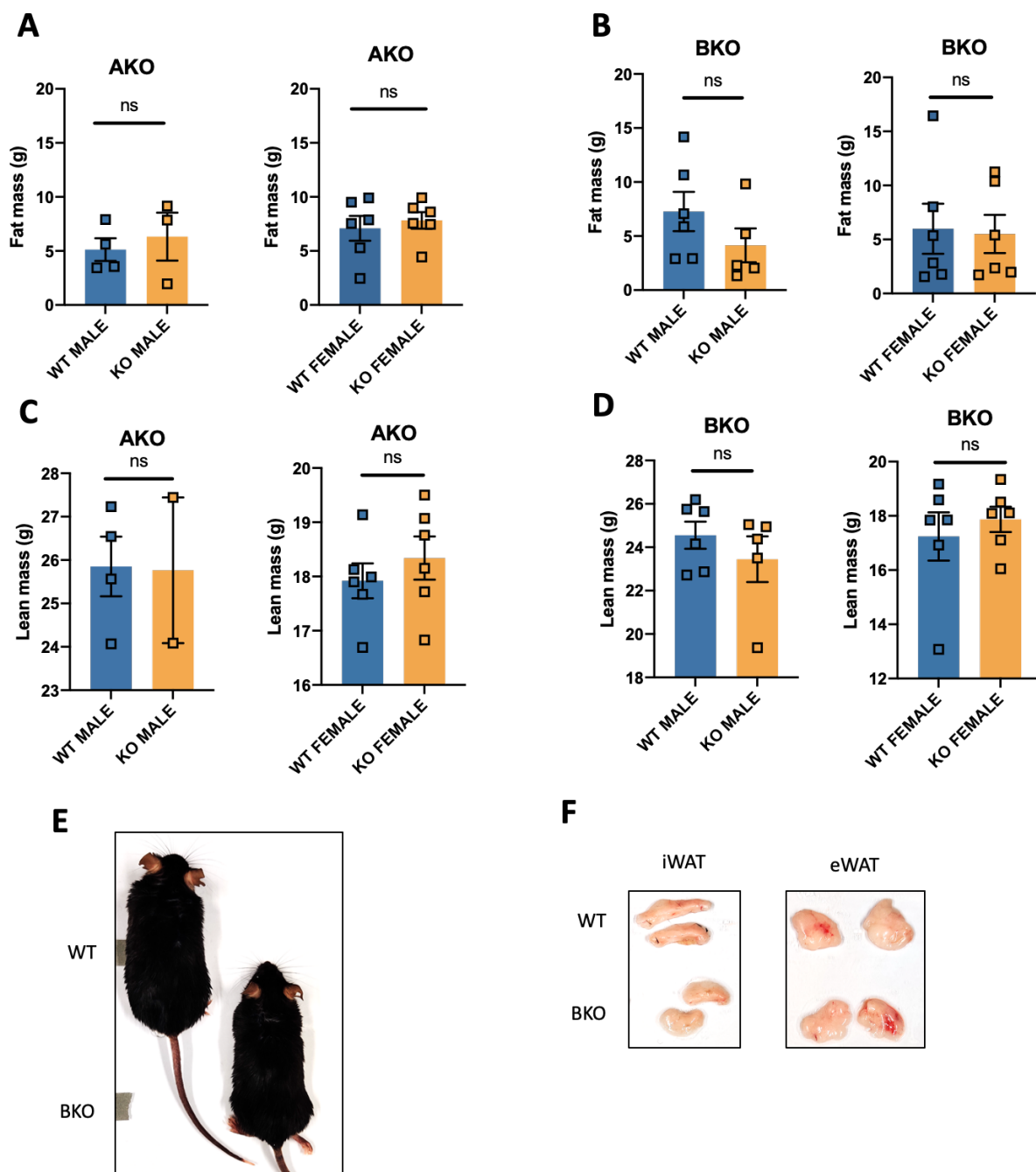
Figure 1.6 Body composition analysis of AKO and BKO mice on HFD. *A-B: Graph showing total fat mass in male and female mice of mentioned genotypes, as measured by NMR at 20 weeks of age. Student's t test, data are presented as means ± SEM. N = 4 and 3 male of WT and AKO genotype respectively, 6 and 6 female of WT and BKO genotype respectively. *$p < 0.05$. C-D: Graph showing total fat mass in male and female mice of mentioned genotypes, as measured by NMR at 20 weeks of age. Student's t test, data are presented as means ± SEM. N = 6 and 5 male of WT and AKO genotype respectively, 6 and 6 female of WT and BKO genotype respectively. *$p < 0.05$. E: Representative images of BKO mice after HFD. F: Representative images showing different adipose tissues in BKO mice.*

First, we investigated the body weight gain of mice during HFD feeding. In consistence with results on NCD, AKO mice (both male and female) did not show any differences in body weight gain compared to control mice (Fig. 1.5A-B).

The BKO male mice displayed a slight but significant protection from weight gain. The mice weighed 5.7% lesser than WT controls at 8 weeks of age and 12.8% lesser at 16 weeks of age (Fig. 1.5C). BKO female mice did not show any reduction in body weight compared to WT female mice (Fig. 1.5D).

Next, we performed body composition analysis of the mice. Neither AKO nor BKO mice showed significant differences in fat mass (Fig. 1.6A-B) or lean mass (Fig. 1.6C-D) upon HFD. Although some BKO male mice did exhibit a leaner phenotype and lower fat content compared to WT control mice (Fig. 1.6E-F), the results were not quantitatively significant due to physiological variation. We next assessed glucose clearance in the mice. AKO mice did not show any improvement in glucose clearance compared to WT control mice (Fig 1.7A-B).
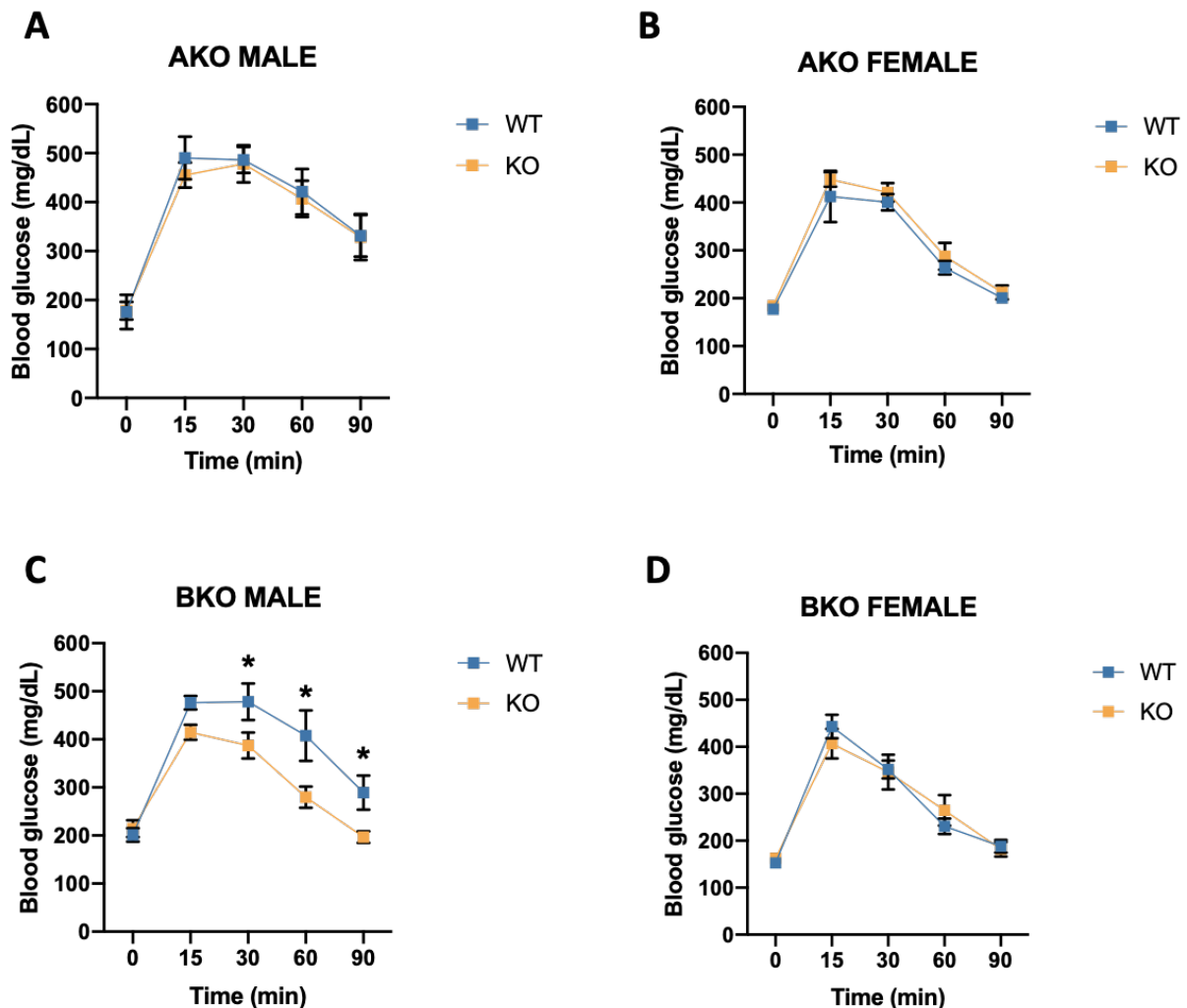
Figure 1.7 GTT analysis of AKO and BKO mice on HFD. *A-B: Graph showing analysis of GTT in male and female AKO mice, Student's t test, data are presented as means ± SEM. N = 3 and 5 male of WT and AKO genotype respectively, 8 and 9 female of WT and BKO genotype respectively C-D: Graph representing traces of glucose clearance with time in male and female BKO mice. GTT was performed in the mice after 6h fast. Student's t test, data are presented as means ± SEM. N = 8 and 4 male of WT and BKO genotype respectively, 6 and 6 female of WT and BKO genotype respectively.*

BKO male mice interestingly showed significantly improved glucose clearance compared to their WT controls in the later phase of GTT assay (Fig. 1.7C). BKO female mice, however, did not phenocopy the improvements seen in the male mice (Fig 1.7D). These results, taken together, indicated that loss of CLPP only in BAT confers very subtle metabolic benefits to the mice, which are pronounced under metabolic stress. It is intriguing to note that removing CLPP from WAT depots in addition to BAT (in AKO mice) leads to reversal of these metabolic benefits.

We further wanted to investigate the molecular underpinnings of CLPP loss in the adipose tissue depots, especially in iWAT and eWAT. To assess the extent to which the mitochondria were affected upon CLPP loss, we isolated mitochondria from these depots in KO and WT mice. They were then subjected to digitonin treatment and run on BN-PAGE (Blue Native Polyacrylamide Gel Electrophoresis) gels followed by immunoblotting to assess the levels of complexes and supercomplexes.

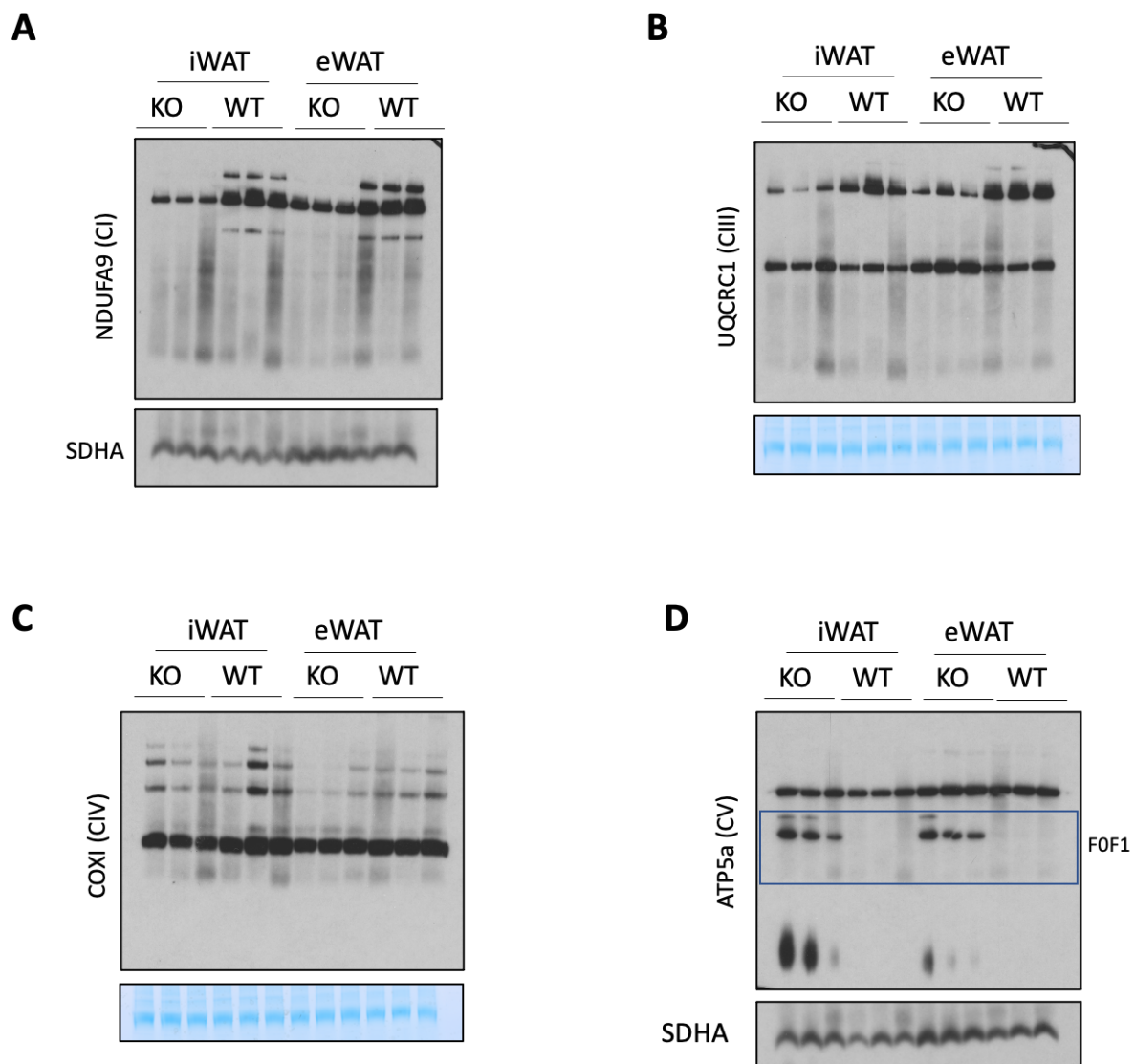**Figure 1.8 BN-PAGE and subsequent western blot analysis of mitochondria isolated from iWAT and eWAT of KO mice showing each mitochondrial supercomplexes.** A: CI, B: CII, C: CIV, D: CV. Antibodies against individual complex subunits (indicated next to the blots) were used for the detection of assembled supercomplexes. N = 3.

The results from BN-PAGE analysis revealed a significant decrease in supercomplex assemblies of CI, CIII and CIV (Fig 1.8 A-C). Additionally, subassemblies of CV were seen to accumulate in KO mitochondria from both iWAT and eWAT (Fig. 1.8D), which were possibly sub-assembled F_1 complex. Unlike mitochondria from other tissues from CLPP KO mice like liver, which did not have altered supercomplex levels, mitochondria from both iWAT and eWAT were moderately affected upon CLPP loss. At this juncture, we decided to examine the molecular details only in iWAT. A significant reason for prioritizing iWAT for further analysis was its potential as a suitable universal model. Unlike eWAT, which is under strict hormonal regulation and can vary in different animals depending on sex and reproductive stage, iWAT offered a more consistent approach to understanding the impact of CLPP loss-mediated mitochondrial dysfunction on WAT physiology.

Next, we performed BN-PAGE analysis on mitochondria from iWAT of the tissue-specific knockout models, AKO and BKO to compare the degree of respiratory supercomplex reduction in comparison to mitochondria from KO. The degree of mitochondrial dysfunction in AKO and BKO was less pronounced than in KO mice (Fig. 1.9). The immunoblot for CI (two independent subunits, NDUFA9 and NDUFV1) showed a milder reduction in steady state levels of supercomplexes in AKO and BKO compared to KO (Fig. 1.9A-B). Likewise, CIV supercomplex assemblies were less severely affected in AKO and BKO compared to KO (Fig 1.9C).

Reduction of supercomlexes from iWAT of BKO mice was an intriguing finding, since these mice have absence of CLPP only from BAT and have functional CLPP in
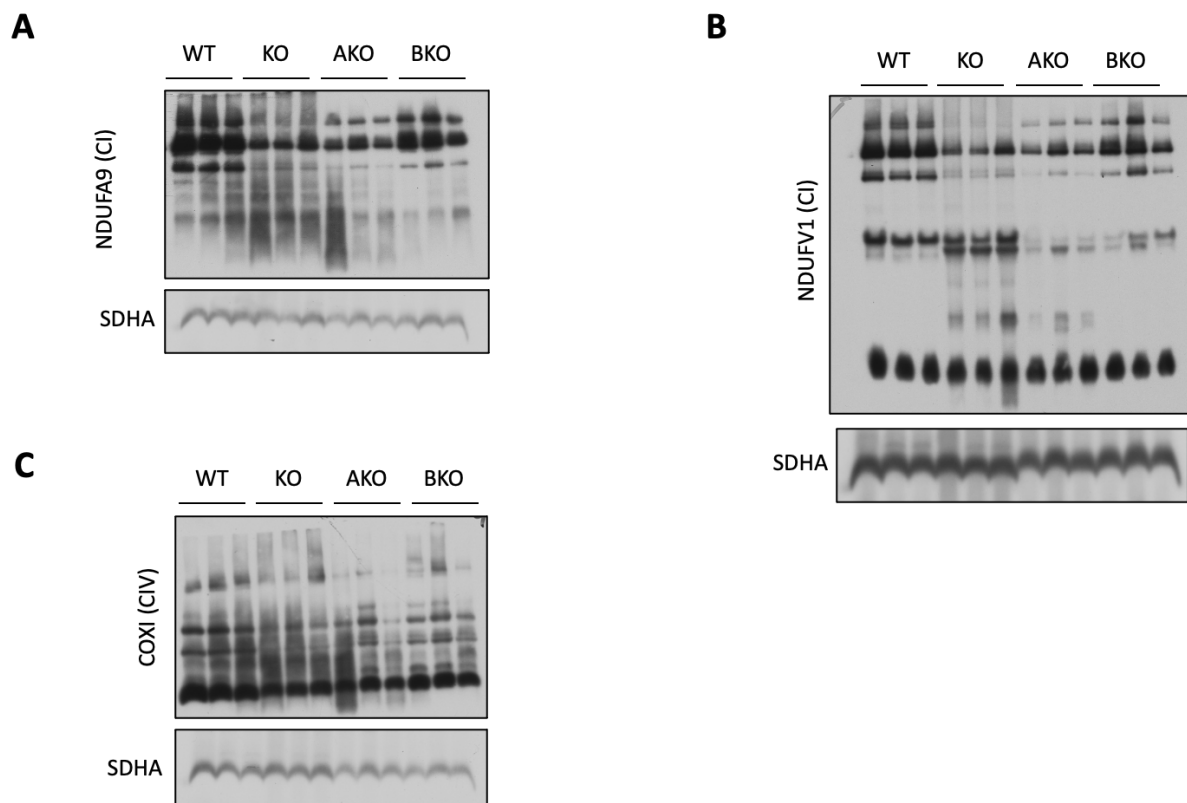

Figure 1.9 Comparative BN-PAGE analysis subsequent western blot analysis of mitochondria isolated from iWAT of KO, AKO and BKO. A: CI, B: CI, C: CIV. Antibodies against individual complex subunits (indicated next to the blots) were used for the detection of assembled supercomplexes. N = 3.

iWAT. This suggested inter-tissue communication or signaling from BAT to iWAT, thereby influencing mitochondrial behavior in iWAT in an endocrine manner.

Our findings so far demonstrated two major points: first, that CLPP loss has an autonomous effect on mitochondrial quality in iWAT, resulting in reduction of respiratory chain complexes and supercomplexes. Second, that there are tissue non-autonomous effects on iWAT mitochondrial quality, primarily influenced by CLPP loss in BAT. These results suggested complex interplay and signaling mechanisms between different adipose tissues, which we investigated further.

Next, to understand in an unbiased manner how CLPP loss and the associated mitochondrial dysfunction reprogrammed the iWAT, we assessed the global gene expression changes in KO, AKO and BKO mice, compared to WT by RNA sequencing (RNA- Seq). We compared the steady - state levels of transcripts isolated from iWAT from each of the knockout models to WT, and applied threshold parameters of log2fold change (FC) > 0.5 or Log2FC > -0.5 and p value < 0.05. As shown in the Venn diagram (Fig. 1.10A), iWAT from KO mice showed the most changes amongst the three models, with 781 transcripts (452-up and 329-down) differentially expressed. AKO mice showed 463 transcripts (335-up and 128-down) to be differentially expressed, which was higher than number of changed transcripts in BKO (Fig 1.10), which had 69 transcripts (60-up and 9-down) to be differentially expressed in BKO (Fig 1.10). We could infer that loss of CLPP had a tissue-intrinsic effect in iWAT from KO and AKO mice. Additionally, there were indications of non-autonomous signalling fom BAT to iWAT in BKO mice, which led to changes in gene expression in iWAT of BKO mice. This formed the basis for further investigation of tissue-autonomous and non-autonomous roles of CLPP.

GSEA analysis of significantly upregulated or downregulated transcripts revealed the enrichment of multiple overlapping pathways in KO and AKO. Amongst the common upregulated pathways were those belonging to systemic inflammation, like cytokine signaling, antigen processing and innate immune response (Fig. 1.11A-B). The common downregulated pathways included tyrosine kinase signaling pathway, skeletal muscle differentiation, collagen accumulation and white fat differentiation-related terms (Fig 1.11A-B).

It was interesting to note that lipid biosynthesis-related terms were enriched in AKO specifically and not in KO (Fig 1.10C). These similarities of enriched pathways between KO and AKO indicated that even though there were phenotypic differences in KO and AKO mice in terms of body fat content and iWAT tissue size (Fig. 1.3E-F), the molecular consequences of loss of CLPP were quite overlapping. Also, the subtle but significant differences in GSEA enrichment in AKO indicated that the upregulation of fatty acid biosynthetic pathways and lipid anabolic processes could be causal for larger fat depots in AKO mice compared to KO mice. Additionally, the upregulation of browning genes was not very apparent from the transcriptome results since there were no different in the levels of *Ucp1, Ucp3, Cidea, Dio2,* and *Mapk14* (which are the typical markers of browning). It will be interesting to perform a histological analysis on iWAT

to examine lipid droplet size, mitochondrial numbers and browning.

Figure 1.10 Transcriptome level changes in iWAT of KO, AKO and BKO mice. *A: Venn diagram depicting the exact numbers of significantly changed transcript abundances in KO, AKO and BKO mice. The size of the circles represent the relative proportions of the number of genes in each model. B-D: GSEA enrichment analysis of significantly changed transcripts from iWAT of KO, AKO and BKO mice. N=4 per genotype.*

We then selected the commonly upregulated genes from KO and AKO and performed a transcription factor (TF) prediction test to identify commonly regulated

gene clusters using iRegulon plugin from Cytoscape. The analysis revealed ATF4 as one of the major TFs that caused upregulation of its target genes in the absence of CLPP from both KO and AKO (data not shown). This was of particular interest to us since ATF4 is a major TF regulating ISR and mitochondrial dysfunction has been typically shown to lead to activation of the ISR pathway [1]. However, due to lack of proper annotation of the ISR genes, the term often gets underrepresented in unbiased GSEA or GO analyses. The GSEA results, as well as DAVID analysis (Database for Annotation, Visualization and Integrated Discovery) of the 69 changed transcripts from iWAT of BKO did not yield any informative pathways or process enrichment. Closer examination of the individual genes revealed that they belonged to mitochondrial complex subunits, myosin and tubulin related genes and genes encoding protein kinases and phosphatases.

To further get insights into the proteomic level changes in the three models, we performed label free quantitative proteomics on iWAT from KO, AKO and BKO mice. Statistically significant changes in the steady state levels of proteins were observed for 476 proteins in KO (259-up and 217-down), 218 proteins in AKO (119-up and 99-down), and 140 proteins in BKO (90-up and 50-down) (Fig 1.11A). iWAT from KO had the highest degree of change in steady state protein levels, followed by AKO and then BKO. It was very interesting to note here that iWAT from BKO mice had many more significant changes at the level of proteins than at the level of transcripts. This provided preliminary indication that some signals from BAT in BKO mice were altering the stability or translational rates of proteins in iWAT without causing massive changes in their corresponding gene expression. Further, GSEA analysis of the proteins whose levels were significantly increased or decreased in iWAT from different models revealed many overlapping enriched pathways between KO and AKO (Fig. 1.11B-D). The top most enriched pathways in both belonged to the inflammation cluster including terms like cytokine production, antigen presentation and innate immune response (Fig 1.11 B-C). The common downregulated pathways included nucleotide metabolism pathways, respiratory chain complex involving pathways, muscle contraction and ATP synthesis (Fig. 1.11 B-C). Additionally, possibly owing to larger changes in steady state protein levels in KO, additional pathway, organic metabolic synthesis unique only to KO was enriched, (Fig. 1.11B). Interestingly, GSEA analysis of proteins from BKO revealed enrichment of terms like translation, mitochondrial transport and innate immunity related pathways (Fig. 1.11D). This was intriguing for us, since it provided another evidence in support of our earlier speculation about upregulated translation in BKO iWAT due to non-autonomous influence from BAT. It was also interesting to note that the terms related to muscle contractions were enriched as downregulated pathways in all the three models, thereby hinting at some strong correlation between loss of CLPP and alteration in muscle or cytoskeletal related proteins (Fig. 1.11).

To gain a deeper understanding of the influence of loss of CLPP in BAT on iWAT, we identified the clusters from proteomics that involved proteins showing similar changes in their steady state levels in BKO and KO (Fig 1.12A). We selected the proteins belonging to those clusters (marked in boxes) and performed a GO molecular function (MF) analysis using DAVID. GO analysis revealed enrichment of terms related to acetyl coA, succinyl coA, fatty acid and carboxylic acid metabolic processes (Fig.

1.12B). Enrichment of these terms indicated a strong interplay between BAT and iWAT via secretory factors such as metabolites or chemokines.
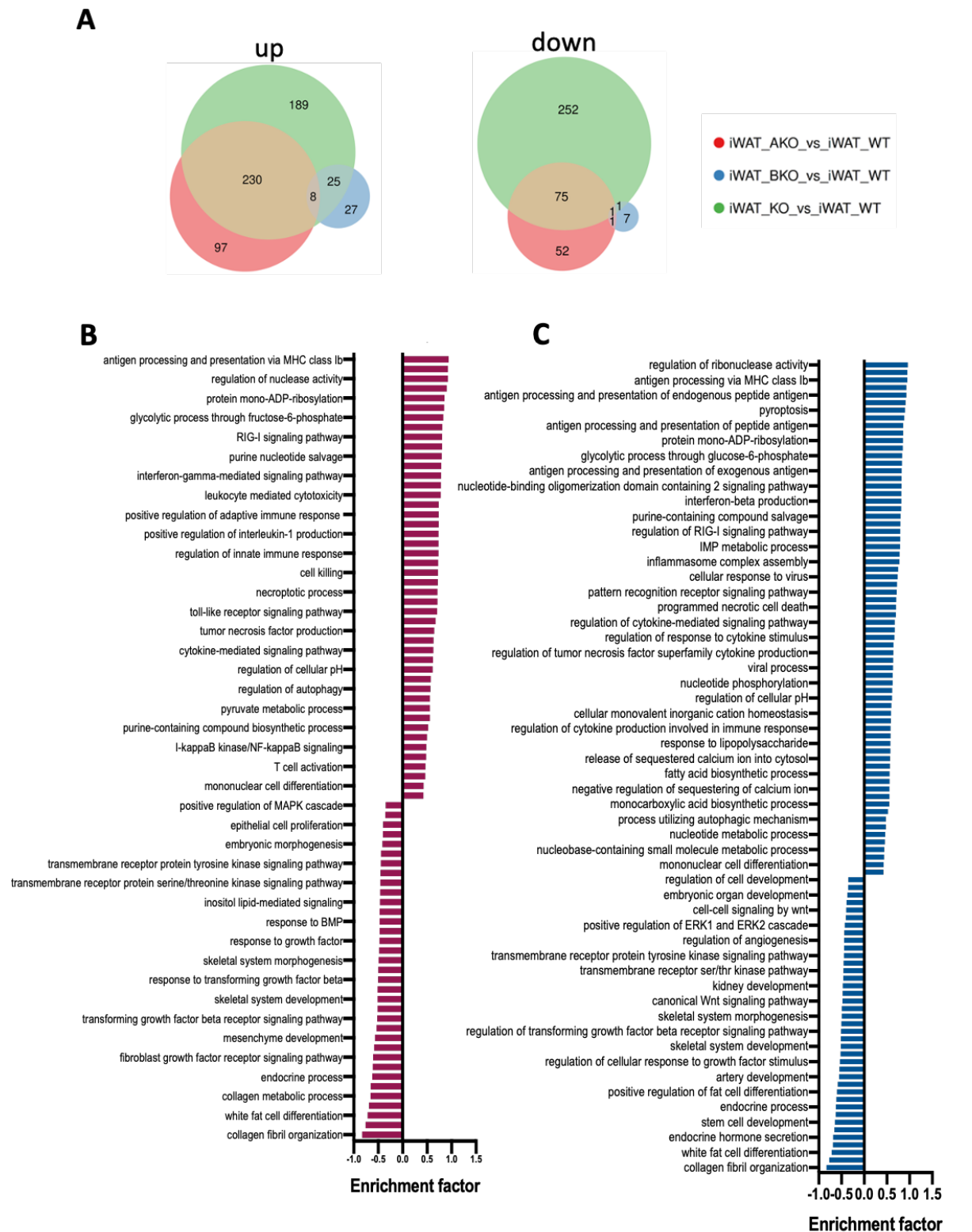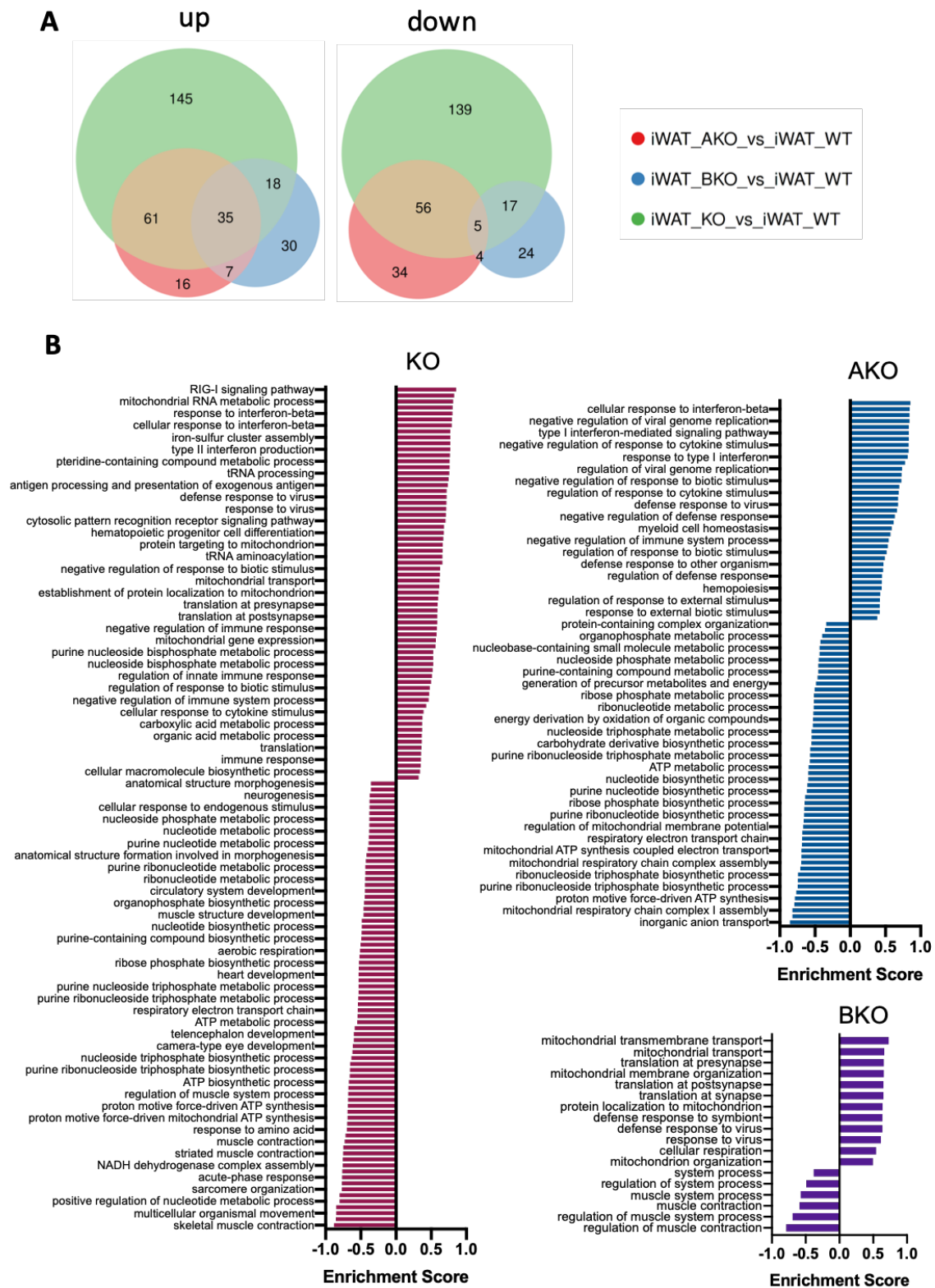

Figure 1.11 Proteome level changes in iWAT of KO, AKO and BKO mice. *A: Venn diagram depicting the exact numbers of significantly changed transcript abundances in KO, AKO and BKO mice. The size of the circles represent the relative proportions of the number of genes*
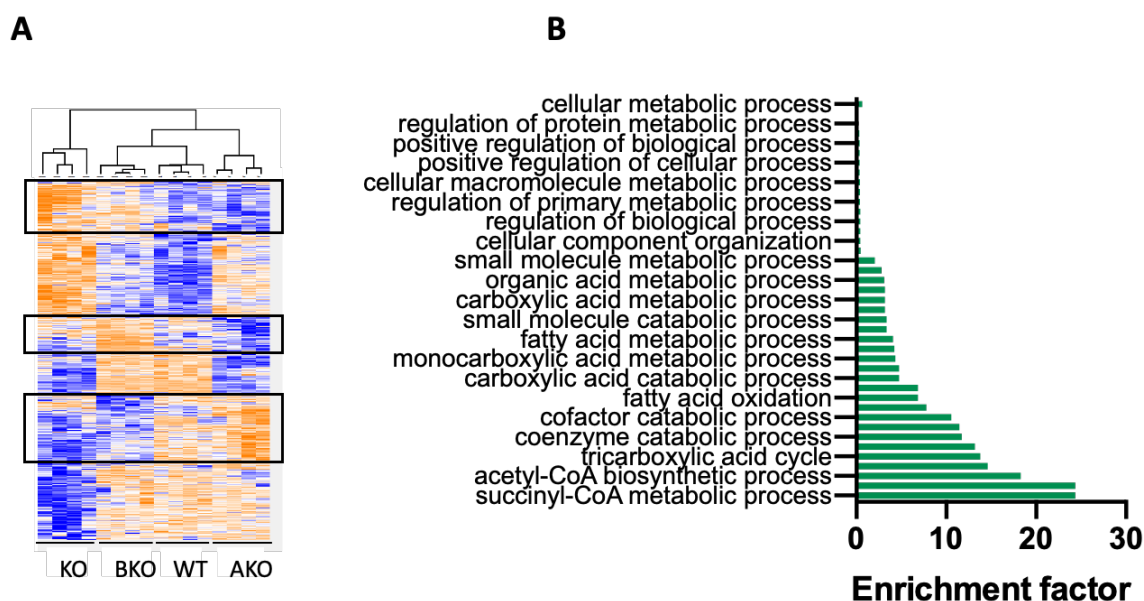
Figure1.12 Representation of proteomic analysis of iWAT from KO, AKO and BKO mice. *A: Heat map showing profile of significantly changed proteins in iWAT of mice. N = 4 per group; B: GO MF enrichment analysis of selected proteome clusters from iWAT of mice of mentioned genotypes.*

This prompted us to explore the mediators of inter-adipose tissue communication in our models. We next performed a metabolomics analysis on iWAT and serum from KO, AKO and BKO mice. Analyzing metabolites parallelly from both iWAT and serum would provide insights into metabolites that are being taken up from the blood by the iWAT, and are possibly released by BAT.

In contrast to other tissues, the number of detected metabolites in the iWAT was notably low (Fig. 1.13A), with levels of only 41 metabolites changed in KO (36-up and 5-down), 6 metabolite levels changed in AKO (2-up and 4-down) and only 5 metabolites changed in BKO (2-up and 3-down) (Fig. 1.13A). This raised questions about the extraction protocol, and further optimization of reagent-to-tissue ratio would be needed. We did not perform any enrichment analysis of these metabolites since the data was non-optimal. However, serum metabolite analysis of KO, AKO and BKO mice in combination with results from KO iWAT offered interesting insights into possible systemic factors. Serum from KO mice had the highest number of significantly changed metabolites, with levels of 8 metabolites increased and levels of 22 metabolites decreased. Serum from AKO mice showed alteration in levels of 3 metabolites (2-up and 1-down) and that from BKO mice showed alteration in abundance of 5 metabolites (1-up and 4-down) (Fig. 1.14). We saw accumulation of two novel metabolites in both iWAT and serum of KO mice- namely homoarginine and homocitrulline (Fig. 1.13B and 1.14A).

These two metabolites are intermediates of lysine metabolism [350] and are of particular interest in our context due to their link to OAT, which is a direct CLPP target and plays role in urea cycle [351]. The fact that neither iWAT nor serum from AKO and BKO mice showed accumulation of these two metabolites led us to conclude that BAT and iWAT might are not the source of these metabolites. Instead, other metabolically relevant tissues could be involved in releasing these metabolites into the bloodstream,

potentially serving as signaling molecules to communicate specific information to different tissues.
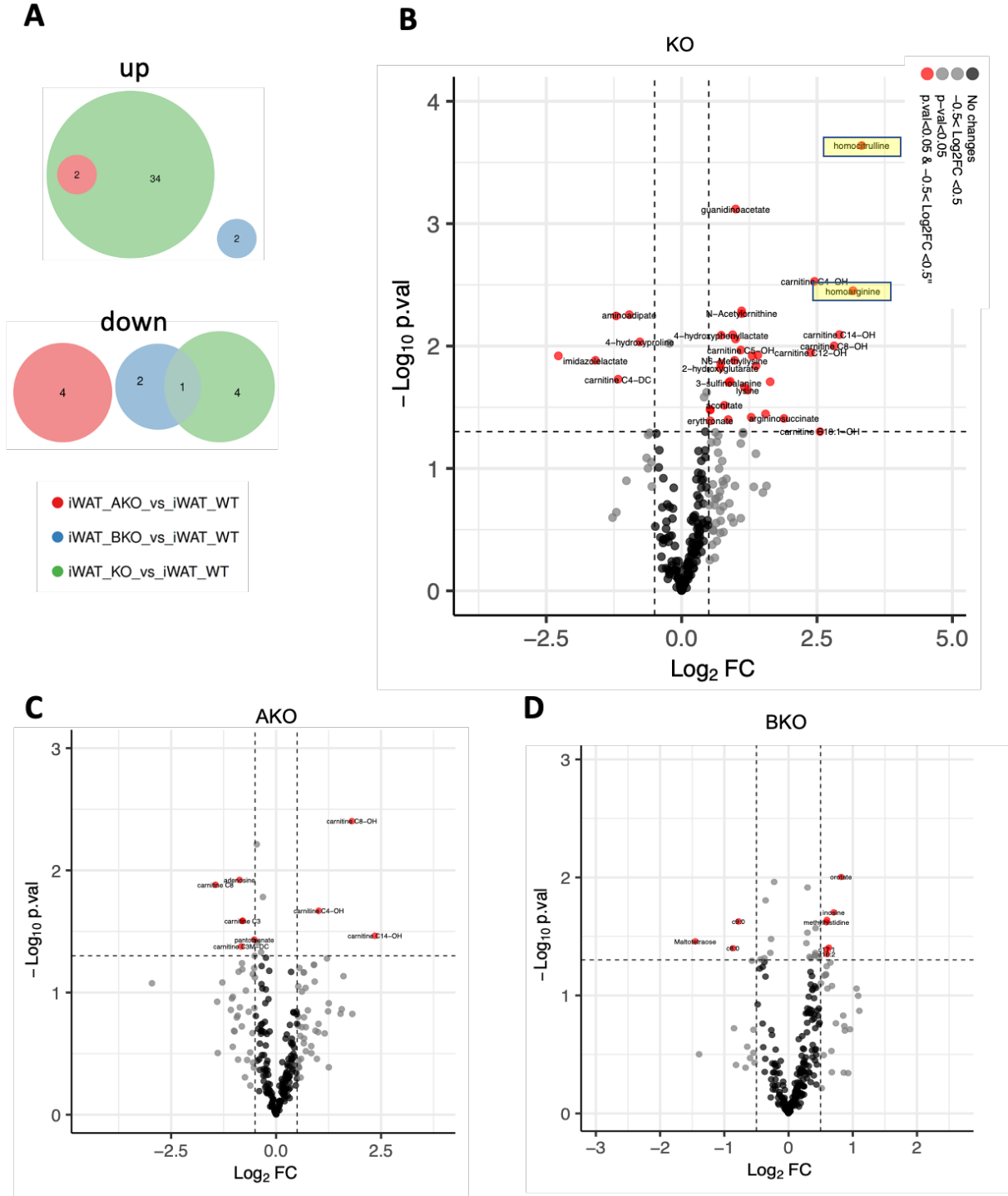
Figure 1.13 iWAT metabolomics from KO, AKO and BKO mice. A: Quantitative changes in metabolome of iWAT from KO, AKO and BKO. B-D: Volcano plot showing fold changes of significantly changed metabolites in KO, AKO and BKO mice compared to WT, Y axis log10 p values and X axis represent log2 fold change, N = 5 per genotype.

To gain preliminary insights into this speculation, we focused our attention on the liver, as homoarginine and homocitrulline are involved in the urea cycle, and the liver is the primary organ handling this process [352].
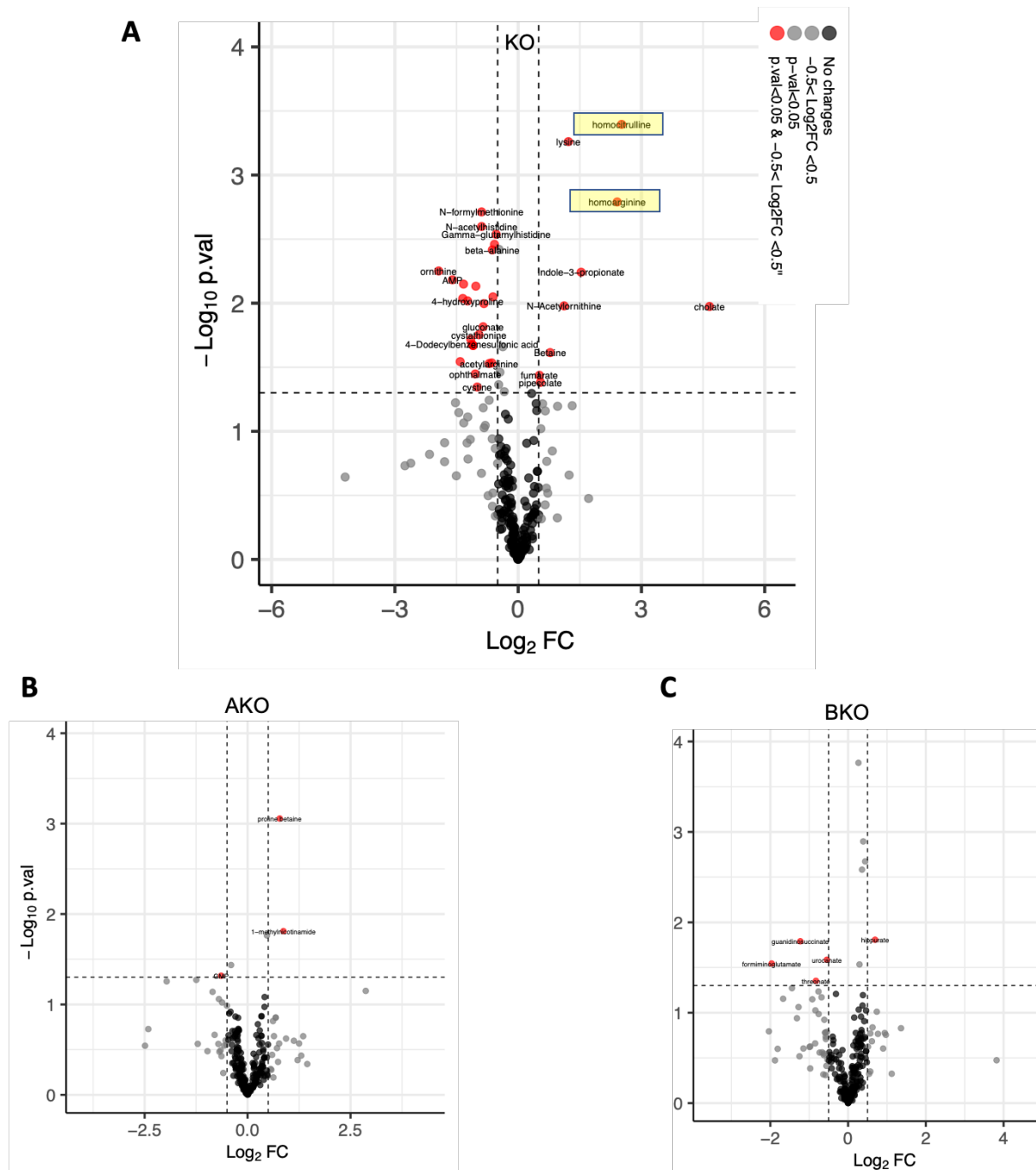
Figure 1.14 Serum metabolomics from KO, AKO and BKO mice. *A: Volcano plot showing fold changes in metabolite levels in KO mice compared to WT, Y axis log10 p values and X axis represent log2 fold change, N = 5. B,C volcano plot showing changes in metabolic profile in AKO and BKO, N = 5 per genotype.*

Analysis of the liver metabolome of KO mice revealed an accumulation of homoarginine and homocitrulline (Fig. 1.15A), similar to what we observed in iWAT and serum. Next, we investigated the metabolite levels in liver from liver-specific knockout (LKO) model and saw the accumulation of homoarginine and homocitrulline (Fig. 1.19B), just as in KO mice. Taken together, our data suggests that liver, and not iWAT or BAT, is the source of these metabolites found in the serum of KO mice.

Figure 1.15 Liver metabolomics from KO and LKO mice. *A-B: Volcano plot showing fold changes in metabolites levels in KO mice compared to WT, Y axis log10 p values and X axis represent log2 fold change, N = 5. B,C volcano plot showing changes in metabolic profile in LKO mice. N = 5 per genotype.*

They could potentially serve as signaling molecules from the liver to the rest of the body, conveying important information about the animal's metabolic status. These newfound insights open up intriguing avenues for further investigation into the roles of homoarginine and homocitrulline in the context of CLPP KO mice, which is beyond the scope of this thesis.

2. CHAPTER 2 | CLPP LOSS-MEDIATED REMODELLING OF BAT

One of the most affected tissues upon loss of CLPP from the whole body is the BAT. Previous studies from lab revealed strong mitochondrial dysfunction in the BAT of KO mice and reduced level of mature oxidative supercomplexes [349]. KO mice were incapable of maintaining their body temperature upon cold exposure, and the BAT was enlarged and whitened, with accumulation of larger lipid droplets [349]. In order to understand whether the whitening of BAT was a tissue-specific effect or due to a broader systemic consequence of loss of CLPP from multiple tissues in the whole body of the mice, we compared BAT from the three models, KO, AKO and BKO. We first tested if the tissue-specific loss of CLPP had an impact on adaptive thermogenesis by subjecting the mice to acute cold temperature of 4°C. In contrast to KO animals, who had a rapid drop in temperature post 2 hours of cold exposure (Fig. 2.1) [349], AKO and BKO animals were able to maintain their body temperature, without any significant drop (Fig 2.1). This clearly indicated that the thermogenesis defect seen in whole body KO mice was possibly stemming from impaired β-adrenergic signaling and was not a BAT-specific effect.
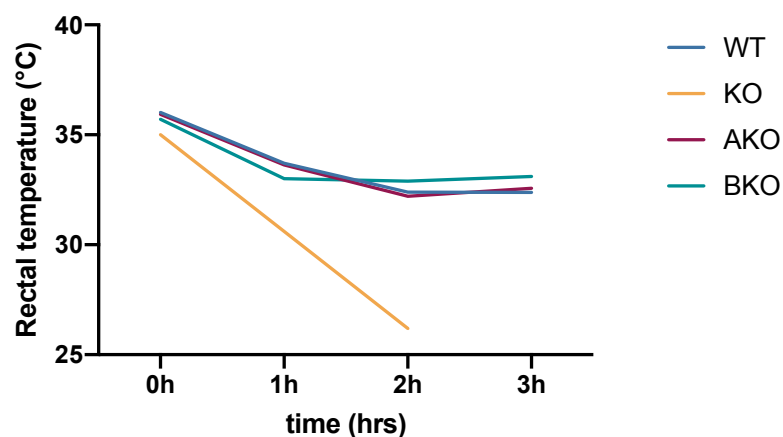
Figure 2.1 CLPP in BAT is dispensable for acute cold induced thermogenesis. *Graph showing temperature trace of mice following cold exposure, students t test data represented as average S.E.M, N =3*

The largest and most accessible BAT depot in mice is present in the dorsal neck region, called the interscapular BAT, and corresponds to the supraclavicular BAT depot (largest and functionally most relevant) described in adult humans [353]. Interscapular BAT is the most widely used depot for understanding BAT function in mice. To understand whether CLPP loss had any impact on BAT, we next investigated the interscapular BAT appearance and morphology in these mice. The BAT from all the three models was enlarged and whitened (Fig. 2.2A), with the consistent accumulation of larger lipid droplets, as evident from the histological analysis (Fig. 2.2B). Remarkably, lipid droplet size and degree of whitening as assessed from qualitative images of the whole tissue, was higher in AKO and BKO compared to KO, with AKO showing largest lipid droplets (Fig 2.2B). These findings suggested that BAT whitening upon CLPP loss was a tissue-specific effect.
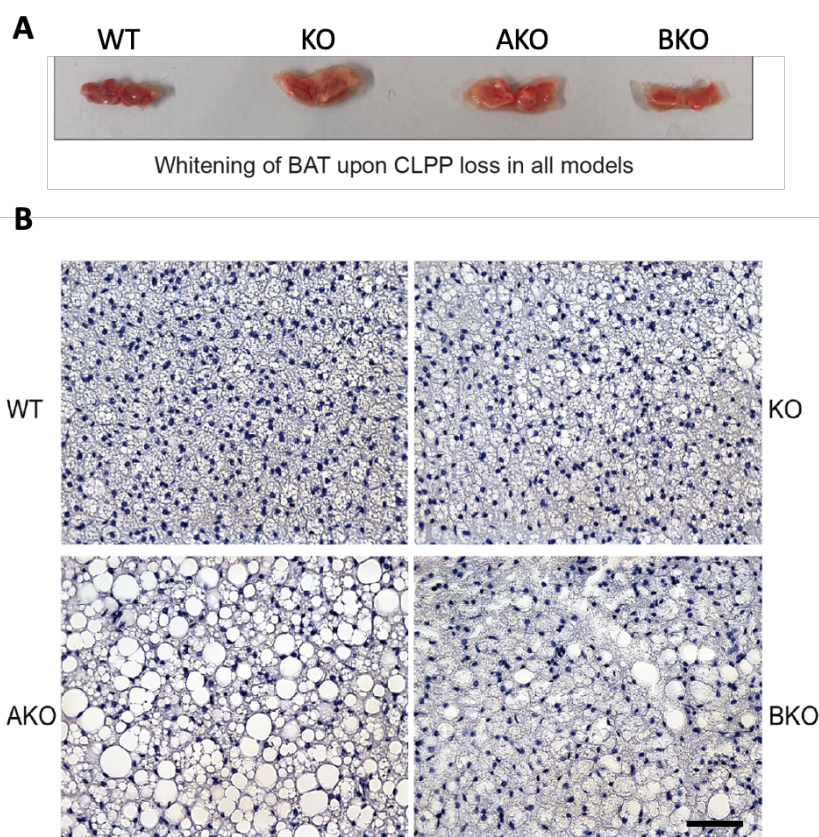
Figure 2.2 Whitening of BAT upon CLPP loss is a tissue autonomous effect. *A: Representative images showing BAT from WT, KO, AKO and BKO mice. B: Images showing H and E staining in the tissue section of WT, KO, AKO, and BKO mice. Scale bar = 200um, N = 3*

We assessed the mitochondrial morphology in KO BAT by TEM analysis on tissue sections. Significant alterations in the ultrastructure of mitochondria were seen in KO (Fig. 2.3A-D). The cristae were disorganized and were concentrated towards the periphery of the mitochondria, resulting in a hollow central portion (Fig. 2.3C-D). An increased number of mitochondria were observed compared to WT control, suggesting increased mitochondrial biogenesis in KO (Fig. 2.3A-B). Additionally, larger lipid droplets were also evident in KO compared to WT in the TEM sections (Fig. 2.3A-B).
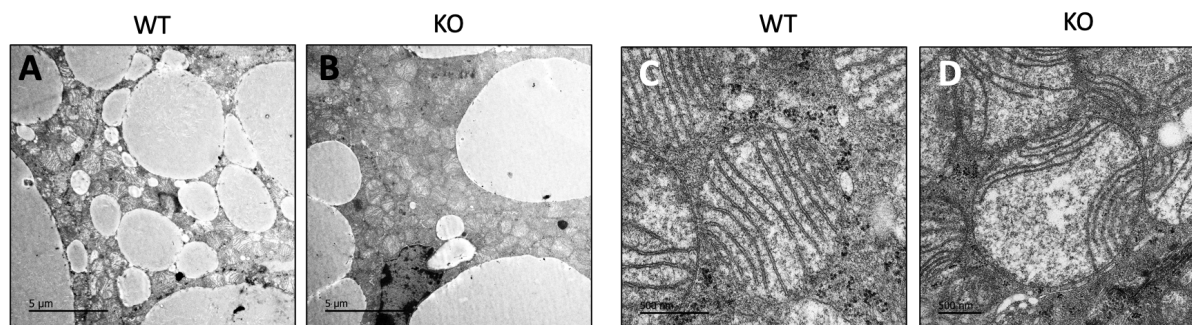
Figure 2.3 Representative TEM images showing disorganization of cristae in the mitochondria of CLPP KO mice. *A: TEM images showing lipid droplets in WT and KO mice, scale bar 5um. B: TEM images of BAT at 15000x showing mitochondrial ultrastructure, N = 2, scale bar 500nm.*

To further characterize the extent of mitochondrial dysfunction, we assessed the complex and supercomplex levels in mitochondria isolated from KO, AKO and BKO by BN-PAGE and subsequent western blot analysis. All the three models exhibited a severe reduction in supercomplexes for CI (Fig. 2.4A-B), while CIII and CIV showed a milder decrease in supercomplex levels (data not shown). Consistent with the BN-PAGE results, we observed lower CI in gel activity in all knockout models compared to WT (Fig. 2.4C). We also detected an upregulation of steady state levels, as well as subassemblies of CV in all the knockout models (Fig. 2.4D), which were also active, as assessed from in gel CV activity assay (Fig. 2.4E). These subassemblies of CV potentially represented the F_1 subcomplex (Fig. 2.4E), often seen to be accumulating in cases of mitochondrial damage and inability to maintain redox balance [354].
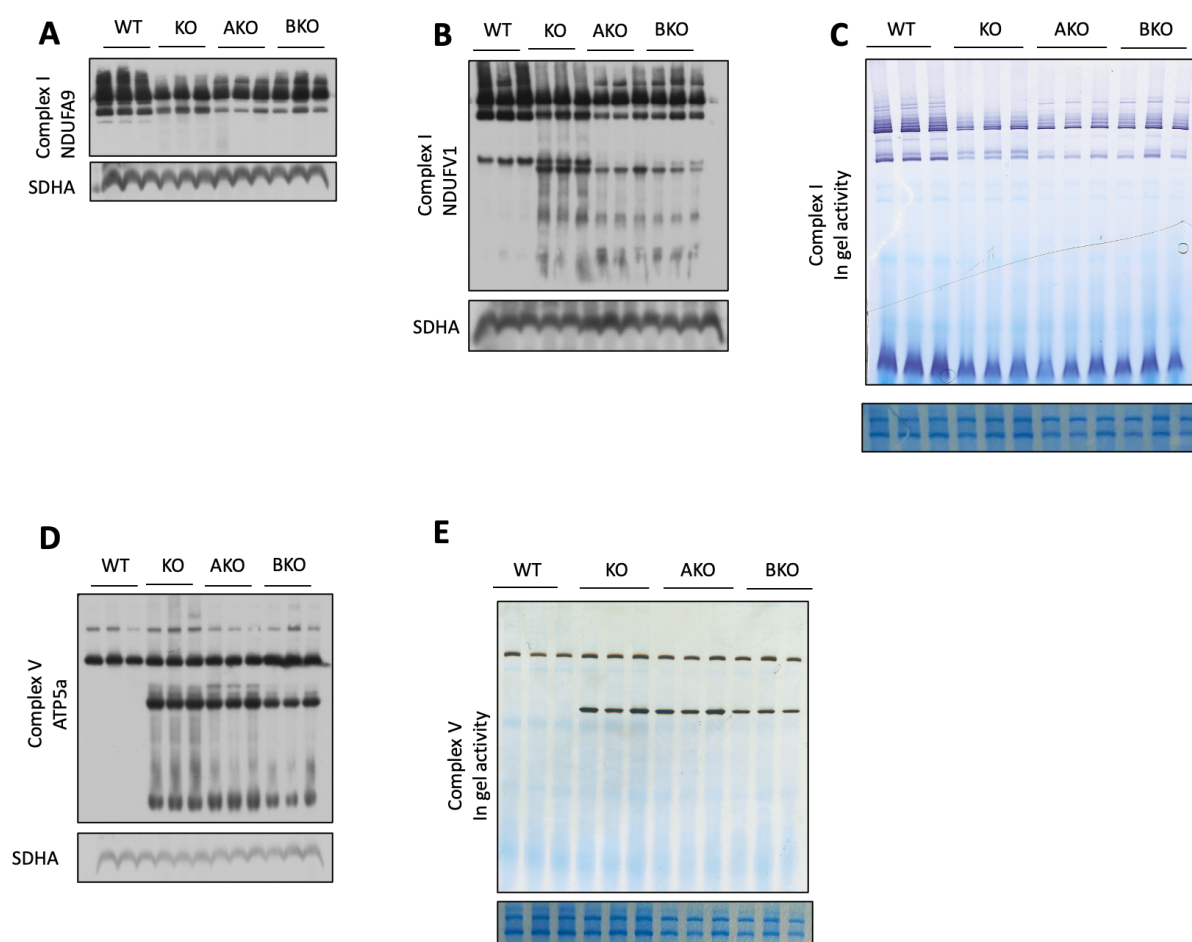
Figure 2.4 Loss of CLPP in BAT leads to respiratory chain deficiency in a tissue-autonomous manner. *A: Immunoblot of NDUFA9 post BN-PAGE analysis showing CI, N = 3. B: Immunoblot of NDUFVI post BN-PAGE analysis showing CI, N = 3., C: Immunoblot of ATP5a post BN-PAGE analysis showing CV, N = 3. D, E: Gel images showing in gel activity assay for CI and CV in WT, KO, AKO and BKO mice, N = 3.*

We investigated the functional consequences of the observed OXPHOS deficiency by measuring mitochondrial respiration with Seahorse bioanalyser on mitochondria isolated from all the three models. We performed two kinds of assays, first with pyruvate and malate as substrates to assess mitochondrial respiratory capacity, and second with octanoyl coA as substrate to measure fatty acid oxidation. We observed a 57.5% decrease in the baseline oxygen consumption and 37.5%

decrease in ADP stimulated state III respiration of mitochondria from KO and BKO BAT compared to WT (Fig. 2.5A). AKO mitochondria, however, had 30% higher respiration compared to KO and BKO, although overall, they still respired lesser than WT (Fig. 2.5A).

The fatty acid oxidation assay showed similar trends (Fig. 2.5B). These results clearly indicated that the respiratory chain deficiency in the mitochondria from CLPP knockout models leads to a lower respiration at both baseline and stimulated levels. Although we do not know why AKO mitochondria showed higher respiration than the other two models, it can be speculated that fluxes within the AKO mitochondria might have led to this difference.
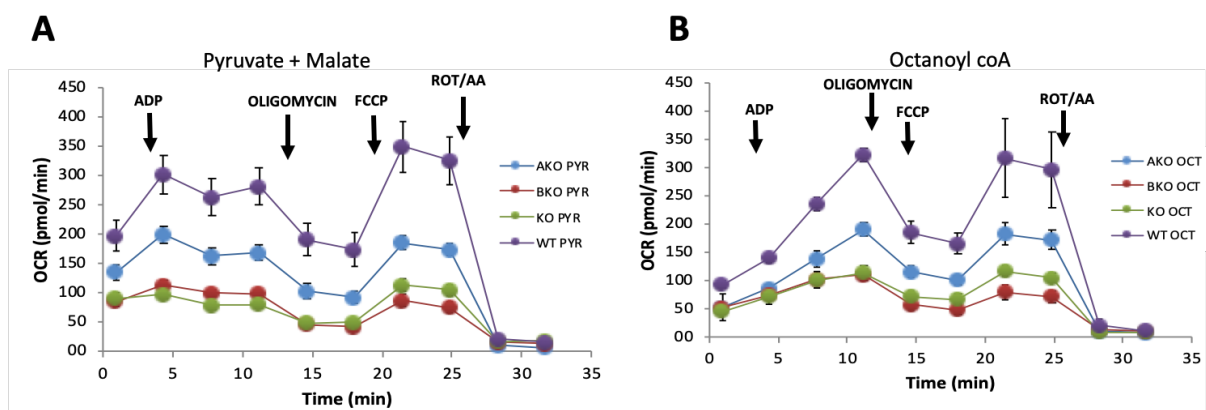
Figure 2.5 Loss of CLPP does not alter respiration at tissue level in BAT. *A: Graph showing OCR of purified mitochondria in WT, KO, BKO and, AKO mice. data are presented as means ± SEM, N =3. Student's t test was performed for pairwise comparisons at each point, and p<0.05 was observed for pairwise comparisons of all knockout models with WT, at all-time points (significance not marked on graph) B: Graph showing fatty acid oxidation based OCR traces . Student's t test was performed for pairwise comparisons at each point, and p<0.05 was observed for pairwise comparisons of all knockout models with WT, at all-time points (significance not marked on graph), data are presented as means ± SEM, N =3.*

To next understand the global changes induced in the BAT due to loss of CLPP, we started with an unbiased omics-based analysis of the tissue. We first assessed transcriptome-level gene expression changes in KO, AKO and BKO, compared to WT by RNA-Seq. As shown in Fig. 2.6A, BAT from KO mice showed the least significant changes amongst the three models, with 1031 transcripts (757-up and 274-down) differentially expressed. AKO BAT showed 2593 transcripts (1671-up and 922-down) to be differentially expressed, which was higher than number of changed transcripts in KO, and 1365 transcripts (932-up and 433-down) were changed in BKO. (Fig. 2.6A) This was reminiscent of the previous data (Fig. 2.2A-B), effects of loss of CLPP appeared to be most pronounced in AKO, followed by BKO and then KO.

To identify the cellular pathways and processes that were changed, a GSEA-BP of differentially expressed genes in KO, AKO and BKO was performed. Qualitative assessment resulted in inflammation related pathways to be among the top 30 pathways in all the three models, and 'response to forskolin' and 'acetyl coA' processes being the common downregulated pathways. Innate immune response, cytoskeletal rearrangement, 'actin filament binding' and fatty acid metabolic pathways were the common upregulated pathways and amongst the downregulated pathways

were acyl coA processes, OXPHOS, 'brown fat differentiation', glycolysis, 'sterol biosynthesis' and protein oxidation. For simplicity, we chose KO BAT to represent the changes from GSEA analysis that are seen across all the three genotypes (Fig. 2.6B).
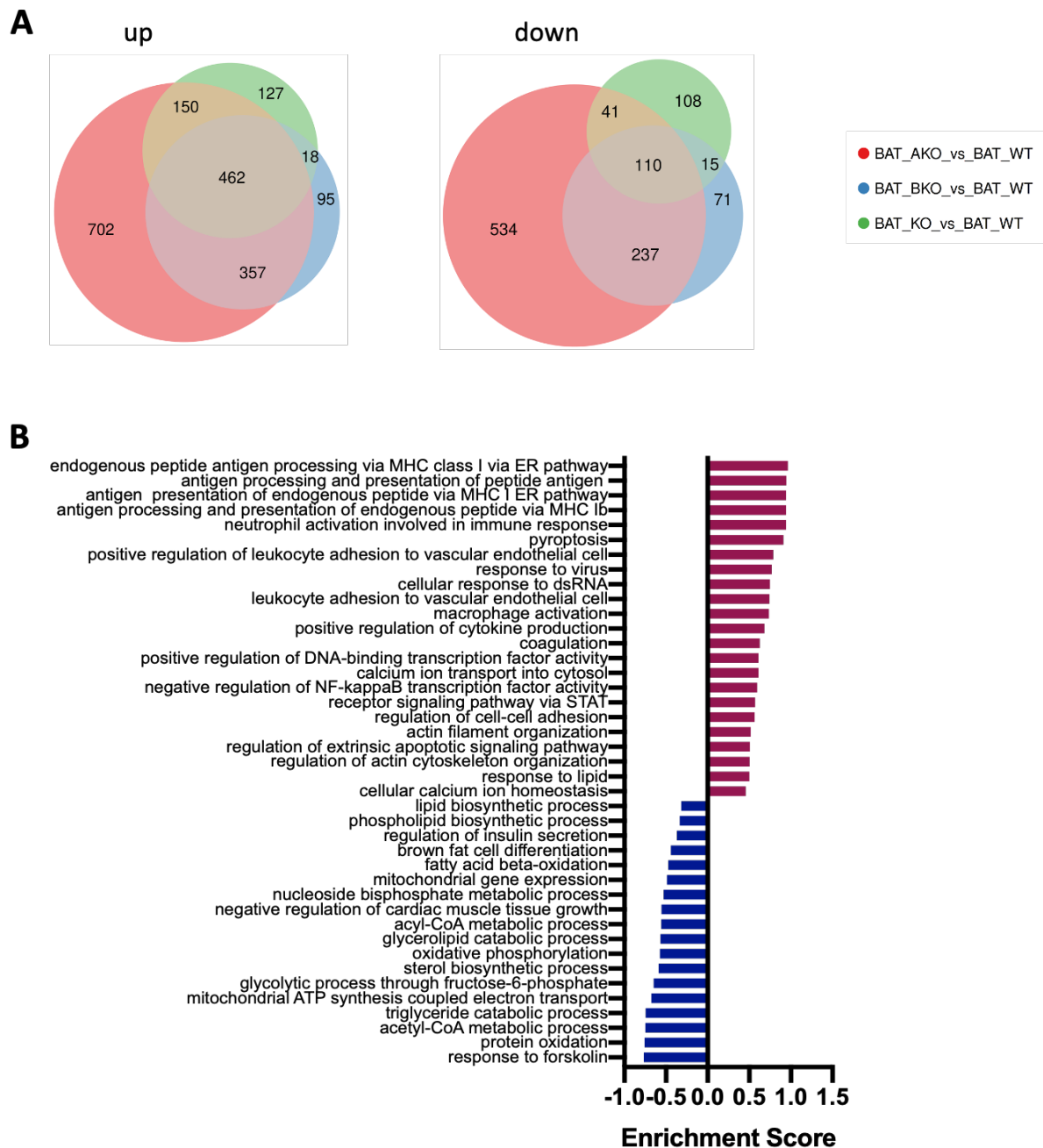
Figure 2.6 Snapshot of major changes in transcriptome of BAT from KO, AKO and BKO mice. *A: Venn diagram depicting the exact numbers of significantly changed transcript abundances in KO, AKO and BKO mice. The size of the circles represents the relative proportions of the number of genes in each model. B: GSEA analysis of the highest enriched pathways involving genes with the highest fold changes. The redundant terms with overlapping genes were removed manually and represented as one term in the graph. If the number of genes in the terms were overlapping by 90%, the terms were pooled. For assessing this, the genes were first sorted according to their enrichment scores and then according to their set size. The top three pathways were represented without pooling. N=4 per genotype.*

Even though not evident from the GSEA, two other gene signatures were upregulated in the transcriptome from all the three models – namely, cytosolic and mitochondrial translation related genes and ISR genes.

The upregulated cluster of inflammation-related genes indicated a prolonged pro-inflammatory state in the tissue. Also, as reflected in the heatmap (Fig. 2.8A), inflammation was highest in AKO BAT, which was consistent with highest lipid accumulation. Amongst the enriched inflammation related terms were cytokine production, NF-κB pathway, JAK-STAT signalling and macrophage activation. The possible mediators of the spread of the inflammatory phenotype in the tissue were NF-κB signaling (activated by tumor necrosis factors (TNFs) [355]), and the JAK-STAT pathway (activated by by interferons (IFNs) and interlukins (ILs) [356]). Consistent with this, was the enrichment of cell death pathways like pyroptosis and apoptosis (Fig. 2.6), thereby emphasizing an activated adaptive cellular response to either curtail the spread of inflammation or eliminate the affected cells.
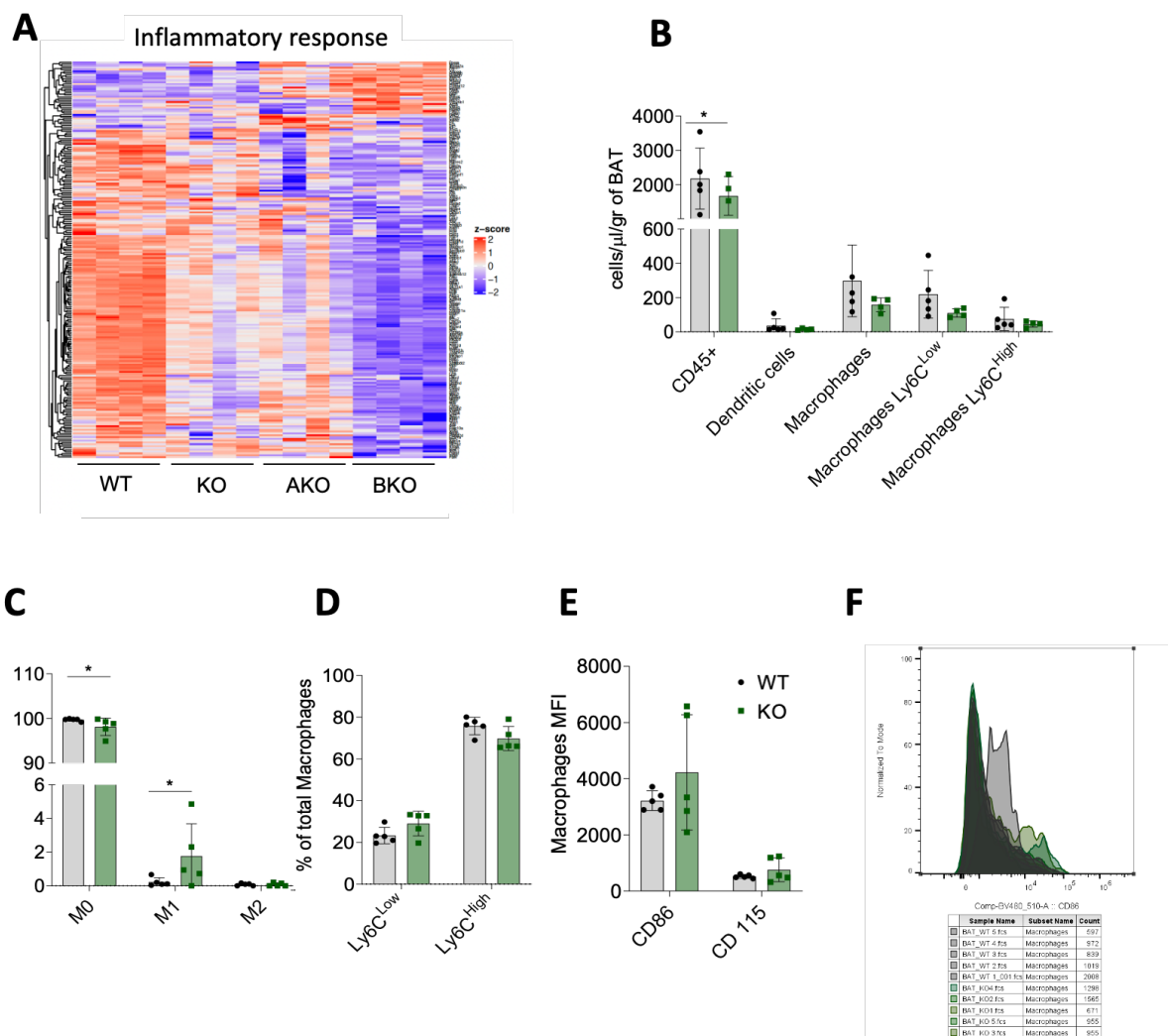
Figure 2.7 Inflammation and macrophage activation in BAT of CLPP knockout mice. *A: Heatmap showing relative z scores of genes belonging to the inflammation cluster in BAT of KO, AKO and BKO mice. B: FACS analysis showing composition of immune cells profile in the BKO mice, Student's t test, data are presented as means ± SEM N = 5 per group *p < 0.05. C: Analysis of macrophage subpopulation in BAT of BKO mice. Student's t test, data are presented as means ± SEM, N = 5 per group *p < 0.05. D. Analysis of macrophages expressing high or low Ly6C marker. E. Two sub populations of macrophages assessed. F: Intensity profile of macrophage markers assessed in C-E. Student's t test, data are presented as means ± SEM N = 5 per group. Student's t test, data are presented as means ± SEM, N = 5, *p < 0.05.*

The upregulation of macrophage activation genes prompted us to examine if this pro-inflammatory signature was due to brown adipocyte-specific responses or due to infiltration of macrophages and/or immune cells from circulation. To address this, we performed single-cell immunophenotyping of inflammation-related markers on isolated cells from BAT of BKO using FACS. We chose BKO as the model for this experiment since it would allow us to tease apart the BAT-intrinsic responses from other systemic factors due to absence of CLPP in other tissues. While the proportions of dendritic cells and macrophages remained relatively unchanged (Fig. 2.8B-F), we observed a significant increase in the activation state of M1 macrophages (Fig. 2.8C), accompanied by a slight decrease in M0 or inactivated macrophages (Fig. 2.8C). This shift suggested that even if immune cell infiltration may not be pronounced, their local activation status leaned towards a pro-inflammatory state.

Additionally, as a control in the same experiment, we aimed to identify if the pro-inflammatory phenotype in BAT was also being reflected in immune progenitor proliferation in the bone marrow, which is the first organ to respond to systemic inflammation and prepare the body for defense. We did not see any significant increase in progenitor populations in the bone marrow of BKO mice (Fig. 2.11A-D), thereby re-confirming that the inflammatory phenotype is BAT-autonomous.
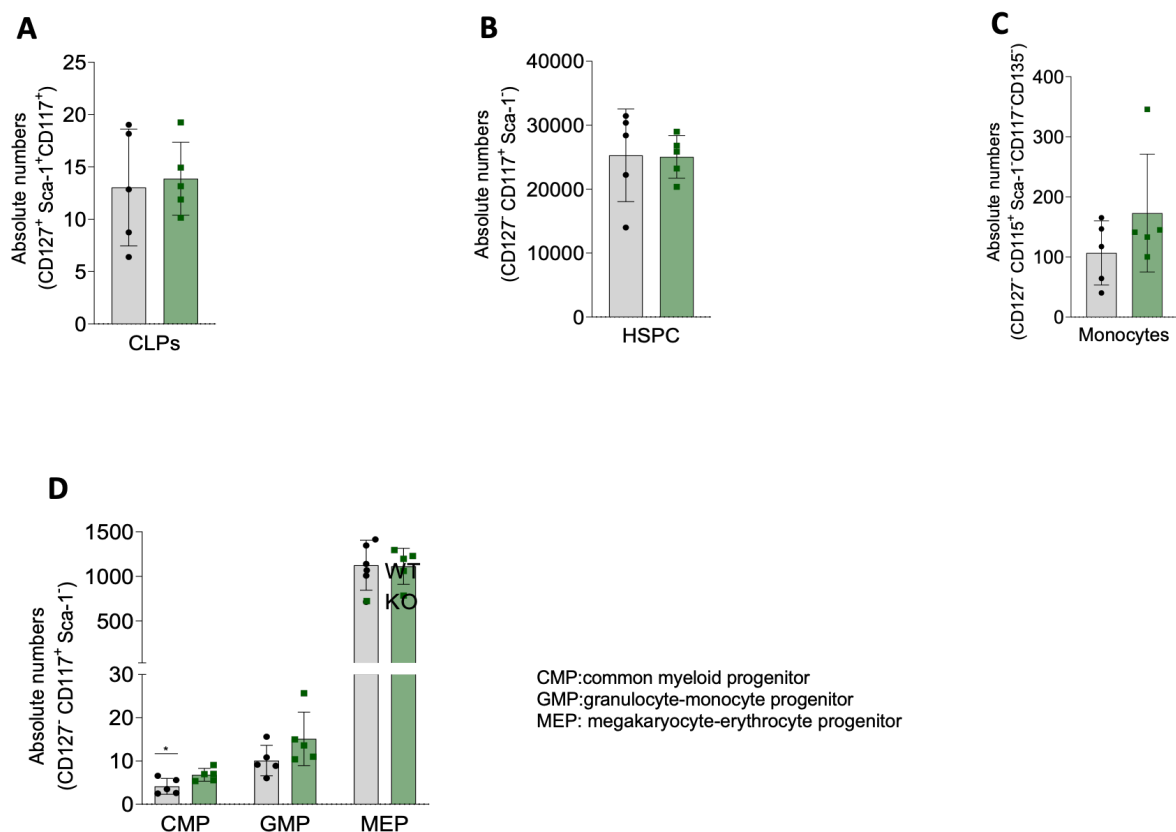
*Figure 2.8 FACS analysis of immune cells from bone marrow of BKO mice. A,B: Graph showing quantification of lymphoid and hematopoietic progenitor cells in BKO mice. Student's t test, data are presented as means ± SEM, N = 5. C,D: Graph showing quantification of monocytes and mentioned progenitor cells. Data presented as means ± SEM, N = 5, *p < 0.05. CLPs- Common lymphoid progenitors, HSPC- Hematopoietic stem cells progenitors, CMP- Common myeloid progenitors, GMP- Granulocyte-monocyte progenitor, MEP- Megakaryocyte+erythrocyte progenitor.*

To get insights into likely triggers for inflammation in BAT, we narrowed down our GSEA analysis by removing the systemic inflammation and cell death-related terms from our analysis and visualized the filtered genes of top enriched pathways in Volcano plots.
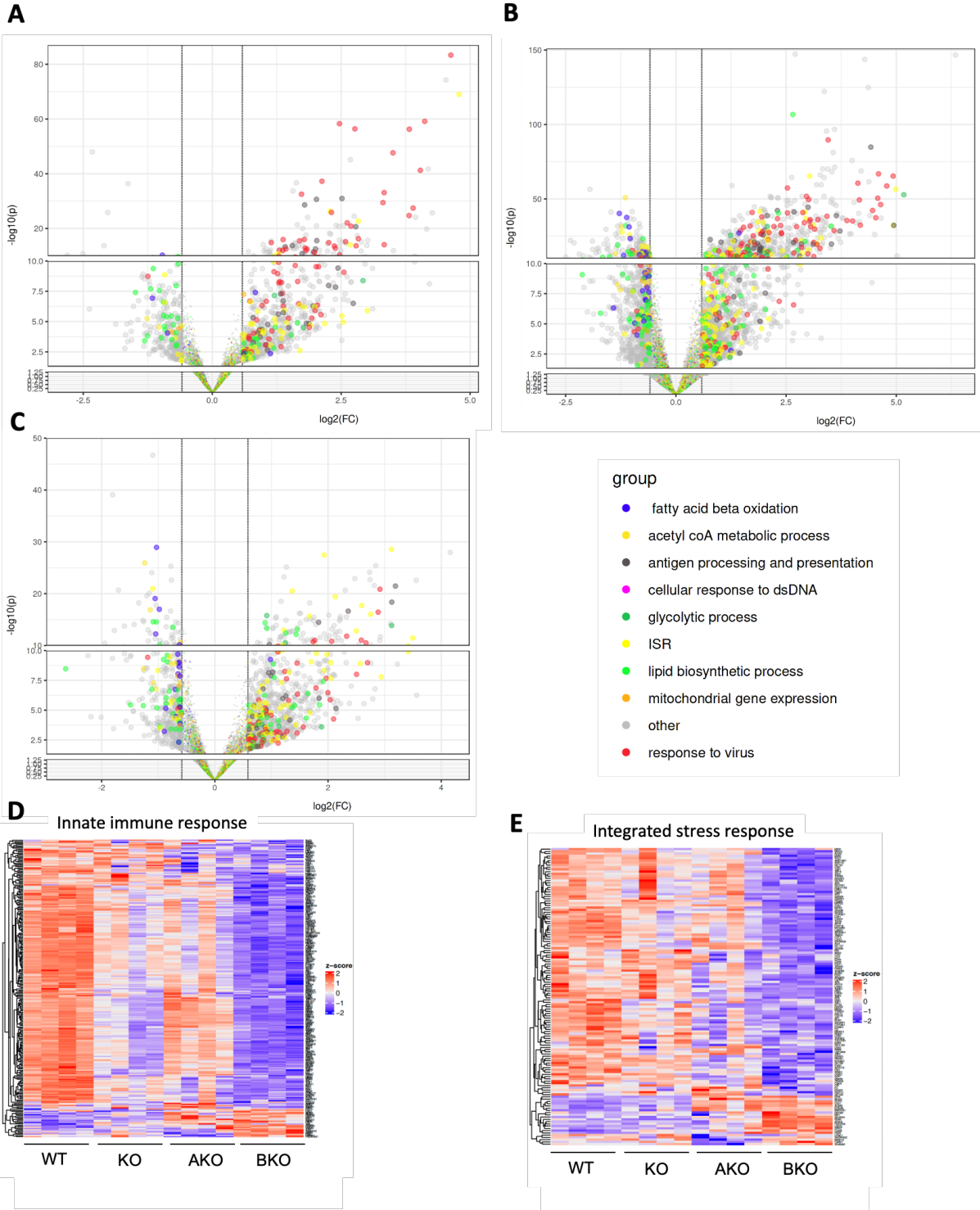
Figure 2.9 Innate immune response and ISR as potential triggers for BAT inflammation. *A-C: Volcano plots showing enriched pathways post filtering. D-E: Heatmaps showing innate immunity and ISR genes) which are ATF4/CHOP targets.*

As seen in Fig. 2.9A-C, the most of the filtered upregulated genes belonged to innate immune response (red dots) and ISR (yellow dots). Activated innate immune

response is a consistent feature of multiple CLPP knockout models, irrespective of the context. Since this was not a BAT-specific response and is rather, a more general effect of loss of CLPP, it is being addressed in an independent study in lab and is beyond the scope of this thesis. This drew our attention to ISR and stress pathways as being instrumental in BAT-intrinsic inflammation and whitening. In fact, ISR genes, which included both ATF4 and CHOP targets, were the highest upregulated genes in BKO (Fig. 2.9C), which once again pointed at the robustness of upregulated stress responses in BAT from CLPP knockout models.

Figure 2.10 Proteomic changes and functional enrichment of significantly changed proteins in proteomics of KO BAT. *A: Venn diagrams showing total number of significantly changed proteins in KO, AKO and BKO mice. B: Bargraph representing enriched terms in GSEA analysis of BAT transcriptome from KO mice. N=4 per genotype.*

Next, we assessed the global proteome-level changes in BAT from all the three mice models. We wanted to understand if the differences between fold changes of genes as seen in AKO (in comparison to KO and BKO) were also reflected in the proteome. Statistically significant changes in the steady state levels of proteins were observed for 344 proteins in KO (198-up and 146-down), 437 proteins in AKO (283-up and 154-down), and 385 proteins in BKO (246-up and 139-down) (Fig. 2.10A). GSEA-BP analysis of upregulated proteins revealed a significant enrichment in inflammation related pathways, mitochondrial gene expression, endothelial cells related terms and actin and cytoskeleton related processes (Fig. 2.10B). The downregulated proteins were mostly enriched in pathways involved in metabolism: carbohydrate and fatty acid metabolism, purine and general nucleotide synthesis (Figure 2.10B). As apparent from the Venn diagram, the extent of changes in protein abundances were relatively more homogenous between the three models (Fig. 2.10A), as compared to the transcriptome. This helped us to choose KO as the representative model for further investigations, since it had minimum of the common changes in both gene and protein abundance.

The significantly regulated genes showed similar patterns in transcriptome and proteome. We hence performed an integrated analysis of the significant changes in transcriptome and proteome, by applying FC thresholds for each and then mapping the gene ID to the corresponding protein ID. Many genes and proteins showed co-directional changes, and next to the innate immune response and inflammation pathways, cytoskeletal rearrangement, actin-related and muscle related proteins were the most abundantly enriched (Fig. 2.11A). This observation was of particular intrigue to us, since brown adipocytes develop from a myogenic lineage, which is in contrast to white adipocytes (which stem from adipogenic lineage) [231]. The substantial upregulation of cytoskeletal and muscle-related genes prompted us to contemplate the possibility of a unique de- differentiation of adipocytes, resulting in cells that display characteristics akin to muscle cells rather than typical fat cells, and were somehow contributing to the whitening phenotype.

Recently published studies employing single cell RNA-seq analysis in BAT showed that that the BAT is composed of a heterogenous population of cells, with pure adipocytes accounting for only 20% of the cell population, and muscle like cells abundance being around 15% of the population [231, 357]. To assess the relative proportions of cellular populations in our models, we employed a bioinformatic deconvolution approach to dissect our bulk RNA-seq data and encode it using the reference single-cell transcriptomic dataset by Shamsi *et. al.* [357]. The process involved disentangling the heterogeneous mixture of transcriptomic signatures into its constituent components using the single cell transcriptome data as reference dataset (Fig 2.11B). We received information from the authors about the marker genes for cell type assignments in the clusters identified by them. We then reproduced the single cell UMAP (Fig 2.16B) and transferred their cell type assignments to our clusters which were defined by the markers. Fig. 2.16C illustrates successful recreation of their single-cell data map using our algorithm, affirming the robustness of our deconvolution technique. Upon application of this algorithm to our bulk RNA-seq data, we generated a UMAP (Uniform Manifold Approximation and Projection) depicting the relative

proportions of distinct cell types for KO, in addition to the WT (Fig. 2.16D). Zooming in on the muscle-related cell types, we did not note an increased muscle cell population (Fig 2.12).
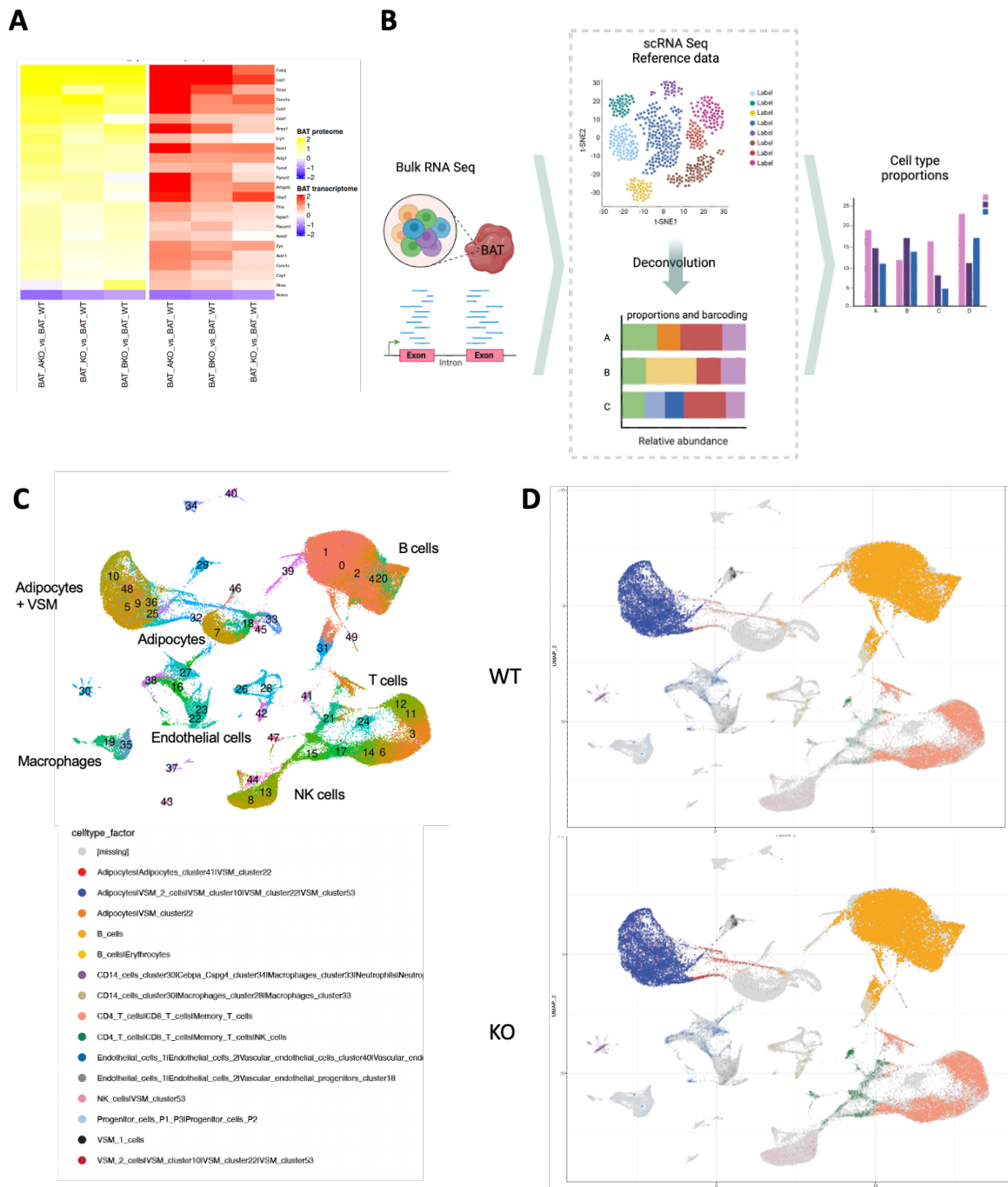
Figure 2.11 Deconvolution analysis reveals single cell maps of WT and KO BAT. *A: Heatmap showing combined transcriptome and proteome analysis of shared genes belonging to actin and cytoskeleton related GSEA terms. B: Representative pipeline for deconvolution analysis followed. C: Annotation of cell type assignments represented as UMAP. D: Deconvoluted data represented as UMAPs, with cell populations marked on the UMAP for BAT transcriptome data from WT and KO mice.*

Even though the relative cellular populations were not altered in the BAT, the possibility of adipocytes getting de-differentiated to a multipotent-like cell stage still existed. To address this question, we isolated the stromal vascular fraction (SVF) from

WT and KO BAT, which is cellular population from BAT enriched with preadipocytes, or multipotent adipose-specific stem cells.
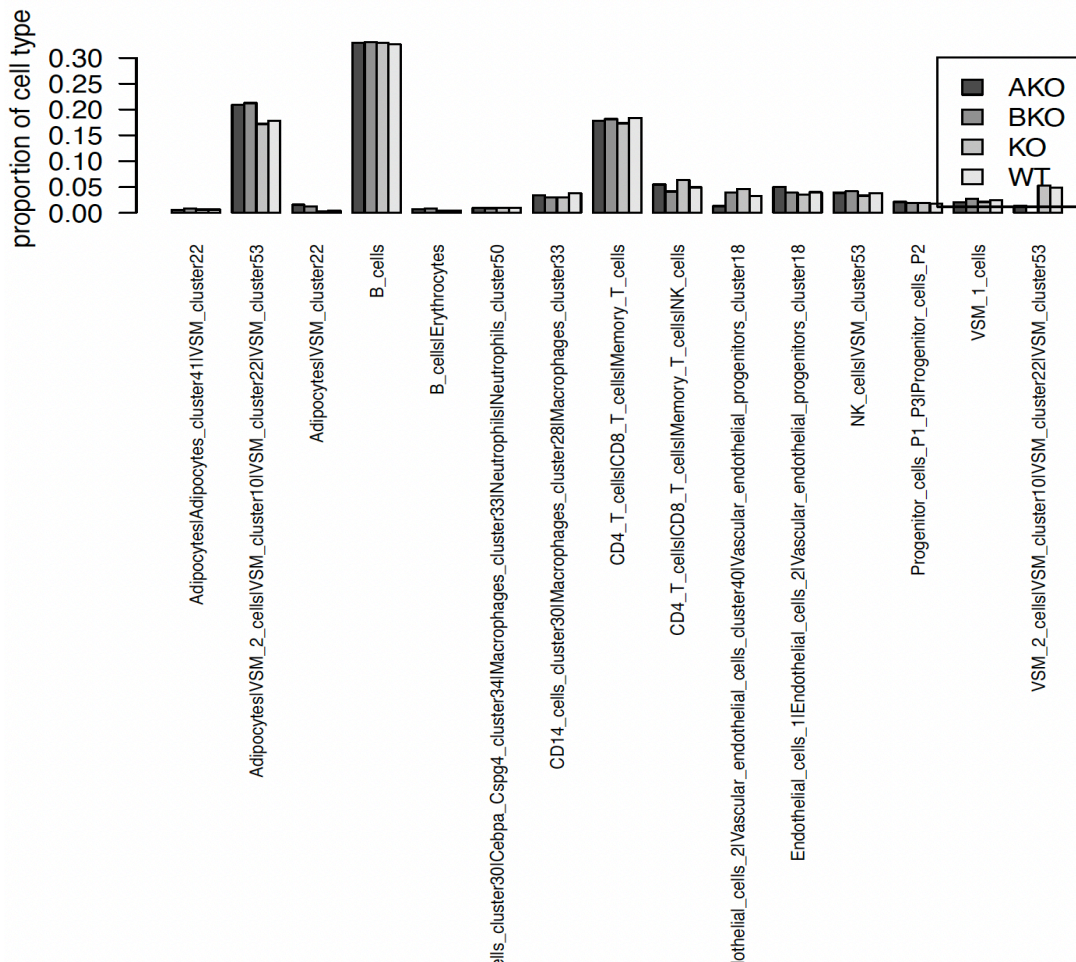
Figure 2.12 Relative proportions of designated cell types from deconvolution reveals no quantitative differences in muscle cell population

We performed proteomics on SVF from KO and WT BAT. Distinctive clusters of upregulated or downregulated proteins were seen in KO compared to the WT (Fig. 2.13). GO-BP analysis of significantly changed proteins using DAVID broadly revealed metabolic processes or mitochondria-related terms, which aligned with expectations for cells experiencing mitochondrial dysfunction (data not shown). However, despite some general differentiation factors like JUN-B being downregulated in KO, we did not see any factors directly linked to brown fat or muscle differentiation or cytoskeleton related genes to be altered. Muscle related proteins and transcription factors like MYOD1 were unchanged in abundance in SVF from WT and KO BAT. Since the SVF did not have any indications of a de-differentiated state of adipocytes, we dismissed this hypothesis and postulated that the upregulation of these genes could be due to cytoskeletal rearrangement within adipocytes due to CLPP loss. In our attempt to investigate the pattern of cytoskeleton in KO BAT from ultrastructural analysis by TEM, we did not see many changes with respect to connections of cytoskeleton to mitochondria or presence of ectopic actin fibres.
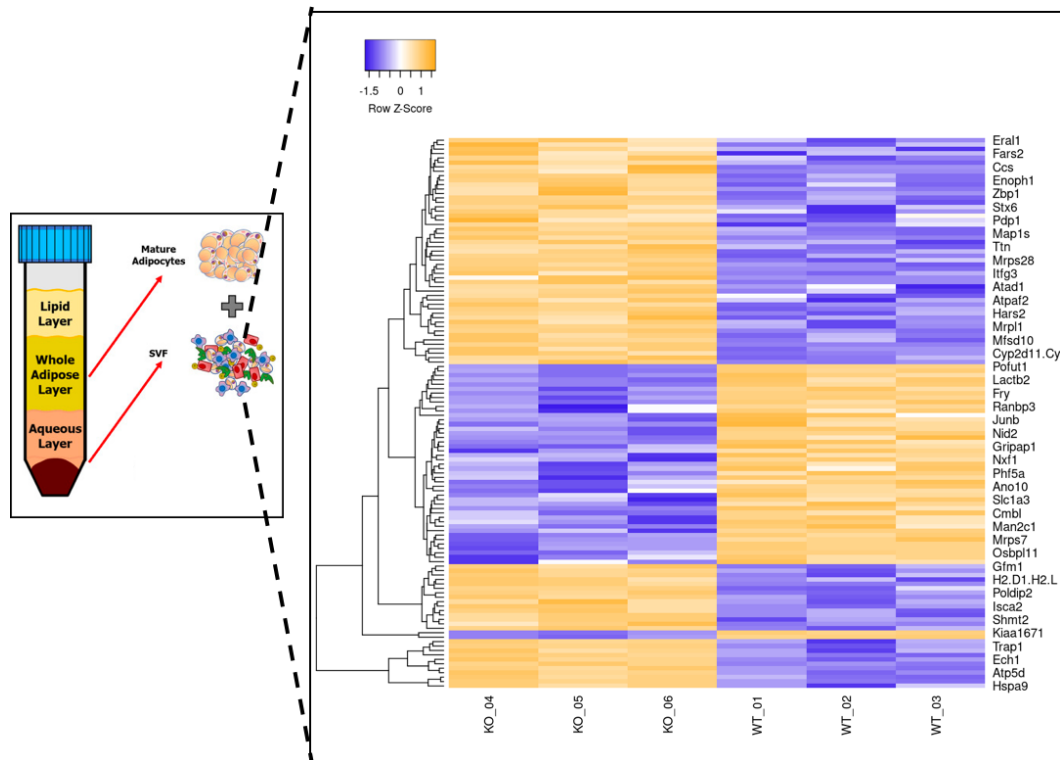
Figure 2.13 Heatmap representing SVF proteomics from WT and KO mice. *N=3 per genotype.*

We saw increased collagen clusters in KO BAT (data not shown), which is generally indicative of altered extracellular matrix due to a hypertrophic fibrous state and has been reported in previous study on whitened BAT [358, 359].

However, during the detailed TEM analyses, we pertinently observed the presence of indentations on the nucleus and concurrent association with mitochondria in KO BAT sections (Fig. 2.14A). The nuclear periphery was impinged by multiple mitochondria throughout the circumference (Fig. 2.14A). Even though there were no apparent contact sites with shared membranes observed between mitochondria and nucleus, the nuclear and mitochondrial membrane were closely positioned to each other. Zoomed in analysis also revealed that most often, these points of contact were juxtaposed between nuclear pores. To further validate the robustness of these observations, we quantified these mitochondria-associated nuclear deformations in WT and KO BAT sections (Fig 2.14B-C). The average number of contacts in WT was 1 (mean, 1.3, rounded off to 1) whereas the that in KO was 3 (mean, 2.89, rounded off to 3) (Fig. 2.14B). In fact, we recorded upto 10 regions of indentations in the nucleus by mitochondria in KO, which is unusually high when compared to WT (Fig. 2.29C). This prompted us to delve deeper into understanding the distribution and extent of these interactions.

We hence employed a 3D ultrastructural approach using serial sectioning and superimposition of sequential TEM images from KO BAT. We selected our region of interest with nucleus, lipid droplets and mitochondria at 4000X zoom and reconstructed a detailed 3D model of the distribution of lipid droplets, nucleus, and mitochondria in the KO BAT of CLPP knockout mice (Fig. 2.15A-D). This visualization clearly depicted multiple points of contact between mitochondria and the nuclear surface spanning

throughout the length of the nucleus and around the entire circumference (Fig. 2.15A-D).

A

B

C
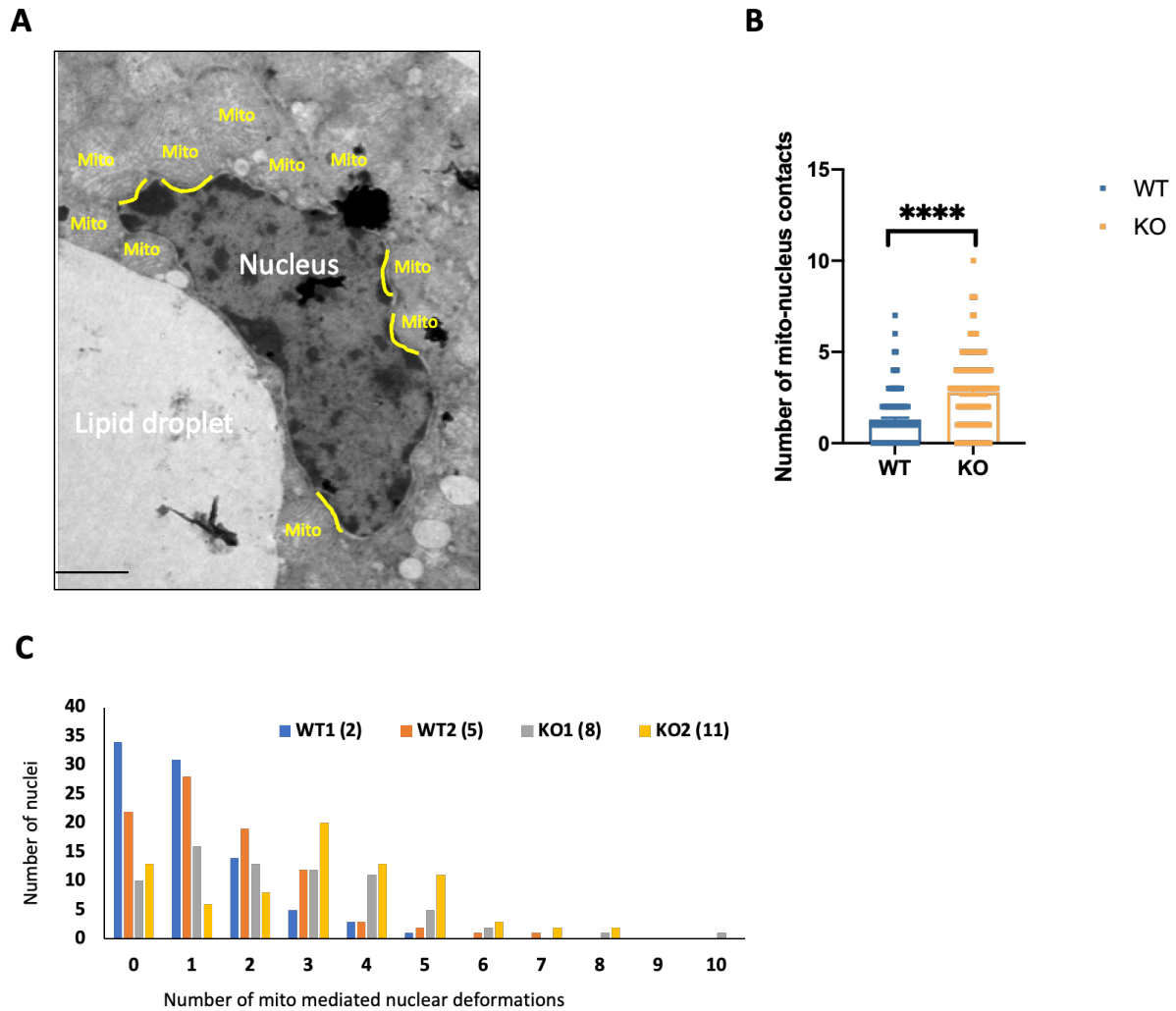
*Figure 2.14 KO BAT shows mitochondria-nucleus contacts and mitochondria mediated indentations on the nucleus. A: Representative TEM image showing nuclear and mitochondrial contact. Scale bar 1um, N = 2 per group. B. Graph showing quantification nuclear-mitochondrial contacts in BAT of KO mice. C: Distribution profile of number of mitochondria-nucleus contacts in WT and KO mice. Data presented as means ± SEM, N = 2, ****p < .0001.*

As apparently visible throughout our TEM analysis, there were significantly large instances of mitochondria associated with lipid droplets. In literature, it has been shown that these distinct population of lipid droplet-associated mitochondria differ from the cytoplasmic mitochondria (CMs) and are called peri-lipid droplet mitochondria (PDMs) [25]. The PDMs enable efficient shuttling of metabolites between mitochondria and nucleus and show greater association under conditions like starvation [25]. In order to understand whether there is more association between PDMs and lipid droplets in KO BAT, we manually marked the contact regions between mitochondria and lipid droplets and calculated the contact perimeter (Fig. 2.16A). A confounding factor for this analysis was that in KO BAT, the lipid droplets were not captured in their entirety in any of the frames, even at lowest magnification since they were very large in size. We hence decided to represent the contact perimeter as a percentage of the perimeter of the

entire mitochondria, which would still indicate the relative extent of contacts of PDMs with LDs.
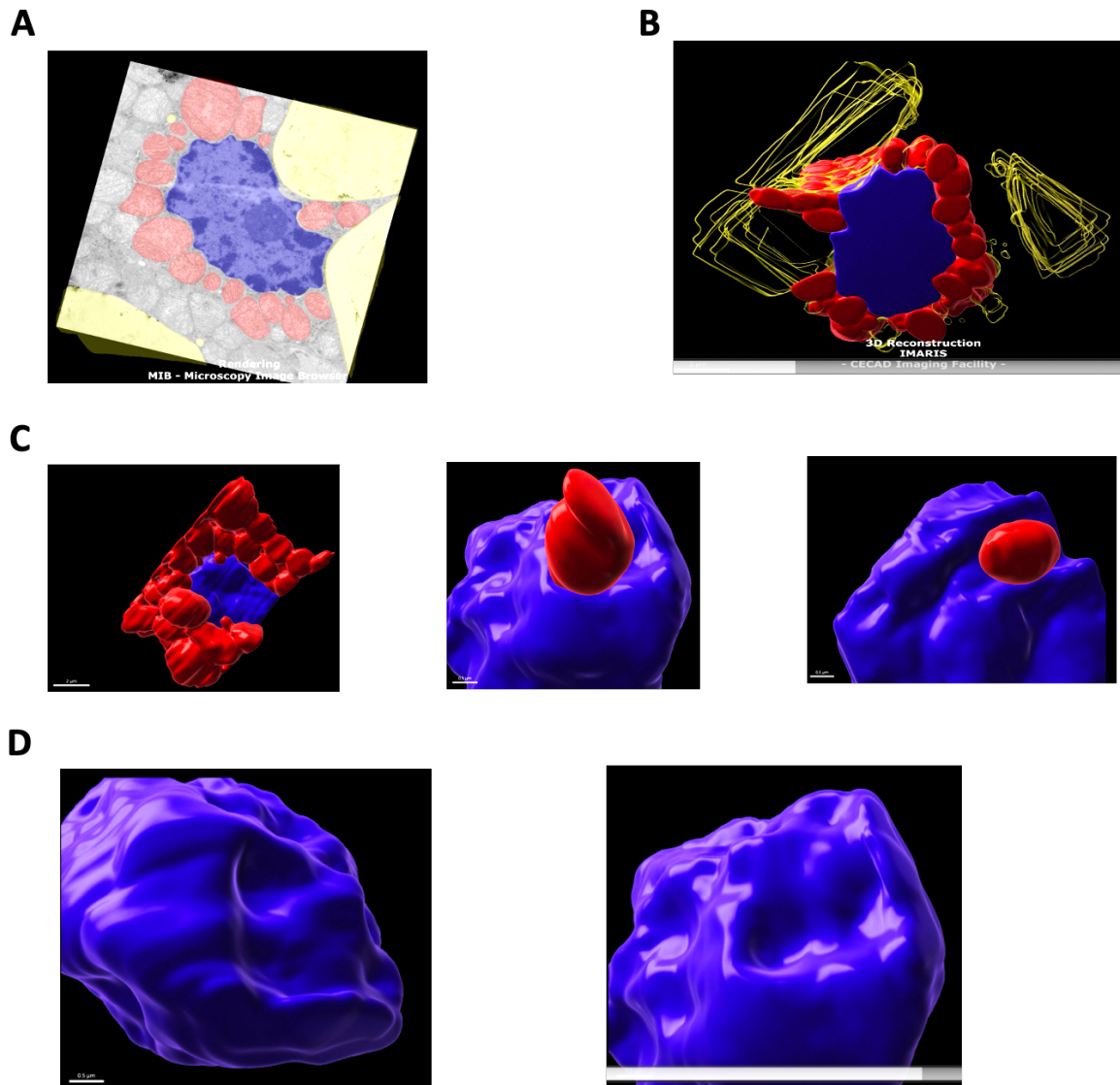
Figure 2.15 A-D: 3-D reconstruction of serial TEM images from KO BAT show pan-nuclear indentations.

There was no change in percent contact perimeter between KO and WT (Fig. 2.16B), and the overall perimeter and area of PDMs was also not significantly changed between WT and KO.

Next, we isolated the CMs and PDMs as separate populations from BAT and performed a BN-PAGE analysis to get a qualitative idea of the levels and distribution of respiratory chain complexes. Clear reduction in supercomplexes were seen in both CMs and PDMs from KO. However, there were only minor differences between CMs and PDMs (Fig. 2.17A-C). To get a complete picture of these organelle interactions, we subjected the isolated PDMs and CMs to organelle proteomic analysis. In total, 1507 proteins were detected, out of which, levels of 618 proteins were significantly changed amongst all the four comparisons.
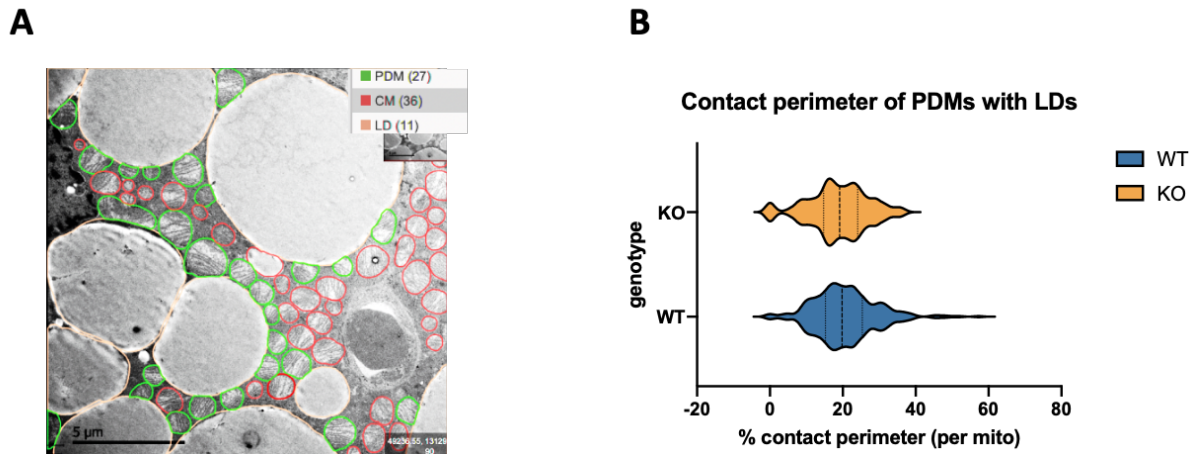
Figure 2.16 PDM contacts with LDs is unaltered in KO BAT. *A: Representative TEM image showing association of PDM with LD, and manual annotation of CMs, PDMs and LD. Scale bar 5um. B. Graph showing quantification of contact perimeter in BAT of KO mice. Data presented as means ± SEM, N = 2.*

As evident from the heatmap in Fig. 2.17D, distinct clusters represent CMs and PDMs, as well as WT and KO, with changes between each of the four combinations. However, since we had not seen major differences in contact perimeter of PDMs, and significant changes at levels of supercomplexes were absent in KO PDMs when compared to CMs, we decided not to perform further functional analysis of the proteome. We dismissed the hypothesis that altered function of PDMs in CLPP KO BAT was causal for whitening. However, we made a noteworthy observation from the proteome of KO PDMs. GO analysis of upregulated proteins in KO PDMs revealed nucleus and mRNA processing related terms. This further indicated (albeit indirect) the possibility of nucleus being co-purified with the PDMs only in KO and not in WT. Taken together, we concluded that even though PDM abundance may not be altered between WT and KO, there could be the presence of *tripartite organellar interactions*, involving the nucleus, LDs and mitochondria, which was very intriguing for us for being pursued further.
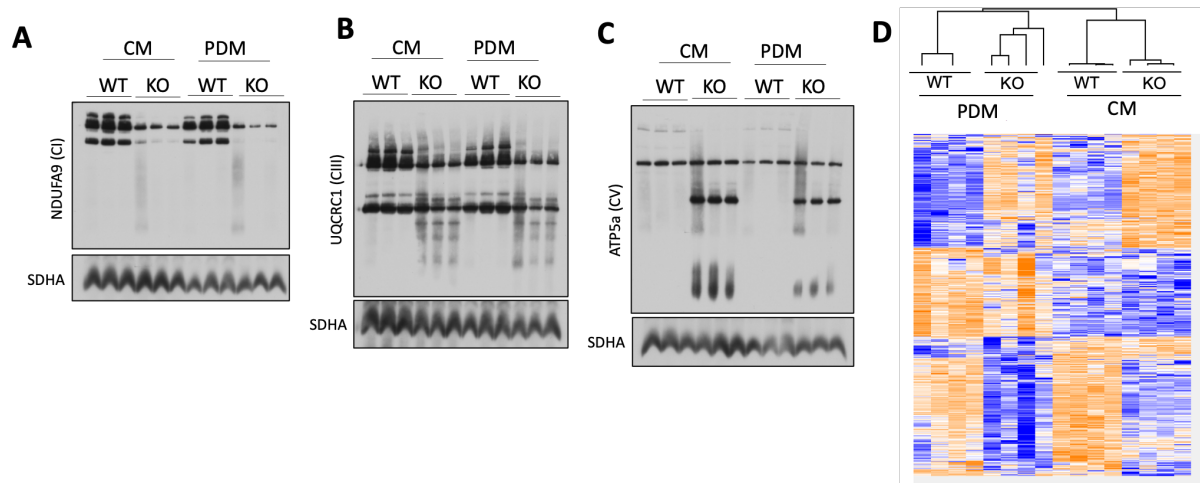
Figure 2.17 Analysis of isolated CMs and PDMs from BAT. *A: Immunoblot of NDUFA9 post BN-PAGE analysis showing CI, N = 3. B: Immunoblot of UQCRC1 post BN-PAGE analysis showing CIII, N = 3., C: Immunoblot of ATP5a post BN-PAGE analysis showing CV, N = 3. D: Heatmap showing the proteome level differences between WT and KO and CMs and PDMs. Hierarchical clustering was performed to identify the distinct clusters belonging to each category.*

At this juncture, we were prompted to delve deeper into the functional relevance of the interplay between these organelles and assess if it had consequence on BAT whitening. Typically, associations between different organelles, specially, LDs and mitochondria, LDs and nucleus, nucleus and mitochondria, actin and nucleus and cytoskeleton and mitochondria - occur to facilitate rapid exchange of signaling molecules and metabolites. To understand how our observations so far on inter-organellar crosstalk connected to metabolism in BAT, we started by performing an unbiased metabolome analysis from KO BAT, and included AKO and BKO as well in the analysis to get a comparative view of the similarities and differences between the three models. In total, 257 metabolites were detected in all three models. Out of these, 39 metabolites were significantly changed (28-up and 11-down) in KO BAT, 57 metabolites were significantly changed in AKO (39-up and 18-down) and 37 metabolites were significantly changed in BKO (34-up and 3-down) (Fig. 2.18A).

As depicted in the volcano plots in Fig. 2.18B-D, the most abundant changes in metabolites were seen in AKO, followed by BKO and then KO. AKO showed the accumulation of highest number of lipid and carnitine species, which were derived from both straight chain and branch chain fatty acids (Fig. 2.18B) and which was reminiscent of largest degree of whitening in AKO compared to KO and BKO (Fig. 2.2). Accumulation of carnitines was consistent across all the three knockout models compared to WT and this has previously been shown to be associated with perturbations in key processes like lipogenesis, lipolysis, and beta oxidation of fatty acids [360]. BAT from BKO did not show many metabolite changes, except for the significant accumulation of 2-hydroxyglutarate (2-HG) and ascorbic acid 2-sulfate. 2-HG is a well-known oncometabolite that is most commonly accumulated in tumours harbouring IDH1 (isocitrate dehydrogenase 1) mutations [361]. Ascorbic acid 2-sulfate is a metabolite of ascorbic acid (Vitamin C) that has been shown to act as an antioxidant, as well as protect mitochondrial DNA from damage [362]. The metabolomics results hence prompted us to examine the functional metabolic changes in KO BAT in further detail.

We turned our attention to examining the functional output from BAT in terms of oxygen consumption. Respiration was measured on BAT tissue lysates from WT and KO with OROBOROS-Oxygraph. Surprisingly, we observed no significant differences in oxygen consumption between the lysates under basal, ADP-stimulated conditions in the presence of succinate, or upon FCCP addition (Fig. 2.19A). This was an interesting observation for us since we had earlier reported lower oxygen consumption by isolated KO mitochondria (Fig. 2.5) and now we observed a reversal of the phenotype at the tissue level. These results taken together, indicated that the increase in mitochondrial numbers was possibly compensating for loss of respiratory supercomplexes and was an adaptive mechanism at the tissue level.

However, an interesting observation emerged when upon examination of *ex vivo* lipolysis in the tissue. As a readout for lipolysis, we measured the glycerol release from the tissue lysate under both basal and norepinephrine (NE) and forskolin - stimulated conditions. Both these compounds are beta adrenergic agonists and stimulate the sympathetic nervous system (SNS), which directly activates BAT to prepare it for thermogenesis.
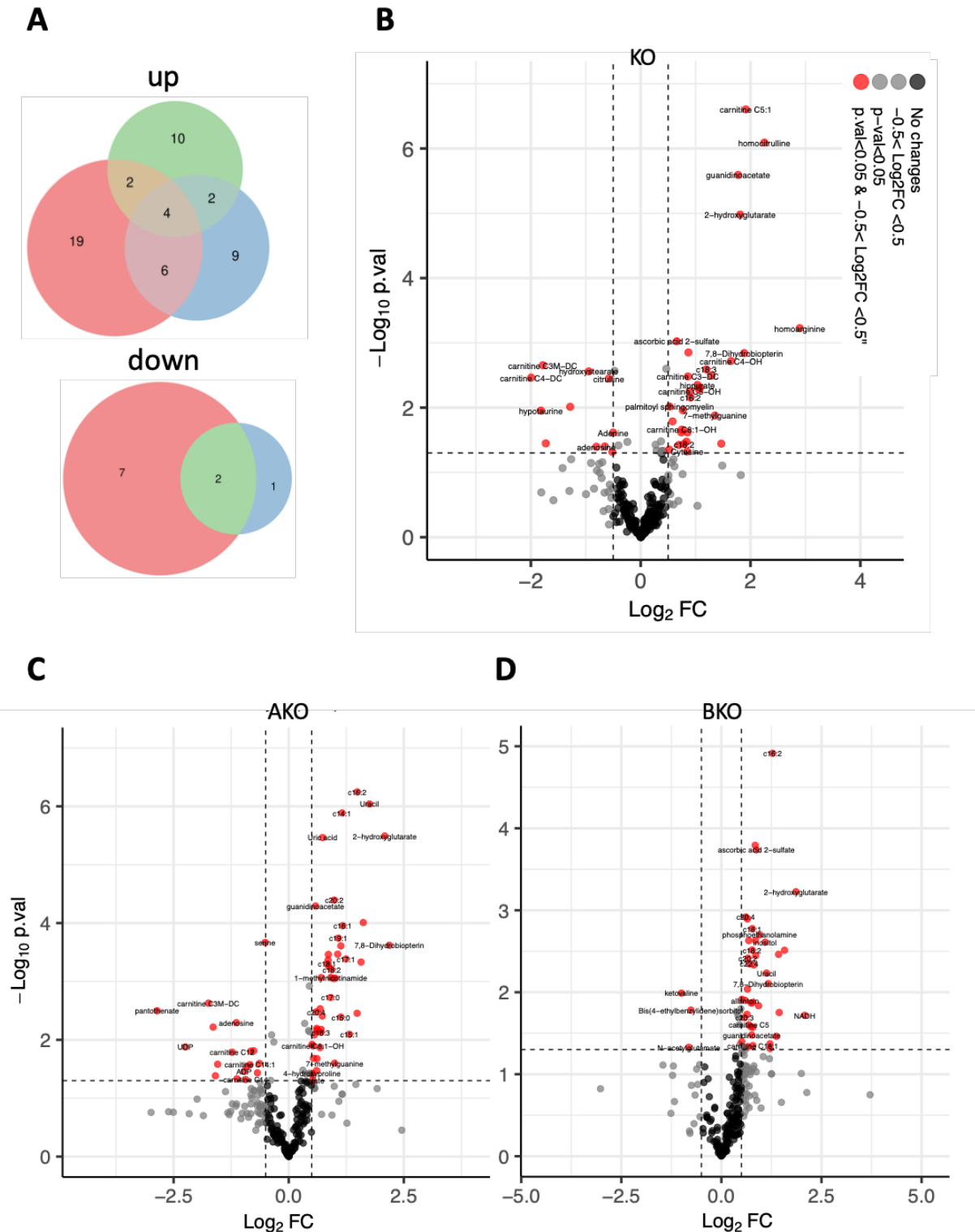
Figure 2.18 BAT metabolomics from KO, AKO and BKO mice. *A: Quantitative changes in metabolites in BAT of KO, AKO and BKO mice. B-D: Volcano plots showing significantly changed metabolites in KO, AKO and BKO mice respectively. N=4 per genotype.*

NE and forskolin treatment typically triggers lipolysis in BAT where lipid droplets are instantaneously broken by lipolysis to release fatty acids, which are channelized into ETC for energy expenditure via uncoupling – and is accompanied by release of glycerol from breakdown of fatty acids. We found a significant 12% decrease in glycerol release in KO lysates compared to the WT under both baseline and stimulated

conditions (Fig 2.19B). The reduced lipolysis provided partial insight into the reason behind the larger lipid droplets observed in the KO BAT.
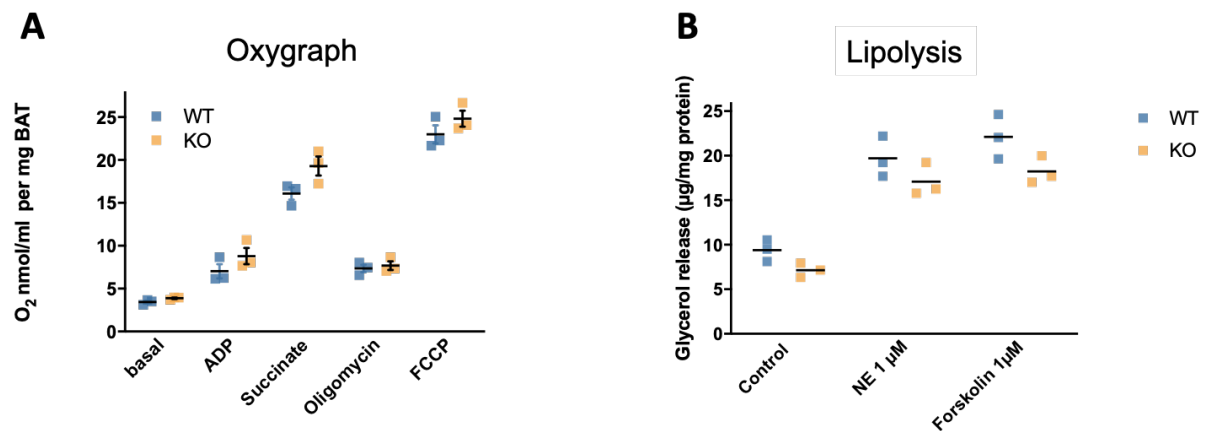
Figure 2.19 ex vivo respiration and lipolysis analysis of WT and KO BAT lysates. *A: Graph showing quantification of O_2 consumption in presence of different substrates of BAT tissue lysates from WT and KO mice, Data presented as means ± SEM, N = 3. B: Graph showing quantification of lipolysis (glycerol release) in BAT of WT and KO mice. Data presented as means ± SEM, N = 3.*

After the comprehensive characterization of BAT remodelling upon CLPP loss, we next delved into uncovering the mechanism behind whitening of BAT. For this, we generated a primary cellular model from BAT tissue. We isolated preadipocytes from WT and KO BAT and immortalized them using SV40 large T antigen. The *in vitro* differentiated mature adipocytes (henceforth referred to as BATi cells) mimicked a tissue-like state which was confirmed with the accumulation of larger lipid droplets in KO cells compared to WT (Fig. 2.20A). This was quantified with FACS analysis of BODIPY (a stain specific for neutral lipids) -stained cells (Fig. 2.20B). This gave us a robust model to understand the brown adipocyte- specific role of CLPP loss, since the phenotypes observed in BAT at the tissue level could stem from a combination of effects from the heterogenous cellular populations harboured within the tissue.
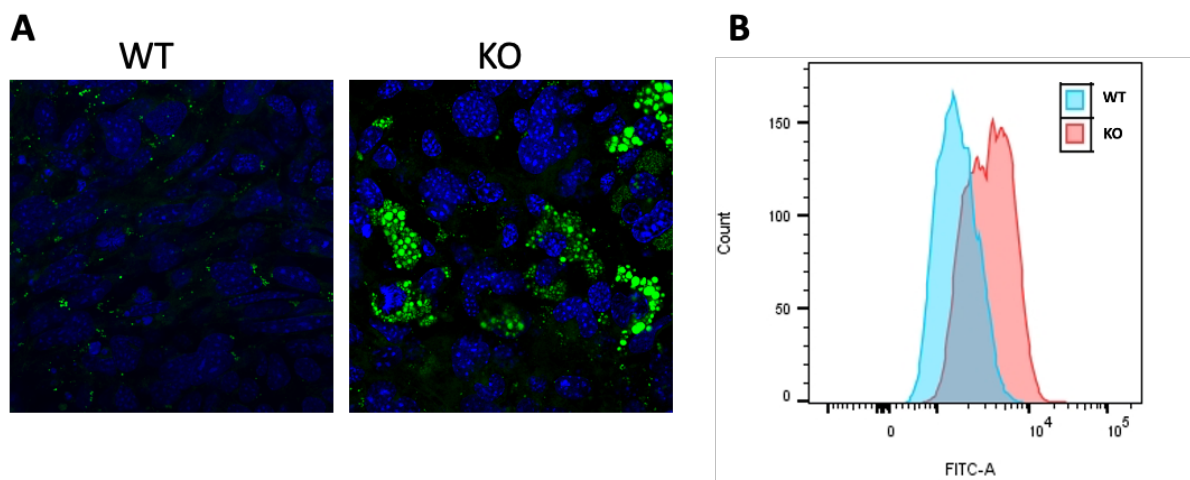
Figure 2.20 BATi cells serve as a faithful cellular model of CLPP KO BAT. *A: Representative confocal images of cultured and in vitro differentiated WT and KO BATi cells, stained with DAPI to mark nuclei and BODIPY to mark lipid droplets. Scale bar 100um. B: Intensity distribution of BODIPY-stained BATi cells in FACS analysis.*

To understand the points of similarities between BATi cells and tissues, we performed proteomic analysis on WT and KO BATi cells. A total of 3631 proteins were detected, out of which the steady state levels of 555 proteins were significantly changed (325-up and 231-down) in KO cells. As seen in the heatmap, distinct clusters of proteins were seen to be differentially abundant in WT and KO BATi cells (Fig. 2.27). GO BP analysis using DAVID revealed that the major terms that were enriched for upregulated proteins involved inflammation and metabolism. The major terms enriched for downregulated proteins were microtubule and cytoskeleton (data not shown). Amongst the enriched metabolic pathways, fatty acid biosynthesis, lipid transport, branch chain fatty acid metabolism and ATP synthesis related terms were dominant. Additionally, steady state levels of starvation related proteins were also significantly high. These results closely mirrored the major changes in proteome observed in the CLPP knockout BAT tissues.
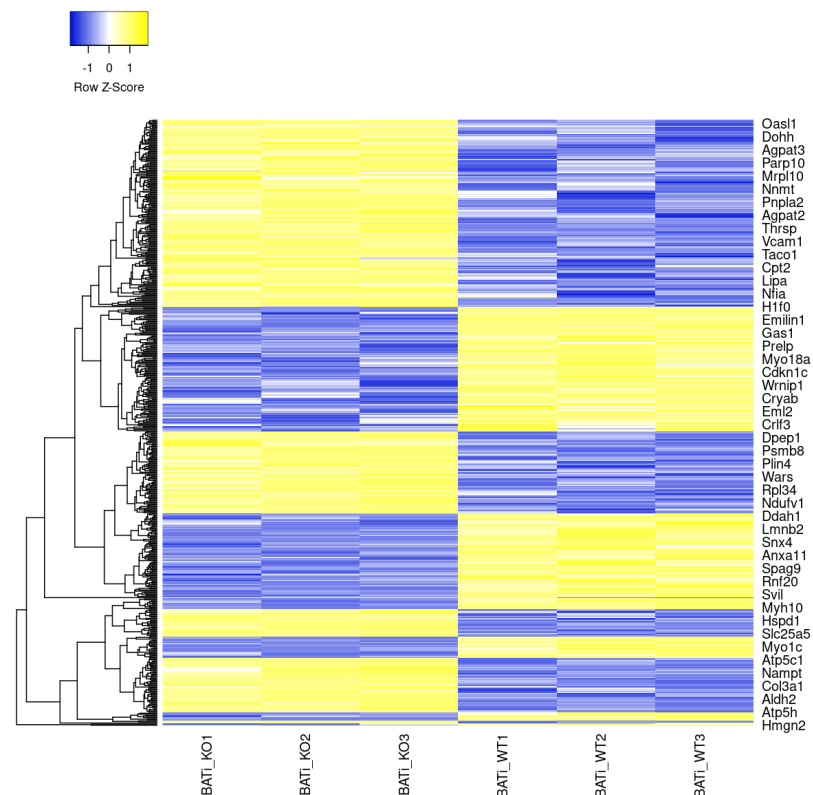
Figure 2.21 Heatmap of proteins with significantly changed abundances in proteomics of WT and KO BATi cells.

Next, to put the major observations from proteomics into functional context and to characterize the respiratory output of the cells, we measured the oxygen consumption in WT and KO cells, both pre and post differentiation, using Seahorse bioanalyzer. We found no significant differences in basal and maximal oxygen consumption between WT and KO cells, including both preadipocytes and differentiated cells (Fig 2.22A-C). However, a neat observation emerged during the assay. Following the addition of oligomycin, oxygen consumption exhibited a steep decline in preadipocytes, indicating coupled respiration in mitochondria (Fig 2.22A). In

contrast, in differentiated adipocytes, the drop in oxygen consumption was less pronounced with a low slope, indicating significant uncoupling (Fig. 2.22A). This functional demonstration of uncoupling in cultured differentiated BATi cells, attributed to the presence of the protein UCP1, and 2.5-fold increase in UCP1 steady state levels in KO BATi proteome further confirmed the efficacy of the differentiation process. In conclusion, our findings at the cellular level paralleled the observations made at the tissue level (Fig. 2.22), indicating no significant differences in respiration between WT and KO. Furthermore, we conducted a fatty acid oxidation assay using palmitate as a substrate and found no functional differences in beta-oxidation capacity between WT and KO, including both preadipocytes and differentiated adipocytes (Fig 2.2D).
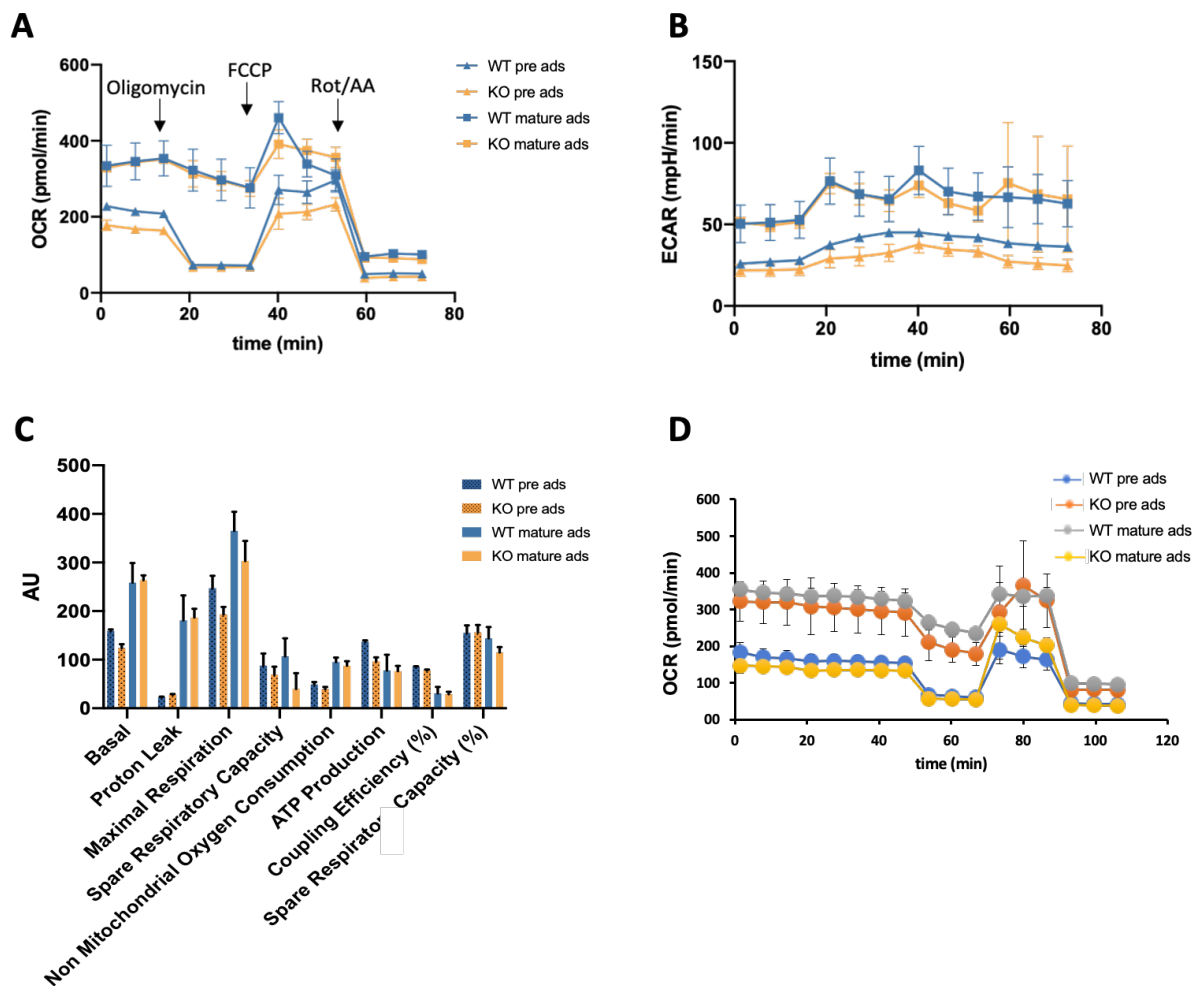
Figure 2.22 KO BATi cells show normal respiration. *A,B: Graph representing trace of OCR and ECAR in mentioned cell types. Data presented as mean± SEM, N = 3. C: Graph showing quantification of metabolic parameters derived from A, Data presented as mean ± SEM, Student's T test, N=3. D: Graph representing trace of OCR using palmitoyl carnitine as FAO substrate in mentioned cell types. Data presented as mean± SEM, N = 3*

In our previous experiments, we had speculated increased numbers of mitochondria in BAT of KO mice to be the underlying cause for normal tissue-level respiration (Fig. 2.3B). We were intrigued to examine if this was also reflected in KO BATi cells. We compared the steady state levels of Mitocarta3.0 proteins (mitochondrially localized protein database) from our proteomics data and as indicated

by the heat map in Fig. 2.23, we observed an increased abundance of majority of the detected mitochondrial proteins. This observation provided a plausible explanation for not observing a diminished respiratory output at cellular level, and matched with the observations that were made in the tissues.

Since the cells phenocopied the tissues so far in terms of respiratory output and whitening, we next examined whether mitochondrial dysfunction (and stress) induced
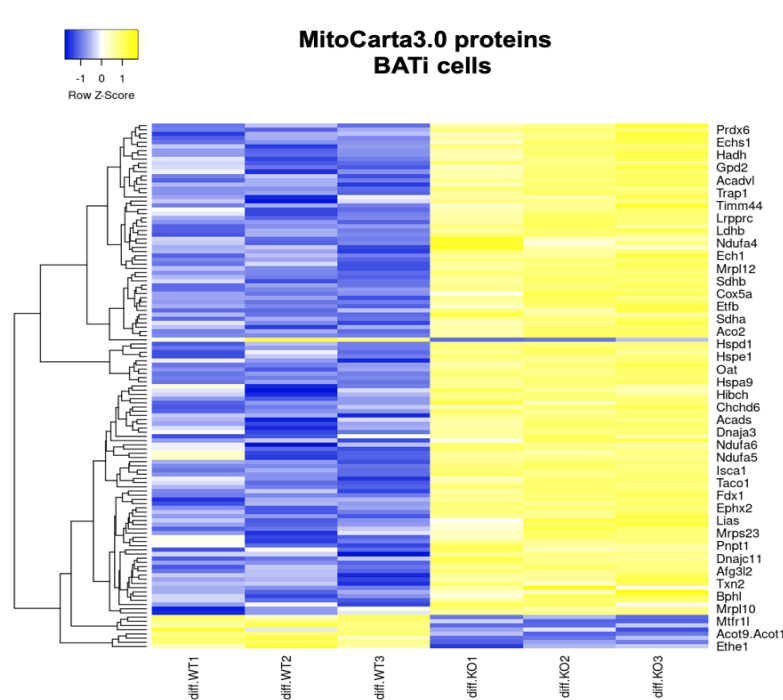
Figure 2.23 MitoCarta proteins in KO BATi cells are upregulated.

metabolic rewiring was evident in KO BATi cells. We performed metabolomics on WT and KO BATi cells to map adipocyte- specific changes in metabolites. 216 metabolites were detected in total (Fig. 2.24A) and interestingly, many more metabolites were differentially enriched in KO BATi cells compared to the KO BAT tissue. This could possibly be because the cultured cells are one homogenous cell type and unlike the tissue, do not have presence of non-adipocyte cells.

As shown in Fig. 2.24A-B, multiple metabolites corresponding to starvation were enriched. The increased metabolites belonged to purine and pyrimidine metabolism, glycolysis and lipid metabolism (including carnitines). Only 20 metabolites were downregulated and interestingly many of them were amino acids like proline, glycine, asparagine and isoleucine. The crosstalk between amino acid metabolism and mitochondrial dysfunction is gaining increased relevance in the context of metabolic pathologies since out of the 20 amino acids, the metabolism of 17 amino acids is dependent on mitochondrial enzymes [363]. Additionally, BCAA degradation occurs in the mitochondrial matrix and impaired amino acid metabolism has been correlated with mitochondrial diseases [363]. The prominent changes in abundance of amino acids in KO BATi cells indicated CLPP loss mediated metabolic rewiring.

We next performed KEGG pathway enrichment analysis on integrated proteome and metabolome data. Significantly changed proteins were annotated to the KEGG pathways and the corresponding metabolites were mapped to the pathway.
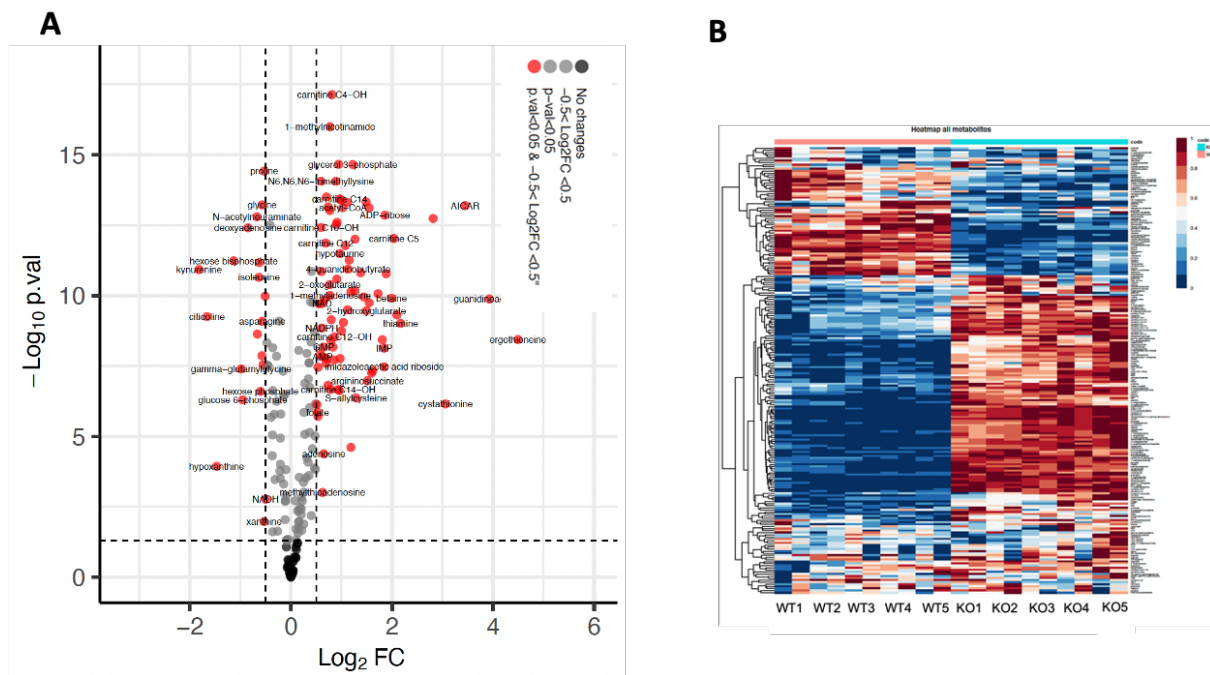
Figure 2.24 Metabolomics of BATi cells. *A: Volcano plot showing significantly changed metabolites in KO BATi cells compared to WT cells. B: Heatmap representing the relative abundances of changed metabolites between WT and KO mice. N=5 per genotype.*

As shown in Fig.2.25A-B, the enriched pathways included OXPHOS, thermogenesis, fatty acid biosynthesis and breakdown, cancer metabolism, as well as terms related to mitochondrial dysfunction mediated metabolic rewiring like one carbon cycle, BCAA metabolism and pentose phosphate pathway. Purine and pyrimidine metabolism, fatty acid degradation and BCAA degradation were the most enriched pathways and the combined analysis for BCAA degradation is depicted in Fig.2.25C. The enzymes in the BCAA degradation pathway are increased (green rectangles) whereas the intermediate metabolites of the pathway are depleted (red circles) (Fig.2.25C), thereby indicating an increased flux through the pathway.

We next consolidated omics data from tissue and cells to get mechanistic hints linking mitochondrial dysfunction (and stress) and BAT whitening. To narrow down to common metabolite features between BAT tissue and BATi cells, we performed two kinds of combined analysis – first, we combined significantly enriched metabolites from BAT tissue from KO, AKO and BKO (Fig. 2.26A) (enrichment of only five metabolites) and second, we did a combined analysis of normalized metabolites from BAT KO tissue and BATi KO cells (Fig. 2.26B). A very interesting metabolite, 2-HG stood out as a common hit in both the integrated analysis (Fig. 2.26A-B). All the knockout BAT tissues had approximately 4.3-4.8 fold increase in the levels of 2-HG and the KO BATi cells had a 4.5 fold increase in 2-HG steady state levels (Fig. 2.27A-B). We found that 2-HG was not accumulated in cultured KO preadipocytes, thereby revealing that this was specific to mature adipocytes and that its production was possibly governed by

the fluxes within adipocytes. In addition, analysis of metabolites released into the media using Capture and extracellular Release (CORe) measurements also revealed increased levels of 2-HG (Fig. 2.27C).
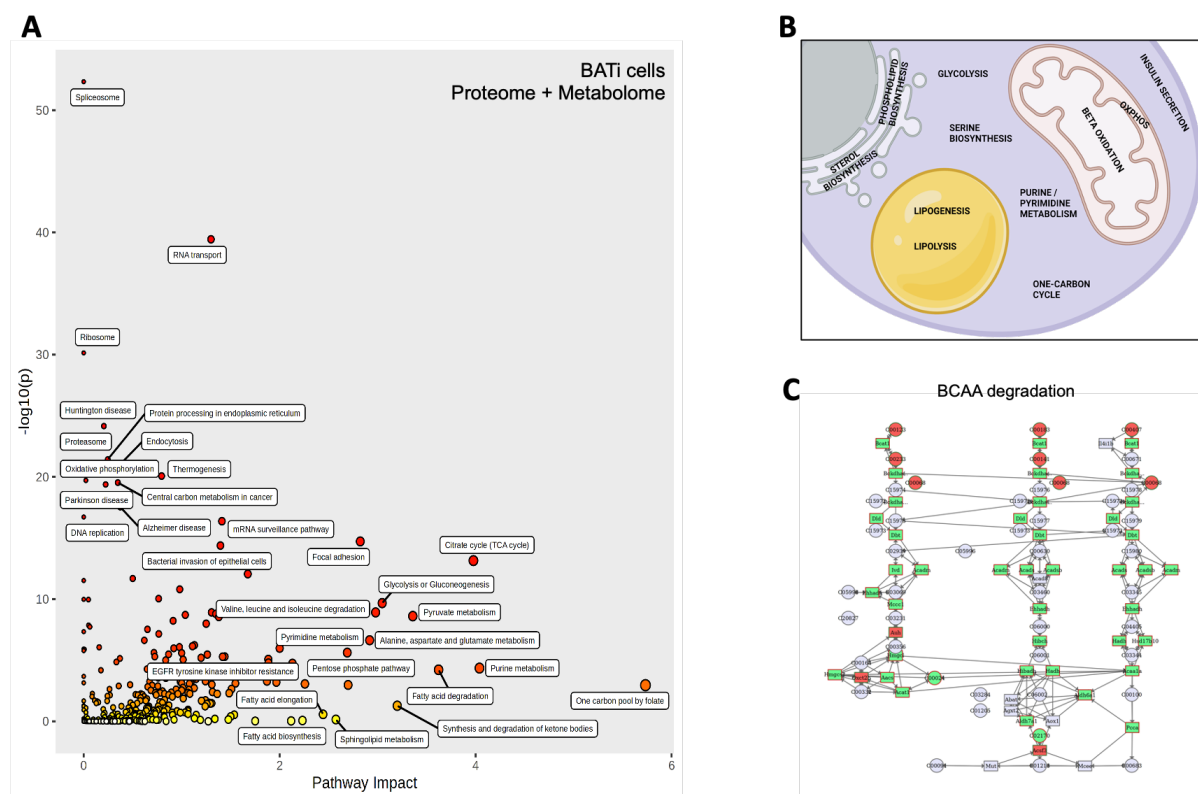
Figure 2.25 KEGG pathway integrated analysis of combined proteome and metabolome analysis of BATi cells *A: Integrated analysis of proteome and metabolome of BATi cells showing major enriched pathways. B: Representative image of altered pathways in KO BATi cells. C: KEGG pathway representation of BCAA degradation as integrated proteome and metabolome analysis.*
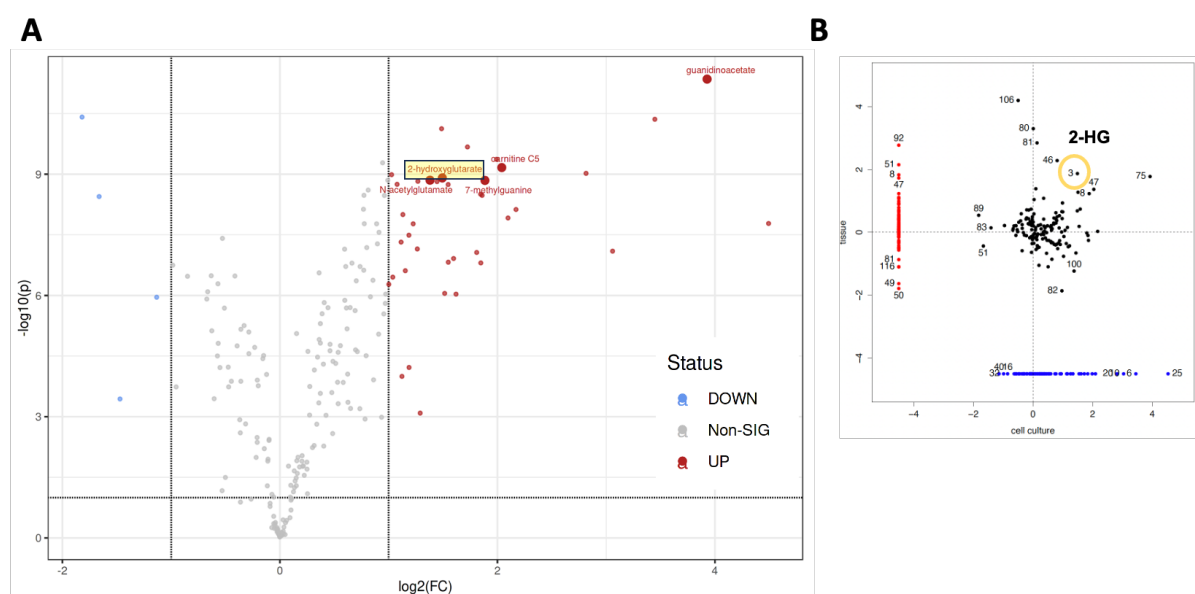
Figure 2.26 Combined metabolome analysis from different models of CLPP knockout BAT. *A: Volcano plot showing significantly changed metabolites in combined analysis of metabolomes of BAT from KO, AKO and BKO mice. B: Graph showing combined analysis of metabolome of BAT KO tissue and BATi KO cells, red colour representing metabolites enriched only in BAT KO tissue, blue colour representing metabolites enriched only in BATi cells and black dots representing metabolites changed in both KO tissue and cells.*

When the CORe analysis was repeated in cells cultured with labelled glutamine, we also saw a time dependent increase in release of 2-HG from cells (Fig. 2.27B). However, the released 2-HG was non labelled, thereby indicating that the source for this was possibly glucose and not glutamine (Fig 2.27B). This consistent elevation and release of 2-HG suggested an intrinsic metabolic perturbation associated with the loss of CLPP across BAT from all the different knockout models and BATi cells assessed so far.
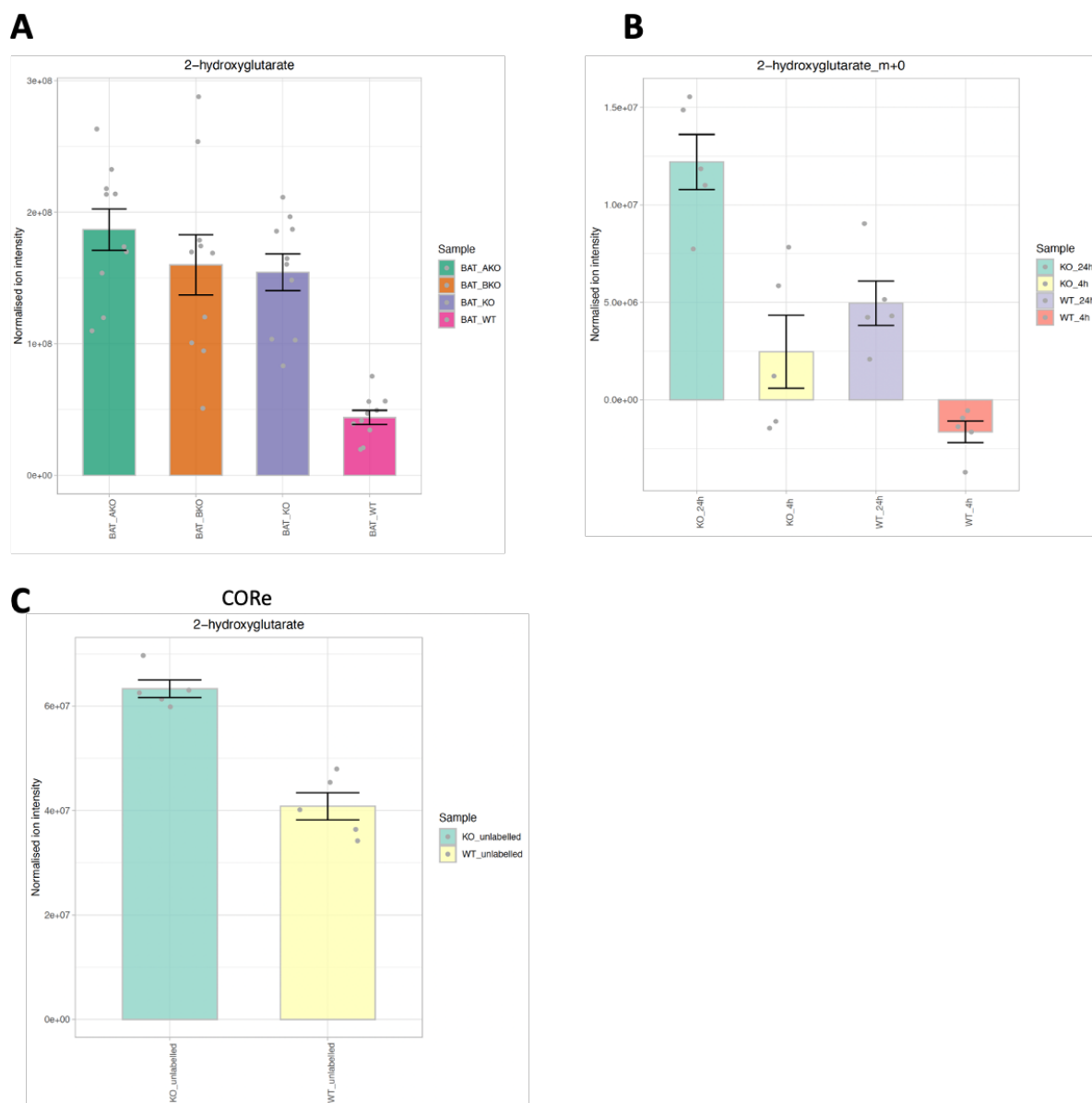
Figure 2.27 Accumulation and Release of 2-HG from BATi KO cells.

*A: Graph showing 2-HG levels in BAT from WT, KO, AKO and BKO mice. Data presented as mean +- SEM, Student's T test, *p < 0.05. B: Graph showing time dependent 2-HG release in WT and CLPP KO BATi cells treated with labeled glutamine. Data presented as mean ± SEM, Student's T test, *p < 0.05. C: CORe analysis showing levels of 2-HG in unlabeled media from cultured WT and KO cells. Data presented as mean ± SEM, Student's T test, *p < 0.05.*

2-HG is an interesting metabolite because it has been implicated in various cellular processes and disease contexts. Its dysregulation is associated with oncogenesis [364] epigenetic modifications [365], and metabolic disorders [366],

making it a subject of significant scientific interest and investigation. Notably, 2-HG has been implicated as an oncogenic metabolite particularly in cases associated with mutations in isocitrate dehydrogenase (IDH) enzymes [367]. In one study, 2-HG has also been shown to be generated through the non-canonical activity of human PHGDH, which converts α-ketoglutarate (α-KG) to 2-HG [368].

Considering that our transcriptome and proteome data had revealed upregulated ATF4 target genes, and that PHGDH is a major enzyme in the serine synthesis pathway that is generally activated as a part of mitochondrial dysfunction induced metabolic rewiring, we determined the extent of upregulation of PHGDH in a combined transcriptome and proteome analysis. In the integrated dataset, we selected only for those targets of ATF4 that are significantly changed at both transcriptome and proteome level. Interestingly, PHGDH stood out as one of the strongly upregulated proteins in KO BAT, in addition to 6 other ATF4 or CHOP targets (Fig. 2.28).
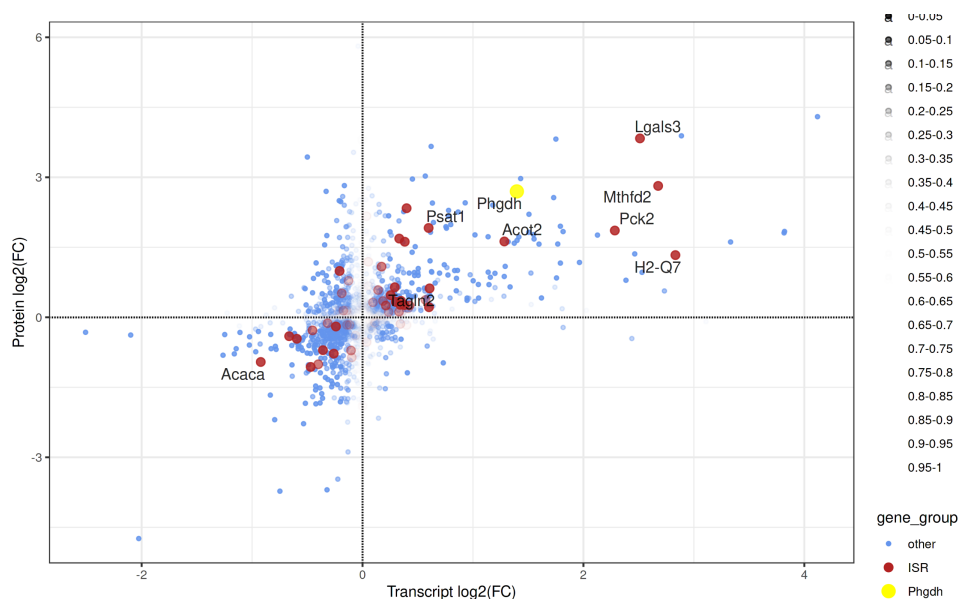
Figure 2.28 Combined transcriptome and proteome analysis from KO BAT tissue post thresholding

We next investigated if PHGDH is indeed the source of 2-HG in KO BATi cells. Initially, we examined the steady state levels of PHGDH in the cells and were surprised to find that the protein levels were not significantly changed in the KO cells (Fig.2.29A). However, we then measured the activity of PHGDH and observed a significantly higher PHGDH activity in the KO cells compared to the wild type (Fig 2.29B). This result clearly indicated that in BATi cells, the activity of PHGDH and not its steady state levels was possibly responsible for 2-HG accumulation and warranted further investigation.

To further establish the role of PHGDH in 2-HG production, we employed a specific pharmacological inhibitor of PHGDH canonical activity, called NCT503. NCT503 has been shown to have high specificity towards PHGDH and is known to successfully inhibit the serine synthesis pathway in cancer cells [369]. This was followed by a targeted metabolomic analysis to specifically measure cellular 2-HG levels in the treated BATi lysates (and relevant controls).
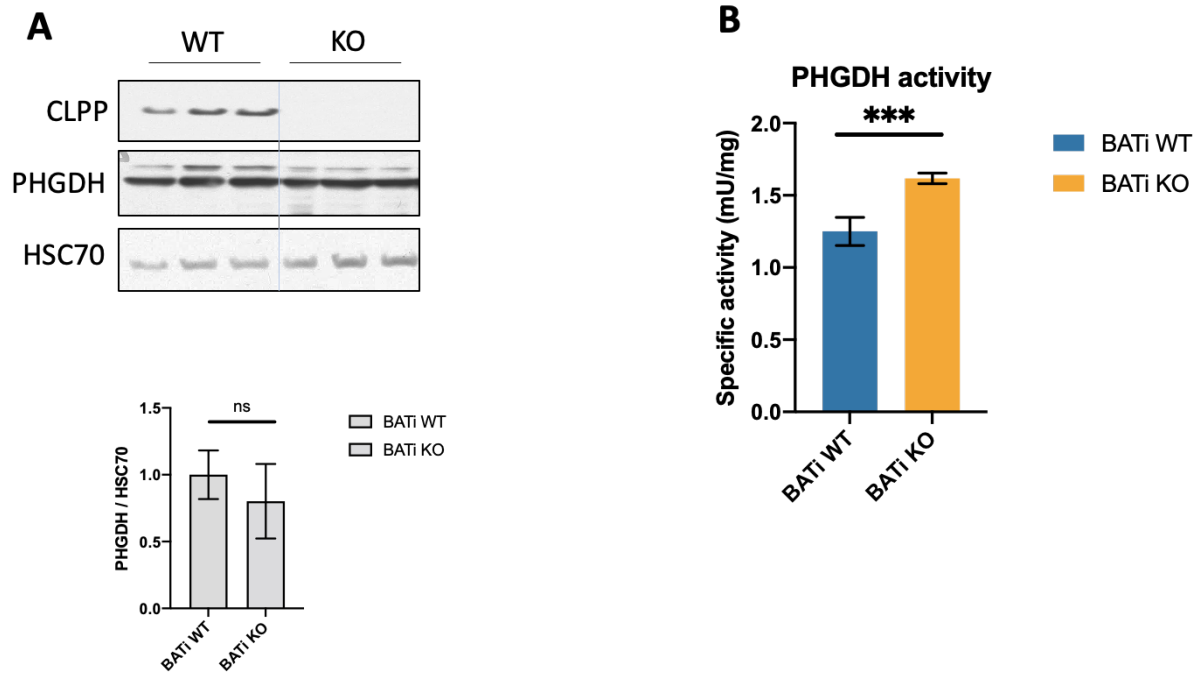
Figure 2.29 PHGDH levels and activity in BATi cells. *A: Immunoblot showing levels and quantification of indicated proteins, N = 3. B: Graph showing quantification of PHGDH enzymatic activity, Data presented as mean ± SEM, Student's T test, *p < 0.01, N = 3.*

KO BATi cells treated with NCT503 did not accumulate 2-HG, and in fact, the levels of this metabolite in the treated KO cells were reduced to the levels similar to that of WT (Fig. 2.30). These findings together provided compelling evidence that the primary source of 2-HG in KO adipocyte cells was PHGDH. This also highlighted the interconnection between the canonical and the moonlighting functions of PHGDH.
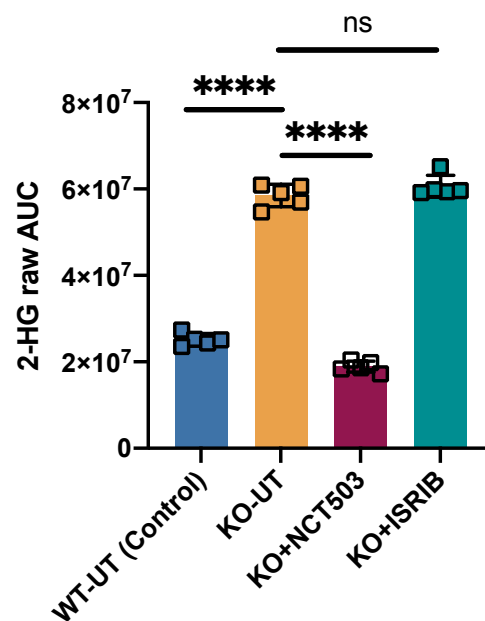
Figure 2.30 2-HG levels in NCT treated BATi cells. *Graph showing quantification of 2HG after targeted metabolomics in NCT503 treated BATi cells, Data presented as mean ± SEM, Student's T test, ****p < 0.0001. N = 5.*

To next assess the impact of PHGDH inhibition and the consequent reduction in 2-HG levels on the whitening (accumulation of more/larger lipid droplets) of BATi KO cells, we subjected the NCT503-treated cells to FACS analysis following staining with BODIPY. We observed a significant decrease in lipid content in the NCT-treated KO cells compared to the untreated KO cells (Fig 2.31A-B). Lipid content was not as low as that seen in untreated WT cells, but showed a significant trend towards reduction in lipids (Fig. 2.31A). This finding solidified the notion that inhibiting PHGDH and subsequently reducing 2-HG levels led to a reversal of the whitening phenotype in BAT.

A

B
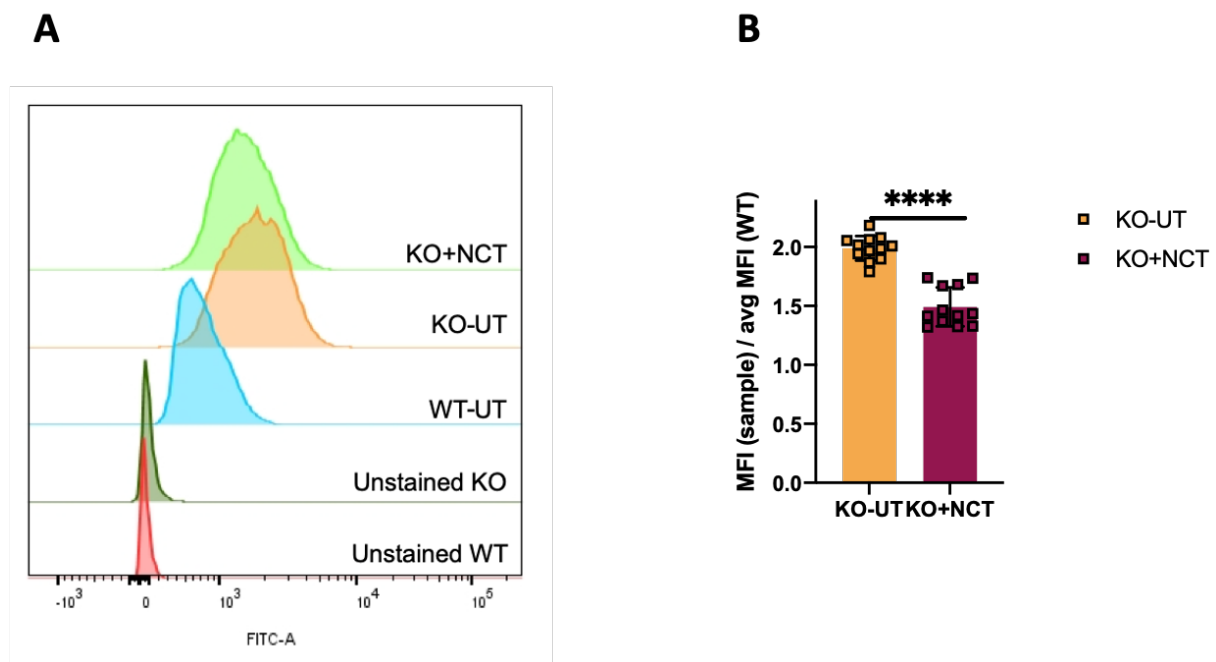
*Figure 2.31 FACS analysis of LD content in treated BATi cells. A: Intensity profile of BODIPY stained treated and untreated BATi cells in FACS analysis. B: MFI quantification of BODIPY stained cells. Data presented as mean ± SEM, Student's T test, ****p < 0.0001, N = 12.*

Typically, not just PHGDH activity but also its levels are upregulated due to active classical ISR. We had, however not seen increased PHGDH protein levels in BATi KO cells. This was in contrast to our expectations, since BAT from all CLPP knockout models had shown more than 3-fold higher levels of *Phgdh* transcript and PHGDH protein. To gain insights into the status of classical ISR under baseline conditions, and upon PHGDH inhibition in BATi KO cells, we conducted qPCR and western blot analysis for genes and proteins related to the ISR. As anticipated and reported earlier [370], we observed a substantial upregulation in gene expression of ISR genes upon NCT treatment (Fig 2.32A). Additionally, we noted an increase in the protein levels of ISR markers as detected by western blot, including phosphorylated eIF2α (Fig 2.32B-C), indicating enhanced flux through the integrated stress response pathway. Taken together, these findings so far, supported our hypothesis that inhibiting PHGDH and reducing 2-HG levels possibly led to further activation of ISR and the likely subsequent activation of lipolysis, leading to lesser LDs in treated KO cells [370]. This, in turn, contributed to the reversal of the whitening phenotype in BATi cells.

It must also be noted that the protein levels of ISR markers like pEIF2a were unaltered in KO BATi cells compared to the WT, under baseline conditions. Likewise, contrary to our observations at tissue level, other proteins of ISR and related pathways, like ASNS and PYCR1 were not altered between WT and KO BATi cells (data not shown). In line with these observations, treatment of these cells with ISRIB did not show any changes in lipid content, or 2-HG levels (data not shown). This brought to limelight that in our model system, maybe it was mitochondrial dysfunction driven fluxes that were possibly driving the whitening. It also indicated the possibility of pEIF2a independent arm of mitochondrial ISR that might be responsible for CLPP loss mediated BAT reprogramming.
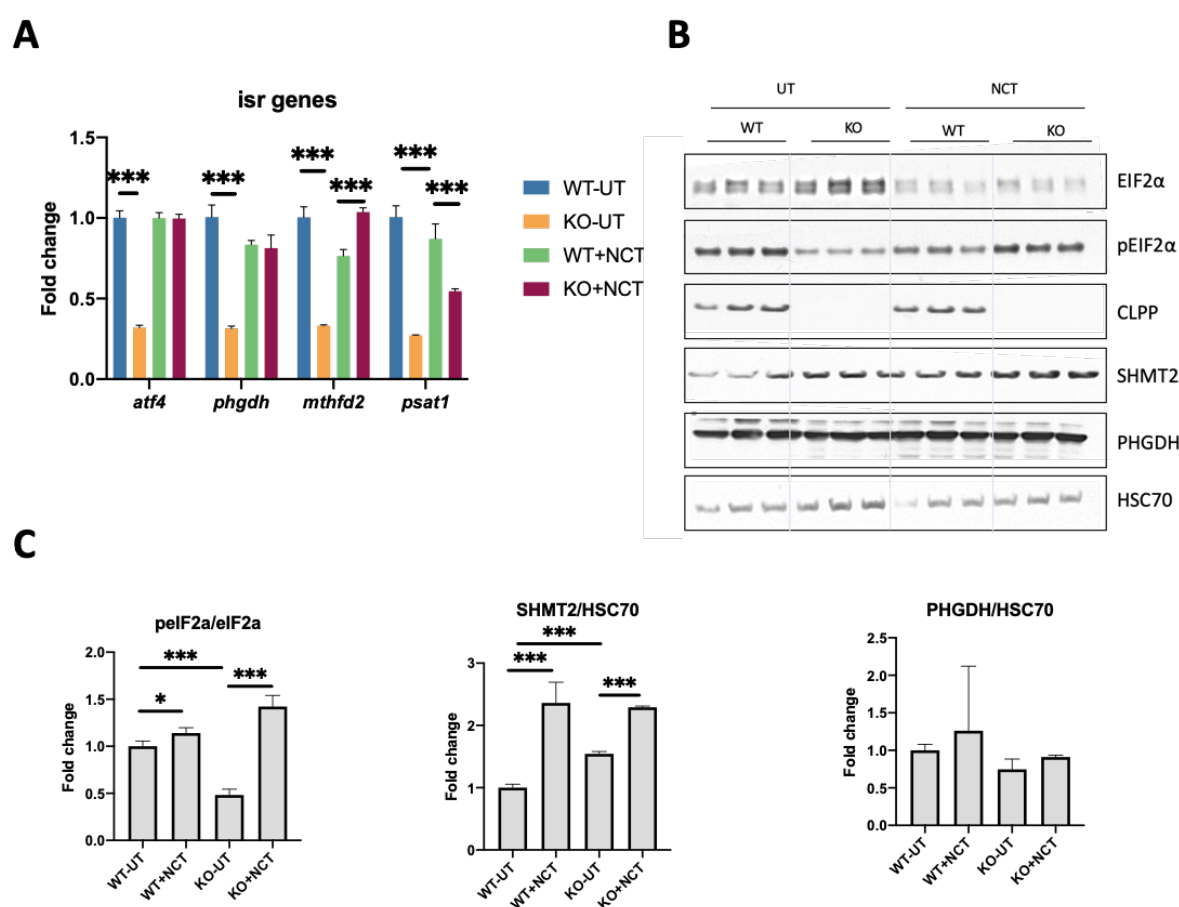
Figure 2.32 NCT treatment in BATi cells leads to upregulation of ISR. *A: qPCR analysis showing relative fold changes of ISR genes in WT and KO BATi cells. Data presented as mean ± SEM, Student's T test, ****p < 0.0001, N = 3. B-C: Immunoblots showing steady state levels of proteins and their relative quantifications. Data presented as mean ± SEM, Student's T test, ****p < 0.0001, N = 3.*

The results so far led us to ascertain that mitochondrial dysfunction and stress response mediated metabolic rewiring was responsible for whitening of BAT. From our exhaustive omics analysis, we were also able to ascertain that the major undertone behind BAT remodeling was gene expression changes, eventually reflected as changes in proteome. We were in search of the exact mechanism that could link mitochondrial dysfunction (and stress) to nuclear gene expression changes. This led us to reflect on the observation made on KO BAT TEM images, pertaining to enhanced mito-nuclear contacts, increased impingement of nucleus by mitochondria and

increased indentations on nuclear surface by mitochondria (Fig 2.19 and 2.20). This brought into our attention the concept of *"Nuclear softening"* in cells which was introduced by a recent publication [371]. The study showed that mechanical stretch deformed the nucleus and the underlying heterochromatin changes protected it against genotoxic stress, while impinging on gene expression due to changes in heterochromatin [371]. Our observations from the 3-D modelling from KO tissue TEMs (Fig. 2.15), showed that the nuclear circumference was indented and pushed in quite frequently by mitochondria and could possibly even be akin to softening. We hence decided to test this in our BATi cells, by measuring stiffness of the nucleus using atomic force microscopy (AFM). The AFM measurements consistently demonstrated a significant 67% lower Young's modulus in KO cells compared to WT cells, indicating a substantial decrease in nuclear stiffness and a softening phenotype of the nucleus in the KO cells (Fig. 2.33).
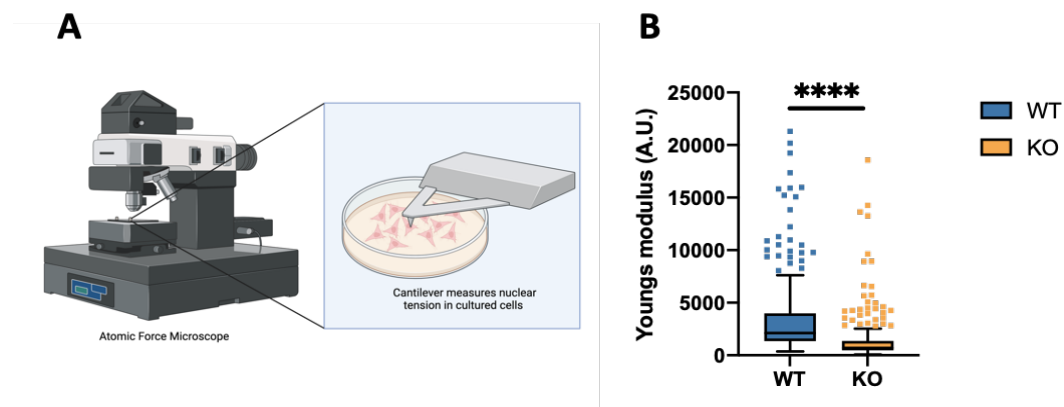
Figure 2.33 AFM measurements on BATi cells show nuclear softening in KO cells. *A: Representation of AFM measurements. B: Graph showing quantification of young's modulus in WT and KO cells. Data presented as mean ± SEM, Kolmogorov-Smirnov test, ****$p < 0.0005$, N =5.*

Following this observation, to test the robustness of mitochondrial dysfunction induced alteration in nuclear architecture, we conducted an additional experiment in a proliferative cell model, treated with rotenone (CI inhibitor) at different concentrations for 12 hours. We measured the stiffness of the nucleus with AFM post 12 hours of treatment. Surprisingly, we observed a consistent reduction in the Young's modulus by 2.5-fold (Fig. 2.34A-C). This nuclear softening was accompanied by a decrease in the levels of Lamin A/C (a protein involved in maintaining nuclear structure), as evident from imaging and western blot analysis (Fig. 2.34A-B). H3K9me3 levels, however, were heterogenous and warrant further investigation Fig. 2.34A).

Previous literature has shown cytoskeleton to be involved in modulating nuclear stiffness and hence regulate global gene expression changes [372]. Our observations on altered cytoskeleton gene and protein expression in CLPP KO BAT further supports our hypothesis. Additionally, one study on tumour cells reported that treatment with staurosporine (broad spectrum kinase inhibitor) induces apoptotic stress on the cell and increases mito-nuclear contacts, similar to what we observe in our BAT KO model [373]. However, there is no direct link till date, between mitochondrial stress and associated metabolic rewiring to nuclear softening in a physiological context. Our observations led us to hypothesize that the upregulated

stress responses in KO BAT could be correlated to, or be causal for, nuclear softening. To test this, we treated WT BATi cells with actinonin and measured nuclear stiffness using AFM. Interestingly we saw a significant reduction in Young's modulus by 54.3% indicative of softening of the nucleus of the treated WT cells compared to the control WT cells (Fig.2.35).
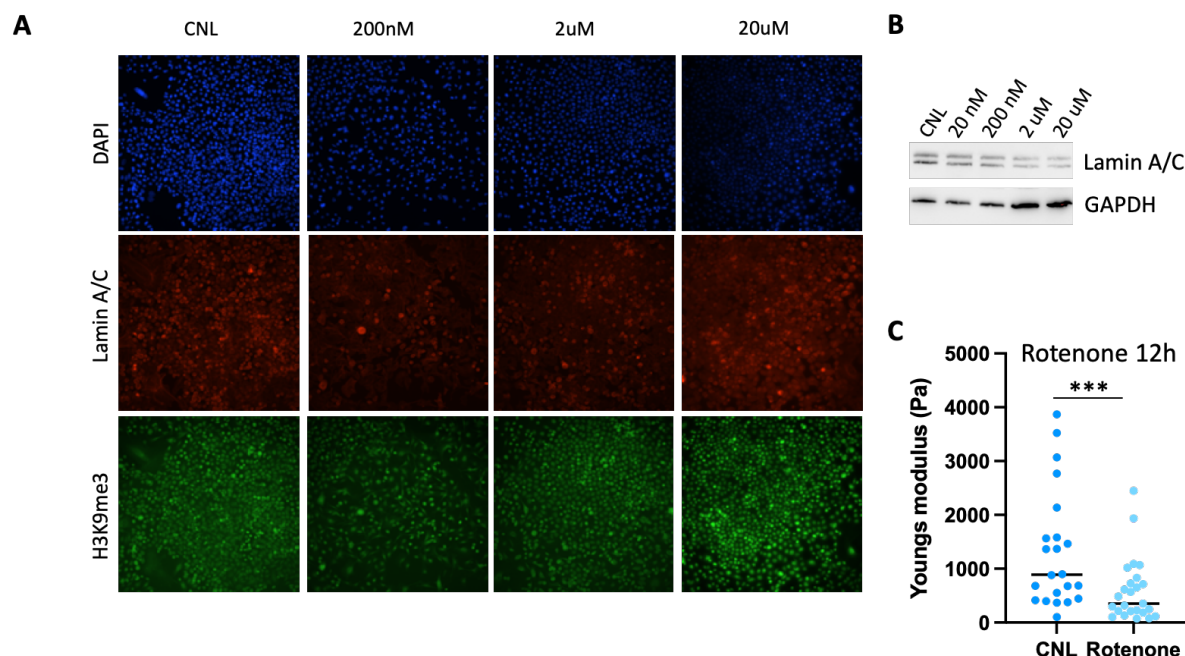
Figure 2.34 Effects of mitochondrial stress on nuclear softening. *A: Representative confocal images showing levels of H3K9me3 and Lamin A/C in rotenone treated proliferating cells, DAPI used as a nuclear marker. B: Immunoblot showing levels of Lamin A/C post rotenone treatment. C: Graph showing Youngs modulus for nucleus in rotenone treated and control cells. Data presented as mean ±SEM, Kolmogorov-Smirnov test, ****p < 0.0005, N =5. Scale bar 100um.*
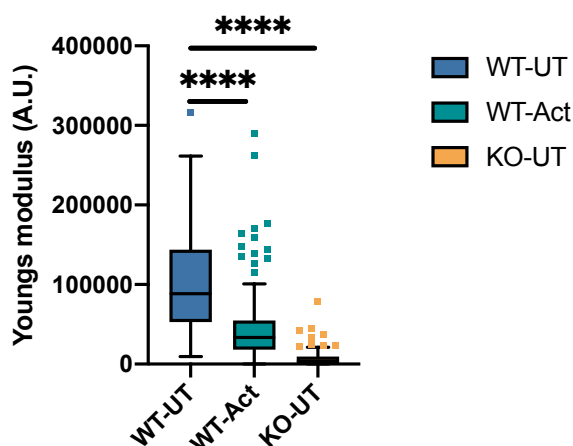
Figure 2.35 ISR induction in BATi cells reduces nuclear stiffness. *Graph showing quantification of Young's modulus in actinonin treated BATi cells. Data presented as mean ± SEM, Kolmogorov-Smirnov test, ****p < 0.0005, N =5.*

Having established the role of mitochondrial dysfunction in mediating nuclear softening, we next investigated the involvement of PHGDH in the same. We performed AFM measurements on NCT503 treated and untreated KO BATi cells and recorded a significant 4.3-fold higher Young's modulus for the treated cells (Fig. 2.36A). This indicated that inhibition of PHGDH led to reversal of softening. We next asked the

question of 'how' exactly does PHGDH lead to nuclear softening and the consequent lipid droplet accumulation. Given our previous results on the link between 2-HG levels and PHGDH activity, we asked the final question of whether 2-HG was responsible for nuclear softening and BAT whitening.

To test this, we treated WT BATi cells with a cell permeable form of 2-HG (octyl D-2-HG) and tested for nuclear softening and lipid droplet accumulation. To our surprise, we indeed saw that 2-HG treatment led to a significant reduction by 64.7% in Young's modulus of treated WT nuclei by compared to untreated controls (Fig. 2.43B). Interestingly, qualitative assessment also showed accumulation of larger lipid droplets, thereby leading us to conclude that *2-HG produced by the moonlighting function of activated PHGDH due to upregulated stress responses in BAT- triggered due to mitochondrial dysfunction upon CLPP loss – led to the accumulation of larger lipid droplets and BAT whitening.*
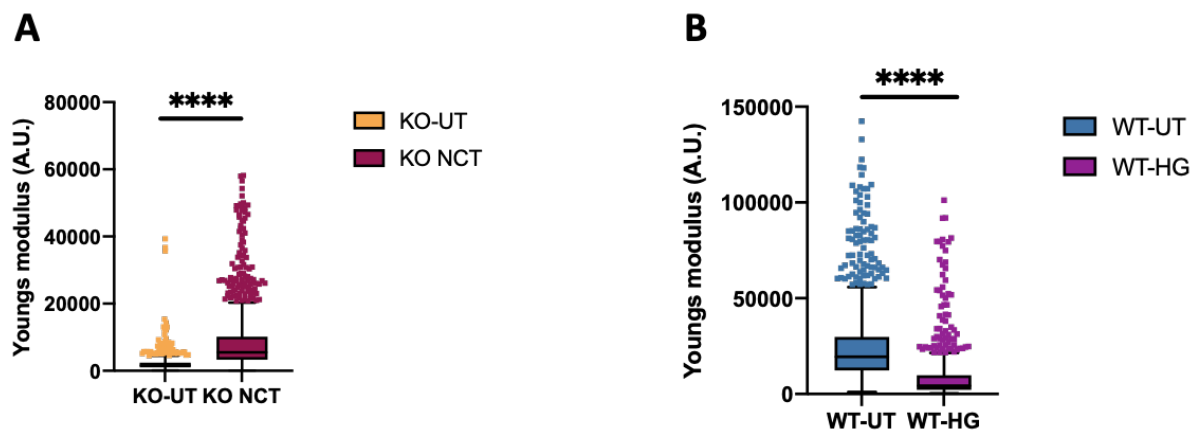
Figure 2.36 AFM measurements of treated WT and KO BATi cells. *A,B: Graph showing quantification Youngs modulus in WT and KO cells treated with HCT, Data presented as mean ± SEM, Kolmogorov-Smirnov test, ****p < 0.0005, N =5.*

This doctoral study hence identified the specific mechanism behind CLPP loss-mediated BAT whitening. To map out the possible underlying chromatin changes in the nucleus at global levels, upon the above-mentioned treatments, we stained the cells for methylation marks, H3K9me3 and H3K27me3. We chose these two markers since previously, H3K9me3 levels have been shown to be decreased upon nuclear softening [371] and 2-HG has also been shown to modulate the levels of these two histone marks [374]. Interestingly, we saw a decrease in H3K9me3 and H3K27me3 levels in BATi KO cells (Fig. 2.44). We also checked for the levels of these two histone marks on NCT treated KO cells and D2-HG treated KO cells and found significant changes. As future follow up studies, it will be interesting to understand how these changes in heterochromatin levels affect expression of specific genes.

In summary, our study so far uncovered a surprising and profound association between mitochondria and the nucleus in BAT. The increased number of nuclear deformations, the redistribution of mitochondria around the nucleus, and the observed nuclear softening provide compelling evidence for the remodeling of nuclear architecture in response to dysfunctional mitochondria. These findings shed light on

the interplay between mitochondrial dysfunction, metabolic rewiring, moonlighting function of PHGDH and production of 2-HG- in the context of CLPP loss in BAT.
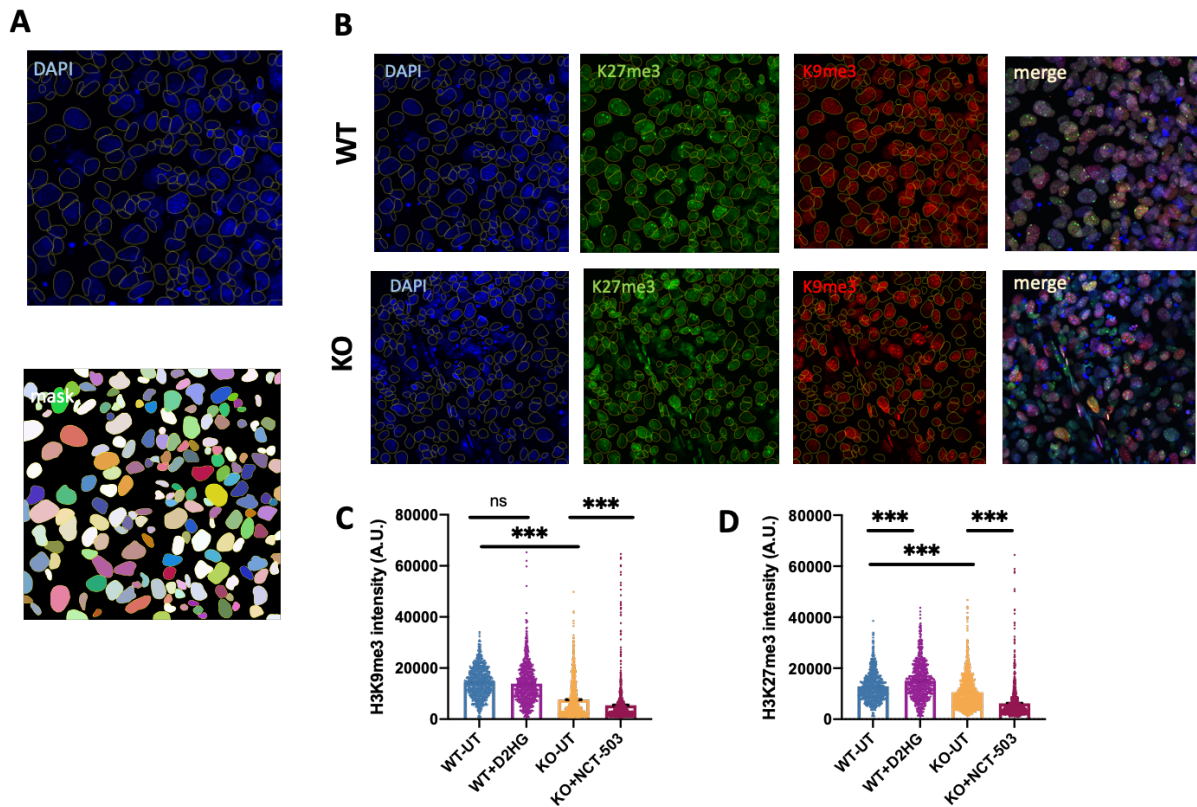
Figure 2.37   Representative Confocal images of histone methylation marks. *A: Nuclei were segmented using Stardist plugin in ImageJ and a nuclear mask was created with the segmented nuclei. The mask was then applied to all channels to quantify the mean signal intensity from each segmented object (nucleus). B. Representative confocal images of nuclei stained for nuclei with DAPI, and for the heterochromatin marks, H3K9me3 and H3K27me3. C: Graph showing single nuclei intensity quantitation of histone marks in treated BATi cells, Data presented as mean ± SEM, Student's T test, *p < 0.05. N = 3*

This warrants further analysis in other tissues and models to understand the connection between nuclear architecture, mitochondrial dysfunction and physiological consequences.

3. DISCUSSION-

This doctoral study provides insights into BAT tissue autonomous and non-autonomous roles of CLPP. Studying different adipose tissue-specific knockout models, AKO and BKO, in junction with whole body model of CLPP loss helped determine the extent of contribution of adipose tissue to the systemic benefits observed in CLPP KO mice. In the context of BAT-intrinsic role of CLPP, the study elucidates molecular underpinnings of whitening of BAT upon loss of CLPP at the mitochondrial and cellular level, followed by assessing its functional consequences at both cellular and tissue levels. Whitening of BAT tissue upon CLPP loss and the associated remodeling at multiple levels of inflammation, cytoskeletal rearrangement, and metabolism – was consistent in all the three models. A comprehensive multi-omics analysis of BAT provided insights into the possible molecular signatures causal for the whitening. Identification of mitochondrial dysfunction mediated metabolic remodeling as a major hallmark ultimately paved way for a detailed examination of the likely mechanism linking mitochondrial dysfunction and whitening of BAT. We discovered an interesting pathway linking the metabolite, 2-HG to softening of the nucleus in whitened BAT. We also show 2-HG to be responsible for larger lipid droplets in BAT. Additionally, 2-HG is produced by the moonlighting function of the enzyme PHGDH, whose levels and activity are upregulated. The study hence identifies a metabolite mediated mechanism behind BAT whitening, while simultaneously highlighting explicit nucleus-mitochondria crosstalk via nuclear softening upon CLPP loss.

Loss of CLPP in BAT partially protects mice from diet induced obesity and insulin resistance- a hormetic effect

The identification of functional BAT in adult humans, and the functional relevance of mitochondria in BAT has sparked significant interest in BAT activation as a potential avenue to enhance energy expenditure and counteract obesity-related issues [375-377]. Moreover, BAT's emerging role as a secretory organ, giving rise to endocrine factors known as BATokines, has garnered attention for its potential to modulate systemic metabolic balance [378]. Mitochondria are at the core of BAT functioning as their numbers and activity in BAT is one of the highest compared to other tissues. Thus, identifying the mitochondrial mechanisms that govern BAT thermogenesis and its ability to act as a metabolic "sink", holds promise for uncovering novel therapeutic avenues aimed at tackling obesity and its associated complications.

Studies have shown that dysfunctional BAT is associated with obesity and metabolic disorders [253, 379]. Reduced BAT activity or impaired thermogenesis can lead to reduced energy expenditure and increased storage of fat in the form of WAT, contributing to weight gain and obesity [253, 254]. The activation of BAT has been proposed as a potential therapeutic target for combating obesity and improving metabolic health [380]. Contrasting to both these observations, our study confirmed systemic benefits upon loss of CLPP, despite mild respiratory chain deficiency in the mitochondria [349]. This concept is known as **'mitohormesis'**, states that mild stress on mitochondria can lead to the activation of adaptive pathways, which in turn confers

metabolic benefits, not just to the tissue where the mitochondria are dysfunctional, but also to overall organismal physiology and healthspan [381]. Our current results show that when challenged with HFD, only BKO (and not AKO) have a mild trend towards protection from obesity and insulin resistance and accumulate less body fat (Fig. 1.3). These observations are in line with previous research on mild dysfunction-induced mitohormetic effect and its beneficial effects on metabolism [382, 383]. Molecularly, multiple loss of function models of diverse proteins have shown to indirectly activate the BAT to improve systemic metabolism. The studies range from BAT specific modulation of epigenetic regulators like LSD1 [384], deletion of mitochondrial proteins involved in lipid metabolism, like CPT2 [304], UCP1 [385, 386] or VLCAD [333] in BAT, or only mitochondria related perturbations like BAT specific COX7 related protein (COX7RP) KO mice [387], OPA1 KO mice [331], MFN2 KO mice [330], and TFAM whole body heterozygous mice [331, 332]. All these models show overall beneficial effects on organismal physiology and show lesser accumulation of fat in the body. In a model of adipose specific TFAM deletion, where TFAM was reduced in subcutaneous WAT and BAT but not in visceral WAT, the mice showed lesser weight gain upon HFD but and were protected from insulin resistance. Despite consuming more food, the mice showed metabolic benefits and were also resistant to hepatosteatosis induced by age and diet [327, 328]. Additionally, another study on adipose specific TFAM knockout mice using a different promoter (that drastically reduced TFAM expression in subcutaneous and visceral WAT as well as BAT), reported a slightly different phenotype. These mice had a lipid storage defect and hence had elevated circulating fatty acids and ectopic lipid accumulation leading to hepatosteatosis, insulin resistance, hypertension and non-fibrotic cardiac hypertrophy [328]. These two studies hinted at the context specificity of loss of proteins from different adipose tissue depots. In alignment with these results, observations from our study also hint at two contrasting effects when CLPP is removed from either all adipose tissues depots or specifically from BAT. We show that mildly affecting BAT mitochondria can confer metabolic benefits to the organism, whereas removing CLPP from WAT and BAT reverses those metabolic benefits. Additionally, results from our lab also show that even liver specific CLPP KO mice (LKO) and muscle specific CLPP KO mice (MKO) do not have the metabolic benefits that BKO mice show, thereby re-instilling the crucial role that BAT plays in regulating systemic metabolism in a beneficial manner [349].

Loss of CLPP in BAT induces proteomic changes in iWAT, thereby hinting at strong communication between two major adipose tissue depots in the body. Since the two tissues are spatially distant in the body of mice, the mode of mediation for this response could either be a specific and direct communication to the iWAT or could be a consequence of a general systemic response initiated by the BAT but transmitted to multiple tissues of the body via serum cytokines. In anticipation of the likely molecular mechanism, indeed, BATokines or chemokines are considered the first responders and group of potential mediators of the systemic responses [388]. Some pro-inflammatory cytokines have also been implicated in being signal transducers in mediating this effect [389]. However, the field still lacks conclusive studies to chart out the exact players involved. As a follow up on our study, serum profiling in KO, AKO

and BKO mice could help identify potential adipokines or BATokines, and correlating them with expression patterns of those genes in BAT and iWAT could help in determining the tissue of origin of the cytokines.

A previous study from our lab showed that contrary to the generalized notion, where chemokines like FGF21 have been shown to mediate lot of these metabolic benefits, FGF21 is mostly dispensable for the metabolic benefits seen in CLPP KO model, and a partial reversal is seen only at old age. [332, 390]. Further, metabolomics analysis of the BAT and serum of KO mice revels two metabolites, homoarginine and homocitrulline to be enriched. They could be potential mediators for the observed systemic effects, but are not released from BAT. Preliminary results show that the primary source of these metabolites might be liver, since liver of LKO mice also accumulate homocitrulline and homoarginine (Fig 1.15). Both these metabolites are intermediates in urea cycle. The upregulation of OAT (a bonafide CLPP target playing role in urea cycle) in our models is hence correlated with accumulation of these metabolites [391]. Homocitrulline is specifically interesting since it is also formed as a byproduct of 'carbamylation'. Carbamylation is the covalent attachment of isocyanic acid to the side chains of lysine residues of proteins and lipoproteins. Homocitrulline is one of the most typical carbamylation derived products (CDPs) and is a bonafide biomarker in the context of various diseases like chronic kidney disease [392, 393].

Overall, the results obtained from the tissue-specific knockout models provide valuable insights into the role of BAT dysfunction in regulating whole-body energy homeostasis and metabolism. Given the potential role of BAT dysfunction in metabolic disorders, including obesity and insulin resistance, researchers have explored various strategies to target and activate BAT as a therapeutic approach [394]. Our findings align with the idea that BAT plays a critical role in metabolic regulation and that CLPP loss in BAT may be one of the factors contributing to the observed metabolic benefits in KO mice. Further research in this area could lead to the development of novel therapeutic strategies targeting CLPP generally or specifically in BAT to combat obesity and metabolic disorders.

Loss of CLPP induces whitening of BAT- with both unique and overlapping hallmarks with other models exhibiting BAT whitening

The striking observation on BAT physiology was the whitening phenotype, characterized by enlarged lipid droplets. The convergence of this whitening phenotype across the three models- KO, AKO and BKO suggested a common underlying mechanism independent of the context of CLPP removal. Initial ultrastructural analysis using TEM had unveiled damaged mitochondria in BAT, evident by cristae disorganization and the presence of a hollow core and enlarged appearance. These observations were consistent with prior studies that highlight the role of CLPP in maintaining mitochondrial integrity and function [173, 175, 194, 395]. The presence of damaged mitochondria and reduced supercomplexes, particularly in complexes I, III and IV (Fig 2.4), is consistent with the established notion of respiratory chain deficiency and dysfunctional mitochondria in other tissues and cell types from CLPP KO model [396, 397]. The reduced CI activity observed in the knockout models (Fig. 2.4C) corroborates with findings in other studies highlighting the critical role of complex I in

overall respiratory output [398]. In addition, upregulation of the nucleus-encoded subunits of complex V, which form a stable sub-assembled F_1 complex in response to severe OXPHOS dysfunction, also corroborates with previous studies that explain this to be a compensatory mechanism to main cellular redox [192, 354, 399].

OXPHOS deficiency was concurrent with cellular phenotypes such as upregulated inflammatory responses, innate immunity, cytoskeletal rearrangement, endothelial and/or vasculature changes and metabolic rewiring. We defined these changes as **"Hallmarks of CLPP loss mediated whitening of BAT"** and it was interesting to compare and contrast our findings with previously published studies that reported a whitening phenotype in BAT.
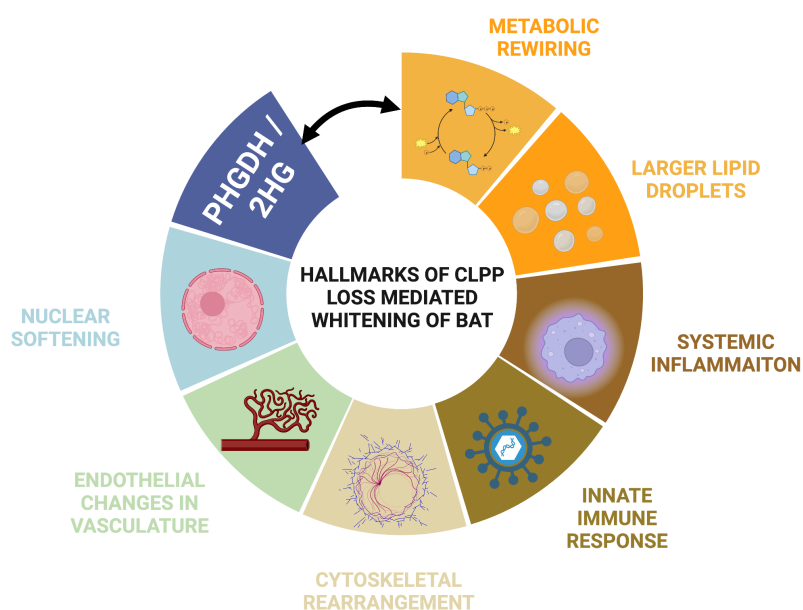
Figure 3.1 Hallmarks of whitening of BAT upon CLPP loss

The observed alterations in lipid metabolism and metabolic rewiring support the existing understanding of the relationship between mitochondrial function and adipose tissue biology. Dysregulation of lipolysis and increased lipid droplet size have been associated with mitochondrial dysfunction in adipose tissue and have been linked to metabolic disorders, including obesity and insulin resistance [327, 400]. Further, the identification of upregulated systemic inflammation in all the three models aligns with previous studies suggesting a reciprocal relationship between adipose tissue function and inflammation, stemming from metabolic dysregulation [401, 402].

Inflammation and innate immune response is the highest upregulated hallmark of KO BAT, but is not the cause for whitening-

Our transcriptome and proteome data from KO, AKO and BKO revealed inflammation and innate immune response to be the most upregulated pathways (Fig. 2.8 and Fig. 2.9). The hallmark of BAT inflammation appears to be a conserved phenotype associated with the whitening of BAT across different models reported in

literature [403]. A previous study compared four models exhibiting a whitened BAT, namely, obese *db/db* mice (leptin receptor deficiency), ß-less mice (inability to respond to cold induced thermogenesis), ATGL KO mice or warm acclimated mice [358]. BAT from all these four models show formation of Crown like structures (CLS). CLS are aggregates with activated macrophages that often fuse together to from syncytia (multinucleated giant cells) and surround dead adipocytes to clear them, a clear readout for a strong inflammatory tone [404]. In our models, we did not observe the presence of CLS-like structures in BAT. A study also established that BAT from ATGL mice showed activation of NLRP3 inflammasome [358]. However, in contrast to our study, where we report a pro-inflammatory state in BAT due to mild mitochondrial dysfunction, their study reported that the inflammation was independent of ER stress or mitochondrial dysfunction [358]. It is known that in obese mice and humans, adipose tissue is infiltrated by inflammatory cells and produces inflammatory mediators that link fat accumulation to cardiovascular and metabolic complications, such as insulin resistance and type 2 diabetes, concomitant with a decline in BAT function [252]. Even though inflammation is reported to be the likely cause of reduced BAT activity and consequent whitening, the studies still lack a mechanistic understanding of why would the tissue attain an inflammatory state. Contrastingly, our study had a very intriguing observation of upregulation of innate immunity and stress responses (Fig. 2.9D) in BAT upon CLPP loss, which could be the potential trigger for the upregulated cascade of pro inflammatory signaling in the tissue. However, this severe upregulation of genes and proteins involved in this pathway was observed not just in BAT of KO mice, but also in the heart and iWAT, and cultured CLPP KO MEFs. Further investigation in the lab detected a strong correlation between elevated innate immunity and mtDNA release in CLPP KO mice [unpublished data]. Additionally, is has been observed that blocking mito-transcription partially decreased the ISG responses. To address this further, two double knockout mice have been generated in lab, where in addition to CLPP, STING (canonical mtDNA sensing signaling pathway) or MAVS (dsRNA sensing signaling pathway) has been removed. In both the mutants, a suppression of innate immune response and inflammation in lung fibroblasts was observed. Interestingly, even though the innate immune response seemed to be blunted, the whitening phenotype of BAT was not rescued in these mutants [unpublished data]. This gave us a strong indication that innate immune response or inflammation was not the causal factor for BAT whitening, and was rather a consequence of release of mtDNA or mtRNA due to mitochondrial dysfunction. For the scope of this study, these observations assisted us to shift our focus on other likely causal mechanisms of CLPP loss mediated BAT whitening.

Whitening Phenotype in Adipose Tissue-Specific CLPP Knockout Models indicates remodeling of BAT at multiple levels-
    The next most abundant gene and protein expression changes were observed in cytoskeletal rearrangement or actin and myosin related processes (Fig. 2.11A). Given that BAT adipocytes share a common myogenic lineage, we had hypothesized that maybe this upregulated muscle signature could be due to de-differentiation of mature adipocytes to a multipotent stage wherein muscle markers are also expressed

in conjunction with having a 'white adipocyte-like' phenotype. This hypothesis was based on results from previous studies which reported PRDM16 to control a bidirectional cell fate switch between skeletal myoblasts and brown fat cells [405]. Loss of PRDM16 from brown fat precursors causes a loss of brown fat characteristics and promotes muscle differentiation [405]. Additionally, PRDM16 KO mice have upregulation of muscle genes in BAT, which is similar to the observations made by us [405]. Typically, the levels of BMP4 go down during brown fat differentiation, and ectopic BMP4 addition induces a brown to white adipocyte shift, leading to upregulation of whitening markers in BAT [406]. These observations are overlapping with what we observe in our model. However, proteomic analysis from isolated preadipocytes form SVF of BAT did not reveal upregulation of either of these determinants of cell fate. In fact, the preadipocytes had slight upregulation of cytoskeletal genes as well. Additionally, deconvolution analysis on our bulk transcriptome data revealed that the muscle-like cell types were not altered in BAT (Fig. 2.11D), thereby leading us to dismiss this hypothesis. We hence concluded that this upregulation of muscle genes, in conjunction with upregulation of calcium responsive genes could be an indication of hypertrophy induced cytoskeletal rearrangement, which has been previously linked to whitened BAT, as well as upregulated ISR [407-409].

Lipid droplets accumulation upon CLPP loss highlights interplay between mitochondrial dysfunction, stress responses and metabolic rewiring-

The presence of enlarged lipid droplets in our study was a consistent observation, that aligns with emerging insights into their pivotal roles as regulators of cellular metabolism and stress response [410-412]. Lipid droplets are increasingly recognized as central hubs that orchestrate multiple facets of lipid uptake, distribution, storage, and utilization within cells [410-414]. Through their ability to buffer toxic lipids and proteins, and by regulating lipid flux to membranes and organelles, lipid droplets may be essential for protein quality control as well as membrane synthesis, composition, and dynamics [411]. Lipid droplet biogenesis is also essential in starved cells for buffering autophagy-derived lipids [24, 415, 416]. In fact, not just in lipid metabolism, they may even act both to prevent the onset of ER stress and to restore ER homeostasis upon UPR activation [417]. Lipid droplets have been proposed to act as "escape hatches" for removal of damaged ER proteins [418]. ER stress has also been shown to induce lipid droplets that bud from the ER membrane. Under these conditions, lipid droplets act as buffers and sequester misfolded proteins and excess lipids to alleviate ER stress. They also hold the capacity to sequester free Ca^{2+} and protect from cytosolic Ca^{2+} overload, often associated with ER stress [419]. ERAD is a mechanism for removing unfolded or misfolded proteins from the ER through ubiquitination and subsequent degradation by the proteasome [420]. Genetic impairment of ERAD-mediated protein degradation in yeast leads to lipid droplet accumulation, opening the possibility that lipid droplets are employed by cells to alleviate ER stress associated with protein misfolding [421]. In conditions of cellular stress, such as the ones observed in our study with upregulated ISR and OXPHOS deficiency (Fig 2.9E), lipid droplets emerge as crucial guardians of energy and redox

homeostasis. Despite the elevated stresses, the cellular output in terms of respiration and response of BAT to beta adrenergic signal (Fig 2.19A) was not altered in KO BAT. We also did not see elevated lipid peroxidation in CLPP KO BAT (data not shown). A possible explanation for not observing lipotoxicity in our models could be that by sequestering toxic lipids into their neutral lipid core, the large lipid droplets defend the BAT against lipotoxicity. The larger lipid droplets could hence be a protective adaptation for adipocytes. Additionally, KO mice appeared to have a starvation like state and metabolomics analysis of cultured differentiated KO adipocytes show accumulation of AICAR and related starvation metabolites (Fig 2.24A), which could also be a contributory factor to larger lipid droplets.

Another noteworthy observation about lipid droplet associations in BAT is their dynamic interactions with mitochondria in the form of PDMs, that facilitate the efficient delivery of fatty acids, optimizing energy production during stress [414]. Additionally, interactions between lipid droplets and the nucleus are an emerging field of research, currently being addressed mostly from two perspectives: the involvement of cytosolic lipid droplets in regulating nuclear function, and the existence of nuclear lipid droplets and their yet uncovered origins and function [422]. Cytosolic lipid droplets are often found proximal to the nucleus and have been proposed to affect its functions, like protein exchange or chromatin assembly [422-424]. In our study, we made a qualitative assessment that the number of PDMs is higher in KO owing to larger lipid droplets, and so is the association of lipid droplets with the nucleus. In fact, we also see larger occurrences of tripartite assemblies (Fig 2.14A), involving the nucleus, mitochondria and lipid droplets, which is also evident form the analysis of proteome of isolated PDMs from KO BAT. Taken together, these observations do highlight the protective role of lipid droplets, not just as storage buffers for fat but also in maintaining cellular homeostasis. As such, our study contributes to the growing appreciation of lipid droplets as crucial orchestrators of cellular homeostasis and stress adaptation. It still remains to be answered, if accumulation of lipid droplets in our KO model is due to blunted lipid breakdown, due to upregulated stress including ER stress, or in part, a combination of the above.

Consistent metabolic reprogramming in BATi cells despite context-specific nature of ISR:

Consistent with previous studies on mitochondrial dysfunction in mammals [2, 192-194, 213], our findings reveal changes in many metabolic pathways which might be consequence of elevated ISR in KO BAT. Key regulators, ATF4 and MYC are prominently involved (as confirmed by strong transcriptional upregulation of their targets), and they serve to rewire metabolism as an adaptive mechanism in the cell. We observe enrichment of genes, proteins and metabolites involved in the serine biosynthesis, 1C metabolism, purine and pyrimidine biosynthesis and BCAA metabolism (Fig 2.6B). Remarkably, MTHFD2 (crucial player in the 1C cycle) [2], as the highest upregulated protein in our proteomics data, and in the integrated analysis of transcriptome and proteome (Fig 2.28), emerges as a potential marker for mitochondrial dysfunction in patients [425]. Additionally, a strong upregulation of PHGDH is seen, which is a direct transcriptional target of ATF4 and plays role in serine

biosynthesis [426]. Typically, the increase in amino acid metabolism and 1C flux compensates by providing intermediates for nucleotide biosynthesis for proliferating cells to ensure continued growth [217]. Our cell model, on the other hand, is a differentiated cell model, without apparent need for factors to promote proliferation. Despite that, the metabolic rewiring is observed, thereby hinting that ISR mediated metabolic rewiring is indeed a homeostatic adaptation mechanism, possibly for maintaining redox balance within the cell, and not merely a solution to sustain proliferation. Past research has elucidated a stage-wise progression of ISR induced by mitochondrial dysfunction in skeletal muscle, using a mouse model called Deletor mice (with a patient mutation in nuclear encoded mtDNA helicase, Twinkle). The initial stage is majorly mediated by ATF5 and leads to upregulated 1C cycle and associated nucleotide level changes, with concomitant release of FGF21 and GDF15 [193]. The progression to 2nd metabolic ISR stage involves activation of ATF3 and ATF4, thereby also affecting glucose uptake, serine biosynthesis, and transsulfuration [193]. The third terminal stage involves mildly activated ATF3 and upregulated mitochondrial HSPs [193]. Our KO model shows upregulated gene signatures of all the above-mentioned pathways in the second stage, thereby implying a state of chronic ISR. The co-operativity observed between the transcription factors sustains the metabolic rewiring, with major upregulation of the serine synthesis pathway (SSP) [1]. It has been shown that in the context of tumours, serine deprivation leads to increase in expression of *Atf3* in a ATF4-dependent manner, and ATF3 further potentiates *Atf4* expression as well as expression of serine synthesis genes like *Psat1* and *Phgdh*, thereby maintaining the metabolically rewired state [427]. Previous research from our lab also sheds light on the interplay between several transcription factors like CHOP, C/EBPβ, and ATF4 that regulate mitochondrial stress responses [211]. We demonstrated that CHOP functions as a rheostat to reduce ISR upon severe mitochondrial dysfunction, prevents unfavorable metabolic changes, and postpones mitochondrial cardiomyopathy [211]. The extent of mitochondrial dysfunction decides the extent of compensatory adaptive changes, which is in congruence with previous research on stages of ISR [211].

Our results from CLPP KO BATi cells provide interesting insights into the *context specificity* of ISR. Following the established paradigms of mitochondrial dysfunction and the concurrent upregulated gene and protein signatures, our KO, AKO and BKO tissue models, characterized by mitochondrial dysfunction since the developmental phase, exhibited a notable regulation of canonical ISR proteins, like PYCR1, ASNS, pEIF2α, SHMT2, MTHFD2 and PHGDH. However, our cellular model of CLPP KO (BATi cells) did not show the upregulation of most of the ISR proteins (Fig. 2.32C-C), with the exception of MTHFD2, whose steady state levels were still higher. In fact, the transcript levels of these proteins were lower in KO cells than in WT cells (Fig 2.32A). Levels of pEIF2α was also not increased in KO cells compared to WT (Fig. 2.32B). We, however, recorded higher activity of PHGDH, the rate limiting enzyme of serine biosynthesis (Fig 2.29B). Similarly, some metabolites which are likely to be by products of the enzymes mentioned above, were still conserved and enriched in KO cells. A combination of these observations led us to conclude that mechanisms beyond just steady state protein levels (such as PTMs, metabolite-protein interactions

etc), and independent of pEIF2α might be playing a role in our cell model. It sheds light on a pEIF2a independent arm of mitochondria mediated stress response, and warrants further investigation. Our experiments on BATi cells with ISRIB treatments (where both WT and KO BATi cells showed similar decrease in ISR protein markers upon treatment) also shed light into this interesting aspect of canonical ISR, which seems to be pEIF2α independent, but ATF4 dependent.

The most accurate way to get further insights into ISR mediated metabolic rewiring for our model would be a metabolic flux analysis with labelled substrates- to chart out relative proportions of activated pathways. It would also be interesting to explore the consequences of specific pathway inhibitions on cellular homeostasis and cell death.

Role of PHGDH activity in KO BAT reveals a connection between canonical and moonlighting function of PHGDH-

The highly upregulated enzyme in BAT of all knockout models, PHGDH, has been previously implicated in promoting the growth of various cancer subtypes by enhancing serine biosynthesis [426, 428]. In fact, among amino acids, serine is a major donor of single carbon units for many biosynthetic reactions [429]. In fact, the interplay between serine and glycine is crucial for 1C metabolism, where their interconversion orchestrated by serine hydroxymethyltransferases (SHMT1 and SHMT2) [225]. This metabolic partnership between serine and glycine manifests through the interplay of catalytic reactions, specifically through SHMT and subsequent glycine cleavage, offering a significant source of methyl groups. This connection anchors the serine-one carbon cycle-glycine (SOG) network to the folate cycle [430].

A recent study had reported a potential non-canonical role of PHGDH in contributing to tumor genesis by producing the onco-metabolite 2-HG through the NADH-dependent reduction of α-ketoglutarate (α-KG) [368]. Independent studies on 2-HG have revealed that it is a direct player in retrograde signaling to the nucleus [365]. Even though there is just one study till date that reports this *moonlighting* activity of PHGDH, the implications can be widespread. The concomitant accumulation of 2-HG and elevated stress in all our CLPP KO models led us to focus on PHGDH's involvement in the accumulation of lipid droplets and the different aspects of the reprogrammed BAT. Our study provides the first physiological evidence of 2-HG production being dependent on PHGDH and linking it to metabolic rewiring in the tissue. The release of 2-HG into media from cultured BATi cells further reveals that 2-HG produced as a consequence of upregulated stress in cells (Fig 2.27), is a potential signaling molecule.

Surprisingly, no change in PHGDH levels in our BATi KO cells contradicted our expectations, and brought to limelight that PHGDH mediated regulation might not be solely about its steady state abundance, but also concerning its activity. This realization directed our attention towards a recent study demonstrating reduced PHGDH levels in hepatocellular carcinoma (HCC) cells, despite a significant accumulation of serine [431]. The study revealed that PHGDH activity could be modulated by PRMT1 mediated methylation, thereby promoting its activation, and ultimately facilitating serine synthesis and tumour growth. This study complemented

our results on increased PHGDH activity being the likely cause for 2HG enrichment, nuclear softening and accumulation of larger lipid droplets. Previous literature also reports acetylation of PHGDH to be responsible for altering its activity [432], in fact, switch in acetylation sites within PHGDH domains can switch the activity from an off to on state [432] Additionally, acetylation at a specific site can prevent its association with E3 ubiquitin ligase to further increase the stability of the enzyme [433]. Taken together, these pave way for further investigations on identifying the likely mechanisms such PTMs that lead to alterations in PHGDH activity, and/or stability, since stress responses alter the redox status of the cells, which further activates cascades of cellular level changes in acetylation, phosphorylation, methylation etc.

The elevated levels of 2-HG in our KO cells were decreased to WT levels upon specific inhibition of by NCT503 [434] (Fig 2.30). This strongly indicated that PHGDH is the major contributor to 2-HG production in CLPP KO BATi cells. This finding also highlighted the intricate relationship between PHGDH's canonical activity and its moonlighting function in 2-HG production [368]. The observation also further suggested that the canonical enzymatic activity of PHGDH is a prerequisite for its non-canonical role in 2-HG synthesis. A likely reason for this could be a decrease in levels of α-KG due to inhibition of serine synthesis. Additionally, it will be interesting to further examine if post translational modifications within domains of PHGDH lead to switch between canonical and moonlighting functions of PHGDH, or whether the moonlighting function is simply a consequence of its canonical activity and metabolite flux in the cells. It also remains to be determined if this reduction in 2-HG upon PHGDH inhibition is due to lower levels of α-KG upon NCT treatment or not.

Although our study is mainly based on observations made on differentiated adipose cell models, which are non-proliferating, our results resonate with the broader context of metabolic alterations during tumor development. As tumors progress, their metabolic demands change significantly, leading to aberrant nutrient acquisition strategies [435, 436]. Metabolites like glucose and amino acids undergo reprogramming to fuel high biogenetic requirements like including nucleotide synthesis, lipid and protein synthesis, polyamine, metabolism, methylation metabolism, and redox balance [437]. This phenomenon, often referred to as "*opportunistic modes of nutrient acquisition",* underscores the importance of understanding metabolic reprogramming mechanisms in cancer cells [436]. Irrespective of the proliferative status of the cells, mitochondrial dysfunction alters the metabolism of our cells, with upregulated serine synthesis, 1C cycle, folate and methionine cycle and branch chain amino acid degradation in our KO models, and appear to be linked to 2-HG production. Inhibiting specific arms of these pathways and studying their effects on PHGDH activity and 2-HG production would help gain intricate understanding on the fluxes at play in our KO cells.

The convergence of our findings on mitochondrial dysfunction mediated stress responses with these broader insights underscores the multifaceted role of PHGDH in altering metabolism. This dual functionality of PHGDH makes it a potential target for therapeutic interventions, not just for anti-tumour applications, but for facilitating lipid homeostasis and organismal physiology by controlling adipocyte functioning.

2-HG driven signaling controls BAT whitening and nuclear softening-

The consistent accumulation of 2-HG in BAT from all CLPP loss of function models signifies a consistent metabolic perturbation (Fig 2.27). 2-HG, a metabolite of substantial interest, has been extensively implicated in various cellular processes and disease contexts [438]. Notably, its dysregulation has been associated with oncogenesis and metabolic disorders, often in the context of isocitrate dehydrogenase (IDH) mutations in various kinds of tumours [439-442]. Our study extends the understanding of 2-HG's role beyond these contexts, highlighting its potential significance in mitochondrial dysfunction in non-proliferative, differentiated cells.

The reversal of whitening phenotype upon inhibition of PHGDH (Fig 2.31) and subsequent reduction in 2-HG levels (Fig 2.30) provides a novel avenue for understanding the mechanistic underpinnings of BAT remodeling. Our study offers a clear connection between PHGDH mediated 2-HG production, mitochondrial dysfunction and accumulation of lipid droplets. Our observations differ from conventional models of tumourigenic 2-HG accumulation at the additional point that unlike cancer models where there is a concomitant decrease in levels of α-KG [361], in our CLPP KO models, levels of α-KG remain unaltered. This could be due to replenishing of the levels by anaplerotic pathways that are upregulated upon mitochondrial dysfunction and that have been previously shown to maintain stable levels of α -KG [443].

In the studies on tumour cells, 2-HG appears to be a potent player in epigenetic modulation [444]. Its ability to inhibit α-KG-dependent dioxygenases provides a mechanistic insight into how 2-HG accumulation could influence histone methylation patterns and consequently tumorigenic gene expression [361, 367]. The metabolite has also very recently been shown to directly alter glycolysis in CD8$^+$ T cells and hence control their polarization [366]. 2-HG has been implicated in controlling adipocyte differentiation in one previous study by altering histone methylation levels at the promoters of adipocyte lineage specific genes [374]. These observed phenomena echo previous researches indicating that both enantiomers of 2-HG, D-2HG, and L-2HG, can exert significant effects on α-KG-dependent dioxygenases, such as TET2 and Jumonji-C (JmjC) histone demethylases [445-448]. The enzymes play pivotal roles in epigenetic regulation and cellular differentiation [365, 444]. Interestingly, 2-HG accumulation has also been correlated with increased susceptibility to DNA damage [364] and delayed resolution and repair post damage induction in tumour cells [449]. Parallely, cisplatin induced DNA damage has been shown to lead to reduction in stiffness of nuclei in HeLa cells [450], as a prerequisite for DNA damage repair.

These prior observations, when put in context of our study, might explain the intriguing outcomes observed by us, where the addition of 2-HG to wild-type BATi cells resulted in a whitening phenotype and nuclear softening. The abovementioned changes could also possibly underlie the differentiation block seen in other cell types when exposed to D-2HG or when expressing mutant IDH enzymes [374]. With changes in global histone methylation levels (Fig 2.37), our study posits that there might be transcriptional cascades under co-regulation by 2-HG mediated control of methylation at promoters. This would be specifically relevant in the context of cytoskeletal rearrangement and stress response genes, who are consistently co-

directional in their expression in our models (up in tissues and down in cells). It could possibly be due to these genes being in a similar topological associated domain (TAD)s, whose architecture is in turn regulated by PTMs (like acetylation) on insulator proteins (like CTCF (CCCTC binding factor)), which can be altered upon mitochondrial dysfunction. Interestingly, 2-HG has been previously implicated in controlling CTCF function and enhancer interactions by causing hypermethylation at CTCF binding genes and leading to insulator dysfunction [451]. Alternatively, 2-HG accumulation in our KO cells might be rendering them more susceptible to DNA damage, thereby leading to nuclear softening as a consequence.

Understanding the links between metabolism, epigenetics, and cellular responses has far-reaching implications. Understanding the impact of 2-HG on nuclear architecture and its implications for cellular physiology could provide valuable insights into metabolite mediated retrograde signaling from mitochondria to nucleus.

Assessing factors underlying nuclear softening in CLPP KO BAT provides insights into epigenetic remodeling mediated by mitochondrial dysfunction:

Our study revealed interesting observations related to dysfunctional mitochondria mediated metabolic rewiring ultimately altering nuclear stiffness and consequent epigenetic changes in the nucleus. The observation of nuclear softening and the reduction in H3K9me3 levels in CLPP knockout models that exhibit explicit spatial crowding is in alignment with recent findings that force-induced changes in nuclear mechanics (and consequent epigenetic changes) can exert profound effects on gene expression [452-455]. Hence, our study has revealed a potential mechanistic link between: the force generated due to spatial crowding, mitochondria associating on the nuclear boundary and stress response-mediated metabolite-altering nuclear stiffness. Functionally, it can be speculated that either the induced local nuclear indentations are causal of chromatin reorganization and gene expression changes, or instead, are a consequence of metabolic rewiring mediated chromatin reorganization [456].

Research has shown that mechanical forces can play a pivotal role in transcriptional regulation, and the physical properties of the nucleus are integral to this process [457, 458]. Force-induced transcriptional up-regulation at the nuclear interior is associated with lower H3K9me3 levels [456]. This demethylation promotes Pol II recruitment to the promoter site, resulting in enhanced transcription. Conversely Pol II recruitment is inhibited at the periphery, and is correlated with higher levels of H3K9me3 [456, 459, 460]. Additionally, heterochromatin driven changes in nuclear stiffness, underscored by reduction in Lamin A levels has been shown to be valuable for protecting cells against genotoxic stress [371]. It would be interesting to study the 3-D chromatin organization in KO cells, to validate this hypothesis further. Our study is unique since it points at the first instance of "intracellular mechanical force" arising from spatial crowding of the mitochondria and lipid droplets in the cytoplasm, thereby creating a densely populated microenvironment for the nucleus (Fig 2.14).

The interplay between mechanical forces, nuclear mechanics, and gene expression is complex and multidimensional. It involves dynamic interactions between the cell's adhesions, cytoskeleton, and the nucleus [452, 457]. These interactions lead

to local tensile stresses at the cell-extracellular matrix interface, which subsequently affect nuclear properties, such as morphology and chromatin modification levels [372]. Our results highlight a co-expression pattern between cytoskeletal genes and stress response genes, thereby hinting at regulation transcriptional programs by global epigenetic modifications. Specific insights into the nature of this co-regulation can be determined by Hi-C analysis of nuclei from BAT tissue, or mapping the chromatin states by ATAC Seq (Fig 3.2). This intersection of mechanics and epigenetics underscores the dynamic and intricate nature of cellular responses to intracellular stresses, opening up exciting avenues for further investigation into the mechanotransduction mechanisms that influence gene expression and cell behavior.
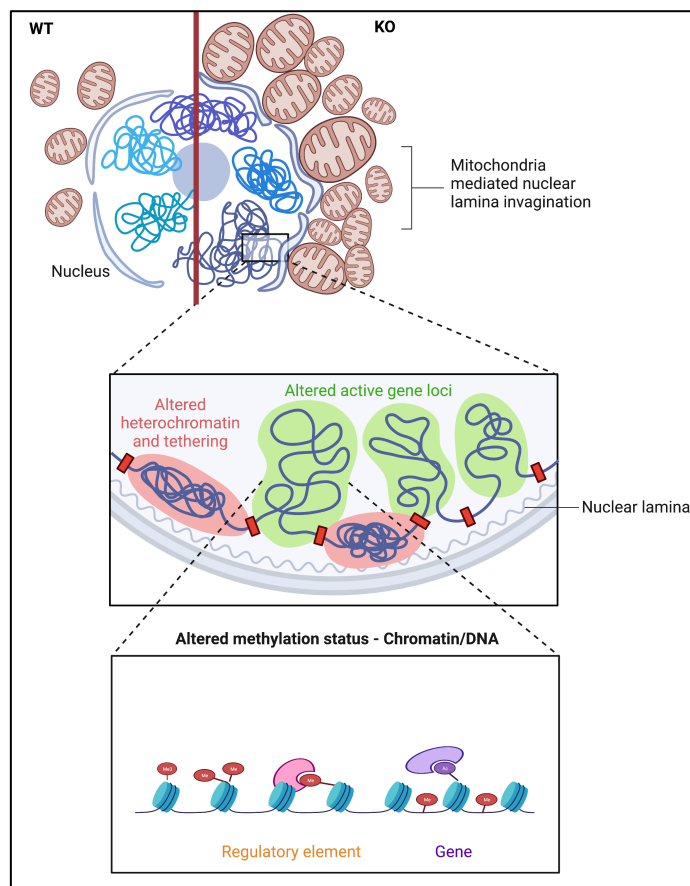
Figure 3.2 Hypothetical mode depicting strategies for future investigations.

Future directions - CLPP KO BAT – a potential model for studying the functional relevance of mitochondria-nucleus contacts

Previous studies have shown mitochondrial stress to lead to increased contacts between mitochondria and nucleus under both tumour-like conditions and in physiological mutants in the skeletal muscle [461]. However, neither the mechanism of these contacts, not their functional importance has been reported yet. Deletor mice show close mitochondrial-nuclear contacts and central nuclei in mouse models and similar observations are made in patients with mitochondrial myopathy [461]. Another study showed that cells stressed by staurosporine (that activates the mitochondrial

retrograde response) led to increased impingement of nucleus by mitochondria [373]. This interaction is facilitated by the translocator protein (TSPO), which prevents the segregation of mitochondria via mitophagy [373]. The study, although correlative and lacking strong evidence, claimed that these interactions enabled the redistribution of cholesterol within the nucleus, thereby sustaining the pro-survival response through inhibition of NF-κB deacetylation [373].

Our study is the first report of a physiological perturbation like mitochondrial dysfunction to be mediating alteration in nuclear stiffness at the cellular level, and at the same time, manifesting as increased contacts and impingement of nucleus by mitochondria at the tissue level. It is intriguing to consider the potential exchange of metabolites, signaling molecules, proteins, and building blocks between the mitochondria and the nucleus. Such exchanges may play a pivotal role in mediating retrograde signaling from the dysfunctional mitochondria to the nucleus, ultimately influencing gene expression changes.

The comprehensive understanding of the intricate network connecting mitochondrial dysfunction, metabolic rewiring, stress responses, and nuclear alterations provides valuable insights into the complex regulatory networks underlying cellular adaptations to organelle dysfunction. These findings also hold implications for therapeutic strategies targeting metabolic disorders and adipose tissue dysfunction.

SUMMARY

In summary, this study highlights two major themes: First, that adipose tissue specific loss of CLPP does not confer any metabolic benefits to the mice whereas BAT-specific CLPP deletion confers mild metabolic benefits to mice under both normal chow diet and under metabolic stress. Loss of CLPP leads to widespread changes in iWAT at transcriptome, proteome and metabolome level, and the tissues communicate to each other potentially via metabolites, homocitrulline and homoarginine. Second, this study characterizes CLPP loss mediated remodelling of whitened BAT. The study also identifies a novel pathway of how dysfunctional mitochondria communicate to the nucleus via a signaling metabolite, 2 hydroxyglutarate, and consequently leads to remodeling of BAT.

REFERENCES

1. Pakos-Zebrucka, K., et al., *The integrated stress response.* EMBO Rep, 2016. **17**(10): p. 1374-1395.
2. Nikkanen, J., et al., *Mitochondrial DNA Replication Defects Disturb Cellular dNTP Pools and Remodel One-Carbon Metabolism.* Cell Metab, 2016. **23**(4): p. 635-48.
3. Wortel, I.M.N., et al., *Surviving Stress: Modulation of ATF4-Mediated Stress Responses in Normal and Malignant Cells.* Trends Endocrinol Metab, 2017. **28**(11): p. 794-806.
4. Lee, J.H., et al., *The Role of Adipose Tissue Mitochondria: Regulation of Mitochondrial Function for the Treatment of Metabolic Diseases.* Int J Mol Sci, 2019. **20**(19).
5. Siersbæk, M.S., et al., *Genome-wide profiling of peroxisome proliferator-activated receptor γ in primary epididymal, inguinal, and brown adipocytes reveals depot-selective binding correlated with gene expression.* Mol Cell Biol, 2012. **32**(17): p. 3452-63.
6. *mt DNA.*
7. Goossens, G. and E. Blaak, *Adipose Tissue Dysfunction and Impaired Metabolic Health in Human Obesity: A Matter of Oxygen?* Frontiers in Endocrinology, 2015. **6**.
8. Pfanner, N., B. Warscheid, and N. Wiedemann, *Mitochondrial proteins: from biogenesis to functional networks.* Nature Reviews Molecular Cell Biology, 2019. **20**(5): p. 267-284.
9. Yu, A.Y.H. and W.A. Houry, *ClpP: A distinctive family of cylindrical energy-dependent serine proteases.* FEBS Letters, 2007. **581**(19): p. 3749-3757.
10. Kühlbrandt, W., *Structure and function of mitochondrial membrane protein complexes.* BMC Biol, 2015. **13**: p. 89.
11. Frey, T.G. and C.A. Mannella, *The internal structure of mitochondria.* Trends Biochem Sci, 2000. **25**(7): p. 319-24.
12. Halabi, D., et al., *Fetal programming of adipose tissue function by gestational chronodisruption.* Sleep Science, 2020. **13**: p. 51-8.
13. Mayr, J.A., et al., *Spectrum of combined respiratory chain defects.* J Inherit Metab Dis, 2015. **38**(4): p. 629-40.
14. Szczepanowska, K. and A. Trifunovic, *Mitochondrial matrix proteases: quality control and beyond.* Febs j, 2022. **289**(22): p. 7128-7146.
15. Ernster, L. and G. Schatz, *Mitochondria: a historical review.* J Cell Biol, 1981. **91**(3 Pt 2): p. 227s-255s.
16. Zimorski, V., et al., *Endosymbiotic theory for organelle origins.* Curr Opin Microbiol, 2014. **22**: p. 38-48.
17. Martin, W.F., S. Garg, and V. Zimorski, *Endosymbiotic theories for eukaryote origin.* Philos Trans R Soc Lond B Biol Sci, 2015. **370**(1678): p. 20140330.
18. Rath, S., et al., *MitoCarta3.0: an updated mitochondrial proteome now with sub-organelle localization and pathway annotations.* Nucleic Acids Res, 2021. **49**(D1): p. D1541-d1547.
19. Iovine, J.C., S.M. Claypool, and N.N. Alder, *Mitochondrial compartmentalization: emerging themes in structure and function.* Trends Biochem Sci, 2021. **46**(11): p. 902-917.
20. Colombini, M., *Voltage gating in the mitochondrial channel, VDAC.* J Membr Biol, 1989. **111**(2): p. 103-11.
21. S, B., *- Molecular Biology of the Cell, Sixth Edition; ISBN: 9780815344643; and Molecular.* Int J Mol Sci, 2015. **16**(12): p. 28123-5.
22. Protasoni, M. and M. Zeviani, *Mitochondrial Structure and Bioenergetics in Normal and Disease Conditions.* Int J Mol Sci, 2021. **22**(2).

23. Yang, Z., et al., *Mitochondrial Membrane Remodeling.* Front Bioeng Biotechnol, 2021. **9**: p. 786806.

24. Rambold, A.S., S. Cohen, and J. Lippincott-Schwartz, *Fatty acid trafficking in starved cells: regulation by lipid droplet lipolysis, autophagy, and mitochondrial fusion dynamics.* Dev Cell, 2015. **32**(6): p. 678-92.

25. Benador, I.Y., et al., *Mitochondria Bound to Lipid Droplets Have Unique Bioenergetics, Composition, and Dynamics that Support Lipid Droplet Expansion.* Cell Metab, 2018. **27**(4): p. 869-885.e6.

26. Khosravi, S. and M.E. Harner, *The MICOS complex, a structural element of mitochondria with versatile functions.* Biol Chem, 2020. **401**(6-7): p. 765-778.

27. Mannella, C.A., *Consequences of Folding the Mitochondrial Inner Membrane.* Front Physiol, 2020. **11**: p. 536.

28. Giacomello, M., et al., *The cell biology of mitochondrial membrane dynamics.* Nat Rev Mol Cell Biol, 2020. **21**(4): p. 204-224.

29. Collins, T.J., et al., *Mitochondria are morphologically and functionally heterogeneous within cells.* Embo j, 2002. **21**(7): p. 1616-27.

30. Westermann, B., *Mitochondrial fusion and fission in cell life and death.* Nat Rev Mol Cell Biol, 2010. **11**(12): p. 872-84.

31. Chan, D.C., *Mitochondrial Dynamics and Its Involvement in Disease.* Annu Rev Pathol, 2020. **15**: p. 235-259.

32. Wai, T. and T. Langer, *Mitochondrial Dynamics and Metabolic Regulation.* Trends Endocrinol Metab, 2016. **27**(2): p. 105-117.

33. Nunnari, J. and A. Suomalainen, *Mitochondria: in sickness and in health.* Cell, 2012. **148**(6): p. 1145-59.

34. Spinelli, J.B. and M.C. Haigis, *The multifaceted contributions of mitochondria to cellular metabolism.* Nat Cell Biol, 2018. **20**(7): p. 745-754.

35. Stehling, O. and R. Lill, *The role of mitochondria in cellular iron-sulfur protein biogenesis: mechanisms, connected processes, and diseases.* Cold Spring Harb Perspect Biol, 2013. **5**(8): p. a011312.

36. Giorgi, C., S. Marchi, and P. Pinton, *The machineries, regulation and cellular functions of mitochondrial calcium.* Nat Rev Mol Cell Biol, 2018. **19**(11): p. 713-730.

37. Ashrafi, G. and T.L. Schwarz, *The pathways of mitophagy for quality control and clearance of mitochondria.* Cell Death Differ, 2013. **20**(1): p. 31-42.

38. Vringer, E. and S.W.G. Tait, *Mitochondria and Inflammation: Cell Death Heats Up.* Front Cell Dev Biol, 2019. **7**: p. 100.

39. Scialò, F., D.J. Fernández-Ayala, and A. Sanz, *Role of Mitochondrial Reverse Electron Transport in ROS Signaling: Potential Roles in Health and Disease.* Front Physiol, 2017. **8**: p. 428.

40. Jensen, P.K., *Antimycin-insensitive oxidation of succinate and reduced nicotinamide-adenine dinucleotide in electron-transport particles. II. Steroid effects.* Biochim Biophys Acta, 1966. **122**(2): p. 167-74.

41. Ikon, N. and R.O. Ryan, *Cardiolipin and mitochondrial cristae organization.* Biochim Biophys Acta Biomembr, 2017. **1859**(6): p. 1156-1163.

42. Zhang, D., et al., *Mitochondria in oocyte aging: current understanding.* Facts Views Vis Obgyn, 2017. **9**(1): p. 29-38.

43. Akram, M., *Citric acid cycle and role of its intermediates in metabolism.* Cell Biochem Biophys, 2014. **68**(3): p. 475-8.

44. Martínez-Reyes, I. and N.S. Chandel, *Mitochondrial TCA cycle metabolites control physiology and disease.* Nat Commun, 2020. **11**(1): p. 102.

45. Houten, S.M. and R.J. Wanders, *A general introduction to the biochemistry of mitochondrial fatty acid β-oxidation.* J Inherit Metab Dis, 2010. **33**(5): p. 469-77.

46. Read, A.D., et al., *Mitochondrial iron-sulfur clusters: Structure, function, and an emerging role in vascular biology.* Redox Biol, 2021. **47**: p. 102164.

47. Galluzzi, L., et al., *Mitochondrial control of cellular life, stress, and death.* Circ Res, 2012. **111**(9): p. 1198-207.

48. Tsatmali, M., et al., *Reactive oxygen species modulate the differentiation of neurons in clonal cortical cultures.* Mol Cell Neurosci, 2006. **33**(4): p. 345-57.

49. Berk, A.J. and D.A. Clayton, *Mechanism of mitochondrial DNA replication in mouse L-cells: asynchronous replication of strands, segregation of circular daughter molecules, aspects of topology and turnover of an initiation sequence.* J Mol Biol, 1974. **86**(4): p. 801-24.

50. Bonekamp, N.A. and N.G. Larsson, *SnapShot: Mitochondrial Nucleoid.* Cell, 2018. **172**(1-2): p. 388-388.e1.

51. Kukat, C., et al., *Cross-strand binding of TFAM to a single mtDNA molecule forms the mitochondrial nucleoid.* Proc Natl Acad Sci U S A, 2015. **112**(36): p. 11288-93.

52. Koh, J.H., et al., *Mitochondrial TFAM as a Signaling Regulator between Cellular Organelles: A Perspective on Metabolic Diseases.* Diabetes Metab J, 2021. **45**(6): p. 853-865.

53. Kukat, C., et al., *Super-resolution microscopy reveals that mammalian mitochondrial nucleoids have a uniform size and frequently contain a single copy of mtDNA.* Proc Natl Acad Sci U S A, 2011. **108**(33): p. 13534-9.

54. Kotrys, A.V. and R.J. Szczesny, *Mitochondrial Gene Expression and Beyond-Novel Aspects of Cellular Physiology.* Cells, 2019. **9**(1).

55. Gray, H. and T.W. Wong, *Purification and identification of subunit structure of the human mitochondrial DNA polymerase.* J Biol Chem, 1992. **267**(9): p. 5835-41.

56. Tiranti, V., et al., *A full-length cDNA encoding a mitochondrial DNA-specific single-stranded DNA binding protein from Xenopus laevis.* Nucleic Acids Res, 1991. **19**(15): p. 4291.

57. Spelbrink, J.N., et al., *Human mitochondrial DNA deletions associated with mutations in the gene encoding Twinkle, a phage T7 gene 4-like protein localized in mitochondria.* Nat Genet, 2001. **28**(3): p. 223-31.

58. Gustafsson, C.M., M. Falkenberg, and N.G. Larsson, *Maintenance and Expression of Mammalian Mitochondrial DNA.* Annu Rev Biochem, 2016. **85**: p. 133-60.

59. Falkenberg, M., *Mitochondrial DNA replication in mammalian cells: overview of the pathway.* Essays Biochem, 2018. **62**(3): p. 287-296.

60. Kelly, J.L., A.L. Greenleaf, and I.R. Lehman, *Isolation of the nuclear gene encoding a subunit of the yeast mitochondrial RNA polymerase.* J Biol Chem, 1986. **261**(22): p. 10348-51.

61. Ngo, H.B., et al., *Distinct structural features of TFAM drive mitochondrial DNA packaging versus transcriptional activation.* Nat Commun, 2014. **5**: p. 3077.

62. Hillen, H.S., et al., *Structural Basis of Mitochondrial Transcription Initiation.* Cell, 2017. **171**(5): p. 1072-1081.e10.

63. Ramachandran, A., et al., *Human mitochondrial transcription factors TFAM and TFB2M work synergistically in promoter melting during transcription initiation.* Nucleic Acids Res, 2017. **45**(2): p. 861-874.

64. Greber, B.J. and N. Ban, *Structure and Function of the Mitochondrial Ribosome.* Annu Rev Biochem, 2016. **85**: p. 103-32.

65. Priesnitz, C. and T. Becker, *Pathways to balance mitochondrial translation and protein import.* Genes Dev, 2018. **32**(19-20): p. 1285-1296.

66. Amunts, A., et al., *Ribosome. The structure of the human mitochondrial ribosome.* Science, 2015. **348**(6230): p. 95-98.

67. Rackham, O. and A. Filipovska, *Organization and expression of the mammalian mitochondrial genome.* Nat Rev Genet, 2022. **23**(10): p. 606-623.

68. Papa, S., et al., *The oxidative phosphorylation system in mammalian mitochondria.* Adv Exp Med Biol, 2012. **942**: p. 3-37.

69. Matsuno-Yagi, A. and Y. Hatefi, *Studies on the mechanism of oxidative phosphorylation. Catalytic site cooperativity in ATP synthesis.* J Biol Chem, 1985. **260**(27): p. 11424-7.

70. Jones, A.J., et al., *Respiratory Complex I in Bos taurus and Paracoccus denitrificans Pumps Four Protons across the Membrane for Every NADH Oxidized.* J Biol Chem, 2017. **292**(12): p. 4987-4995.

71. Mitchell, P., *Possible molecular mechanisms of the protonmotive function of cytochrome systems.* J Theor Biol, 1976. **62**(2): p. 327-67.

72. Snyder, C.H., et al., *Role of the Rieske iron-sulfur protein midpoint potential in the protonmotive Q-cycle mechanism of the cytochrome bc1 complex.* J Bioenerg Biomembr, 1999. **31**(3): p. 235-42.

73. Vercellino, I. and L.A. Sazanov, *The assembly, regulation and function of the mitochondrial respiratory chain.* Nat Rev Mol Cell Biol, 2022. **23**(2): p. 141-161.

74. Lencina, A.M., et al., *Type 2 NADH Dehydrogenase Is the Only Point of Entry for Electrons into the Streptococcus agalactiae Respiratory Chain and Is a Potential Drug Target.* mBio, 2018. **9**(4).

75. Fiedorczuk, K., et al., *Atomic structure of the entire mammalian mitochondrial complex I.* Nature, 2016. **538**(7625): p. 406-410.

76. Stroud, D.A., et al., *Accessory subunits are integral for assembly and function of human mitochondrial complex I.* Nature, 2016. **538**(7623): p. 123-126.

77. Koopman, W.J., P.H. Willems, and J.A. Smeitink, *Monogenic mitochondrial disorders.* N Engl J Med, 2012. **366**(12): p. 1132-41.

78. Morais, V.A., et al., *Parkinson's disease mutations in PINK1 result in decreased Complex I activity and deficient synaptic function.* EMBO Mol Med, 2009. **1**(2): p. 99-111.

79. Gatt, A.P., et al., *Dementia in Parkinson's disease is associated with enhanced mitochondrial complex I deficiency.* Mov Disord, 2016. **31**(3): p. 352-9.

80. Sun, F., et al., *Crystal structure of mitochondrial respiratory membrane protein complex II.* Cell, 2005. **121**(7): p. 1043-57.

81. Dourado, D., M. Swart, and A.T.P. Carvalho, *Why the Flavin Adenine Dinucleotide (FAD) Cofactor Needs To Be Covalently Linked to Complex II of the Electron-Transport Chain for the Conversion of FADH(2) into FAD.* Chemistry, 2018. **24**(20): p. 5246-5252.

82. Bandara, A.B., J.C. Drake, and D.A. Brown, *Complex II subunit SDHD is critical for cell growth and metabolism, which can be partially restored with a synthetic ubiquinone analog.* BMC Mol Cell Biol, 2021. **22**(1): p. 35.

83. Moosavi, B., et al., *The assembly of succinate dehydrogenase: a key enzyme in bioenergetics.* Cell Mol Life Sci, 2019. **76**(20): p. 4023-4042.

84. Cecchini, G., *Function and structure of complex II of the respiratory chain.* Annu Rev Biochem, 2003. **72**: p. 77-109.

85. Miyadera, H., et al., *Atpenins, potent and specific inhibitors of mitochondrial complex II (succinate-ubiquinone oxidoreductase).* Proc Natl Acad Sci U S A, 2003. **100**(2): p. 473-7.

86. Solmaz, S.R. and C. Hunte, *Structure of complex III with bound cytochrome c in reduced state and definition of a minimal core interface for electron transfer.* J Biol Chem, 2008. **283**(25): p. 17542-9.

87. Meinhardt, S.W., et al., *Identification of a stable ubisemiquinone and characterization of the effects of ubiquinone oxidation-reduction status on the Rieske iron-sulfur protein in the three-subunit ubiquinol-cytochrome c oxidoreductase complex of Paracoccus denitrificans.* J Biol Chem, 1987. **262**(18): p. 8702-6.

88. Zhu, J., et al., *Simultaneous reduction of iron-sulfur protein and cytochrome b(L) during ubiquinol oxidation in cytochrome bc(1) complex.* Proc Natl Acad Sci U S A, 2007. **104**(12): p. 4864-9.

89. Acín-Pérez, R., et al., *Respiratory complex III is required to maintain complex I in mammalian mitochondria.* Mol Cell, 2004. **13**(6): p. 805-15.

90. Protasoni, M., et al., *Respiratory supercomplexes act as a platform for complex III-mediated maturation of human mitochondrial complexes I and IV.* Embo j, 2020. **39**(3): p. e102817.

91. Kadenbach, B., et al., *Mitochondrial energy metabolism is regulated via nuclear-coded subunits of cytochrome c oxidase.* Free Radic Biol Med, 2000. **29**(3-4): p. 211-21.

92. Kadenbach, B., *Complex IV - The regulatory center of mitochondrial oxidative phosphorylation.* Mitochondrion, 2021. **58**: p. 296-302.

93. Timón-Gómez, A., et al., *Mitochondrial cytochrome c oxidase biogenesis: Recent developments.* Semin Cell Dev Biol, 2018. **76**: p. 163-178.

94. Jonckheere, A.I., J.A. Smeitink, and R.J. Rodenburg, *Mitochondrial ATP synthase: architecture, function and pathology.* J Inherit Metab Dis, 2012. **35**(2): p. 211-25.

95. Ueno, H., et al., *ATP-driven stepwise rotation of F_oF_1-ATP synthase.* Proceedings of the National Academy of Sciences, 2005. **102**(5): p. 1333-1338.

96. Anand, R., A.S. Reichert, and A.K. Kondadi, *Emerging Roles of the MICOS Complex in Cristae Dynamics and Biogenesis.* Biology (Basel), 2021. **10**(7).

97. Strauss, M., et al., *Dimer ribbons of ATP synthase shape the inner mitochondrial membrane.* Embo j, 2008. **27**(7): p. 1154-60.

98. Angeli, S., et al., *The mitochondrial permeability transition pore activates the mitochondrial unfolded protein response and promotes aging.* eLife, 2021. **10**: p. e63453.

99. Schägger, H. and K. Pfeiffer, *Supercomplexes in the respiratory chains of yeast and mammalian mitochondria.* Embo j, 2000. **19**(8): p. 1777-83.

100. Letts, J.A., K. Fiedorczuk, and L.A. Sazanov, *The architecture of respiratory supercomplexes.* Nature, 2016. **537**(7622): p. 644-648.

101. Gu, J., et al., *The architecture of the mammalian respirasome.* Nature, 2016. **537**(7622): p. 639-43.

102. Vercellino, I. and L.A. Sazanov, *Structure and assembly of the mammalian mitochondrial supercomplex CIII(2)CIV.* Nature, 2021. **598**(7880): p. 364-367.

103. Guo, X., et al., *Mitochondrial stress is relayed to the cytosol by an OMA1-DELE1-HRI pathway.* Nature, 2020. **579**(7799): p. 427-432.

104. Brzezinski, P., A. Moe, and P. Ädelroth, *Structure and Mechanism of Respiratory III-IV Supercomplexes in Bioenergetic Membranes.* Chem Rev, 2021. **121**(15): p. 9644-9673.

105. Hackenbrock, C.R., B. Chazotte, and S.S. Gupte, *The random collision model and a critical assessment of diffusion and collision in mitochondrial electron transport.* J Bioenerg Biomembr, 1986. **18**(5): p. 331-68.

106. Dudkina, N.V., et al., *The higher level of organization of the oxidative phosphorylation system: mitochondrial supercomplexes.* J Bioenerg Biomembr, 2008. **40**(5): p. 419-24.

107. Fedor, J.G. and J. Hirst, *Mitochondrial Supercomplexes Do Not Enhance Catalysis by Quinone Channeling.* Cell Metab, 2018. **28**(3): p. 525-531.e4.

108. Javadov, S., et al., *Mitochondrial respiratory supercomplexes in mammalian cells: structural versus functional role.* J Mol Med (Berl), 2021. **99**(1): p. 57-73.

109. Wallace, D.C., *Mitochondrial diseases in man and mouse.* Science, 1999. **283**(5407): p. 1482-8.

110. Schon, E.A., S. DiMauro, and M. Hirano, *Human mitochondrial DNA: roles of inherited and somatic mutations.* Nat Rev Genet, 2012. **13**(12): p. 878-90.

111. Webb, B.D., G.A. Diaz, and P. Prasun, *Mitochondrial translation defects and human disease.* J Transl Genet Genom, 2020. **4**: p. 71-80.

112. Götz, A., et al., *Exome sequencing identifies mitochondrial alanyl-tRNA synthetase mutations in infantile mitochondrial cardiomyopathy.* Am J Hum Genet, 2011. **88**(5): p. 635-42.

113. Jose, C., et al., *Mitoplasticity: adaptation biology of the mitochondrion to the cellular redox state in physiology and carcinogenesis.* Antioxid Redox Signal, 2013. **18**(7): p. 808-49.

114. Deshwal, S., K.U. Fiedler, and T. Langer, *Mitochondrial Proteases: Multifaceted Regulators of Mitochondrial Plasticity.* Annu Rev Biochem, 2020. **89**: p. 501-528.

115. Levytskyy, R.M., I. Bohovych, and O. Khalimonchuk, *Metalloproteases of the Inner Mitochondrial Membrane.* Biochemistry, 2017. **56**(36): p. 4737-4746.

116. Song, J., J.M. Herrmann, and T. Becker, *Quality control of the mitochondrial proteome.* Nat Rev Mol Cell Biol, 2021. **22**(1): p. 54-70.

117. Quirós, P.M., T. Langer, and C. López-Otín, *New roles for mitochondrial proteases in health, ageing and disease.* Nat Rev Mol Cell Biol, 2015. **16**(6): p. 345-59.

118. Hanson, P.I. and S.W. Whiteheart, *AAA+ proteins: have engine, will work.* Nat Rev Mol Cell Biol, 2005. **6**(7): p. 519-29.

119. Neuwald, A.F., et al., *AAA+: A class of chaperone-like ATPases associated with the assembly, operation, and disassembly of protein complexes.* Genome Res, 1999. **9**(1): p. 27-43.

120. Puchades, C., et al., *Structure of the mitochondrial inner membrane AAA+ protease YME1 gives insight into substrate processing.* Science, 2017. **358**(6363).

121. Leonhard, K., et al., *Membrane protein degradation by AAA proteases in mitochondria: extraction of substrates from either membrane surface.* Mol Cell, 2000. **5**(4): p. 629-38.

122. Ohba, Y., T. MacVicar, and T. Langer, *Regulation of mitochondrial plasticity by the i-AAA protease YME1L.* Biol Chem, 2020. **401**(6-7): p. 877-890.

123. Koppen, M., et al., *Variable and tissue-specific subunit composition of mitochondrial m-AAA protease complexes linked to hereditary spastic paraplegia.* Mol Cell Biol, 2007. **27**(2): p. 758-67.

124. Wai, T., et al., *The membrane scaffold SLP2 anchors a proteolytic hub in mitochondria containing PARL and the i-AAA protease YME1L.* EMBO Rep, 2016. **17**(12): p. 1844-1856.

125. Almajan, E.R., et al., *AFG3L2 supports mitochondrial protein synthesis and Purkinje cell survival.* J Clin Invest, 2012. **122**(11): p. 4048-58.

126. Nolden, M., et al., *The m-AAA protease defective in hereditary spastic paraplegia controls ribosome assembly in mitochondria.* Cell, 2005. **123**(2): p. 277-89.

127. Anand, R., et al., *The i-AAA protease YME1L and OMA1 cleave OPA1 to balance mitochondrial fusion and fission.* J Cell Biol, 2014. **204**(6): p. 919-29.

128. Rainbolt, T.K., et al., *Stress-regulated translational attenuation adapts mitochondrial protein import through Tim17A degradation.* Cell Metab, 2013. **18**(6): p. 908-19.

129. Potting, C., et al., *TRIAP1/PRELI complexes prevent apoptosis by mediating intramitochondrial transport of phosphatidic acid.* Cell Metab, 2013. **18**(2): p. 287-95.

130. Vande Walle, L., et al., *The mitochondrial serine protease HtrA2/Omi cleaves RIP1 during apoptosis of Ba/F3 cells induced by growth factor withdrawal.* Cell Res, 2010. **20**(4): p. 421-33.

131. Polianskyte, Z., et al., *LACTB is a filament-forming protein localized in mitochondria.* Proc Natl Acad Sci U S A, 2009. **106**(45): p. 18960-5.

132. Lee, Y.G., et al., *LONP1 and ClpP cooperatively regulate mitochondrial proteostasis for cancer cell survival.* Oncogenesis, 2021. **10**(2): p. 18.

133. Pryde, K.R., J.W. Taanman, and A.H. Schapira, *A LON-ClpP Proteolytic Axis Degrades Complex I to Extinguish ROS Production in Depolarized Mitochondria.* Cell Rep, 2016. **17**(10): p. 2522-2531.

134. Pomatto, L.C., R. Raynes, and K.J. Davies, *The peroxisomal Lon protease LonP2 in aging and disease: functions and comparisons with mitochondrial Lon protease LonP1.* Biol Rev Camb Philos Soc, 2017. **92**(2): p. 739-753.

135. Teng, H., et al., *Oxygen-sensitive mitochondrial accumulation of cystathionine β-synthase mediated by Lon protease.* Proc Natl Acad Sci U S A, 2013. **110**(31): p. 12679-84.

136. Bezawork-Geleta, A., et al., *Mitochondrial matrix proteostasis is linked to hereditary paraganglioma: LON-mediated turnover of the human flavinylation factor SDH5 is regulated by its interaction with SDHA.* Faseb j, 2014. **28**(4): p. 1794-804.

137. Kita, K., T. Suzuki, and T. Ochi, *Diphenylarsinic acid promotes degradation of glutaminase C by mitochondrial Lon protease.* J Biol Chem, 2012. **287**(22): p. 18163-72.

138. Fukuda, R., et al., *HIF-1 regulates cytochrome oxidase subunits to optimize efficiency of respiration in hypoxic cells.* Cell, 2007. **129**(1): p. 111-22.

139. Bota, D.A. and K.J. Davies, *Lon protease preferentially degrades oxidized mitochondrial aconitase by an ATP-stimulated mechanism.* Nat Cell Biol, 2002. **4**(9): p. 674-80.

140. Granot, Z., et al., *Turnover of mitochondrial steroidogenic acute regulatory (StAR) protein by Lon protease: the unexpected effect of proteasome inhibitors.* Mol Endocrinol, 2007. **21**(9): p. 2164-77.

141. Tian, Q., et al., *Lon peptidase 1 (LONP1)-dependent breakdown of mitochondrial 5-aminolevulinic acid synthase protein by heme in human liver cells.* J Biol Chem, 2011. **286**(30): p. 26424-30.

142. Matsushima, Y., Y. Goto, and L.S. Kaguni, *Mitochondrial Lon protease regulates mitochondrial DNA copy number and transcription by selective degradation of mitochondrial transcription factor A (TFAM).* Proc Natl Acad Sci U S A, 2010. **107**(43): p. 18410-5.

143. Matsushima, Y., et al., *Mitochondrial Lon protease is a gatekeeper for proteins newly imported into the matrix.* Communications Biology, 2021. **4**(1): p. 974.

144. Wang, N., et al., *A human mitochondrial ATP-dependent protease that is highly homologous to bacterial Lon protease.* Proc Natl Acad Sci U S A, 1993. **90**(23): p. 11247-51.

145. Quirós, P.M., et al., *ATP-dependent Lon protease controls tumor bioenergetics by reprogramming mitochondrial activity.* Cell Rep, 2014. **8**(2): p. 542-56.

146. Xu, Z., et al., *Disuse-associated loss of the protease LONP1 in muscle impairs mitochondrial function and causes reduced skeletal muscle mass and strength.* Nature Communications, 2022. **13**(1): p. 894.

147. Guo, Q., et al., *Mitochondrial proteostasis stress in muscle drives a long-range protective response to alleviate dietary obesity independently of ATF4.* Science Advances, 2022. **8**(30): p. eabo0340.

148. Liu, K., A. Ologbenla, and W.A. Houry, *Dynamics of the ClpP serine protease: a model for self-compartmentalized proteases.* Crit Rev Biochem Mol Biol, 2014. **49**(5): p. 400-12.

149. Kang, S.G., et al., *Human mitochondrial ClpP is a stable heptamer that assembles into a tetradecamer in the presence of ClpX.* J Biol Chem, 2005. **280**(42): p. 35424-32.

150. Lowth, B.R., et al., *Substrate recognition and processing by a Walker B mutant of the human mitochondrial AAA+ protein CLPX.* J Struct Biol, 2012. **179**(2): p. 193-201.

151. Mabanglo, M.F. and W.A. Houry, *Recent structural insights into the mechanism of ClpP protease regulation by AAA+ chaperones and small molecules.* J Biol Chem, 2022. **298**(5): p. 101781.

152. Fei, X., et al., *Structures of the ATP-fueled ClpXP proteolytic machine bound to protein substrate.* eLife, 2020. **9**: p. e52774.

153. Moreno-Cinos, C., et al., *ClpP Protease, a Promising Antimicrobial Target.* Int J Mol Sci, 2019. **20**(9).

154. Nakano, M.M., et al., *Mutations conferring amino acid residue substitutions in the carboxy-terminal domain of RNA polymerase alpha can suppress clpX and clpP with respect to developmentally regulated transcription in Bacillus subtilis.* Mol Microbiol, 2000. **37**(4): p. 869-84.

155. Nakano, S., et al., *A regulatory protein that interferes with activator-stimulated transcription in bacteria.* Proc Natl Acad Sci U S A, 2003. **100**(7): p. 4233-8.

156. Neher, S.B., et al., *Proteomic profiling of ClpXP substrates after DNA damage reveals extensive instability within SOS regulon.* Mol Cell, 2006. **22**(2): p. 193-204.

157. Hengge, R., *Proteolysis of sigmaS (RpoS) and the general stress response in Escherichia coli.* Res Microbiol, 2009. **160**(9): p. 667-76.

158. Zhou, Y., et al., *The RssB response regulator directly targets sigma(S) for degradation by ClpXP.* Genes Dev, 2001. **15**(5): p. 627-37.

159. Aljghami, M.E., et al., *Cellular functions of the ClpP protease impacting bacterial virulence.* Front Mol Biosci, 2022. **9**: p. 1054408.

160. Simmer, F., et al., *Genome-wide RNAi of C. elegans using the hypersensitive rrf-3 strain reveals novel gene functions.* PLoS Biol, 2003. **1**(1): p. E12.

161. Haynes, C.M., et al., *ClpP mediates activation of a mitochondrial unfolded protein response in C. elegans.* Dev Cell, 2007. **13**(4): p. 467-80.

162. Benedetti, C., et al., *Ubiquitin-like protein 5 positively regulates chaperone gene expression in the mitochondrial unfolded protein response.* Genetics, 2006. **174**(1): p. 229-39.

163. Haynes, C.M., et al., *ClpP Mediates Activation of a Mitochondrial Unfolded Protein Response in C. elegans.* Developmental Cell, 2007. **13**(4): p. 467-480.

164. Zhao, Q., et al., *A mitochondrial specific stress response in mammalian cells.* Embo j, 2002. **21**(17): p. 4411-9.

165. Gerth, U., et al., *Stress induction of the Bacillus subtilis clpP gene encoding a homologue of the proteolytic component of the Clp protease and the involvement of ClpP and ClpX in stress tolerance.* Mol Microbiol, 1998. **28**(4): p. 787-802.

166. Zheng, B., et al., *Characterization of Chloroplast Clp proteins in Arabidopsis: Localization, tissue specificity and stress responses.* Physiol Plant, 2002. **114**(1): p. 92-101.

167. Aldridge, J.E., T. Horibe, and N.J. Hoogenraad, *Discovery of genes activated by the mitochondrial unfolded protein response (mtUPR) and cognate promoter elements.* PLoS One, 2007. **2**(9): p. e874.

168. Guillon, B., et al., *Frataxin deficiency causes upregulation of mitochondrial Lon and ClpP proteases and severe loss of mitochondrial Fe-S proteins.* Febs j, 2009. **276**(4): p. 1036-47.

169. Choi, S.E., et al., *Mitochondrial protease ClpP supplementation ameliorates diet-induced NASH in mice.* J Hepatol, 2022. **77**(3): p. 735-747.

170. Hansen, J., et al., *Decreased expression of the mitochondrial matrix proteases Lon and ClpP in cells from a patient with hereditary spastic paraplegia (SPG13).* Neuroscience, 2008. **153**(2): p. 474-82.

171. Jenkinson, E.M., et al., *Perrault syndrome is caused by recessive mutations in CLPP, encoding a mitochondrial ATP-dependent chambered protease.* Am J Hum Genet, 2013. **92**(4): p. 605-13.

172. Gispert, S., et al., *Loss of mitochondrial peptidase Clpp leads to infertility, hearing loss plus growth retardation via accumulation of CLPX, mtDNA and inflammatory factors.* Hum Mol Genet, 2013. **22**(24): p. 4871-87.

173. Szczepanowska, K., et al., *CLPP coordinates mitoribosomal assembly through the regulation of ERAL1 levels.* EMBO J, 2016. **35**(23): p. 2566-2583.

174. Wang, T., et al., *Mitochondrial unfolded protein response gene Clpp is required to maintain ovarian follicular reserve during aging, for oocyte competence, and development of pre-implantation embryos.* Aging Cell, 2018. **17**(4): p. e12784.

175. Szczepanowska, K., et al., *A salvage pathway maintains highly functional respiratory complex I.* Nat Commun, 2020. **11**(1): p. 1643.

176. Seiferling, D., et al., *Loss of CLPP alleviates mitochondrial cardiomyopathy without affecting the mammalian UPRmt.* EMBO Rep, 2016. **17**(7): p. 953-64.

177. Rumyantseva, A., M. Popovic, and A. Trifunovic, *CLPP deficiency ameliorates neurodegeneration caused by impaired mitochondrial protein synthesis.* Brain, 2022. **145**(1): p. 92-104.

178. Hofsetz, E., et al., *The Mouse Heart Mitochondria N Terminome Provides Insights into ClpXP-Mediated Proteolysis.* Mol Cell Proteomics, 2020. **19**(8): p. 1330-1345.

179. Cole, A., et al., *Inhibition of the Mitochondrial Protease ClpP as a Therapeutic Strategy for Human Acute Myeloid Leukemia.* Cancer Cell, 2015. **27**(6): p. 864-76.

180. Bonkovsky, H.L., J.F. Healey, and J. Pohl, *Purification and characterization of heme oxygenase from chick liver. Comparison of the avian and mammalian enzymes.* Eur J Biochem, 1990. **189**(1): p. 155-66.

181. Kardon, J.R., et al., *Mitochondrial ClpX activates an essential biosynthetic enzyme through partial unfolding.* Elife, 2020. **9**.

182. Kardon, J.R., et al., *Mitochondrial ClpX Activates a Key Enzyme for Heme Biosynthesis and Erythropoiesis.* Cell, 2015. **161**(4): p. 858-67.

183. Kubota, Y., et al., *Novel Mechanisms for Heme-dependent Degradation of ALAS1 Protein as a Component of Negative Feedback Regulation of Heme Biosynthesis.* J Biol Chem, 2016. **291**(39): p. 20516-29.

184. Zurita Rendón, O. and E.A. Shoubridge, *LONP1 Is Required for Maturation of a Subset of Mitochondrial Proteins, and Its Loss Elicits an Integrated Stress Response.* Mol Cell Biol, 2018. **38**(20).

185. Fischer, F., et al., *Human CLPP reverts the longevity phenotype of a fungal ClpP deletion strain.* Nat Commun, 2013. **4**: p. 1397.

186. Strack, P.R., et al., *Polymerase delta-interacting protein 38 (PDIP38) modulates the stability and activity of the mitochondrial AAA+ protease CLPXP.* Commun Biol, 2020. **3**(1): p. 646.

187. Butow, R.A. and N.G. Avadhani, *Mitochondrial signaling: the retrograde response.* Mol Cell, 2004. **14**(1): p. 1-15.

188. Parikh, V.S., et al., *The mitochondrial genotype can influence nuclear gene expression in yeast.* Science, 1987. **235**(4788): p. 576-80.

189. Liu, S., S. Liu, and H. Jiang, *Multifaceted roles of mitochondrial stress responses under ETC dysfunction - repair, destruction and pathogenesis.* Febs j, 2022. **289**(22): p. 6994-7013.

190. Martinus, R.D., et al., *Selective induction of mitochondrial chaperones in response to loss of the mitochondrial genome.* Eur J Biochem, 1996. **240**(1): p. 98-103.

191. Yoneda, T., et al., *Compartment-specific perturbation of protein handling activates genes encoding mitochondrial chaperones.* J Cell Sci, 2004. **117**(Pt 18): p. 4055-66.

192. Kühl, I., et al., *Transcriptomic and proteomic landscape of mitochondrial dysfunction reveals secondary coenzyme Q deficiency in mammals.* Elife, 2017. **6**.

193. Forsström, S., et al., *Fibroblast Growth Factor 21 Drives Dynamics of Local and Systemic Stress Responses in Mitochondrial Myopathy with mtDNA Deletions.* Cell Metab, 2019. **30**(6): p. 1040-1054.e7.

194. Dogan, S.A., et al., *Tissue-specific loss of DARS2 activates stress responses independently of respiratory chain deficiency in the heart.* Cell Metab, 2014. **19**(3): p. 458-69.

195. Harding, H.P., et al., *An integrated stress response regulates amino acid metabolism and resistance to oxidative stress.* Mol Cell, 2003. **11**(3): p. 619-33.

196. Quirós, P.M., et al., *Multi-omics analysis identifies ATF4 as a key regulator of the mitochondrial stress response in mammals.* J Cell Biol, 2017. **216**(7): p. 2027-2045.

197. Tahmasebi, S., et al., *Translation deregulation in human disease.* Nat Rev Mol Cell Biol, 2018. **19**(12): p. 791-807.

198. Girardin, S.E., et al., *The eIF2α kinase HRI in innate immunity, proteostasis, and mitochondrial stress.* Febs j, 2021. **288**(10): p. 3094-3107.

199. García, M.A., E.F. Meurs, and M. Esteban, *The dsRNA protein kinase PKR: virus and cell control.* Biochimie, 2007. **89**(6-7): p. 799-811.

200. Lemaire, P.A., J. Lary, and J.L. Cole, *Mechanism of PKR activation: dimerization and kinase activation in the absence of double-stranded RNA.* J Mol Biol, 2005. **345**(1): p. 81-90.

201. Rozpedek, W., et al., *The Role of the PERK/eIF2α/ATF4/CHOP Signaling Pathway in Tumor Progression During Endoplasmic Reticulum Stress.* Curr Mol Med, 2016. **16**(6): p. 533-44.

202. Ni, M., et al., *Regulation of PERK signaling and leukemic cell survival by a novel cytosolic isoform of the UPR regulator GRP78/BiP.* PLoS One, 2009. **4**(8): p. e6868.

203. Liu, Z., et al., *Protein kinase R-like ER kinase and its role in endoplasmic reticulum stress-decided cell fate.* Cell Death Dis, 2015. **6**(7): p. e1822.

204. Ye, J., et al., *The GCN2-ATF4 pathway is critical for tumour cell survival and proliferation in response to nutrient deprivation.* Embo j, 2010. **29**(12): p. 2082-96.

205. Costa-Mattioli, M. and P. Walter, *The integrated stress response: From mechanism to disease.* Science, 2020. **368**(6489).

206. Koromilas, A.E., *Roles of the translation initiation factor eIF2α serine 51 phosphorylation in cancer formation and treatment.* Biochim Biophys Acta, 2015. **1849**(7): p. 871-80.

207. Hinnebusch, A.G., I.P. Ivanov, and N. Sonenberg, *Translational control by 5'-untranslated regions of eukaryotic mRNAs.* Science, 2016. **352**(6292): p. 1413-6.

208. Pavitt, G.D., *Regulation of translation initiation factor eIF2B at the hub of the integrated stress response.* Wiley Interdiscip Rev RNA, 2018. **9**(6): p. e1491.

209. Novoa, I., et al., *Feedback inhibition of the unfolded protein response by GADD34-mediated dephosphorylation of eIF2alpha.* J Cell Biol, 2001. **153**(5): p. 1011-22.

210. Jousse, C., et al., *Inhibition of a constitutive translation initiation factor 2alpha phosphatase, CReP, promotes survival of stressed cells.* J Cell Biol, 2003. **163**(4): p. 767-75.

211. Kaspar, S., et al., *Adaptation to mitochondrial stress requires CHOP-directed tuning of ISR.* Sci Adv, 2021. **7**(22).

212. Fessler, E., et al., *A pathway coordinated by DELE1 relays mitochondrial stress to the cytosol.* Nature, 2020. **579**(7799): p. 433-437.

213. Bao, X.R., et al., *Mitochondrial dysfunction remodels one-carbon metabolism in human cells.* Elife, 2016. **5**.

214. Tyynismaa, H., et al., *Mitochondrial myopathy induces a starvation-like response.* Hum Mol Genet, 2010. **19**(20): p. 3948-58.

215. Khan, N.A., et al., *mTORC1 Regulates Mitochondrial Integrated Stress Response and Mitochondrial Myopathy Progression.* Cell Metab, 2017. **26**(2): p. 419-428.e5.

216. Yatsuga, S., et al., *Growth differentiation factor 15 as a useful biomarker for mitochondrial disorders.* Ann Neurol, 2015. **78**(5): p. 814-23.

217. Ducker, G.S. and J.D. Rabinowitz, *One-Carbon Metabolism in Health and Disease.* Cell Metab, 2017. **25**(1): p. 27-42.

218. Clare, C.E., et al., *One-Carbon Metabolism: Linking Nutritional Biochemistry to Epigenetic Programming of Long-Term Development.* Annu Rev Anim Biosci, 2019. **7**: p. 263-287.

219. Chattopadhyay, S., R.G. Moran, and I.D. Goldman, *Pemetrexed: biochemical and cellular pharmacology, mechanisms, and clinical applications.* Mol Cancer Ther, 2007. **6**(2): p. 404-17.

220. Dickhout, J.G., et al., *Integrated stress response modulates cellular redox state via induction of cystathionine γ-lyase: cross-talk between integrated stress response and thiol metabolism.* J Biol Chem, 2012. **287**(10): p. 7603-14.

221. Torrence, M.E., et al., *The mTORC1-mediated activation of ATF4 promotes protein and glutathione synthesis downstream of growth signals.* Elife, 2021. **10**.

222. Lange, P.S., et al., *ATF4 is an oxidative stress-inducible, prodeath transcription factor in neurons in vitro and in vivo.* J Exp Med, 2008. **205**(5): p. 1227-42.

223. Ye, J., et al., *Pyruvate kinase M2 promotes de novo serine synthesis to sustain mTORC1 activity and cell proliferation.* Proc Natl Acad Sci U S A, 2012. **109**(18): p. 6904-9.

224. Pathria, G., et al., *Targeting the Warburg effect via LDHA inhibition engages ATF4 signaling for cancer cell survival.* Embo j, 2018. **37**(20).

225. Amelio, I., et al., *Serine and glycine metabolism in cancer.* Trends Biochem Sci, 2014. **39**(4): p. 191-8.

226. Sánchez-González, C., et al., *Dysfunctional oxidative phosphorylation shunts branched-chain amino acid catabolism onto lipogenesis in skeletal muscle.* Embo j, 2020. **39**(14): p. e103812.

227. Burrill, J.S., et al., *Inflammation and ER stress regulate branched-chain amino acid uptake and metabolism in adipocytes.* Mol Endocrinol, 2015. **29**(3): p. 411-20.

228. Newgard, C.B., *Interplay between lipids and branched-chain amino acids in development of insulin resistance.* Cell Metab, 2012. **15**(5): p. 606-14.

229. Herman, M.A., et al., *Adipose tissue branched chain amino acid (BCAA) metabolism modulates circulating BCAA levels.* J Biol Chem, 2010. **285**(15): p. 11348-56.

230. Richard, A.J., et al., *Adipose Tissue: Physiology to Metabolic Dysfunction*, in *Endotext*, K.R. Feingold, et al., Editors. 2000, MDText.com, Inc.
Copyright © 2000-2023, MDText.com, Inc.: South Dartmouth (MA).

231. Shinde, A.B., A. Song, and Q.A. Wang, *Brown Adipose Tissue Heterogeneity, Energy Metabolism, and Beyond.* Front Endocrinol (Lausanne), 2021. **12**: p. 651763.

232. Rosen, E.D. and B.M. Spiegelman, *Adipocytes as regulators of energy balance and glucose homeostasis.* Nature, 2006. **444**(7121): p. 847-53.

233. Cypess, A.M., et al., *Identification and importance of brown adipose tissue in adult humans.* N Engl J Med, 2009. **360**(15): p. 1509-17.

234. Cinti, S., *Adipocyte differentiation and transdifferentiation: plasticity of the adipose organ.* J Endocrinol Invest, 2002. **25**(10): p. 823-35.

235. Parra-Peralbo, E., A. Talamillo, and R. Barrio, *Origin and Development of the Adipose Tissue, a Key Organ in Physiology and Disease.* Front Cell Dev Biol, 2021. **9**: p. 786129.

236. Farmer, S.R., *Transcriptional control of adipocyte formation.* Cell Metab, 2006. **4**(4): p. 263-73.

237. Seale, P., et al., *Transcriptional control of brown fat determination by PRDM16.* Cell Metab, 2007. **6**(1): p. 38-54.

238. Puigserver, P., et al., *A cold-inducible coactivator of nuclear receptors linked to adaptive thermogenesis.* Cell, 1998. **92**(6): p. 829-39.

239. Lin, J., C. Handschin, and B.M. Spiegelman, *Metabolic control through the PGC-1 family of transcription coactivators.* Cell Metab, 2005. **1**(6): p. 361-70.

240. Loncar, D., *Convertible adipose tissue in mice.* Cell Tissue Res, 1991. **266**(1): p. 149-61.

241. Wu, J., et al., *Beige adipocytes are a distinct type of thermogenic fat cell in mouse and human.* Cell, 2012. **150**(2): p. 366-76.

242. Lo, K.A. and L. Sun, *Turning WAT into BAT: a review on regulators controlling the browning of white adipocytes.* Biosci Rep, 2013. **33**(5).

243. Cheng, L., et al., *Brown and beige adipose tissue: a novel therapeutic strategy for obesity and type 2 diabetes mellitus.* Adipocyte, 2021. **10**(1): p. 48-65.

244. Guerra, C., et al., *Emergence of brown adipocytes in white fat in mice is under genetic control. Effects on body weight and adiposity.* J Clin Invest, 1998. **102**(2): p. 412-20.

245. Wu, J., P. Cohen, and B.M. Spiegelman, *Adaptive thermogenesis in adipocytes: is beige the new brown?* Genes Dev, 2013. **27**(3): p. 234-50.

246. Seale, P., et al., *PRDM16 controls a brown fat/skeletal muscle switch.* Nature, 2008. **454**(7207): p. 961-7.

247. Gavrilova, O., et al., *Surgical implantation of adipose tissue reverses diabetes in lipoatrophic mice.* J Clin Invest, 2000. **105**(3): p. 271-8.

248. Orava, J., et al., *Different metabolic responses of human brown adipose tissue to activation by cold and insulin.* Cell Metab, 2011. **14**(2): p. 272-9.

249. Bartelt, A., et al., *Brown adipose tissue activity controls triglyceride clearance.* Nat Med, 2011. **17**(2): p. 200-5.

250. Stock, M.J. and N.J. Rothwell, *Role of brown adipose tissue thermogenesis in overfeeding: a review.* J R Soc Med, 1983. **76**(1): p. 71-3.

251. Betz, M.J. and S. Enerbäck, *Human Brown Adipose Tissue: What We Have Learned So Far.* Diabetes, 2015. **64**(7): p. 2352-60.

252. Goossens, G.H., *The role of adipose tissue dysfunction in the pathogenesis of obesity-related insulin resistance.* Physiol Behav, 2008. **94**(2): p. 206-18.

253. Villarroya, F., et al., *Inflammation of brown/beige adipose tissues in obesity and metabolic disease.* J Intern Med, 2018. **284**(5): p. 492-504.

254. Chait, A. and L.J. den Hartigh, *Adipose Tissue Distribution, Inflammation and Its Metabolic Consequences, Including Diabetes and Cardiovascular Disease.* Front Cardiovasc Med, 2020. **7**: p. 22.

255. Bournat, J.C. and C.W. Brown, *Mitochondrial dysfunction in obesity.* Curr Opin Endocrinol Diabetes Obes, 2010. **17**(5): p. 446-52.

256. Fischer, B., et al., *Inverse relationship between body mass index and mitochondrial oxidative phosphorylation capacity in human subcutaneous adipocytes.* Am J Physiol Endocrinol Metab, 2015. **309**(4): p. E380-7.

257. Heinonen, S., et al., *Impaired Mitochondrial Biogenesis in Adipose Tissue in Acquired Obesity.* Diabetes, 2015. **64**(9): p. 3135-45.

258. Wilson-Fritch, L., et al., *Mitochondrial remodeling in adipose tissue associated with obesity and treatment with rosiglitazone.* J Clin Invest, 2004. **114**(9): p. 1281-9.

259. Rong, J.X., et al., *Adipose mitochondrial biogenesis is suppressed in db/db and high-fat diet-fed mice and improved by rosiglitazone.* Diabetes, 2007. **56**(7): p. 1751-60.

260. Chen, X.H., et al., *TNF-alpha induces mitochondrial dysfunction in 3T3-L1 adipocytes.* Mol Cell Endocrinol, 2010. **328**(1-2): p. 63-9.

261. Dahlman, I., et al., *Downregulation of electron transport chain genes in visceral adipose tissue in type 2 diabetes independent of obesity and possibly involving tumor necrosis factor-alpha.* Diabetes, 2006. **55**(6): p. 1792-9.

262. Vankoningsloo, S., et al., *Mitochondrial dysfunction induces triglyceride accumulation in 3T3-L1 cells: role of fatty acid beta-oxidation and glucose.* J Lipid Res, 2005. **46**(6): p. 1133-49.

263. Pidoux, G., et al., *Optic atrophy 1 is an A-kinase anchoring protein on lipid droplets that mediates adrenergic control of lipolysis.* Embo j, 2011. **30**(21): p. 4371-86.

264. Nicholls, D.G. and R.M. Locke, *Thermogenic mechanisms in brown fat.* Physiol Rev, 1984. **64**(1): p. 1-64.

265. Meyer, C.W., et al., *Adaptive thermogenesis and thermal conductance in wild-type and UCP1-KO mice.* Am J Physiol Regul Integr Comp Physiol, 2010. **299**(5): p. R1396-406.

266. Guarnieri, A.R., T.W. Benson, and M. Tranter, *Calcium cycling as a mediator of thermogenic metabolism in adipose tissue.* Mol Pharmacol, 2022. **102**(1): p. 51-9.

267. Ikeda, K., et al., *UCP1-independent signaling involving SERCA2b-mediated calcium cycling regulates beige fat thermogenesis and systemic glucose homeostasis.* Nat Med, 2017. **23**(12): p. 1454-1465.

268. Townsend, K.L. and Y.H. Tseng, *Brown fat fuel utilization and thermogenesis.* Trends Endocrinol Metab, 2014. **25**(4): p. 168-77.

269. Jiang, L. and R.J. Deberardinis, *Cancer metabolism: When more is less.* Nature, 2012. **489**(7417): p. 511-2.

270. Daikoku, T., et al., *Specific elevation of transcript levels of particular protein subtypes induced in brown adipose tissue by cold exposure.* Biochim Biophys Acta, 2000. **1457**(3): p. 263-72.

271. Yu, X.X., et al., *Cold elicits the simultaneous induction of fatty acid synthesis and beta-oxidation in murine brown adipose tissue: prediction from differential gene expression and confirmation in vivo.* Faseb j, 2002. **16**(2): p. 155-68.

272. Fujimoto, Y., et al., *Metabolic changes in adipose tissues in response to β(3) -adrenergic receptor activation in mice.* J Cell Biochem, 2019. **120**(1): p. 821-835.

273. Winther, S., et al., *Restricting glycolysis impairs brown adipocyte glucose and oxygen consumption.* Am J Physiol Endocrinol Metab, 2018. **314**(3): p. E214-e223.

274. Herzig, S., et al., *Identification and functional expression of the mitochondrial pyruvate carrier.* Science, 2012. **337**(6090): p. 93-6.

275. Bricker, D.K., et al., *A mitochondrial pyruvate carrier required for pyruvate uptake in yeast, Drosophila, and humans.* Science, 2012. **337**(6090): p. 96-100.

276. Rajagopalan, K.N., et al., *Metabolic plasticity maintains proliferation in pyruvate dehydrogenase deficient cells.* Cancer Metab, 2015. **3**: p. 7.

277. Cheng, T., et al., *Pyruvate carboxylase is required for glutamine-independent growth of tumor cells.* Proc Natl Acad Sci U S A, 2011. **108**(21): p. 8674-9.

278. Wang, Z., et al., *Chronic cold exposure enhances glucose oxidation in brown adipose tissue.* EMBO Rep, 2020. **21**(11): p. e50085.

279. Panic, V., et al., *Mitochondrial pyruvate carrier is required for optimal brown fat thermogenesis.* Elife, 2020. **9**.

280. Cooney, G.J., et al., *In vivo insulin sensitivity of the pyruvate dehydrogenase complex in tissues of the rat.* Am J Physiol, 1993. **265**(1 Pt 1): p. E102-7.

281. Bryson, J.M., et al., *High-fat feeding alters the response of rat PDH complex to acute changes in glucose and insulin.* Am J Physiol, 1995. **268**(4 Pt 1): p. E752-7.

282. Holness, M.J. and M.C. Sugden, *The impact of increased dietary lipid on the regulation of glucose uptake and oxidation by insulin in brown- and a range of white-adipose-tissue depots in vivo.* Int J Obes Relat Metab Disord, 1999. **23**(6): p. 629-38.

283. Hao, Q., et al., *Transcriptome profiling of brown adipose tissue during cold exposure reveals extensive regulation of glucose metabolism.* Am J Physiol Endocrinol Metab, 2015. **308**(5): p. E380-92.

284. Barquissau, V., et al., *White-to-brite conversion in human adipocytes promotes metabolic reprogramming towards fatty acid anabolic and catabolic pathways.* Mol Metab, 2016. **5**(5): p. 352-365.

285. Müller, S., et al., *Proteomic Analysis of Human Brown Adipose Tissue Reveals Utilization of Coupled and Uncoupled Energy Expenditure Pathways.* Sci Rep, 2016. **6**: p. 30030.

286. Shackney, S.E. and C.D. Joel, *Stimulation of glucose metabolism in brown adipose tissue by addition of insulin in vitro.* J Biol Chem, 1966. **241**(17): p. 4004-10.

287. Isler, D., H.P. Hill, and M.K. Meier, *Glucose metabolism in isolated brown adipocytes under beta-adrenergic stimulation. Quantitative contribution of glucose to total thermogenesis.* Biochem J, 1987. **245**(3): p. 789-93.

288. Saggerson, E.D., T.W. McAllister, and H.S. Baht, *Lipogenesis in rat brown adipocytes. Effects of insulin and noradrenaline, contributions from glucose and lactate as precursors and comparisons with white adipocytes.* Biochem J, 1988. **251**(3): p. 701-9.

289. Jiang, L., et al., *Quantitative metabolic flux analysis reveals an unconventional pathway of fatty acid synthesis in cancer cells deficient for the mitochondrial citrate transport protein.* Metab Eng, 2017. **43**(Pt B): p. 198-207.

290. Jiang, L., et al., *Leptin contributes to the adaptive responses of mice to high-fat diet intake through suppressing the lipogenic pathway.* PLoS One, 2009. **4**(9): p. e6884.

291. Chondronikola, M., et al., *Brown Adipose Tissue Activation Is Linked to Distinct Systemic Effects on Lipid Metabolism in Humans.* Cell Metab, 2016. **23**(6): p. 1200-1206.

292. Labbe, S.M., et al., *mTORC1 is Required for Brown Adipose Tissue Recruitment and Metabolic Adaptation to Cold.* Sci Rep, 2016. **6**: p. 37223.

293. Baba, S., et al., *CT Hounsfield units of brown adipose tissue increase with activation: preclinical and clinical studies.* J Nucl Med, 2010. **51**(2): p. 246-50.

294. Ma, S.W. and D.O. Foster, *Uptake of glucose and release of fatty acids and glycerol by rat brown adipose tissue in vivo.* Can J Physiol Pharmacol, 1986. **64**(5): p. 609-14.

295. Li, Y., et al., *Taking control over intracellular fatty acid levels is essential for the analysis of thermogenic function in cultured primary brown and brite/beige adipocytes.* EMBO Rep, 2014. **15**(10): p. 1069-76.

296. Mottillo, E.P., et al., *Lipolytic products activate peroxisome proliferator-activated receptor (PPAR) α and δ in brown adipocytes to match fatty acid oxidation with supply.* J Biol Chem, 2012. **287**(30): p. 25038-48.

297. Haemmerle, G., et al., *Defective lipolysis and altered energy metabolism in mice lacking adipose triglyceride lipase.* Science, 2006. **312**(5774): p. 734-7.

298. Ahmadian, M., et al., *Desnutrin/ATGL is regulated by AMPK and is required for a brown adipose phenotype.* Cell Metab, 2011. **13**(6): p. 739-48.

299. Shin, H., et al., *Lipolysis in Brown Adipocytes Is Not Essential for Cold-Induced Thermogenesis in Mice.* Cell Metab, 2017. **26**(5): p. 764-777.e5.

300.	Chitraju, C., et al., *Lipid Droplets in Brown Adipose Tissue Are Dispensable for Cold-Induced Thermogenesis.* Cell Rep, 2020. **33**(5): p. 108348.

301.	Ouellet, V., et al., *Brown adipose tissue oxidative metabolism contributes to energy expenditure during acute cold exposure in humans.* J Clin Invest, 2012. **122**(2): p. 545-52.

302.	Wolfgang, M.J. and M.D. Lane, *The role of hypothalamic malonyl-CoA in energy homeostasis.* J Biol Chem, 2006. **281**(49): p. 37265-9.

303.	Wang, Z., et al., *Energy metabolism in brown adipose tissue.* Febs j, 2021. **288**(12): p. 3647-3662.

304.	Lee, J., J.M. Ellis, and M.J. Wolfgang, *Adipose fatty acid oxidation is required for thermogenesis and potentiates oxidative stress-induced inflammation.* Cell Rep, 2015. **10**(2): p. 266-79.

305.	Simcox, J., et al., *Global Analysis of Plasma Lipids Identifies Liver-Derived Acylcarnitines as a Fuel Source for Brown Fat Thermogenesis.* Cell Metab, 2017. **26**(3): p. 509-522.e6.

306.	Trayhurn, P., *Fatty acid synthesis in vivo in brown adipose tissue, liver and white adipose tissue of the cold-acclimated rat.* FEBS Lett, 1979. **104**(1): p. 13-6.

307.	Buckley, M.G. and E.A. Rath, *Regulation of fatty acid synthesis and malonyl-CoA content in mouse brown adipose tissue in response to cold-exposure, starvation or re-feeding.* Biochem J, 1987. **243**(2): p. 437-42.

308.	Jiang, L., et al., *Metabolic reprogramming during TGFβ1-induced epithelial-to-mesenchymal transition.* Oncogene, 2015. **34**(30): p. 3908-16.

309.	Festuccia, W.T., et al., *Expression of glycerokinase in brown adipose tissue is stimulated by the sympathetic nervous system.* Am J Physiol Regul Integr Comp Physiol, 2003. **284**(6): p. R1536-41.

310.	Mottillo, E.P., et al., *Coupling of lipolysis and de novo lipogenesis in brown, beige, and white adipose tissues during chronic β3-adrenergic receptor activation.* J Lipid Res, 2014. **55**(11): p. 2276-86.

311.	Irshad, Z., et al., *Diacylglycerol acyltransferase 2 links glucose utilization to fatty acid oxidation in the brown adipocytes.* J Lipid Res, 2017. **58**(1): p. 15-30.

312.	Sanchez-Gurmaches, J., et al., *Brown Fat AKT2 Is a Cold-Induced Kinase that Stimulates ChREBP-Mediated De Novo Lipogenesis to Optimize Fuel Storage and Thermogenesis.* Cell Metab, 2018. **27**(1): p. 195-209.e6.

313.	Adlanmerini, M., et al., *Circadian lipid synthesis in brown fat maintains murine body temperature during chronic cold.* Proc Natl Acad Sci U S A, 2019. **116**(37): p. 18691-18699.

314.	Mills, E.L., et al., *Accumulation of succinate controls activation of adipose tissue thermogenesis.* Nature, 2018. **560**(7716): p. 102-106.

315.	Jedrychowski, M.P., et al., *Facultative protein selenation regulates redox sensitivity, adipose tissue thermogenesis, and obesity.* Proc Natl Acad Sci U S A, 2020. **117**(20): p. 10789-10796.

316.	Chouchani, E.T., et al., *Mitochondrial ROS regulate thermogenic energy expenditure and sulfenylation of UCP1.* Nature, 2016. **532**(7597): p. 112-6.

317.	Wang, G., et al., *Regulation of UCP1 and Mitochondrial Metabolism in Brown Adipose Tissue by Reversible Succinylation.* Mol Cell, 2019. **74**(4): p. 844-857.e7.

318.	Yoneshiro, T., et al., *BCAA catabolism in brown fat controls energy homeostasis through SLC25A44.* Nature, 2019. **572**(7771): p. 614-619.

319.	Wallace, M., et al., *Enzyme promiscuity drives branched-chain fatty acid synthesis in adipose tissues.* Nat Chem Biol, 2018. **14**(11): p. 1021-1031.

320. Weir, G., et al., *Substantial Metabolic Activity of Human Brown Adipose Tissue during Warm Conditions and Cold-Induced Lipolysis of Local Triglycerides.* Cell Metab, 2018. **27**(6): p. 1348-1355.e4.

321. López-Soriano, F.J. and M. Alemany, *Effect of alanine on in vitro glucose utilization by rat interscapular brown adipose tissue.* Biochim Biophys Acta, 1989. **1010**(3): p. 338-41.

322. Kazak, L., et al., *A creatine-driven substrate cycle enhances energy expenditure and thermogenesis in beige fat.* Cell, 2015. **163**(3): p. 643-55.

323. Rahbani, J.F., et al., *Creatine kinase B controls futile creatine cycling in thermogenic fat.* Nature, 2021. **590**(7846): p. 480-485.

324. Bertholet, A.M., et al., *Mitochondrial Patch Clamp of Beige Adipocytes Reveals UCP1-Positive and UCP1-Negative Cells Both Exhibiting Futile Creatine Cycling.* Cell Metab, 2017. **25**(4): p. 811-822.e4.

325. Kazak, L., et al., *Genetic Depletion of Adipocyte Creatine Metabolism Inhibits Diet-Induced Thermogenesis and Drives Obesity.* Cell Metab, 2017. **26**(4): p. 693.

326. Forner, F., et al., *Proteome differences between brown and white fat mitochondria reveal specialized metabolic functions.* Cell Metab, 2009. **10**(4): p. 324-35.

327. Vernochet, C., et al., *Adipose-specific deletion of TFAM increases mitochondrial oxidation and protects mice against obesity and insulin resistance.* Cell Metab, 2012. **16**(6): p. 765-76.

328. Vernochet, C., et al., *Adipose tissue mitochondrial dysfunction triggers a lipodystrophic syndrome with insulin resistance, hepatosteatosis, and cardiovascular complications.* Faseb j, 2014. **28**(10): p. 4408-19.

329. Sriskanthadevan-Pirahas, S., et al., *Adipose mitochondrial metabolism controls body growth by modulating systemic cytokine and insulin signaling.* Cell Rep, 2022. **39**(6): p. 110802.

330. Boutant, M., et al., *Mfn2 is critical for brown adipose tissue thermogenic function.* EMBO J, 2017. **36**(11): p. 1543-1558.

331. Pereira, R.O., et al., *OPA1 deletion in brown adipose tissue improves thermoregulation and systemic metabolism via FGF21.* Elife, 2021. **10**.

332. Bean, C., et al., *The mitochondrial protein Opa1 promotes adipocyte browning that is dependent on urea cycle metabolites.* Nat Metab, 2021. **3**(12): p. 1633-1647.

333. Zhang, D., et al., *Resistance to high-fat diet-induced obesity and insulin resistance in mice with very long-chain acyl-CoA dehydrogenase deficiency.* Cell Metab, 2010. **11**(5): p. 402-11.

334. Tormos, K.V., et al., *Mitochondrial complex III ROS regulate adipocyte differentiation.* Cell Metab, 2011. **14**(4): p. 537-44.

335. Chouchani, E.T., L. Kazak, and B.M. Spiegelman, *Mitochondrial reactive oxygen species and adipose tissue thermogenesis: Bridging physiology and mechanisms.* J Biol Chem, 2017. **292**(41): p. 16810-16816.

336. Ewels, P.A., et al., *The nf-core framework for community-curated bioinformatics pipelines.* Nature Biotechnology, 2020. **38**(3): p. 276-278.

337. *The targets R package: a dynamic Make-like function-oriented pipeline toolkit for reproducibility and high-performance computing.*

338. Love, M.I., W. Huber, and S. Anders, *Moderated estimation of fold change and dispersion for RNA-seq data with DESeq2.* Genome Biol, 2014. **15**(12): p. 550.

339. Wu, T., et al., *clusterProfiler 4.0: A universal enrichment tool for interpreting omics data.* Innovation (Camb), 2021. **2**(3): p. 100141.

340. Huber, W., et al., *Orchestrating high-throughput genomic analysis with Bioconductor.* Nat Methods, 2015. **12**(2): p. 115-21.

341. *AnnotationDbi.*

342. Jew, B., et al., *Accurate estimation of cell composition in bulk expression through robust integration of single-cell information.* Nat Commun, 2020. **11**(1): p. 1971.

343. Shamsi, F., et al., *Vascular smooth muscle-derived Trpv1(+) progenitors are a source of cold-induced thermogenic adipocytes.* Nat Metab, 2021. **3**(4): p. 485-495.

344. *UMAP: Uniform Manifold Approximation and Projection for Dimension Reduction.*

345. Stuart, T., et al., *Comprehensive Integration of Single-Cell Data.* Cell, 2019. **177**(7): p. 1888-1902.e21.

346. Andreatta, M. and S.J. Carmona, *UCell: Robust and scalable single-cell gene signature scoring.* Comput Struct Biotechnol J, 2021. **19**: p. 3796-3798.

347. Gu, Z., R. Eils, and M. Schlesner, *Complex heatmaps reveal patterns and correlations in multidimensional genomic data.* Bioinformatics, 2016. **32**(18): p. 2847-9.

348. Chong, J. and J. Xia, *MetaboAnalystR: an R package for flexible and reproducible analysis of metabolomics data.* Bioinformatics, 2018. **34**(24): p. 4313-4314.

349. Becker, C., et al., *CLPP deficiency protects against metabolic syndrome but hinders adaptive thermogenesis.* EMBO Rep, 2018. **19**(5).

350. Greenstein, J.P., et al., *Studies on the metabolism of amino acids and related compounds in vivo. III. Prevention of ammonia toxicity by arginine and related compounds.* Archives of Biochemistry and Biophysics, 1956. **64**(2): p. 342-354.

351. Ryan, W.L. and I.C. Wells, *HOMOCITRULLINE AND HOMOARGININE SYNTHESIS FROM LYSINE.* Science, 1964. **144**(3622): p. 1122-7.

352. Bigot, A., et al., *Liver involvement in urea cycle disorders: a review of the literature.* J Inherit Metab Dis, 2017. **40**(6): p. 757-769.

353. Mo, Q., et al., *Identification and characterization of a supraclavicular brown adipose tissue in mice.* JCI Insight, 2017. **2**(11).

354. Mourier, A., et al., *Loss of LRPPRC causes ATP synthase deficiency.* Hum Mol Genet, 2014. **23**(10): p. 2580-92.

355. van Loo, G. and M.J.M. Bertrand, *Death by TNF: a road to inflammation.* Nature Reviews Immunology, 2023. **23**(5): p. 289-303.

356. Briukhovetska, D., et al., *Interleukins in cancer: from biology to therapy.* Nature Reviews Cancer, 2021. **21**(8): p. 481-499.

357. Shamsi, F., et al., *Comprehensive analysis of intercellular communication in the thermogenic adipose niche.* Commun Biol, 2023. **6**(1): p. 761.

358. Kotzbeck, P., et al., *Brown adipose tissue whitening leads to brown adipocyte death and adipose tissue inflammation.* J Lipid Res, 2018. **59**(5): p. 784-794.

359. Sun, K., X. Li, and P.E. Scherer, *Extracellular Matrix (ECM) and Fibrosis in Adipose Tissue: Overview and Perspectives.* Compr Physiol, 2023. **13**(1): p. 4387-4407.

360. Sahlin, K., *Boosting fat burning with carnitine: an old friend comes out from the shadow.* J Physiol, 2011. **589**(Pt 7): p. 1509-10.

361. Dang, L., et al., *Cancer-associated IDH1 mutations produce 2-hydroxyglutarate.* Nature, 2010. **465**(7300): p. 966.

362. *ascorbic acid.*

363. Li, Q. and T. Hoppe, *Role of amino acid metabolism in mitochondrial homeostasis.* Front Cell Dev Biol, 2023. **11**: p. 1127618.

364. Wang, P., et al., *Oncometabolite D-2-Hydroxyglutarate Inhibits ALKBH DNA Repair Enzymes and Sensitizes IDH Mutant Cells to Alkylating Agents.* Cell Rep, 2015. **13**(11): p. 2353-2361.

365. Xu, W., et al., *Oncometabolite 2-hydroxyglutarate is a competitive inhibitor of α-ketoglutarate-dependent dioxygenases.* Cancer Cell, 2011. **19**(1): p. 17-30.

366. Notarangelo, G., et al., *Oncometabolite d-2HG alters T cell metabolism to impair CD8(+) T cell function.* Science, 2022. **377**(6614): p. 1519-1529.

367. Kernytsky, A., et al., *IDH2 mutation-induced histone and DNA hypermethylation is progressively reversed by small-molecule inhibition.* Blood, 2015. **125**(2): p. 296-303.

368. Fan, J., et al., *Human phosphoglycerate dehydrogenase produces the oncometabolite D-2-hydroxyglutarate.* ACS Chem Biol, 2015. **10**(2): p. 510-6.

369. Spillier, Q. and R. Frédérick, *Phosphoglycerate dehydrogenase (PHGDH) inhibitors: a comprehensive review 2015-2020.* Expert Opin Ther Pat, 2021. **31**(7): p. 597-608.

370. Jackson, C.B., et al., *De novo serine biosynthesis is protective in mitochondrial disease.* bioRxiv, 2023: p. 2023.03.23.533952.

371. Nava, M.M., et al., *Heterochromatin-Driven Nuclear Softening Protects the Genome against Mechanical Stress-Induced Damage.* Cell, 2020. **181**(4): p. 800-817.e22.

372. Maurer, M. and J. Lammerding, *The Driving Force: Nuclear Mechanotransduction in Cellular Function, Fate, and Disease.* Annu Rev Biomed Eng, 2019. **21**: p. 443-468.

373. Desai, R., et al., *Mitochondria form contact sites with the nucleus to couple prosurvival retrograde response.* Sci Adv, 2020. **6**(51).

374. Lu, C., et al., *IDH mutation impairs histone demethylation and results in a block to cell differentiation.* Nature, 2012. **483**(7390): p. 474-8.

375. Finlin, B.S., et al., *The β3-adrenergic receptor agonist mirabegron improves glucose homeostasis in obese humans.* J Clin Invest, 2020. **130**(5): p. 2319-2331.

376. Ruiz, J.R., et al., *Role of Human Brown Fat in Obesity, Metabolism and Cardiovascular Disease: Strategies to Turn Up the Heat.* Prog Cardiovasc Dis, 2018. **61**(2): p. 232-245.

377. Cypess, A.M., et al., *Activation of human brown adipose tissue by a β3-adrenergic receptor agonist.* Cell Metab, 2015. **21**(1): p. 33-8.

378. Villarroya, J., et al., *New insights into the secretory functions of brown adipose tissue.* J Endocrinol, 2019. **243**(2): p. R19-r27.

379. Félix-Soriano, E., et al., *Changes in brown adipose tissue lipid mediator signatures with aging, obesity, and DHA supplementation in female mice.* Faseb j, 2021. **35**(6): p. e21592.

380. Chondronikola, M., et al., *Brown adipose tissue improves whole-body glucose homeostasis and insulin sensitivity in humans.* Diabetes, 2014. **63**(12): p. 4089-99.

381. Yun, J. and T. Finkel, *Mitohormesis.* Cell Metab, 2014. **19**(5): p. 757-66.

382. Yi, H.S., J.Y. Chang, and M. Shong, *The mitochondrial unfolded protein response and mitohormesis: a perspective on metabolic diseases.* J Mol Endocrinol, 2018. **61**(3): p. R91-r105.

383. Palmeira, C.M., et al., *Mitohormesis and metabolic health: The interplay between ROS, cAMP and sirtuins.* Free Radic Biol Med, 2019. **141**: p. 483-491.

384. Duteil, D., et al., *Lsd1 Ablation Triggers Metabolic Reprogramming of Brown Adipose Tissue.* Cell Rep, 2016. **17**(4): p. 1008-1021.

385. Liu, X., et al., *Paradoxical resistance to diet-induced obesity in UCP1-deficient mice.* J Clin Invest, 2003. **111**(3): p. 399-407.

386. Anunciado-Koza, R., et al., *Inactivation of UCP1 and the glycerol phosphate cycle synergistically increases energy expenditure to resist diet-induced obesity.* J Biol Chem, 2008. **283**(41): p. 27688-27697.

387. Ikeda, K., et al., *A stabilizing factor for mitochondrial respiratory supercomplex assembly regulates energy metabolism in muscle.* Nat Commun, 2013. **4**: p. 2147.

388. Yang, F.T. and K.I. Stanford, *Batokines: Mediators of Inter-Tissue Communication (a Mini-Review).* Curr Obes Rep, 2022. **11**(1): p. 1-9.

389. Stanford, K.I., et al., *Brown adipose tissue regulates glucose homeostasis and insulin sensitivity.* J Clin Invest, 2013. **123**(1): p. 215-23.

390. Croon, M., et al., *FGF21 modulates mitochondrial stress response in cardiomyocytes only under mild mitochondrial dysfunction.* Sci Adv, 2022. **8**(14): p. eabn7105.

391. Kaczmarczyk, A., et al., *A neonate with ornithine aminotransferase deficiency; insights on the hyperammonemia-associated biochemical phenotype of gyrate atrophy.* Mol Genet Metab Rep, 2022. **31**: p. 100857.

392. Jaisson, S., et al., *Measurement of Homocitrulline, A Carbamylation-derived Product, in Serum and Tissues by LC-MS/MS.* Curr Protoc Protein Sci, 2018. **92**(1): p. e56.

393. Sirpal, S., *Myeloperoxidase-mediated lipoprotein carbamylation as a mechanistic pathway for atherosclerotic vascular disease.* Clin Sci (Lond), 2009. **116**(9): p. 681-95.

394. Huang, Y., et al., *Brown adipose TRX2 deficiency activates mtDNA-NLRP3 to impair thermogenesis and protect against diet-induced insulin resistance.* J Clin Invest, 2022. **132**(9).

395. Tang, D., et al., *Degradation of mitochondrial structure and deficiency of complex I were associated with the transgenic CMS of rice.* Biol Res, 2021. **54**(1): p. 6.

396. Mannella, C.A., et al., *Topology of the mitochondrial inner membrane: dynamics and bioenergetic implications.* IUBMB Life, 2001. **52**(3-5): p. 93-100.

397. Gorman, G.S., et al., *Mitochondrial diseases.* Nat Rev Dis Primers, 2016. **2**: p. 16080.

398. Murphy, M.P., *How mitochondria produce reactive oxygen species.* Biochem J, 2009. **417**(1): p. 1-13.

399. Li, X.Y. and Y.L. Yang, *[Mitochondrial disorders associated with mitochondrial respiratory chain complex V deficiency].* Zhongguo Dang Dai Er Ke Za Zhi, 2013. **15**(7): p. 596-600.

400. Sargeant, J.A., et al., *A Review of the Effects of Glucagon-Like Peptide-1 Receptor Agonists and Sodium-Glucose Cotransporter 2 Inhibitors on Lean Body Mass in Humans.* Endocrinol Metab (Seoul), 2019. **34**(3): p. 247-262.

401. Weisberg, S.P., et al., *Obesity is associated with macrophage accumulation in adipose tissue.* J Clin Invest, 2003. **112**(12): p. 1796-808.

402. Xu, H., et al., *Chronic inflammation in fat plays a crucial role in the development of obesity-related insulin resistance.* J Clin Invest, 2003. **112**(12): p. 1821-30.

403. Ziqubu, K., et al., *An insight into brown/beige adipose tissue whitening, a metabolic complication of obesity with the multifactorial origin.* Front Endocrinol (Lausanne), 2023. **14**: p. 1114767.

404. Geng, J., et al., *3D microscopy and deep learning reveal the heterogeneity of crown-like structure microenvironments in intact adipose tissue.* Sci Adv, 2021. **7**(8).

405. Seale, P., S. Kajimura, and B.M. Spiegelman, *Transcriptional control of brown adipocyte development and physiological function--of mice and men.* Genes Dev, 2009. **23**(7): p. 788-97.

406. Modica, S., et al., *Bmp4 Promotes a Brown to White-like Adipocyte Shift.* Cell Rep, 2016. **16**(8): p. 2243-2258.

407. Shimizu, I., et al., *Vascular rarefaction mediates whitening of brown fat in obesity.* J Clin Invest, 2014. **124**(5): p. 2099-112.

408. Rangel-Azevedo, C., et al., *Progressive brown adipocyte dysfunction: Whitening and impaired nonshivering thermogenesis as long-term obesity complications.* J Nutr Biochem, 2022. **105**: p. 109002.

409. Hurwitz, B., et al., *The integrated stress response remodels the microtubule-organizing center to clear unfolded proteins following proteotoxic stress.* Elife, 2022. **11**.

410. Welte, M.A. and A.P. Gould, *Lipid droplet functions beyond energy storage.* Biochim Biophys Acta Mol Cell Biol Lipids, 2017. **1862**(10 Pt B): p. 1260-1272.

411. Petan, T., E. Jarc, and M. Jusović, *Lipid Droplets in Cancer: Guardians of Fat in a Stressful World.* Molecules, 2018. **23**(8).

412. Olzmann, J.A. and P. Carvalho, *Dynamics and functions of lipid droplets.* Nat Rev Mol Cell Biol, 2019. **20**(3): p. 137-155.

413. Henne, W.M., M.L. Reese, and J.M. Goodman, *The assembly of lipid droplets and their roles in challenged cells.* Embo j, 2018. **37**(12).

414. Jarc, E. and T. Petan, *Lipid Droplets and the Management of Cellular Stress.* Yale J Biol Med, 2019. **92**(3): p. 435-452.

415. Nguyen, T.B., et al., *DGAT1-Dependent Lipid Droplet Biogenesis Protects Mitochondrial Function during Starvation-Induced Autophagy.* Dev Cell, 2017. **42**(1): p. 9-21.e5.

416. Herms, A., et al., *AMPK activation promotes lipid droplet dispersion on detyrosinated microtubules to increase mitochondrial fatty acid oxidation.* Nat Commun, 2015. **6**: p. 7176.

417. Bosma, M., et al., *Sequestration of fatty acids in triglycerides prevents endoplasmic reticulum stress in an in vitro model of cardiomyocyte lipotoxicity.* Biochim Biophys Acta, 2014. **1841**(12): p. 1648-55.

418. Ploegh, H.L., *A lipid-based model for the creation of an escape hatch from the endoplasmic reticulum.* Nature, 2007. **448**(7152): p. 435-8.

419. Barba, I., et al., *Effect of intracellular lipid droplets on cytosolic Ca2+ and cell death during ischaemia-reperfusion injury in cardiomyocytes.* J Physiol, 2009. **587**(Pt 6): p. 1331-41.

420. Stevenson, J., E.Y. Huang, and J.A. Olzmann, *Endoplasmic Reticulum-Associated Degradation and Lipid Homeostasis.* Annu Rev Nutr, 2016. **36**: p. 511-42.

421. Vevea, J.D., et al., *Role for Lipid Droplet Biogenesis and Microlipophagy in Adaptation to Lipid Imbalance in Yeast.* Dev Cell, 2015. **35**(5): p. 584-599.

422. Welte, M.A., *Expanding roles for lipid droplets.* Curr Biol, 2015. **25**(11): p. R470-81.

423. Li, Z., et al., *Drosophila lipid droplets buffer the H2Av supply to protect early embryonic development.* Curr Biol, 2014. **24**(13): p. 1485-91.

424. Gallardo-Montejano, V.I., et al., *Nuclear Perilipin 5 integrates lipid droplet lipolysis with PGC-1α/SIRT1-dependent transcriptional regulation of mitochondrial function.* Nat Commun, 2016. **7**: p. 12723.

425. Gustafsson Sheppard, N., et al., *The folate-coupled enzyme MTHFD2 is a nuclear protein and promotes cell proliferation.* Sci Rep, 2015. **5**: p. 15029.

426. Tajan, M., et al., *Serine synthesis pathway inhibition cooperates with dietary serine and glycine limitation for cancer therapy.* Nat Commun, 2021. **12**(1): p. 366.

427. Li, X., et al., *ATF3 promotes the serine synthesis pathway and tumor growth under dietary serine restriction.* Cell Rep, 2021. **36**(12): p. 109706.

428. Muthusamy, T., et al., *Serine restriction alters sphingolipid diversity to constrain tumour growth.* Nature, 2020. **586**(7831): p. 790-795.

429. Labuschagne, C.F., et al., *Serine, but not glycine, supports one-carbon metabolism and proliferation of cancer cells.* Cell Rep, 2014. **7**(4): p. 1248-58.

430. Locasale, J.W., *Serine, glycine and one-carbon units: cancer metabolism in full circle.* Nat Rev Cancer, 2013. **13**(8): p. 572-83.

431. Wang, K., et al., *PHGDH arginine methylation by PRMT1 promotes serine synthesis and represents a therapeutic vulnerability in hepatocellular carcinoma.* Nat Commun, 2023. **14**(1): p. 1011.

432. Dai, Z., et al., *Multi-omics Analysis of the Role of PHGDH in Colon Cancer.* Technol Cancer Res Treat, 2023. **22**: p. 15330338221145994.

433. Wang, C., et al., *Acetylation Stabilizes Phosphoglycerate Dehydrogenase by Disrupting the Interaction of E3 Ligase RNF5 to Promote Breast Tumorigenesis.* Cell Rep, 2020. **32**(6): p. 108021.

434. Pacold, M.E., et al., *A PHGDH inhibitor reveals coordination of serine synthesis and one-carbon unit fate.* Nat Chem Biol, 2016. **12**(6): p. 452-8.

435. Sullivan, M.R., et al., *Increased Serine Synthesis Provides an Advantage for Tumors Arising in Tissues Where Serine Levels Are Limiting.* Cell Metab, 2019. **29**(6): p. 1410-1421.e4.

436. Geeraerts, S.L., et al., *The ins and outs of serine and glycine metabolism in cancer.* Nat Metab, 2021. **3**(2): p. 131-141.

437. Mehrmohamadi, M. and J.W. Locasale, *Context dependent utilization of serine in cancer.* Mol Cell Oncol, 2015. **2**(4): p. e996418.

438. Du, X. and H. Hu, *The Roles of 2-Hydroxyglutarate.* Front Cell Dev Biol, 2021. **9**: p. 651317.

439. Chaturvedi, A., et al., *Mutant IDH1 promotes leukemogenesis in vivo and can be specifically targeted in human AML.* Blood, 2013. **122**(16): p. 2877-87.

440. Bardella, C., et al., *Expression of Idh1(R132H) in the Murine Subventricular Zone Stem Cell Niche Recapitulates Features of Early Gliomagenesis.* Cancer Cell, 2016. **30**(4): p. 578-594.

441. Philip, B., et al., *Mutant IDH1 Promotes Glioma Formation In Vivo.* Cell Rep, 2018. **23**(5): p. 1553-1564.

442. Saha, S.K., et al., *Mutant IDH inhibits HNF-4α to block hepatocyte differentiation and promote biliary cancer.* Nature, 2014. **513**(7516): p. 110-4.

443. Wu, N., et al., *Alpha-Ketoglutarate: Physiological Functions and Applications.* Biomol Ther (Seoul), 2016. **24**(1): p. 1-8.

444. Chowdhury, R., et al., *The oncometabolite 2-hydroxyglutarate inhibits histone lysine demethylases.* EMBO Rep, 2011. **12**(5): p. 463-9.

445. Figueroa, M.E., et al., *Leukemic IDH1 and IDH2 mutations result in a hypermethylation phenotype, disrupt TET2 function, and impair hematopoietic differentiation.* Cancer Cell, 2010. **18**(6): p. 553-67.

446. Shelar, S., et al., *Biochemical and Epigenetic Insights into L-2-Hydroxyglutarate, a Potential Therapeutic Target in Renal Cancer.* Clin Cancer Res, 2018. **24**(24): p. 6433-6446.

447. Shim, E.H., et al., *L-2-Hydroxyglutarate: an epigenetic modifier and putative oncometabolite in renal cancer.* Cancer Discov, 2014. **4**(11): p. 1290-8.

448. Shenoy, N., et al., *Ascorbic acid-induced TET activation mitigates adverse hydroxymethylcytosine loss in renal cell carcinoma.* J Clin Invest, 2019. **129**(4): p. 1612-1625.

449. Xiang, K., et al., *Accumulation of oncometabolite D-2-Hydroxyglutarate by SLC25A1 inhibition: A metabolic strategy for induction of HR-ness and radiosensitivity.* Cell Death & Disease, 2022. **13**(7): p. 641.

450. Dos Santos, Á., et al., *DNA damage alters nuclear mechanics through chromatin reorganization.* Nucleic Acids Res, 2021. **49**(1): p. 340-353.

451. Flavahan, W.A., et al., *Insulator dysfunction and oncogene activation in IDH mutant gliomas.* Nature, 2016. **529**(7584): p. 110-4.

452. Kirby, T.J. and J. Lammerding, *Emerging views of the nucleus as a cellular mechanosensor.* Nat Cell Biol, 2018. **20**(4): p. 373-381.

453. Lele, T.P., R.B. Dickinson, and G.G. Gundersen, *Mechanical principles of nuclear shaping and positioning.* J Cell Biol, 2018. **217**(10): p. 3330-3342.

454. Stephens, A.D., et al., *Chromatin histone modifications and rigidity affect nuclear morphology independent of lamins.* Mol Biol Cell, 2018. **29**(2): p. 220-233.

455. Stephens, A.D., et al., *Chromatin and lamin A determine two different mechanical response regimes of the cell nucleus.* Mol Biol Cell, 2017. **28**(14): p. 1984-1996.

456. Sun, J., et al., *Force-induced gene up-regulation does not follow the weak power law but depends on H3K9 demethylation.* Sci Adv, 2020. **6**(14): p. eaay9095.

457.   Miroshnikova, Y.A., M.M. Nava, and S.A. Wickström, *Emerging roles of mechanical forces in chromatin regulation.* J Cell Sci, 2017. **130**(14): p. 2243-2250.

458.   Le, H.Q., et al., *Mechanical regulation of transcription controls Polycomb-mediated gene silencing during lineage commitment.* Nat Cell Biol, 2016. **18**(8): p. 864-75.

459.   Wintner, O., et al., *A Unified Linear Viscoelastic Model of the Cell Nucleus Defines the Mechanical Contributions of Lamins and Chromatin.* Adv Sci (Weinh), 2020. **7**(8): p. 1901222.

460.   Alisafaei, F., et al., *Regulation of nuclear architecture, mechanics, and nucleocytoplasmic shuttling of epigenetic factors by cell geometric constraints.* Proc Natl Acad Sci U S A, 2019. **116**(27): p. 13200-13209.

461.   Mito, T., et al., *Mosaic dysfunction of mitophagy in mitochondrial muscle disease.* Cell Metab, 2022. **34**(2): p. 197-208.e5.

Acknowledgements

This thesis is a culmination of the hard work and awesomeness of many special people who supported me through the PhD journey. I would like to start by expressing deep heartfelt gratitude to **Prof. Dr. Aleksandra Trifunovic** for her scientific mentorship and insightful discussions in the lab. At the very starting point itself you perceived the underlying genuine passion in me and channelized it into a very exciting work. My most memorable moments with you are the numerous hours we spent in deciding what not to follow for the project. Your incessant efforts to instill scientific rigour into your students is magnetic. Thank you for bearing with my stubbornness and bigger thanks for always compassionately understanding my personal commitments. Sandra, this balance of ambition and compassion that you embody, is something I am deeply inspired by. I cannot seem to fathom how you can step into the shoes of every single person you meet, and offer them just the exact support they need at every point! You and your journey have inspired me at multiple levels and my wish will be to become a

human like you and uphold scientific principles just the way you do. Even though I can go on and on with my *poetic expressions* (wink), I just want to say that you were everything that I had imagined the ideal mentor to be. I would not trade the moments spent in the lab with any other experience in the world and when I look back to the last four years, all I feel is a deep sense satisfaction and the feeling of being blessed to have found you. Thanks for making Trifunovic lab, a Home.

I would like to thank **Prof. Elena Rugarli**, **Dr. Lena Pernas** and **Prof. Thomas Wunderlich** for being a part of my thesis advisory committee. Your inputs and discussions were insightful. Thanks for encouraging me to 'let go' of certain aspects of the project and helping me develop a solid area of focus at every crucial step. I am also grateful to **Prof. Thomas Langer** for evaluating my thesis. Your comment on my poster at the EMBO conference 'Harshita, all this is very cool but what is the mechanism?' had filled me unparalleled passion to keep the search on for a mechanism. Thanks for inspiring all of us with your science and rigour. I would also like to thank **Prof. Guenter Schwarz** for agreeing to chair my thesis defense. I would also like to thank all our collaborators, for contributing to the varied aspects of this thesis. Special thanks and love to **Prof. Sara Wickstrom** for her incessant support with AFM experiments and for being there with me through every experiment.

Big words of gratitude and love for CGA co-ordination. Julia, Daniela and Jenny, thanks for supporting me through every step of the PhD journey. After having already expressed my love and admiration for you, the only thing I feel is a deep sense of gratitude. Wishing the best for you and the future of CGA.

This thesis would have been incomplete without the support and involvement of a great colleague and a dear friend, **Dr. Ulrike Göbel**. I always used to envy other institutes for having a very solid and well-advertised bioinformatics facility. But finding you was a real discovery! Your passion and sense of perfection for bioinformatics is very charming. Something just instantly clicked with us and now I have you as a friend for life. I think in the last leg of my PhD, I have had the most scientific discussions with you! Developing an entire pipeline, with so many things to offer was a daunting yet fulfilling task. Nothing could have been possible without you and cheers to spending sleepless thesis and bioinformatics nights together. Your high quality and persistent work has inspired me at multiple levels. I think the facility stands on your strong shoulders and I will very proudly advertise our bioinformatics facility whenever I can! Thanks for your understanding and support and I wish the best for you!

Many thanks to our amazing imaging facility members, Astrid, Katrin, Christian, Felix and Peter. Each of you have played a huge role in this thesis and I am thankful for all the laughs and frowns we have shared together. **Katrin**, you, specially, have inspired me and encouraged me at many levels. Thanks for loving me and I look upto you a lot. I loved our chai conversations and wish you the best for your inner journey.

Dr. Alexandra Kukat, a.k.a **Alex**, my one-woman army and support system in the lab. I think I shared an entire life with you on so many levels. Figuring out life with you was the best thing for me and concluding most of our conversations with 'das leben ist nicht einfach' was even better than the best! Shopping for you was the highlight of a lot of my trips and I have not felt this way for a lot of people- that should tell you how special you are for me! Thank you for being the unspoken therapist for a lot of people

in the lab and thank you for always upholding humility and compassion. You know the deepest details of my life and I have never been so raw and frank in front of anyone until today, as I have been with you. You have been my constant grounding force in lab and I will always remember how you put things in perspective for me. I transitioned from being an optimist to being a realist in your company and that has helped me deal with adulting a lot. I wish the best for you and your life and a deep sense of fulfilment and happiness envelops me when I look back to the times we spent together. By the way, Alex, 'Every night in my dreams I see you, I feel you… My heart will go on and on' (wink). Love you!

Lea Isermann, Franziska Bauman, Lance Chao Wu and Nidhi Nair, my bunch of ambitious and energetic mitochondriacs!!! You four are a complete package! Honestly, you guys are the exact kind of labmates that I had dreamt of having, you came in late into my life, but your impact on me has been the deepest amongst all my peers. Your energies are infectious! Together, I think you are torch bearers for taking the lab and our research to newer and unmeasurable heights- I am so excited to see how your perseverance and deep scientific insights enrich the lab.

Lea, my partner in crime! It only took me one frank discussion with you fall in love with your deep sense of understanding and objectivity. Somehow, your constant support and encouragement towards me would magically motivate me to hang in there. No one managed to encourage me the way you did! Our great bonding sessions in the animal house and the iconic 'being pushy together' moments will be forever etched in my heart. I cannot forget how many times (the number is embarrassing to state) you have reminded me of Maousoleum tasks and also helped me manage things I was not particularly good at! I think I saw you grow exponentially as a person in the last one year. I will always remember the advice from you on how to wear my confidence and walk on the streets- whenever I recollect that discussion, I end up laughing in tears! You are a very rare and powerful combination of a lot of things and I am looking forward to seeing the hypoxic magic you create!! XOXO.

Franzi, let me start by acknowledging that you have seen parts of me that no one else in the lab and my friend circle has seen (literally and figuratively) (wink)! Your sense of compassion and perfection is unparalleled. Being around you is like being around the calm in chaos. The sense of poise and maturity that you embody is very inspiring! And I am a big fan of how you mix creativity with science and invent ways to be more organized while doing experiments. You also have been my partner in crime for all things creative and compassionate in lab and those moments of chai with you were indeed special! Let's design some merch together. I am sure after our PhDs, we can make loads of money with it. I am looking forward to seeing the muscular magic you create in the lab (sticking out my tongue while writing this haha).

Lance, you have been a surprise package for me! I have always wondered how and when do you get so many things done!! I have realized that unlike many of us, you are a silent perfectionist. The sense of experience and coolness that you bring to lab is amazing. You have supported me at so many points and I find you a very cool person! It always feels special when I receive your origamis. I am very ambitious about you and am looking forward to seeing your learning curve and innate immune magic you create in the lab.

Nidhi! My very 'paavam kanya' (wink). Your scientific rigour and sense of confidence is infectious! It is amazing to revel in the sheer awesomeness that you embody. To me, you seem to be one of those few people who will make it work, at any cost and I love that about you. You are the dose of dopamine that sets my day right in many ways! I am addicted to our gossips and I am counting on you to find yourself a jiju. With you, I am confident that you won't ever change no matter what and that's really cool!! I am looking forward to witnessing your learning curve in lab and the inflammatory magic you create.

Four very special people who were a very integral part of my PhD journey are Matthijs, Hien, Gregor and Milica. **Matthijs**, I unconditionally look upto you. The most sorted, non judgemental and level headed person I have met. You have been a big bag full of knowledge and wisdom for me. I want to share something with you- a lot of times when I faced tricky situations in lab, I used to imagine, 'How would Matthijs handle it?' and it always used to help me imagine the past of least resistance to navigate a way out. I cannot tell you how much it meant to me when you called me a friend! It was a very special moment for me. Wishing you and Romy a very enriching parenthood. **Hien,** my companion through the transition phase in lab. I think your experiences and the wisdom you gained form them were a huge turning point in the dynamics in lab. The wave of love and togetherness started with you and I am so grateful for you. You have been and will be a very special person for me and I am thankful for the beautiful moments we spent together. I felt that you 'were' being the change that you wanted to see and that inspired all of us to level up our compassion and love game. Thanks for that and also thanks for gifting me with a wonderful jiju. Wish you and Simon a very enriching parenthood. **Gregor**, one of my favourite people! You are one crazy person and I do not understand how you balance the craziness with such a deep sense of responsibility! I am inspired by your energy. If I was ever crazy with someone about work and science in this lab, it was you! Remember our plans with preadipocytes? I am still in awe of how meticulously you had planned it all. Love you and hope that the consultant Gregor crosses paths with future Harshita. **Milica**, the moments shared with you in the lab were super nice. Thanks for being a very compassionate guide during our trips. As you say, you have the remarkable quality of being a non-judgmental mirror for everyone and its very nice to see you navigate life with this special quality. You are one of the smartest people I have met and I wish you the best for all your future endeavours.

Marijana, thanks for being supportive when nothing was working in the project. I am grateful to you for having frankly shared with me what you went through and those discussions helped me pick myself up when I had thought it would be impossible to do so. Thanks also for always being concerned for me and for your cool presence in the lab. Wish you a great parenthood ahead. **Aca,** as I have always shared with you, your ambition and eye for detail makes me a big big fan of you. Sometimes I wonder, how can Aca be so close to perfect in every respect? You are one big source of knowledge and scientific rigour! You have always offered a compassionate and helping attitude towards me and I am also very ambitious about you. Needless to say, your fashion sense is unparalleled. Cannot wait to witness the worm magic you create in lab. **Katha,** heartfelt gratitude for all your support to me for the project. You had stepped in to help

me at very critical moments in my PhD journey and I am thankful for all your help. I like how you balance various aspects of your life and I am inspired by it. **Linda**, you have held a very remarkable space in my PhD journey. I am inspired by how you manage diverse portfolios and work so hard on multiple levels. You are the personification of growth for me and thanks for being compassionate. **Karolina**, even though we overlapped for rather little time together, but your scientific inputs and training during my initial phase in lab was great. Thank you for your time and inputs and for always encouraging me to narrow down the scope of my work, step by step. **Ben**, you have been a surprise package for me. The deep wisdom you have shared with me, about life and science have left me speechless many times. Thanks for being a very compassionate colleague and I am looking forward to seeing the purified magic you create in lab!

A big thank you to the past members of the lab, Dr. Marija Herholz, Dr. Sophie Kaspar, Dr. Eddy Hofsetz, Dr. Sarah Miciej, and Dr. Anastasia Rumyantseva.

Personally, my biggest strength and pillar is my mom. I don't think a paragraph can do justice to the depth of influence her life has on me. Those who know me, know it that there are very few people for whom I have fought with the world, and you are one of them. **Dr. Reena Kaul**, thanks for being the inspiration for the future Dr. Harshita Kaul and for bearing with all the nonsense I have to offer. I think I stand on your shoulders and you are the base of my existence and powerful presence. Fighting with you and being dominating over you as if it is my birth right (which it is), are the best moments during my day. A lot of people cannot understand my love and fascination for you and I cannot seem to explain it to anyone. So cheers to living our dream life together, one dream at a time! Luboo. **Late. Smt Renu Kaul**, thanks for always showering your blessings and laying a strong value system for mamma and me to follow.

Special words of thanks for the friends in Cologne who became family. We have all gone through big phases together and grew and supported each other throughout. Thanks for making Cologne home for me. Love you all.

Last but not the least, I would like to thank one very special person, without whom this thesis would not have been possible, and that is **Harshita**. Thanks a lot for not giving up and always finding weird yet creative ways of keeping the ball rolling. You 'trusted the process' unconditionally, and let the project guide you, instead of attaching expectations to it. In many ways, you have displayed resilience and I am super grateful for always following your inner guidance. Dr. Harshita would always be grateful to Harshita for having created the abundance that she always wanted to experience and for letting that abundance be created. Let your PhD journey be a testimony that contrary to popular opinion, the PhD journeys can be beautiful, cherishable and biggest highlights of peoples' lives, as a growth phase, not just in science but also in philosophy. From here, it ought to be onwards and upwards. Cheers!

HARSHITA KAUL

PHD STUDENT

+49 151413350369

https://www.globalshapers.org/impact/vasudhaiva-kutumbakam-project-vk

harshita.kaul.gsc@gmail.com

MY PROFILE

II am an active social changemaker and have led pro bono projects in the area of public health, equity and women and refugee upliftment. Mentored by Dr. Soumya Swaminathan (Chief Scientist, World Health Organization), I am also currently pursuing my PhD in the area of fundamental biology of ageing and ageing related disorders.

EDUCATION

PhD / OCT 2019 - / Cologne Graduate School of Ageing / EIT Health Ageing PhD School

Aleksandra Trifunovic lab, CECAD Research Center, Cologne, Germany.

M.Sc by Resaerch / JULY 2016 - JULY 2019 / Junior Research Scholarship

Ullas Kolthur Lab, Tata Institute of Fundamental Research, Mumbai, India.

B.Sc (Hons.) / JUNE 2013 - June 2016 / MICROBIOLOGY

St. Xavier's College, Kolkata, India.

WORK EXPERIENCE (NON-ACADEMIC) AND LEADERSHIP POSITIONS

LEAD, UPLIFT-REFUGEE LEADERSHIP LAB AND INDO GERMAN INITIATIVE

Global Shapers, Dusseldorf / The initiative is currently running and includes skill development workshops for refugees in Germany and underprivileged students in Baramati, India- capacity building sessions, activist network of human rights activists and advocacy for refugee rights.

LEAD, GSC JUNIOR BOOTCAMP / INDO-GERMAN-NIGERIAN YOUTH LEADERSHIP TRAINING

Global Shapers, Dusseldorf / The bootcamp brought together young school and early college students from India, Germany and Nigeria to get trained into leadership and social changemaking. In cross country teams, they were mentored to launch local pro bono projects in the area of public health.

LEAD, VASUDHAIVA KUTUMBAKAM / INDO-GERMAN MENTAL HEALTH RELIEF INITIATIVE

Global Shapers, Dusseldorf / The initiative mobilized youth in Germany and India to provide mental health support to people in India during and after second COVID wave. Its poised to start its second phase soon.
https://www.globalshapers.org/impact/vasudhaiva-kutumbakam-project-vk

INCOMING HEAD, VICE CURATOR AND IMPACT OFFICER / GLOBAL SHAPERS DUSSELDORF

Leading and managing our registered NGO and leading impactful pro bono projects on women and refugee empowerment, sustainability, equity, education and public health.

WORK EXPERIENCE (NON-ACADEMIC) AND LEADERSHIP POSITIONS (CONT.)..

MEMBER, GERMAN ALLIANCE FOR GLOBAL HEALTH RESEARCH (GLOHRA)

....

CORE COMMITTEE MEMBER AND SPEAKER / TIFR OUTREACH COMMITTEE

Delivered public talks at multiple events and organised national science events.

....

HEAD, ENTREPRENEURSHIP DEVELOPMENT CELL / ST. XAVIER'S COLLEGE

Convener for the first chapter national level B fest, BizTatva. Led a team of 40+ people in the cell.

....

CORE COMMITTEE / ENACTUS SOCIAL ENTREPRENEURSHIP, ST. XAVIERS COLLEGE

Launched indigenous business for women from red light areas and provided voctional training. Led a team of 30 students and organized multiple inter college events.

....

HEAD GIRL (2010-2011) / DEBATE CAPTAIN (2012-2013) / OUR LADY QUEEN OF THE MISSIONS SCHOOL, KO

WORK EXPERIENCE (ACADEMIC) ....

July, 2016 – July, 2019 / Advisor: Prof. Ullas Kolthur-Seetharam
Title: Spermatogenesis and DNA damage repair: Regulation by SIRT1

The project aims at studying the role of the metabolic sensor SIRT1 in DNA damage response, spermatogenesis and transgenerational transmission of information from parent to offspring. Thesis published; Manuscript submitted for publication.

....

May, 2014 – July, 2014 / Advisor: Prof. Hemalatha Balaram
Summer Research Fellowship Programme at Jawaharlal Nehru Centre for Advanced Scientific Research, Bangalore, India.
Title: "Recombineering and generation of knock out construct in *Plasmodium berghei*"

....

Oct, 2014 – Dec, 2015 / Advisor(s): Dr. Abhijit Kar (JBNSTS), Dr. Riddhi Majumder (St. Xavier's College)
Scholars' project at Jagadis Bose National Science Talent Search, Kolkata.
Title: "Green Synthesis of Silver nanoparticles using Alpinia galanga and their antimicrobial activities"

HARSHITA KAUL
PHD STUDENT

+49 151413350369
https://www.globalshapers.org/impact/vasudhaiva-kutumbakam-project-vk

harshita.kaul.gsc@gmail.com

ACADEMIC AWARDS AND SCHOLARSHIPS

Plos Genetics Best Poster Award / Chromosome Stability Meeting, 2018, JNCASR, Bangalore.

Overall topper, Basic and Advanced coursework / M.Sc by research in Biology.

Gold medalist and topper / B.Sc (Hons.) in Microbiology

Jagadis Bose National Science Talent Search Scholarship, 2013.
Department of Science and Technology, India.

Innovation in Science Pursuit for Inspired Research (INSPIRE) Scholarship, 2013
Department of Science and Technology, India.

Medha Samman Award / First prize in independent research presentation JBNSTS, India.

A++ in Mathematics Talent Search Examination, 2009, JMMC, Kolkata.

DEBATING AWARDS AND EXPERIENCE

International champions / Debating matters India v/s UK, 2013 / British Council, Institute of Ideas

Invited debate judge by British Council- 03 / Debates, extempores won- 09

PUBLIC TALKS / ORAL PRESENTATIONS

Oral Presentation / Metabolism of ageing conference, September, 2021.

Science slam- Epigenetics- charms on the DNA, Cologne.

Science slam- A fatty affair / National science day and Science slam show, Cologne.
https://www.youtube.com/watch?v=2z6Ilqinz78

Soapbox science and Pint of science- Invited speaker / 2021

Public talk- METABOL: When you eat your body talks / National science day, TIFR.

Public talk- Gut Microbiome: the unseen majority / Frontiers of science, TIFR.

Oral Presentation / Indian Science Congress, January, 2016.

Science talk- Atoms and molecules / All India Radio (Akashwani), 2015.

Science talk- Science and spirituality / Modern trends in microbiology, 2014.

HARSHITA KAUL
PHD STUDENT

+49 151413350369

https://www.globalshapers.org/impact/vasudhaiva-kutumbakam-project-vk

harshita.kaul.gsc@gmail.com

PUBLICATIONS / MEDIA ACKNOWLEDGEMENTS ....

Research manuscripts

1. *NAD+-dependent deacetylase SIRT1 is essential for meiotic progression and controls repair-recombination efficiency*
Harshita Kaul, Shaunak Deota, Amit Fulzele, Anne Gonzalez-de-Peredo, Ullas Kolthur-Seetharam
(http://sci-hub.tw/10.1101/666891, preprint available on Bioarchives, manuscript under submission)

2. *Thioredoxin reductase controls the capacity of peroxiredoxins to limit mitochondrial H2O2 release*
Michaela Nicole Hoehne, Lianne J.H.C. Jacobs, Kim Jasmin Lapacz, Gaetano Calabrese, Lena Maria Murschall, Teresa Marker, Harshita Kaul, Aleksandra Trifunovic, Bruce Morgan, Mark Fricker, Vsevolod V. Belousov, Jan Riemer.

3. *FGF21 modulates mitochondrial stress response in cardiomyocytes only under mild mitochondrial dysfunction*
Marijana Croon, Karolina Szczepanowska, Milica Popovic, Christina Lienkamp, Katharina Senft, Christoph Paul Brandscheid, Theresa Bock, Leoni Gnatzy-Feik, Artem Ashurov, Richard James Acton, Harshita Kaul, Claire Pujol, Stephan Rosenkranz, Marcus Krüger, Aleksandra Trifunovic

4. *Isolation of Functional Mitochondria and Pure mtDNA from Murine Tissues*
Dieu Hien Roszivalova, Milica Popovic, Harshita Kaul

....

Vasudhaiva Kutumbakam (Project VK) features

https://theprint.in/ani-press-releases/covid-warriors-of-india-steps-forward-to-unconditional-support-covid-patients/688698/

....

CECAD / Women in science

https://www.cecad.uni-koeln.de/career/cecad-celebrates-its-women-in-science

....

Invited Health article / What's your gut feeling? / Mumbai Mirror, Bangalore Mirror and Pune Mirror, Times of India.

https://mumbaimirror.indiatimes.com/others/health-lifestyle/whats-your-gutfeeling/articleshow/61888332.cms

HARSHITA KAUL
PHD STUDENT

+49 151413350369

https://www.globalshapers.org/impact/vasudhaiva-kutumbakam-project-vk

harshita.kaul.gsc@gmail.com

WORKSHOPS / ADDITIONAL COURSES ....

Frailty in real life / University of Cologne, Germany
....

IPN Innovation & Entrepreneurship / Instituto Pedro Nunes, Coimbra, Portugal
....

Accelerate your career- Entrepreneurship for MINT students / University of Cologne, Germany
....

Metabolic remodeling in health and disease- from molecules to organelles to society / University of Coimbra, Portugal
....

Bringing science to primary schools / Institute for Bioengineering of Catalonia, Spain
....

Introduction into patent issues / University of Cologne, Germany
....

AGEING Workshop: Leading People & Mission / Dynargie, Portugal

CONFERENCES AND POSTER PRESENTATIONS (ACADEMIC) ....

TOTAL ACADEMIC OCNFERENCES ATTENDED- 15
....

TOTAL RESEARCH POSTER PRESENTATIONS MADE- 12
....

EXAMINATION SCORES ....

GRE- 313/340
TOEFL- 111/120
ISC (STD 12 BOARD EXAM) - 94.75%
ISCE (STD 10 BOARD EXAM) - 95.8%

PRO & PERSONAL SKILLS ....

Leadership / Research / Strategy and planning / Team work / Communication and oration / Compassion / Adaptability / Analytical / Conflict resolution / Philanthropy / Data analytics

EXTRA CURRICULAR INTERESTS ....

Kathak (Indian classical dance) / Travel / Singing / Philosophy / Debate

ADDITIONAL PROFILES..

LINKEDIN - https://www.linkedin.com/in/harshita-kaul-95340255/
TWITTER - https://twitter.com/harshitakaul
LAB WEBSITE - https://trifunovic.cecad-labs.uni-koeln.de/index.php?id=371&type=0